University of Szeged
Faculty of Science and Informatics
Doctoral School of Geosciences
Department of Physical Geography and Geoinformatics

Landslide hazard assessment using advanced remote sensing techniques and GIS

Ph.D. dissertation

Prepared by

Muhannad Hammad

Supervisors

Dr. Mucsi Lászlo
Associate professor

Dr. Boudewijn van Leeuwen
Assistant professor

Szeged

2020

CONTENTS

1. Introduction

1.1 Background

Geohazards are natural phenomena containing all the different geological processes and geographical features that are capable of triggering catastrophic events or natural disasters that threaten human beings and damage property, critical infrastructure and the natural environment in the areas where they occur.

The impact of these catastrophic events is higher in developing countries than in developed countries due to the fact that developing countries do not have advanced disaster mitigation and disaster preparedness programs like in developed countries (Zorn, 2018).

Tens of thousands of people around the world lost their lives during the last decade due to various natural disasters such as earthquakes, landslides, volcanoes and avalanches, etc. Among them, around a thousand died due solely to landslides (Figure 1.1).

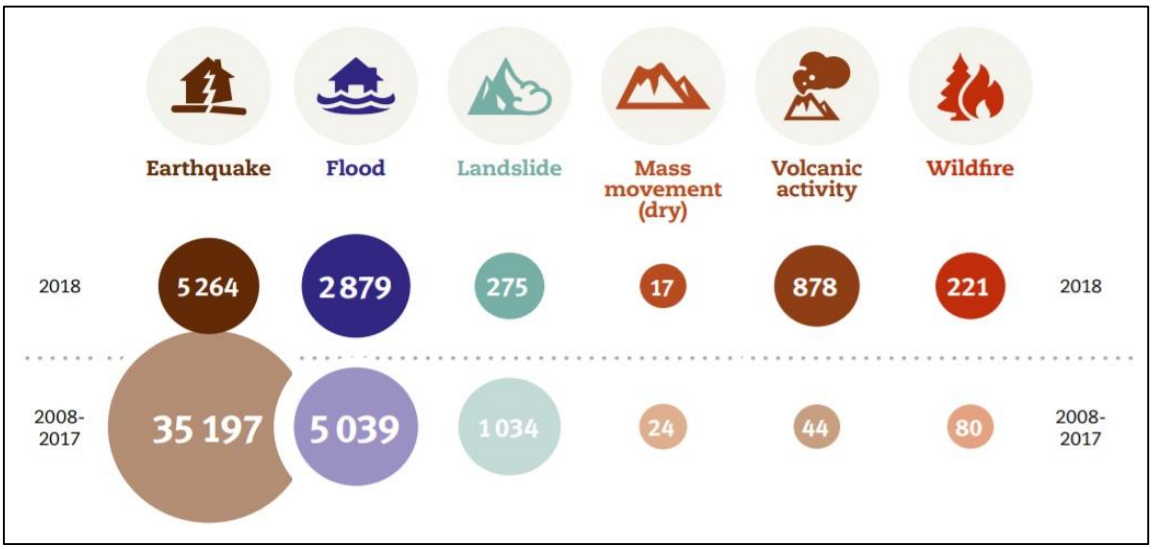

Figure 1.1: Number of deaths around the world by disaster type: 2018 compared to 2008-2017 annual average (CRED, 2019).

In general, a geohazard map delineates the most vulnerable areas to a specified natural hazard. Since landslides are an important type of geohazards, it is necessary to assess and map the susceptibility and hazard of landslides with the highest available spatial and temporal resolution. In principle, landslide susceptibility and hazard maps are important to understand and assess the relative contributions of all causative factors involved in landslide processes within an area. Moreover, landslide hazard maps identify potential locations and sites that could be affected by landslides in an area, to reduce the risk to people in that area and to help local authorities in future regional planning processes. In general, landslide susceptibility and hazard maps are becoming increasingly important in many places around the world, including in the coastal mountain region of Syria, where landslides normally occur (Figure 1.2).

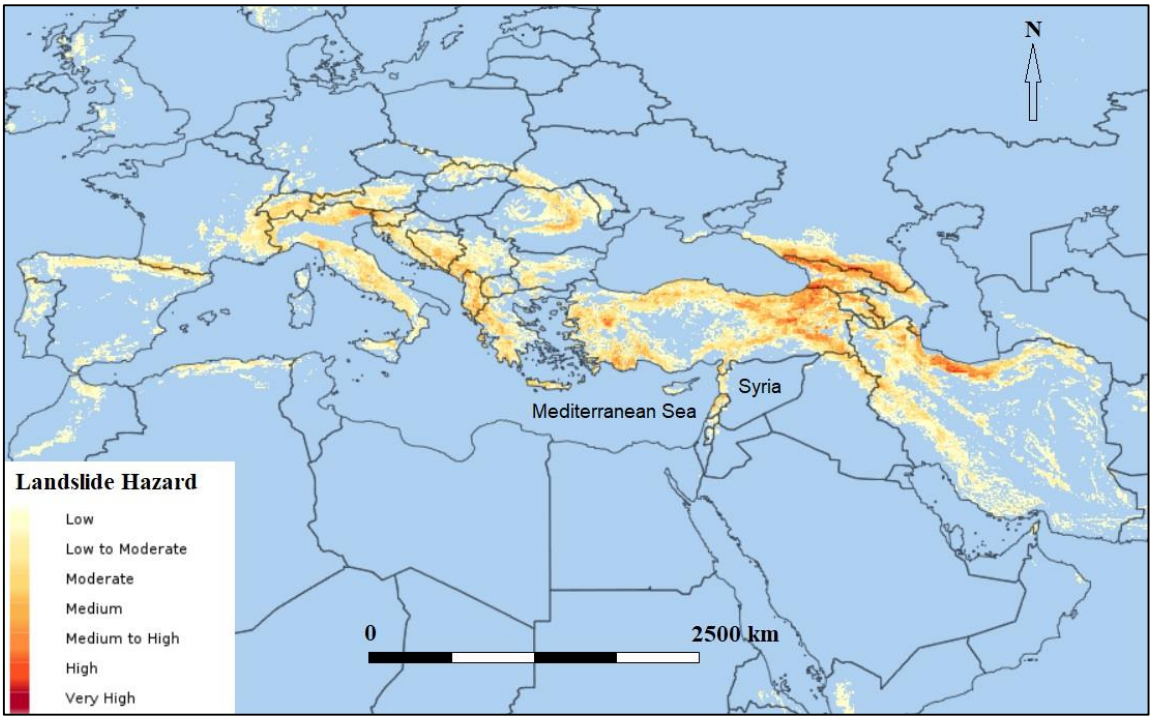

Figure 1.2: Landslide hazard distribution (after CHRR et al., 2005; Dilley et al., 2005).

Previous attempts of using Earth observation data for landslides investigation were typically based on field work and visual interpretation of aerial photos which are relatively time-consuming and not always easy to be carried out. Later, with the start of the satellite data era, processing and analysing of optical satellite data has been applied to detect relief changes between different dates. Furthermore, landslide investigation has been developed providing remarkable results, especially through the integration of optical remote sensing data and Geographic Information System (GIS) using different statistical analysis models to investigate and map landslide susceptibility zones (Biswajeet and Saro, 2007).

Later, it has been shown that Synthetic Aperture Radar (SAR) satellite data can be used as a complementary data source providing useful and precise information about ground-surface deformation and landslides. In this direction, some approaches have already considered the use of radar time series Interferometry SAR (InSAR) techniques for providing information on slope stability by analysing the total value and velocity of these ground-surface deformations. The most effective approaches of using interferometry for investigating and measuring ground-surface deformations have applied mainly the Differential InSAR (D-InSAR) and Persistent Scatterer Interferometry (PSI) techniques (Gabriel et al., 1989; Hooper, 2006).

New approaches to landslide hazard assessment are constantly needed to make use of the latest, freely available remote sensing data and techniques. Therefore, this research attempts to integrate all available data with the help of GIS in order to investigate and predict the locations of high-hazard areas for landslides. Also, this research attempts to assist future landslide hazard and risk studies in northwest Syria.

1.2 Problem statement and motivation

The road network in northwest Syria is susceptible to unforeseen landslides. Several roads are damaged by landslides annually after intense rainfall events. These unforeseen landslides and the resulting damage to the road network threaten the lives and property of the people who live there and cause both direct and indirect losses.

The main direct losses are costs of removing debris from the roads and costs of roads construction, especially the highway between Latakia city, the main city in the Syrian coastal region, and the Turkish border near Kassab city in the north (Figure 1.3). The main indirect losses are disruption of economic and social activities which can hamper local and regional development.

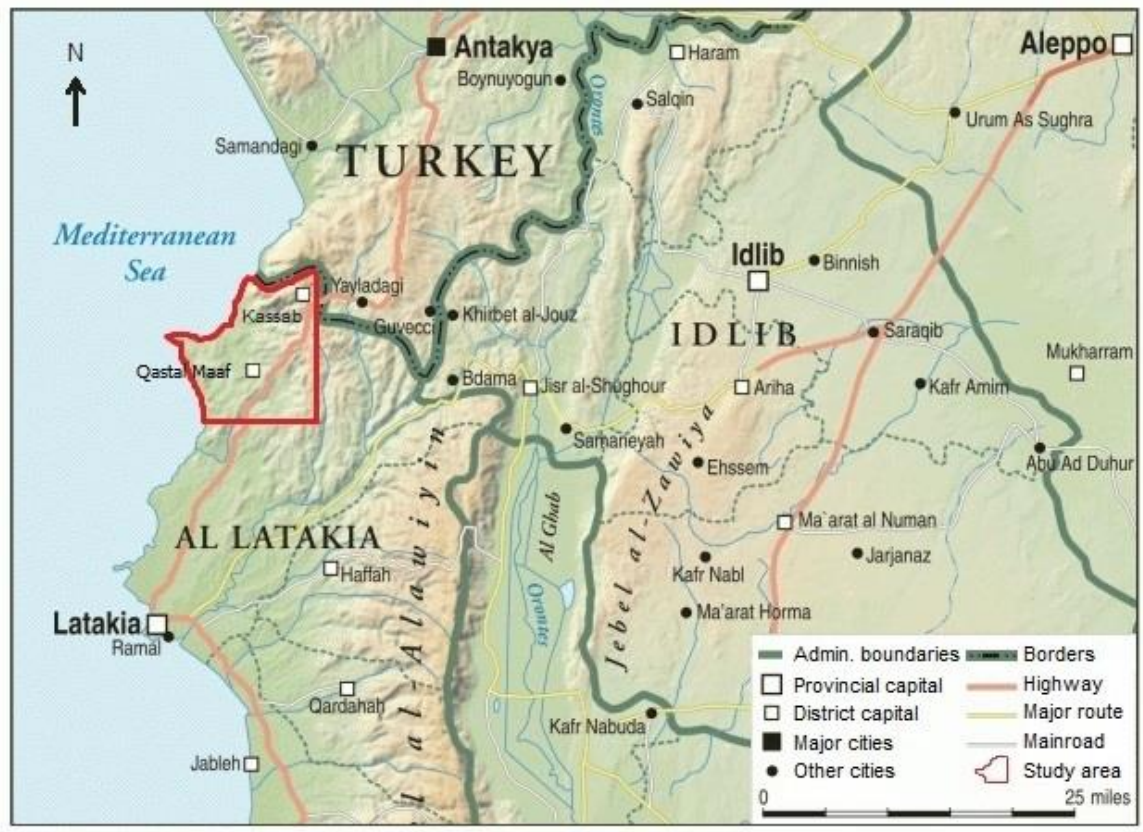

Figure 1.3: The location of the study area and the highway to the Syrian-Turkish border.

Some pervious geological and geotechnical studies were carried out after significant landslides events in the study area, but these studies were more descriptive geotechnical reports and were limited to specific and sporadic sites with limited spatial extents (Tahhan et al., 2009).

More specifically, the area in northwest Syria needs a comprehensive landslide susceptibility and hazard assessment study, leading to produce a landslide hazard map and identify potential landslide areas to be taken into account by the authorities in order to guide the regional planning processes and minimize the risk in these potential landslide areas.

1.3 Aims and objectives

The main aim of this research was to develop a workflow for the creation of the landslide hazard map for the entire study area that can be updated regularly to identify all sites with a high hazard for landslides throughout the area and along the road network, in particular along the highway. This will help local authorities to take the necessary precautions at all these sites to avoid losses due to possible future landslides along the highway. Based on the research aim, the following main objectives were defined:

- Determining the relative influence of each causative factor on the occurrence of landslides in the study area according to the statistical analysis process.
- Verifying the efficiency of the four different statistical analysis methods applied in this research for predicting landslide susceptibility.
- Using Sentinel-1 SAR data to generate a DEM of the study area and to measure the mean velocities of ground-surface deformations during the study period.
- Assessment of the landslide hazard using a landslide hazard matrix based on the landslide susceptibility and the ground-surface deformation intensity resulting from the mean velocity data of the PSI technique.

In the same context, the following research questions were answered:

- ❖ What are the most factors influencing and controlling the spatial distribution of landslides in northwest Syria?
- ❖ What is the best statistical analysis method of landslide susceptibility among the four statistical analysis methods applied in this research to pick out the optimal landslide susceptibility map?
- ❖ What are the advantages and disadvantages of using Sentinel-1 SAR data to generate a DEM or investigate ground-surface deformations?
- ❖ What is the spatial distribution and percentage of the low, medium and high hazard zones for landslides along the road network in northwest Syria during the study period? And what are the sites along the highway that could be considered high hazard areas for landslides?

1.4 Hypotheses

Within the framework of this research, the following hypotheses related to the main research objectives and questions regarding the study area in northwest Syria were constructed:

- ➢ **The first hypothesis:** The spatial distribution of rainfall-induced shallow landslides in northwest Syria, like similar places vulnerable to shallow landslides worldwide, is more influenced and controlled by land cover, lithology and slope gradient causative factors than by other causative factors.

- **The second hypothesis:** The statistical analysis method of artificial neural networks provides more accurate results of landslide susceptibility compared to the statistical analysis methods of frequency ratio, weight-of-evidence and logistic regression, which is consistent with related studies that compared two or more of these methods.
- **The third hypothesis:** The PSI technique and Sentinel-1 data can be used to measure millimetre mean velocities of ground-surface deformations in the satellite line-of-sight direction and determine where severe ground-surface deformations have occurred.
- **The fourth hypothesis:** The landslide hazard matrix based on the landslide susceptibility and ground-surface deformation intensity data, can be used in a GIS environment to identify high-hazard sites for landslides along the road network.

1.5 Framework

This dissertation has been divided into six main chapters which can be described briefly as follows:

Chapter one contains an introduction to the main topics of this dissertation and presents the research aims and objectives as well as the problem and hypotheses.

Chapter two describes the scientific background and basic concepts related to landslides and their classification, as well as their triggers and causative factors. Besides, this chapter describes the susceptibility and hazard mapping in GIS, with particular attention to the statistical analysis methods used to derive the landslide susceptibility map. Moreover, this chapter illustrates the role of remote sensing and GIS in landslide hazard assessment, and describes the PSI and D-InSAR interferometry techniques used for ground-surface deformation and landslide investigation.

Chapter three deals with the geological and geographical characteristics of the study area.

Chapter four is dedicated to the data and methods used in this research for preparing the Digital Elevation Models (DEM) of the study area and all main causative factors raster maps used in the landslide susceptibility mapping process. Moreover, this chapter describes the four statistical analysis methods used, including Frequency Ratio (FR), Logistic Regression (LR), Weight-of-Evidence (WoE) and Artificial Neural Networks (ANN). Furthermore, this chapter illustrates the validation and comparison process of the different statistical analysis methods as well as the landslide hazard assessment and mapping process.

Chapter five shows the final results of the research and discusses and analysis them, highlighting the best statistical analysis method for the study area, and showing strengths and weaknesses of SAR interferometry techniques regarding to landslide hazard assessment.

Chapter six contains the conclusion that can be derived from the overall results of this research.

2. Literature review

2.1 Landslides

Landslides as a sign of slope instability are defined as downward gravitational displacements of slope materials, whether bedrock, soil or a mixture of both (Varnes, 1978). Another widely used definition is given as downslope movement of rock, debris or soil that leads to a geomorphic change in the ground surface (Cruden, 1991; Cruden and Varnes, 1996; Mezösi et al., 2013).

In general, a landslide occurs when shearing strengths acting upon a slope exceed shearing resistance of this slope materials and reach the shear threshold (Terzaghi, 1950; Hungr et al., 2005). Landslides usually develop along defined surfaces called slip surfaces as shown in figure 2.1 which shows also the other main morphological elements of a landslide:

- Crown at the top of the landslide;
- Main scrap, which separates between the landslide crown and the head;
- Head of landslide along the contact between the displaced material and the main scarp.;
- Minor scrap of landslide or the steep surface along the displaced material;
- Main body of landslide or the displaced material of the landslide next to the minor scrap;
- Landslide foot or the portion that moved beyond the toe and overlies the original surface;
- Landslide toe at the bottom of the landslide.

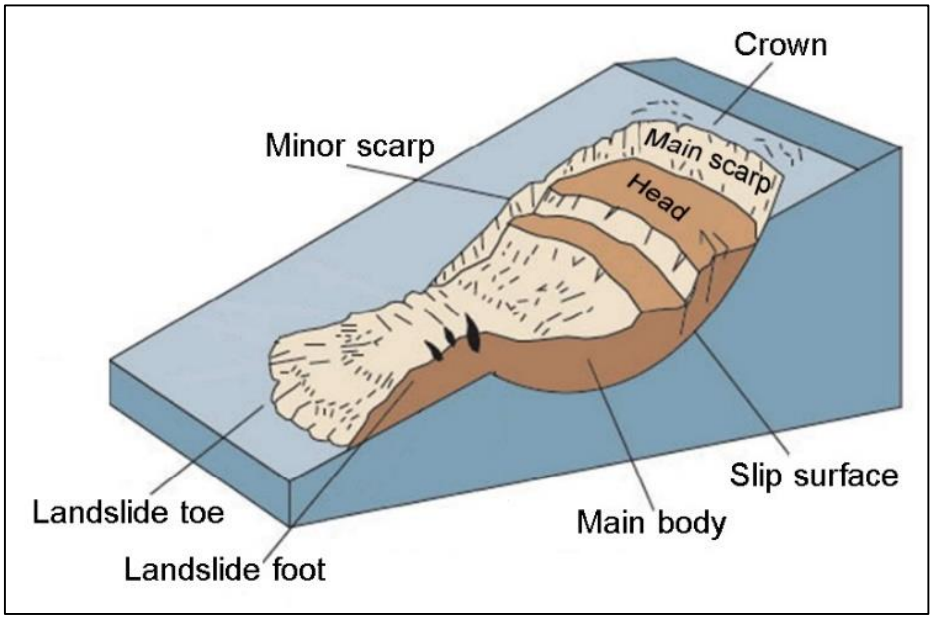

Figure 2.1: Landslide elements (after Highland and Bobrowsky, 2008).

However, a distinction must be made between a number of terms used in landslides studies:

- **Hazard:**
  Landslide hazard is defined as the probability of landslide occurrence with a particular intensity within a given area and period of time (Varnes, 1984). According to this definition, the landslide hazard should take both spatial and temporal probability into consideration.

- **Susceptibility:**
  Landslide susceptibility is simply the spatial probability of landslide occurrence (Fell et al., 2008). It focuses more on causative factors. While landslide hazard maps provide zones with predictions of where landslide is closer to occur or how large it will be, based on quantitative analysis, landslide susceptibility maps provide zones with certain conditions that allow landslide to occur. So, susceptibility is the spatial component of the hazard (Guzzetti, 2005).

- **Vulnerability**:
  Landslide vulnerability represents the potential for loss and damage from landslides. It distinguishes between human vulnerability, i.e. the potential number of deaths and injuries, and socio-economic vulnerability, i.e. direct damage to infrastructure, the disturbance of the economic activity and the disturbance of some social functions such as health and education. The value of landslide vulnerability ranges from 0, i.e. no damage, to 1, i.e. total damage (Morgan et al., 1992; Fell, 1994).

- **Risk:**
  The landslide risk shows the expected annual cost of landslide damage over all the affected area through combining both of the probability information from a landslide hazard map and the vulnerability analysis information of all possible consequences such as loss of lives, injuring of people, property damage, environmental damage and loss of service (Spieker and Gori 2000).

This research focused mainly on landslide susceptibility analysis and landslide hazard assessment using the integration of GIS and advanced remote sensing techniques.

2.1.1 Landslide Classification

Landslides are very diverse phenomena in shape and size, movement speed and other characteristics. In fact, landslide classifications follow diverse criteria, but the main classifications consider two criteria; the first one is the type of the slope material involved and the second one is the process type, speed and conditions (Varnes, 1978).

In general, as shown in figure 2.2, traditional slope movement classification has the following categories (Varnes, 1978):

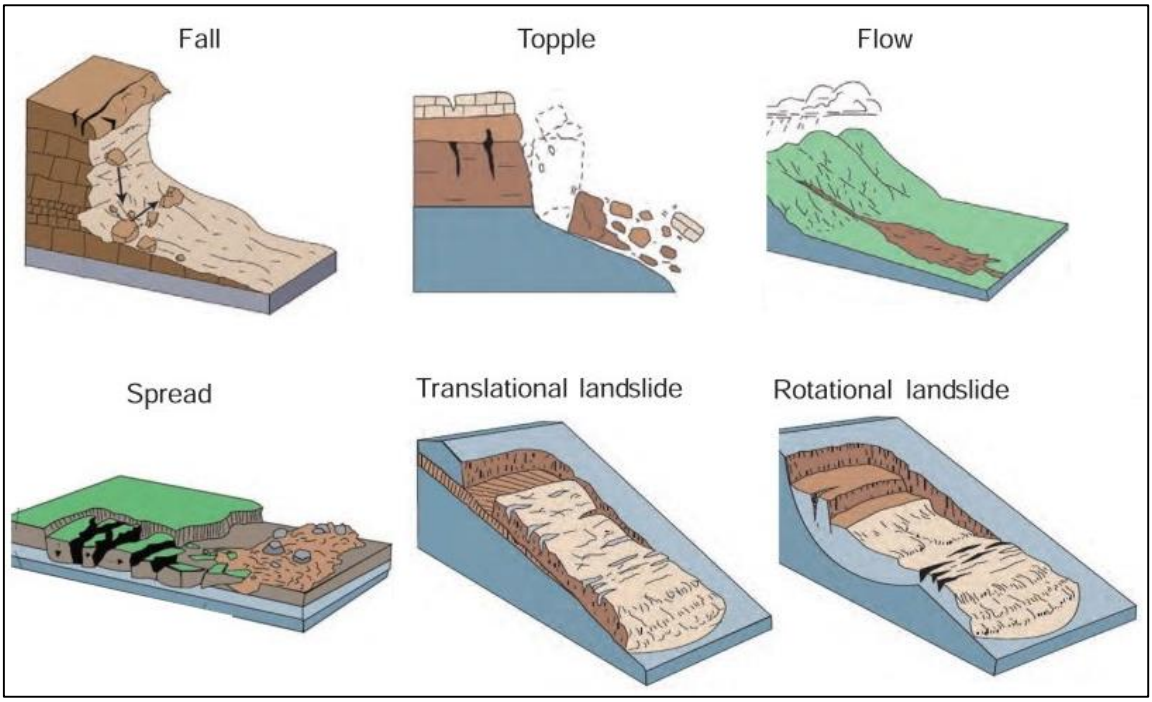

Figure 2.2: slope movement classification (after Highland and Bobrowsky, 2008).

- **Fall:** A descent of slope materials mainly through the air by falling or rolling.

- **Topple:** A forward rotation of the slope mass around an axis below the gravity centre of the displaced mass.

- **Flow:** A debris flow is a form of rapid mass movement in which a combination of different materials mobilizes as a slurry that flows downslope. Debris flows are usually caused by intense surface-water flow, due to heavy rainfall or rapid snow melt.

- **Spread:** A movement that usually takes place on very gentle slopes or on semi-flat terrain. The spread extension is accompanied by shear or tensile fractures. The spread is caused commonly due to liquefaction processes of the saturated fine deposits such as loose, sand and silt.

- **Landslide:** A downward movement of the mass that occurs predominantly on rupture surfaces. Landslide can be classified in two main sub-categories depending on the type of the movement, curved, which produces a rotational landslide, and planar, which produce a translational landslide:

  - **Translational landslides:** A translational landslide is a slope movement that involves translation of a slide mass along a relatively planar surface, occasionally followed by small rotational deposition at the landslide foot.
    The slope failures commonly occur along geological discontinuities, such as the intersection of jointing surface, fault, inclination or sub-horizontal bedding surfaces and along contact between rocks and soil. The materials involved in translational landslides range from unconsolidated sediments to large-scale blocks of rocks.

- **Rotational landslides:** A rotational landslide is a slope movement, observable at the surface through series of surface ruptures that are commonly characterized by concave and convex surfaces. The rotational landslides may occur along one or more sliding surfaces which could occur due to single or sequential sliding events. Rotational landslides often form due to human activities, and they are common along roads where slopes have been over-steepened during construction. They are also common along river banks and sea coasts, where erosion has under-cut the slopes. Heavy rains and earthquakes can trigger rotational landslides as well.

2.1.2 Main triggers and causative factors of landslides

Landslides can occur due to one or more landslide triggers such as intense rainfall, natural seismic activity such as earthquakes and volcanic eruptions (Alexander, 1989). In general, intense rainfall events can saturate sediments, allowing slope materials to slide past one another more easily. A slope that was stable under dry conditions can fail in wet conditions. Actually, intensive rainfall is considered to be one of the main triggers of landslides in the Mediterranean region to which the study area belongs (Tahhan et al., 2009; Lazzari and Piccarreta, 2018). Also, it was indicated that with increasing rainfall duration the minimum intensity that can cause slope failures decreases linearly (Guzzetti et al., 2007). In particular cases, intense rainfall does not produce effects due to the presence of karst, which absorbs a large part of the runoff water from surrounding areas (Khawlie and Hassanain, 1984; Pellegrini and Surian, 1996; Móga et al., 2013).

There are indications that the number of intense rainstorms worldwide is steadily increasing in recent years due to climate change (De Ploey et al., 1991; Joftic et al., 1992). In the eastern Mediterranean region, the maximum daily rainfall reached about 130 mm (Tayara, 1998). Furthermore, the effects of climate change on the precipitation regime in the eastern Mediterranean region show a remarkable shift towards semi-arid or arid conditions, which implies a reduction in rainfall quantities and concentrations in a small number of strong showers (Khawlie, 2003). These strong showers can initiate landslides through slipping inherently weak zones of rock and soil, and contribute in removing supporting materials along the toe of the slopes (Montgomery and Dietrich, 1994).

In addition to landslide triggers, there are many causative factors that facilitate the landslide occurrence process. These factors influence the stability of the slopes over time, and every factor can act as an accelerator allowing other factors to operate more effectively. Landslide causative factors are mainly summarized in five main classes as follows:

• **Geology:** This includes all unconsolidated deposits, faults, lineaments, joints, fractures and specific lithology types such as ribbon radiolarite and all clayey deposits which basically are very potential shear horizons as they retain water and once saturated they behave like a liquid resulting in occurrence of rapidly ground-surface movement (Varnes, 1978; Tahhan et al., 2009).

• **Topography:** This includes slope gradient, slope aspect and terrain curvature. In general, steep slopes are common in mountains throughout the Mediterranean region. The steeper the slope, the more likely it is to slide and the easier it is to disturb stability. Most landslides occur along slopes that are steeper than 20 degrees of slope gradient (Keefer, 1993; Cardinali et al., 2002). Moreover, slope aspect is strongly affected by the microclimate. For example, in the Mediterranean region, south-facing slope aspects are warmer and have higher evaporation rates than other-facing slope aspects, and this impacts soil development there and in some cases influences the occurrence of landslides (Dietrich et al., 1995; Brunsden, 1999; Capitani et al., 2013). Furthermore, an important factor of slope stability is the total curvature which consists of a plan curvature component across the slope, and a profile curvature component along the slope. Higher negative values of total curvature represent concave surfaces and in contrast higher positive values of total curvature represent convex surfaces, while zero values of total curvature represent planar surfaces (Figure 2.3). Basically, a planar surface with a total curvature value of zero is a more stable surface, and any absolute increase in the total curvature value in either direction, positive or negative, leads to a decrease in the overall stability of the surface (Sharma, 2013).

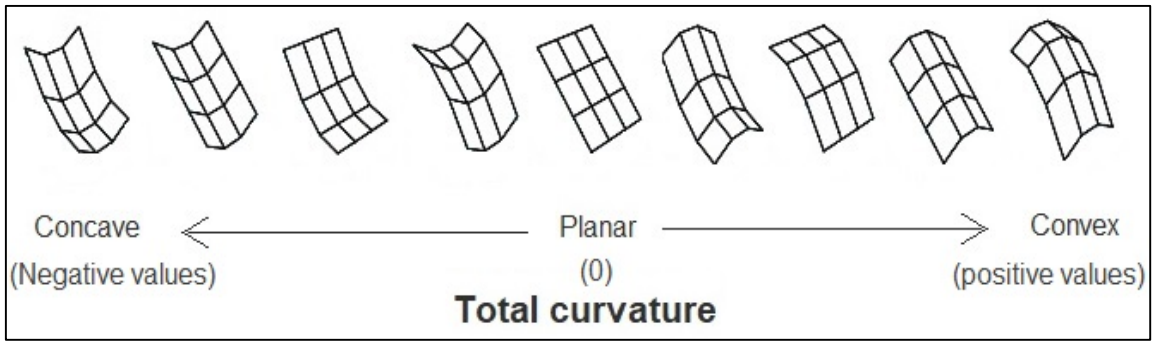

Figure 2.3: Terrain curvature types according to the total curvature value (after Sharma, 2013).

• **Vegetation:** Many studies have indicated a strong relation between vegetation cover and slope stability or landslide occurrence, especially for shallow landslides (Gomez and Kavzoglu, 2005). Forest or any type of tree vegetation cover helps stabilize slopes, especially for shallow landslides, since the roots of the trees can extend into soil layers improving this soil shear strength and its cohesion (Abe and Ziemer, 1990). Conversely, lack of vegetation cover would create favourable conditions for slope failure. Accordingly, Land cover and normalized difference vegetation index (NDVI) are important indicators of vegetation existence or absence over a specific area.

• **Water:** Stream network controls the surface water runoff and the development of the stream network and its continuous branching promotes in slope steepening process and causes slope failure (Mandal and Mondal, 2018).

• **Humans:** Usually, all human activities related to the urbanization and road constructions including extra-loading of a slope, changes in the slope profile, deforestation and land cover changes effect the slope stability and play an important role in increasing the probability of landslide occurring (Guzzetti et al., 2005).

2.1.3 Landslide susceptibility

Landslide susceptibility mapping usually delineates the degree to which a terrain can be affected by future slope movement. In other words, it is an estimate of where landslides will most likely occur. So, landslide susceptibility mapping is the probability of a landslide occurring in an area based on local terrain conditions (Brabb, 1984).

Susceptibility does not consider the temporal probability of failure such as when or how frequently landslides happen, nor the magnitude of the expected landslide such as how large or destructive the failure will be (Committee on the Review of the National Landslide Hazards Mitigation Strategy, 2004). In mathematical language, landslide susceptibility is an analysis of spatial occurrence probability of slope movements depending on a set of geo-environmental conditions (Vandine et al., 2004).

In general, landslide susceptibility can be distinguished and mapped as either qualitative or quantitative methods. The qualitative methods are based on the judgment and knowledge of experts, so they provide subjective and pure descriptive, i.e. non-quantitative, estimates of the landslide susceptibility level which tend to reduce the adoptability and objectivity of these methods (Aleotti and Chowdhury, 1999; Ayalew and Yamagishi, 2005). In contrast, the quantitative methods provide the landslide susceptibility in numerical terms, i.e. the probability of landslide occurrence in an area. The adoptability and objectivity of these methods have increased especially by the utilization of specialized tools and data such as Geographical Information System (GIS) tools, Global Positioning System (GPS) and all very high resolution remote sensing data (Metternicht et al., 2005; Van Westen et al., 2008; Józsa et al., 2019).

In general, the methods of landslide susceptibility mapping can be grouped into five main categories (Guzzetti, 2005):

• **Geomorphological mapping methods:** These methods of landslide susceptibility mapping are direct or semi-direct methods, and they give qualitative results depending on the ability of the investigator to recognize actual and potential slope failures (Kienholz et al., 1983; Hansen et al., 1995; Ayenew and Barbieri, 2005; Reichenbach et al., 2005). They are a form of expert judgement, and when pursued by well-trained investigators who have a good knowledge and background of the slope instability phenomena, these methods can provide reliable results (Guzzetti, 2005).

• **Heuristic or index-based methods:** These methods are also qualitative and indirect or semi-direct methods based on a prior knowledge of landslides' causative factors in the area under investigation. Causative factors in these methods are classified, ranked and weighted according to investigators' assumptions of their expected importance in causing landslides. Based on investigators' decision which involves certain subjectivity, heuristic rules are established to define and zone possibly unstable areas and landslide susceptibility accordingly (Nilsen and Brabb, 1977; Hollingsworth and Kovacs, 1981; Montgomery et al., 1991; Pachauri and Pant, 1992; Moreiras, 2005; Schleier et al., 2013).

• **Analysis of inventories:** These methods are indirect and their results are quantitative, and they provide some estimates of landslide susceptibility and hazard based solely on landslide intensity maps, without taking into account any causative factor that may lead to misleading or incorrect estimates (Guzzetti, 2005).

• **Conceptual or process-based models:** Conceptual models for landslide susceptibility mapping rely upon the understanding of the physical laws controlling slope instability. These methods are quantitative and indirect, and were mainly developed to investigate the effects of a specific trigger, such as an intense rainy period or an earthquake (Jibson et al., 1998; Miles and Ho, 1999; Luzi and Pergalani, 2000; Lin and Tung, 2004). In general, conceptual models attempt to extend spatially the simplified stability models widely adopted in geotechnical engineering, and calculate the stability of a slope using parameters such as normal stress, angle of internal friction, cohesion, pore water pressure, seismic acceleration, external weights, etc. (Guzzetti, 2005).

• **Statistical analysis methods:** Statistical analysis methods are quantitative and indirect methods attempting to predict future instability and landslide susceptibility through a statistical analysis of the functional relationships between the causative factors and the distribution of the existed landslides. Statistical analysis methods have consistently been demonstrating satisfactory accuracy and high adoptability in the landslides investigation studies (Guzzetti, 2005; Mancini et al., 2010; Nandi and Shakoor, 2010; Pradhan et al., 2011; Lee et al., 2012).

This research focused on the statistical analysis methods to produce the optimal landslide susceptibility map of the study area in order to produce a landslide hazard map which can be updated regularly in a GIS environment by using advanced remote sensing techniques.

2.1.4 Statistical analysis methods for landslide susceptibility mapping

In general, statistical analysis methods for landslide susceptibility mapping depend on some basic assumptions such as:

- Slope failures leave discernible features that can be recognized, classified and mapped in the field or through remote sensing imagery (Rib and Liang, 1978; Varnes, 1978; Hansen, 1984; Hutchinson, 1988; Cruden and Varnes, 1996; Dikau et al., 1996; Griffiths, 1999).
- Landslides are controlled by mechanical laws that can be determined empirically, statistically or using deterministic methods. The related causative factors can be used to build predictive models of landslide occurrence (Crozier, 1986; Hutchinson, 1988; Dietrich et al., 1995).
- For landslides, the past and present are keys to the future (Varnes and IAEG Commission on Landslides and other Mass-Movements, 1984; Carrara et al., 1991; Hutchinson, 1995). In principle, future landslides will be more probable to occur under the same conditions which led to the past and present landslides.

The traditional statistical analysis methods for landslide susceptibility mapping are based on the probability model, the so-called frequency ratio (Lee et al., 2004; Yilmaz, 2009). The frequency ratio method remains one of the most popular methods for its simplicity, as well as accepted prediction accuracy as reflected in most comparative studies (Lee and Pradhan, 2007; Poudyal et al., 2010; Lepore et al., 2011; Mohammady et al., 2012; Solaimani et al., 2012; Ozdemir and Altural, 2013). Some studies have indicated that the logistic regression and Bayesian weights-of-evidence methods have better prediction accuracy than others (Chung and Fabbri, 1999; Dai and Lee, 2003; Lee, 2004; Oh et al., 2009; Pradhan and Lee, 2009; Akgun, 2011; Shahabi et al., 2014).

Also, advanced statistical analysis methods have been used recently for landslide susceptibility mapping, and the most popular method nowadays is the Artificial Neural Network (ANN) method (Biswajeet and Saro, 2007; Lee, 2007; Choi et al., 2009; Yilmaz, 2009; Chauhan et al., 2010; Pradhan et al., 2010a; Conforti et al., 2014).

To date, there is no definitive statistical analysis method for landslide susceptibility and the effectiveness of any method largely depends on the applied method, the characteristics of the study area, the input data and finally the experience of the modeller (Soeters and van Westen, 1996). However, in case of applying different statistical analysis methods, all results need to be integrated in a GIS environment in order to be compared to each other and the optimal results can be used to derive the final map of the landslide susceptibility (Xu et al., 2012).

Any statistical analysis must be validated in order to assess its efficiency and compare it with other statistical analyses. Area Under the Curve (AUC) analysis is one of the best means for this process. AUC can be calculated using a cumulative validation curve, known as a prediction rate, using a testing set of landslides which was not included in the landslide training set used during statistical analysis. In the cumulative validation curve, the x-axis represents 100 equal interval classes of the landslide susceptibility index, while the y-axis represents the cumulative percentages of the landslide area in each susceptibility class based on the total landslide area of the landslide testing dataset (Remondo et al., 2003; Pradhan et al., 2017).

The AUC gives a good evaluation of the statistical analysis efficiency, and it also allows comparison of different statistical analyses with each other for determining the optimal analysis for the study area (Yesilnacar and Topal, 2005). In general, an AUC with a value less than 60% reflects that the statistical analysis has no ability to discriminate areas with high susceptible to landslide, while an AUC with a value between 60% and 70% reflects an acceptable statistical analysis, an AUC with a value between 70% and 80% reflects a good statistical analysis, an AUC with a value between 80% and 90% reflects a very good statistical analysis, and an AUC with a value more than 90% reflects an excellent statistical analysis (Silalahi et al., 2019).

More details are described in chapter four about the statistical analysis methods used for landslide susceptibility mapping and their validation process.

2.1.5 Landslide hazard

Sometimes, the terms susceptibility and hazard are erroneously used as synonyms, therefore some so-called landslide hazard maps are actually susceptibility maps, as they do not consider the temporal and intensity dimensions along with the spatial aspect (Hervás and Bobrowsky, 2009).

Basically, landslide hazard is the probability of landslide occurrence with a particular magnitude or intensity in a given area within a reference time period (Guzzetti et al., 1999). The landslide intensity can be mainly expressed in terms of average velocity or volume (Amatruda et al., 2004; Ojeda-Moncayo et al., 2004; Lee and Jones, 2004; Li et al., 2010). In addition, landslide hazard can be assessed using a hazard matrix of both susceptibility and intensity, or even by analysing the recurrence of landslides or analysing the relationship between landslides and the chronological records of any landslide trigger such as rainfall or earthquakes of known magnitude (Fernández et al., 2013).

In general, many approaches to landslide hazard assessment using a hazard matrix of both susceptibility and intensity defined landslide intensity mainly as a function of the mean velocity of deformations (Lateltin et al., 2005; Righini et al., 2012; Cigna et al., 2013; Bianchini et al., 2017; Pellicani et al., 2017; Solari et al., 2020). Actually, these approaches rely on the fact that the inverse of this mean velocity can be used for a temporal prediction of a slope failure depending on the linear relation between the logarithms of the first and second derivatives of slope deformation (Fukuzono, 1990; Hungr et al., 2005) (Figure 2.4).

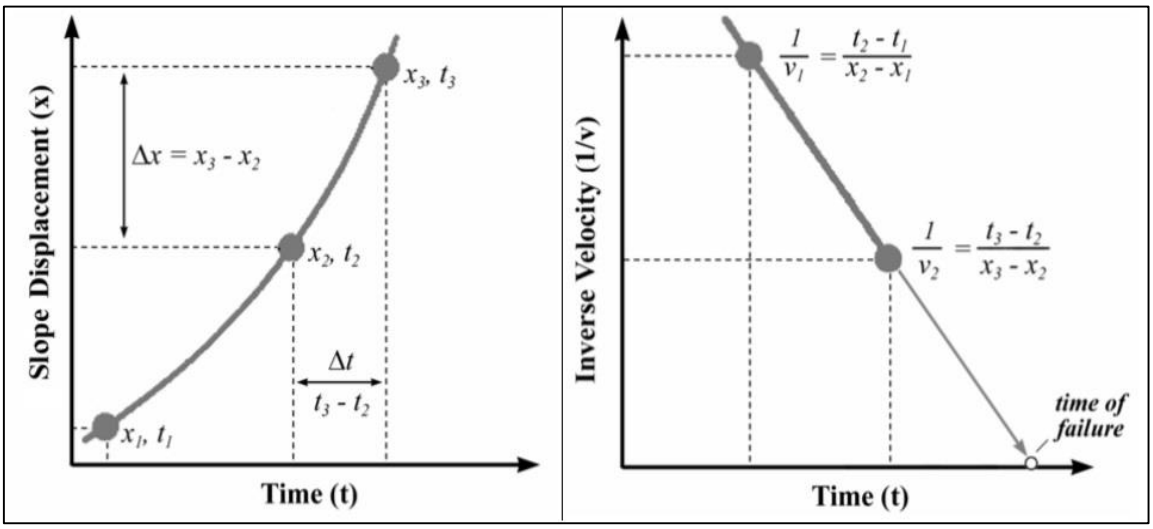

Figure 2.4: Method for a temporal prediction of a slope failure based on slope deformation and mean velocity (Fukuzono, 1990).

The mean velocity data of ground-surface deformations used in landslide hazard assessment can be obtained by using advanced interferometric techniques as it can be seen later in this dissertation.

2.2 The role of remote sensing in landslide hazard assessment

Remote sensing as an approach of obtaining information without physical contact (Lillesand and Kiefer, 1994) is capable to survey all areas even inaccessible areas or where field works are difficult to be carried out. Basically, remote sensing is the major source of spatial information about the ground surface cover and can be considered a valuable tool for landslide studies at different stages such as detection, monitoring, susceptibility analysis and hazard mapping (Mantovani et al., 1996).

The advances of remote sensing techniques and data accessibility are always developing rapidly. New remote sensing techniques are often developed in very short time, and landslide hazard studies using remote sensing techniques become more and more applicable. Actually, remote sensing data and techniques are being used in landslide studies starting with stereoscopic aerial photo interpretation up to all the optical and radar satellite data and advanced techniques available nowadays.

On one hand, optical remote sensing data is used through visual inspections for landslide inventory mapping, and also through analytical methods for landslide susceptibility analysis and mapping. Maps of some causative factors can be prepared depending on the derivative products from optical remote sensing data using related techniques such as colour composites, Principal Component Analysis (PCA) and Band Ratios (BR) (Canuti et al., 2004; Metternicht et al., 2005). Accordingly, multispectral satellite images have been used widely to discriminate differences in lithology, land cover and NDVI, which are all considered as major causative factors of landslide occurrence. Principal Component Analysis (PCA) of multispectral satellite imagery is a technique that transforms a set of correlated variables, i.e. original bands, into other uncorrelated variables, i.e. principal components, in which the first few components will account for a large part of the total variance with substantial improvement in the signal-to-noise ratio (Singh and Harrison, 1985). Also, Band Ratios (BR) is a technique consisting of ratio operations between the values of the corresponding pixels of at least two different bands in order to enhance the capability of lithological discrimination between different rock types (Rothery, 1984; Sabins, 1999; Abdelmalik and Abd-Allah, 2018; El-Atillah et al., 2019). Besides, band ratios technique uses Red (R) and Near-InfraRed (NIR) bands to calculate NDVI value which is a simple method that can be useful to maximize the contrast between areas depending on vegetation density (Weier and Herring, 2000).

On the other hand, radar remote sensing has an advantage for the acquisition of ground information over optical remote sensing because radar remote sensing is capable of penetrating clouds and operating independently of weather conditions. Moreover, radar satellite data and advanced time-series interferometric techniques can be used in landslide studies and can provide very precise results regarding landslide investigation, monitoring and hazard mapping (Casagli et al., 2017). The most important radar satellites and their specification in addition to their revisit period are shown in figure 2.5.

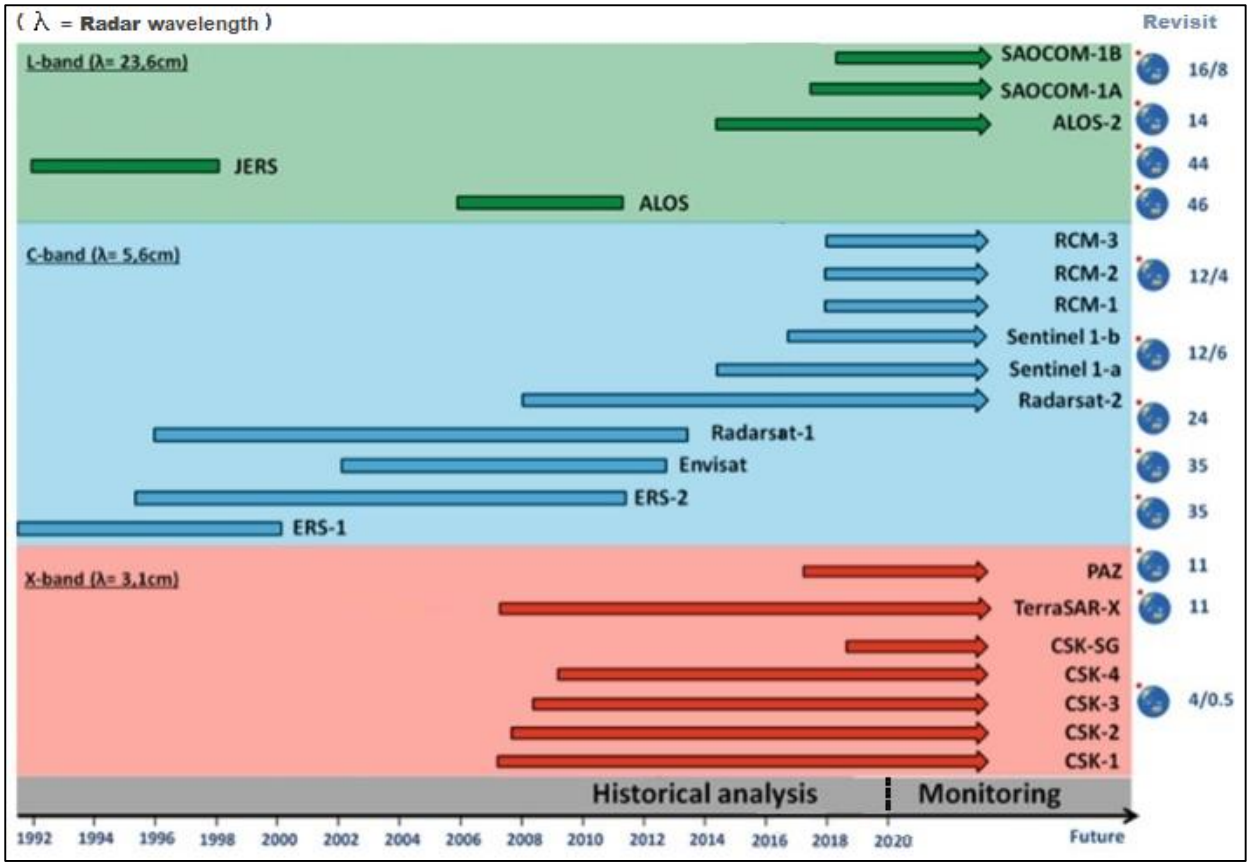

Figure 2.5: Most important radar satellites (after Casagli et al., 2017).

Interferometric Synthetic Aperture Radar (InSAR) contains a group of advanced radar remote sensing techniques in which amplitude and phase components of the backscattered radar signal are used to extract information about topography and deformation of the ground surface. In general, amplitude is the strength of the radar backscatter based on the local reflectivity of the terrain, while the phase of the SAR images records primarily information on the distance between the satellite antenna and the ground surface (Bunch and Hellemans, 2004).

InSAR techniques can identify ground-surface deformations depending on the phase shift between the same ground pixels of at least two different SAR acquisitions from different passes for the same portion of terrain. Therefore, in the case of good coherence between two SAR images, it is possible to obtain information with sub-centimetre precision about ground-surface deformations in the satellite Line-Of-Sight (LOS) direction by unwrapping the displacement phase of the interferogram generated from these two images (Gens and Van Genderen, 1996; Fielding et al., 1998; Vasco et al., 2010; Ng et al., 2012; Capes and Teeuw, 2017; Pepe, 2017; Hammad et al., 2018b). The phase shift can be resulted as a set of interferometric fringes appear as cycles of colours in the displacement phase of the interferogram generated from the two SAR images. Each of these cycles corresponds to half of the SAR wavelength and is represented as 2 π radians (Gabriel et al., 1989; Garthwaite et al., 2015) (Figure 2.6).

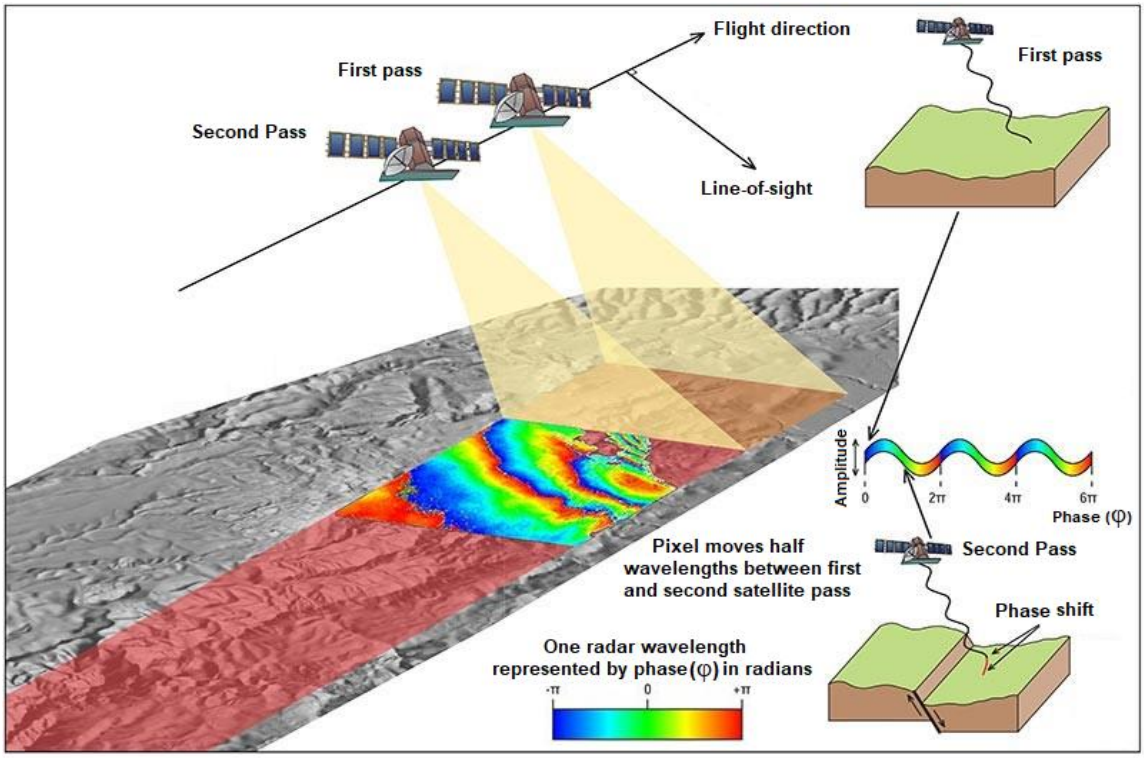

Figure 2.6: Interferometric synthetic aperture radar technique (after Garthwaite et al., 2015).

The complex phase of an interferogram can be expressed as the sum of five components (Mora et al., 2003; Veci, 2016):

$$\varphi = \varphi_{elev} + \varphi_{disp} + \varphi_{atmos} + \varphi_{flat} + \varphi_{noise} \quad (1)$$

Where, φ is the complex phase of an interferogram generated from SAR acquisitions;

φ_{elev} is the topographic phase component;

φ_{disp} is the displacement phase component caused by a deformation of a scatterer between SAR acquisitions;

φ_{atmos} is the atmospheric phase component that represents a signal delay error due to humidity, temperature and pressure changes between SAR acquisitions;

φ_{flat} is the flat-earth phase component which is an error caused by the curvature of the surface or the reference plane; and

φ_{noise} is the phase component of noise caused by variability in the scattering of a pixel due to volume scattering, different look angles, or co-registration errors.

In addition to using the complex phase to obtain information about ground-surface deformations by subtracting all components except the displacement phase component, it is also possible to use the complex phase to obtain information about the topography of an area by subtracting all components except the topographic phase component and unwrapping this phase component to generate the digital elevation model of the area (Hammad et al., 2017).

It should be noted that the phase unwrapping process can be performed applying different interferometry techniques using different advanced algorithms and software packages, such as SNAPHU and StaMPS, to generate the final unwrapped phase from the wrapped phase according to geometric rules to obtain the required deformation data (Ferretti et al., 2007).

InSAR techniques can be used in various geological hazard studies, including landslides, earthquakes, volcanic activity and subsidence processes caused by groundwater or hydrocarbon extraction (Capes and Teeuw, 2017). Particularly for landslide studies, InSAR techniques play an important role since they have the capability to measure both the total value and the mean velocity of ground-surface deformations with millimetre precision (Squarzoni et al., 2003; Rott and Nagle, 2006; Corsini et al., 2006; Canuti et al., 2007). Although there are different InSAR techniques used for landslide studies, there are some common limitations of using InSAR in landslide hazard studies because its results generally degrade significantly in dense vegetated areas and snow-covered surfaces (Stumpf, 2013).

The SAR data used in this research was acquired by the Sentinel-1 satellite constellation which was launched by the European Space Agency (ESA) starting with Sentinel-1A in 2014 and followed by its twin satellite Sentinel-1B in 2016. These two satellites carry an identical C-band SAR sensor with a wavelength of 5.547 cm and offer four acquisition modes: Stripmap (SM), Wave (WV), Interferometric Wide swath (IW) and Extra Wide swath (EW), as well as three product types: Single-Look Complex (SLC), Ground-Range Detected (GRD) and Ocean (OCN), with medium to high resolution and wide ground coverage of 250 km. They provide single and dual polarisation capability, short revisit time of 12 days and rapid product delivery with precise measurements of spacecraft position and attitude (Yagüe-Martínez et al., 2016).

Two main InSAR techniques were applied in this research. The first technique was Persistent Scatterer Interferometry which was used for generating the mean velocity map of the ground-surface deformations. The second technique was Differential Interferometric Synthetic Aperture Radar which was used for generating the map of total ground-surface deformations.

2.2.1 Persistent scatterer interferometry technique

The Persistent Scatterer Interferometry (PSI) technique was developed to be applicable in areas where slow ground-surface deformation can occur even without prior knowledge of variations in this deformation rate, and to overcome most of the limitations of the decorrelation associated with traditional interferometric techniques, which makes the PSI applicable even when acquisitions have a large amount of noise or when there is atmospheric inhomogeneity (Ferretti et al., 2001; Hooper, 2006).

The main goal of PSI technique is to identify individual pixels known as Persistent Scatterers (PS), which are coherent over time intervals, even from different look-angles, and whose electromagnetic characteristics do not vary significantly from acquisition to acquisition. On each of these PS points, a millimetre ground-surface deformation rate can be achieved in addition to other time-series parameters from their amplitudes and phases, even if the coherence is not high in surrounding area (Ruccia et al., 2012) (Figure 2.7).

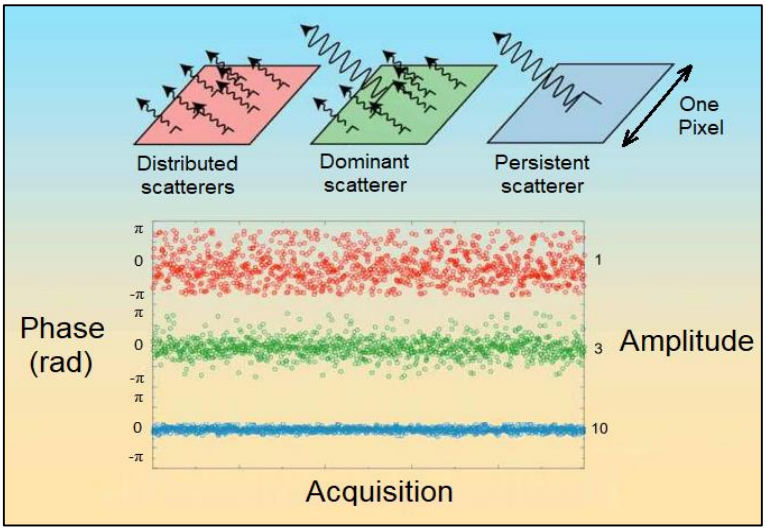

Figure 2.7: Scatterer types (after Tarikhi, P., 2010).

The PSI technique requires a large number of SAR images to select the statistically reliable PS points that are immune to the effects of decorrelation phenomena, and to estimate the contribution of atmospheric and noise phases to be removed from each PS point to accurately estimate the mean velocity of deformation at these points. The results of the mean velocity should be sorted or reclassified, according to specific thresholds depending on the resulting values, in order to classify active deformations or landslides and in some cases to overcome strong noise (Kalia, 2018; Kovács et al., 2019).

In the PSI technique, first a group of SAR acquisitions for same area is co-registered as slave images on a unique master imagery with different temporal and geometric baselines using a topographic reference of this area. Next, interferograms between each slave and the master must be generated, so the unwrapped phases can be obtained from these interferograms using advanced phase unwrapping logarithms which allow to measure the mean velocity of ground-surface deformation in satellite LOS direction for each PS point averaged over the total study period, provided that the signal-to-noise ratio is high enough (Hooper et al., 2012; Hooper et al., 2013).

2.2.2 Differential interferometric synthetic aperture radar technique

For deformation purpose, D-InSAR technique uses two corresponding SAR acquisitions and a topographic reference to generate an interferogram which can be used to extract the displacement phase component after subtracting and removing all other components from the complex phase of this interferogram. By unwrapping the displacement phase using a software package called the Statistical-cost, Network-flow Algorithm for Phase Unwrapping (SNAPHU), it is possible to compute the unwrapped phase and sum the number of InSAR fringes to get the relative values of all related ground-surface deformations (Massonnet and Feigl, 1998; Rosen et al., 2000). Several researchers have indicated the usefulness of D-InSAR in landslide studies (Fruneau et al., 1996; Singhroy et al., 1998; Rott et al., 1999; Ye et al., 2004; Strozzi et al., 2005; Catani et al., 2005; Putri et al., 2013; Hammad et al., 2019).

In general, good candidate images for producing accurate interferometric displacement results must have strong similarities, therefore coherence between master and slave must be taken into consideration. Loss of coherence can be caused due to temporal reasons such as different acquisition times; geometric reasons such as orbit errors or volumetric reasons such as vegetation. Relative values of ground-surface deformation in the satellite LOS direction have a strong relation with absolute vertical ground-surface deformation values, since the ground-surface deformation in the satellite LOS direction is considered as the projection of vertical deformation in the LOS direction. This deformation can be converted from radian values in the unwrapped phase to millimetre values using the following equation (Ferretti et al., 2007; Braun and Veci, 2020):

$$\mathrm{def}_{\mathrm{mm}} = \mathrm{def}_{\mathrm{rad}} * (\lambda/4\pi) \quad (2)$$

Where, $\mathrm{def}_{\mathrm{mm}}$ is the ground-surface deformation in the LOS direction in millimetre values;

$\mathrm{def}_{\mathrm{rad}}$ is the ground-surface deformation in the LOS direction in radian values; and

λ is the SAR wavelength in millimetres.

In interferometry, the linear relation between the subsidence profile and the horizontal displacement measurements in the satellite LOS direction can be drawn taking into consideration that the tilt was defined as the first derivative of the subsidence profile as shown in figure 2.8 (Esfahany et al., 2009).

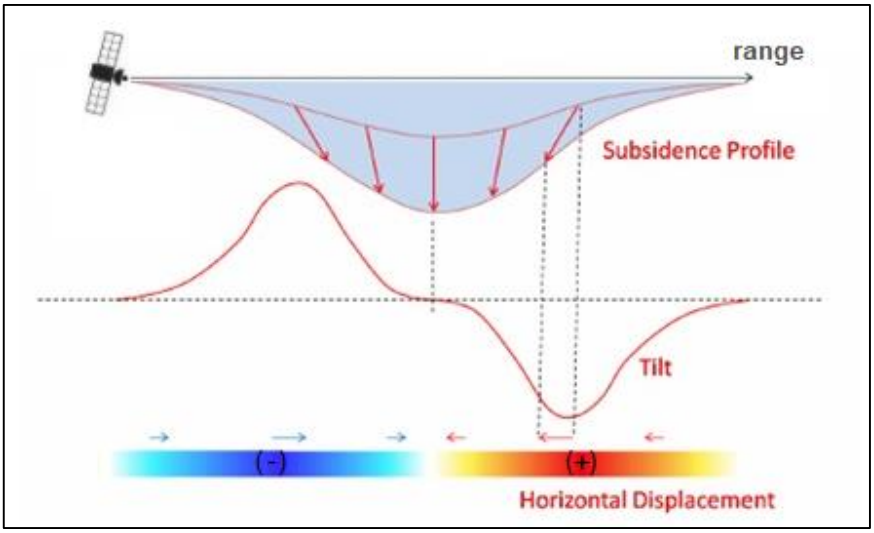

Figure 2.8: The linear relation between subsidence profile, tilt and horizontal displacement measurements in the satellite LOS direction (after Esfahany et al., 2009).

Basically, positive values in the displacement maps and mean velocity maps of the deformations indicate movement towards the satellite, while negative values in the displacement maps and mean velocity maps of the deformations indicate movement away from the satellite (Hooper et al., 2013).

2.3 The role of GIS in landslide hazard assessment

Over the last decades, computer technologies became useful and unique means for solving different kinds of problems in Earth science field and other different fields. One of important achievements of computer-based research is the use of Geographic Information System (GIS).

Geographic information system is a computer-assisted system for capture, storage, retrieval, analysis and display of spatial data. it allows short-time processing and reliable analysing of a huge amount of data and information (Clarke, 1986).

Traditionally, there are two broad types used to store data in GIS environment: raster data and vector data. Raster data is any type of digital image represented by reducible and enlargeable grids or cells. These cells are called pixels, and each of these pixels stores a specific colour value. Therefore, a combination of the pixels will make up a colour formation of an image and will compose details of an image, and this is distinct from the commonly vector data presenting formats of point, line and polygon features used in modelling an attribute of an area (Reddy, 2001).

In general, GIS is an effective tool in landslide investigations, monitoring, hazard zone mapping and other related applications using remote sensing data (Gomez et al., 2000; Naithani, 2007). Additionally, GIS is an important tool in the statistical analysis process for landslide susceptibility mapping since it has functions of collection, storage, manipulation, display, and analysis of spatially referenced data related to these processes (Guzzetti et al., 1999).

The role of GIS in landslide susceptibility and hazard studies is primarily linking all the input data spatially to each other and preparing them for the statistical analysis process mainly through symmetric rasterization of all the involved data, and classifying them into classes (Carrara et al., 1991), including landslide inventory maps and all the available input data such as:

- Input data derived from the available topographic map:
  - Slope gradient, slope aspect, terrain curvature, distance to streams, and distance to roads.

- Input data derived from the geological map:
  - Lithology and distance to faults.

- Input data derived from the optical remote sensing data:
  - Land cover and Normalized Difference Vegetation Index (NDVI).

- Input data derived from the SAR remote sensing data:
  - LOS ground-surface deformation and mean velocity data.

GIS is essential to the statistical analysis process to assess all the classes of the input data in order to identify and calculate the pixel-based areas affected by landslides in each class

and to determine the relationship between the classes of each causative factor and the landslides. Specifically, GIS can store all the results of the spatial overlay analysis (Figure 2.9) in tables related to each input causative factor in order to be used in landslide statistical analysis process. Also, the results of the statistical analysis related to the relative influence of all causative factors in each pixel can be added to each of these pixels with the help of GIS in order to achieve the final map of landslide susceptibility for the area.

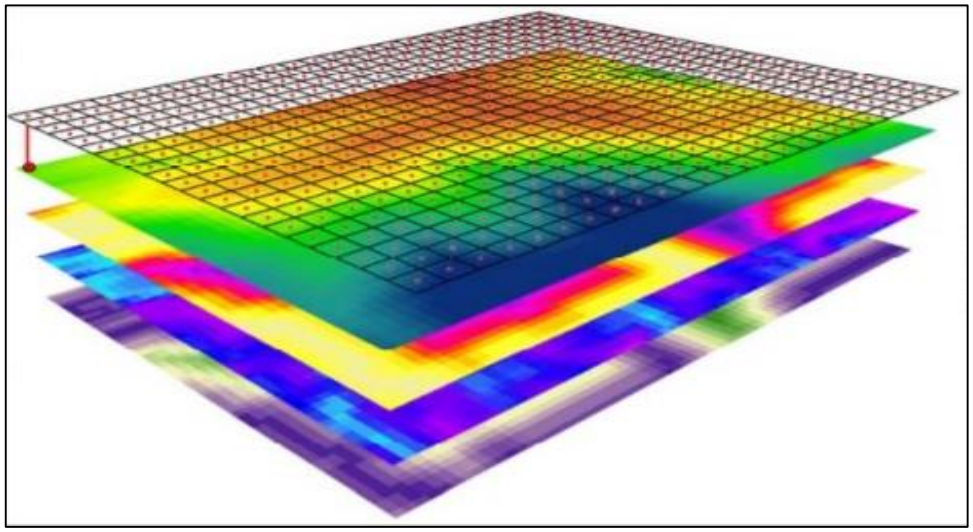

Figure 2.9: Schematic illustration of GIS-based spatial overlay analysis.

Moreover, GIS plays an important role in landslide hazard assessment by integrating the results of the final map of landslide susceptibility and the final map of landslide intensity which can be prepared from the PSI technique's result by using GIS interpolation tools on its points data to get its raster map in order to be applied in the landslide hazard matrix and achieve the landslide hazard map. The Inverse Distance Weighted (IDW) interpolation, which can be used to predict unknown values for any geographic point data, estimates pixel values by averaging the values of sample data points in the neighbourhood of each processing pixel (Watson and Philip, 1985).

Furthermore, GIS has the ability to spatially compare the results of different techniques and methods which can be exploited in the validation processes and the comparison between InSAR deformation results and GPS field measurements.

3. Study area

3.1 Geographical and climatic conditions

Syria is located in the north of the Arabian Peninsula, with a latitude between 32° and 38°, and a longitude between 35° and 43°. Its topography consists of plain lands in the east and mountain ranges in the west. The study area in this research is located in northwest Syria within the coastal mountains region and 30 km north of Latakia, the main port and the biggest coastal city in Syria.

The study area covers an area of 264.58 km^2 from 35.75° in the south to 35.94° at the Turkish border in the north, and from 36.00° in the east to 35.80° at the Mediterranean Sea in the west, which corresponds to the extension of the topographical map of Kassab at a scale of 1: 25000.

The elevation in the study area lies between 0 and 1130 metres above sea level (Figure 3.1). It should be noted that adjacent to the study area in the north is the highest mountain in the coastal mountain region, the Jebel Al-Aqra mountain, which rises from a narrow coastal plain and reaches a height of 1717 metres.

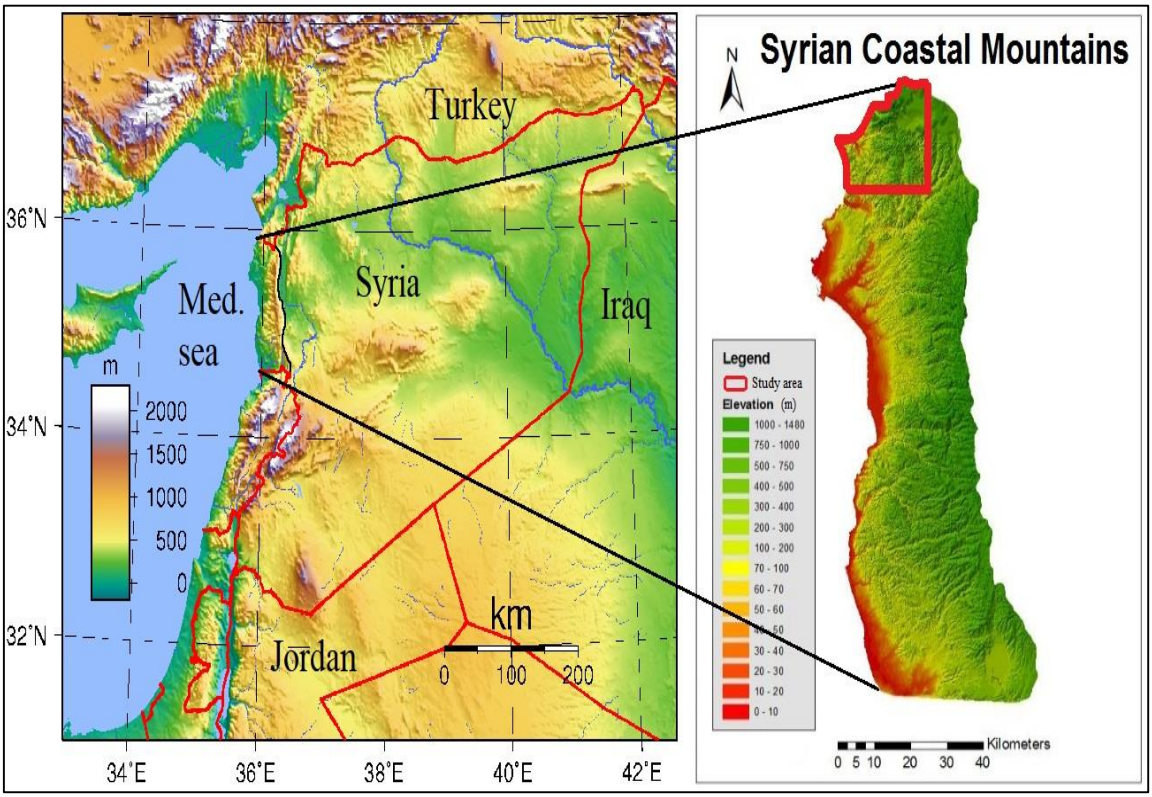

Figure 3.1: The location map and topography of Syria and the study area.

Although the total area of Syria is relatively small 185,180 km^2, it has diversity in climate. The climate of Syria has a hot desert climate in the eastern desert, semi-arid in the middle of the country and a mild Mediterranean climate in the west. In general, winter is the cold and wet season and summer is the hot and dry season.

In Syria, precipitation falls mainly from October to March due to humid air carried by the Mediterranean wind, and most precipitation falls in the coastal mountains region and significantly less in the interior. Annual rainfall begins with 50 mm in the eastern part of Syria and reaches over 800 mm in the north-western part of Syria where the study area is located (Figure 3.2). The study area has the highest average annual rainfall in the whole of Syria.

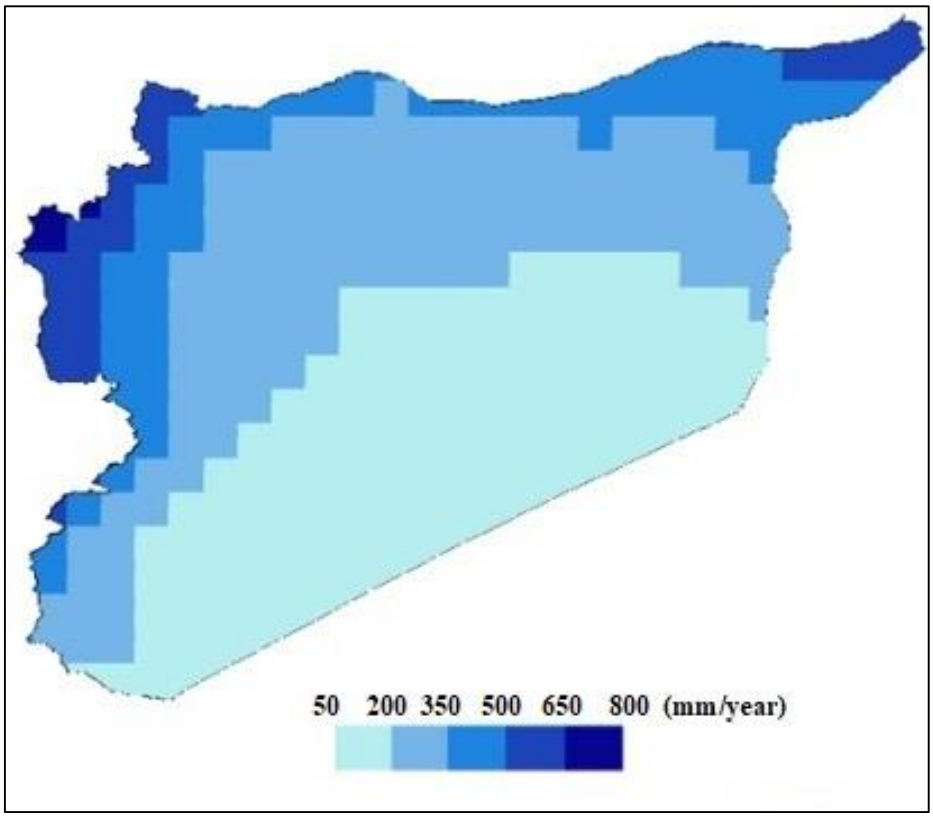

Figure 3.2: Spatial variability of average annual rainfall in Syria from WorldClim-2.1 data for the period 1970-2000 (Fick and Hijmans, 2017).

The highest average monthly rainfall in the study area is around 125 mm in both December and January (Figure 3.3), while the maximum monthly rainfall reached 379 mm in January 2012 and the maximum annual rainfall in the study area reached 1284 mm in 2012 (NASA-POWER, 2019). Heavy rain events occur every year in the study area, with daily rainfall sometimes exceeding 50 mm, making these heavy rain events a major trigger for landslides in this area (Tahhan et al., 2009). During the study period from 16 October 2018 to 21 March 2019, the highest daily rainfall in the study area was around 40 mm on 19 December 2018 (Figure 3.4).

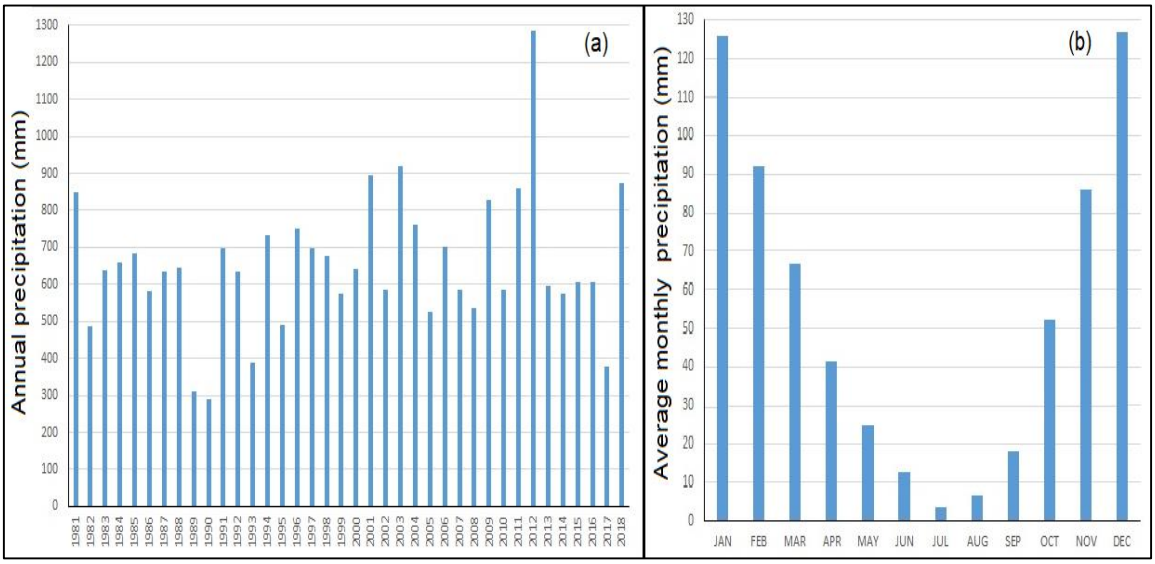

Figure 3.3: Rainfall in the study area for the period 1981-2018. a- Annual rainfall. b- Average monthly rainfall (NASA-POWER, 2019).

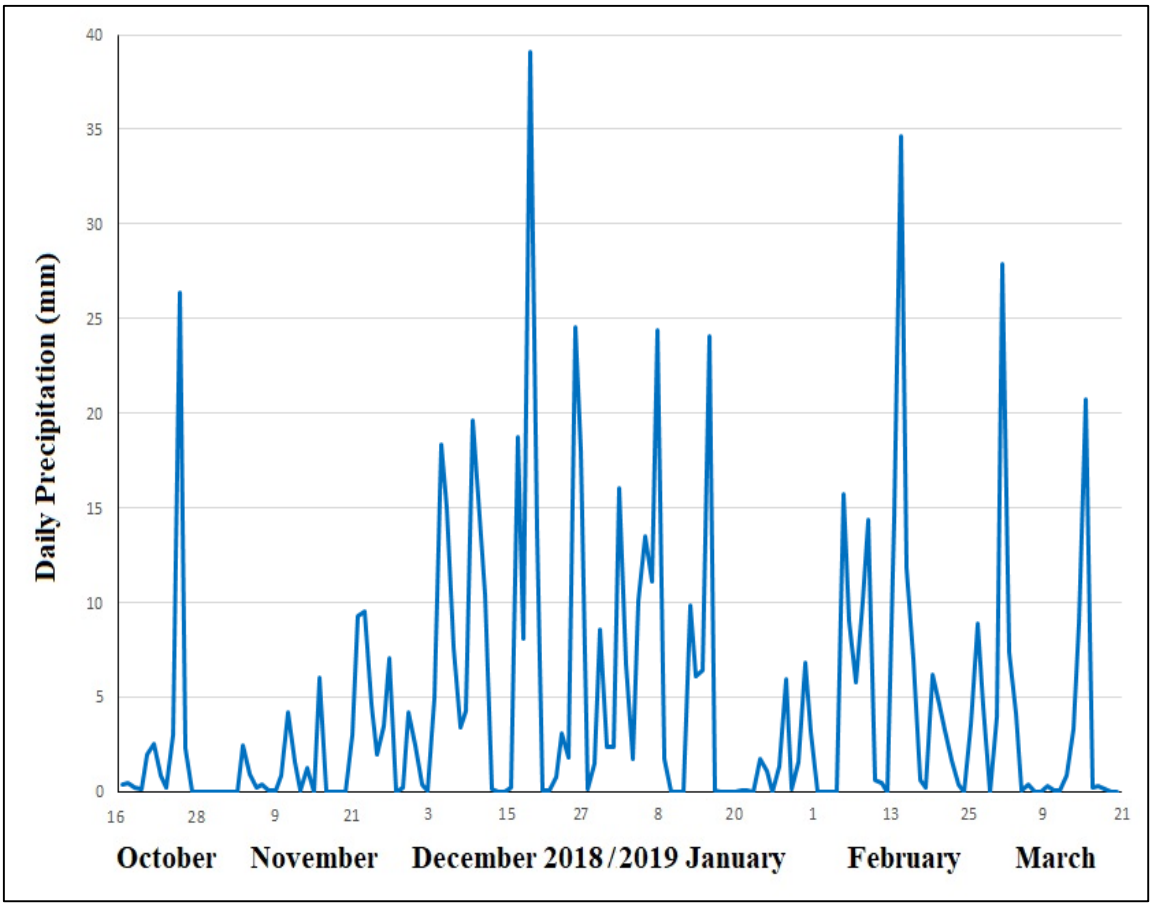

Figure 3.4: Daily rainfall in the study area during the study period from 16 October 2018 to 21 March 2019 (NASA-POWER, 2019).

The average temperature in Syria is between 12° C in the western part and 23° C in the eastern desert (Figure 3.5). January is the coldest month and August the hottest. Before the war in Syria, Syria experienced several intense droughts in 2007, 2008 and 2010, causing environmental and economic damage (Kelley et al., 2015).

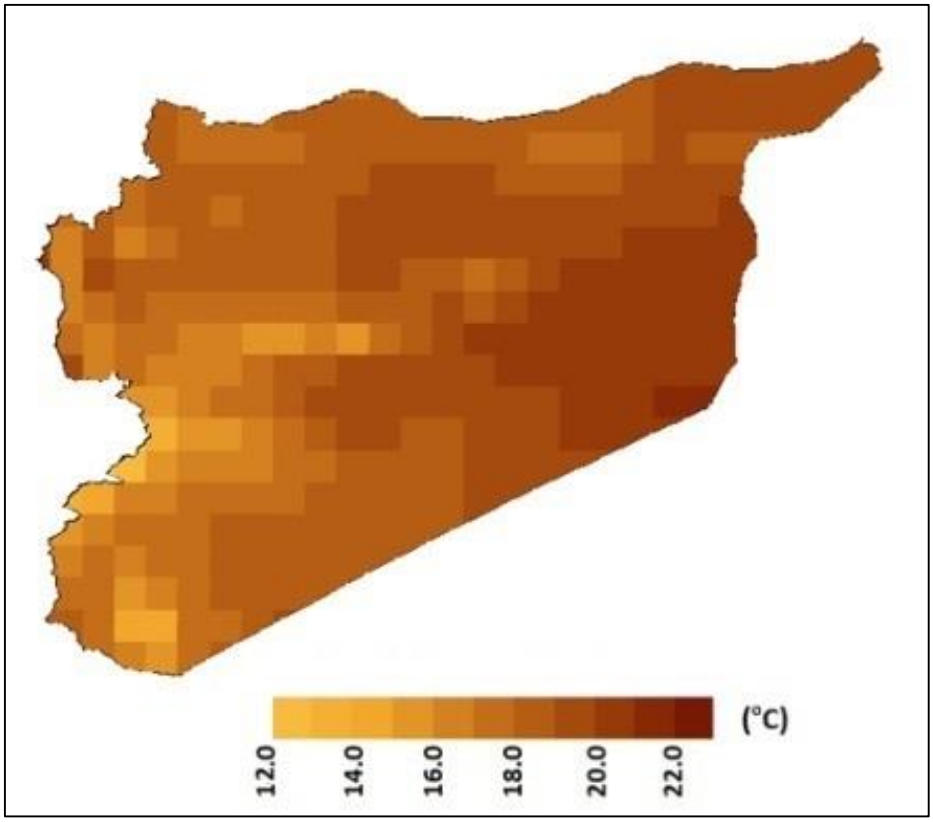

Figure 3.5: Spatial variability in average annual temperature in Syria from WorldClim-2.1 data for the period 1970-2000 (Fick and Hijmans, 2017).

The study area consists of the Badrousieh basin, most of the Al-Bassit basin, a very small part of Alkabir Alshamali basin, and almost the half of Wadi Qandil basin within which the Balloran Dam is located being in service since 1982 with a maximum capacity of about 15 million cubic meters (Tahhan et al., 2009) (Figure 3.6). The study area also has a good road network linking all towns and villages in the area with the main city of Latakia and with the Turkish border gate in Kassab. The main sub-districts are Qastal Maaf sub-district which consists of 19 localities with a total population of 16,784 in 2004 official census, and Kassab sub-district which has a total population of around 2,500 along with the surrounding villages. Prior to the current Syrian war, locals' income depended mainly on fishing, agriculture and tourism.

According to many geotechnical reports about several landslide events in the study area, carried out by the General Establishment of Geology and Mineral Resources in Syria, heavy rainstorm events are the main trigger for all of those landslides (Tahhan et al., 2009). In recent years, these events have increased and different landslides have occurred at various locations and sites in the study area and along its road network, causing serious damage to the roads as well as threatening the lives and properties of people living there (Figure 3.7).

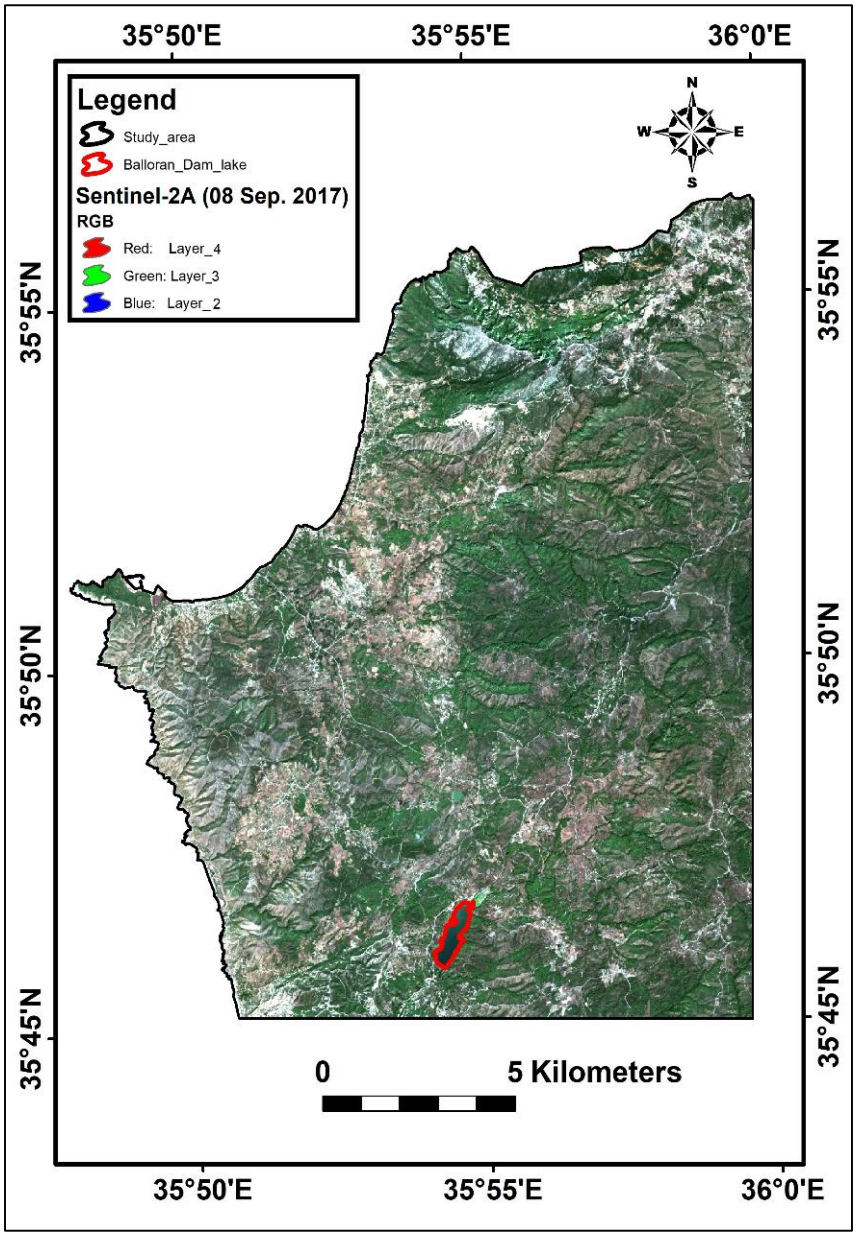

Figure 3.6: The location of the Balloran Dam lake within the study area on a true colour composite image of Sentinel-2A data acquired on 8 September 2017.

Figure 3.7: Damage to the road network caused by a landslide near Balloran in 2019.

3.2 Geological conditions

The northeast corner of the Mediterranean Sea, including northwest Syria, forms the boundary zone between the Anatolian, African and Arabian plates. This boundary zone is characterized by the spread of ophiolite complex deposits (Al-Riyami et al., 2000).

The study area contains the Baer-Bassit ophiolite complex deposits in addition to the Phanerozoic sedimentary rocks as shown in the geological map of the area (Figure 3.8) and the two cross-sections across it (Figure 3.9). The main geological map of the Latakia region which reveals the extent of the Baer-Bassit ophiolite complex deposits, was compiled in 1962 and published in 1968 on a scale of 1: 50000 (Kazmin and Kulakov, 1968).

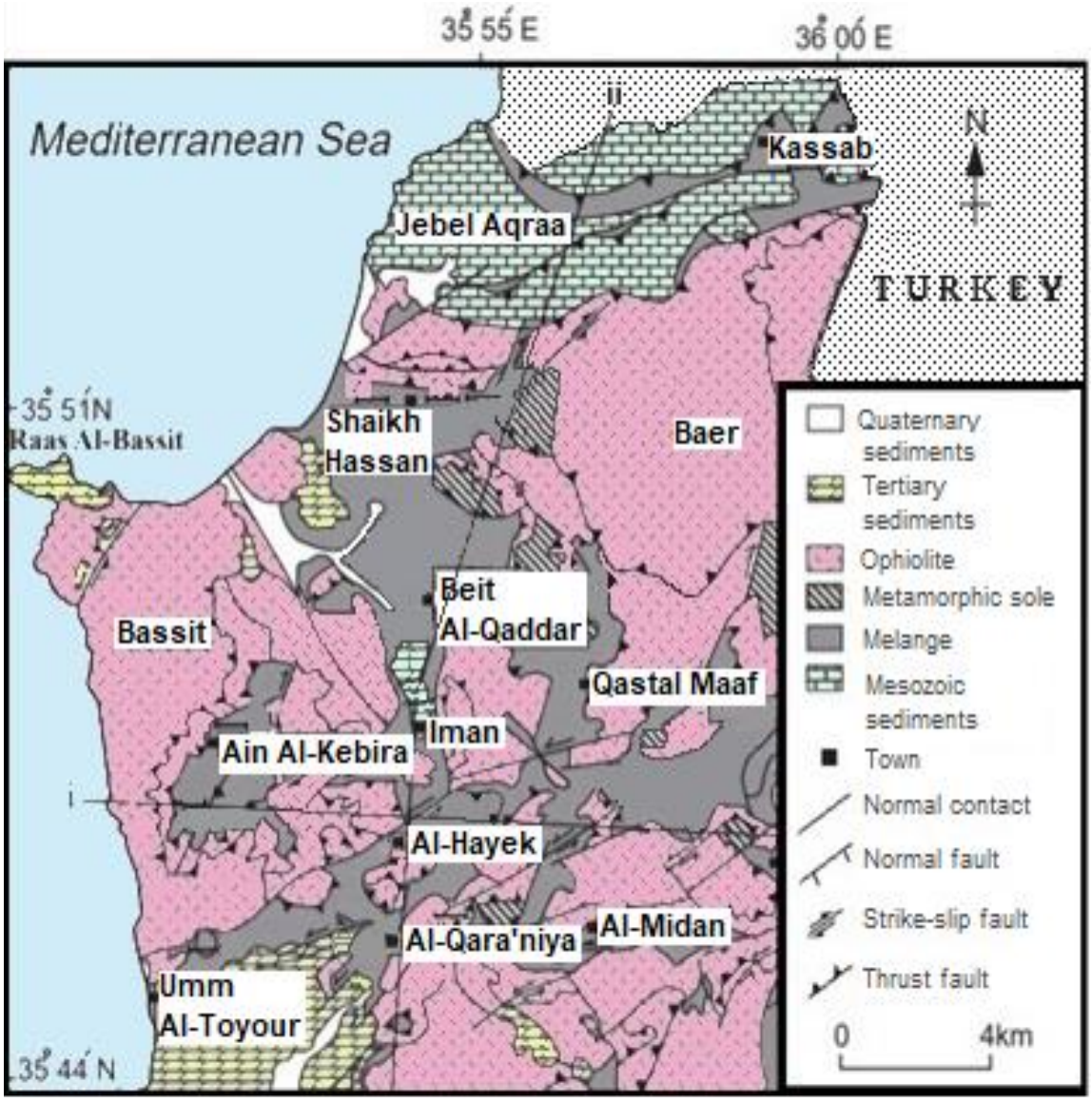

Figure 3.8: Geological map of the study area, and the location of the two cross-sections, i and ii (after Al-Riyami et al., 2000).

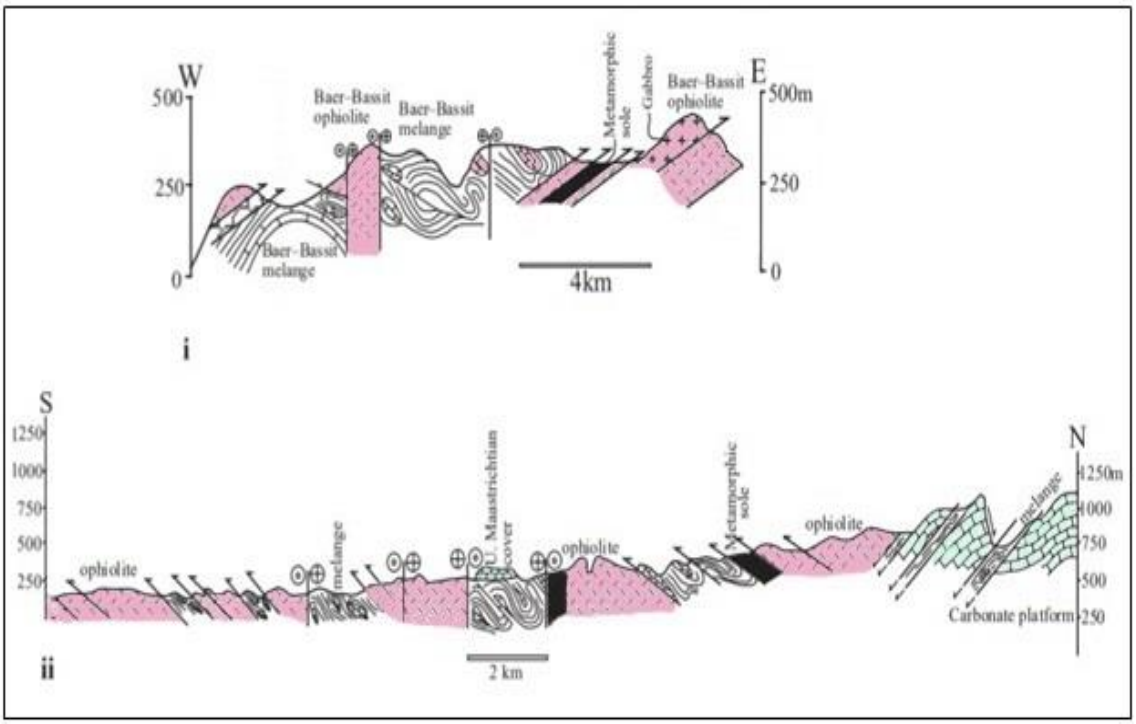

Figure 3.9: (i) E-W and (ii) N-S cross-sections across the study area (after Al-Riyami et al., 2000). See figure 3.8 for the locations of the cross-sections.

In general, sediments from Mesozoic and Cenozoic in addition to ophiolite complex deposits can be distinguished in the study area.

3.2.1 Mesozoic and Cenozoic sedimentary deposits

The lithology of the sedimentary deposits in the study area consists of mainly pelagic and neritic carbonate, radiolarian chert, conglomerate, clayey and sandy deposits.

The oldest recorded sedimentary rocks are from the Upper Triassic age which is mainly composed of carbonate sediments in addition to radiolarian chert which indicate a deposition in deep-water conditions in which radiolarians prospered, the main lithological facies of Upper Triassic age are fine-grained limestone and bedded radiolarian chert (Kazmin and Kulakov, 1968).

The Jurassic age was characterized in the area by deposition of non-calcareous muds and siliceous deposits, although some shallow-water carbonates were introduced. Local intercalations of some volcanic sedimentary deposits during Late Jurassic age indicate the presence of alkaline volcanism nearby. Besides, tuff deposits derived from subaerial conditions were not recorded, indicating that this volcanism was subaqueous. The main lithological facies of the Jurassic age are both claystone and siliceous claystone (Al-Riyami et al., 2000).

Early Cretaceous was distinguished due to the change from mainly siliceous sedimentation into the vastly calcareous sedimentation again. During Early Cretaceous, accompanying process of redeposited shallow-water carbonates with local contributions of sandstone occurred between Late Aptian time and Middle Albian time (Dubertret, 1955).

In Upper Cretaceous and due to the briefly emergent of the area after the emplacement phase, the main deposits were non-marine (fluvial) and shallow-marine sediments, presumably deposited after the erosion of extrusive rocks. In general, the main lithological facies of Cretaceous age are fine-grained limestone of Cenomanian, packstone calcarenite, conglomerates, claystone, quartzose sandstone and sandy limestone of Late Aptian (Delaune-Mayere and Saint-Marc, 1979/80).

After the Cretaceous, the region was rapidly transgressed and a Tertiary carbonate platform was established and continued till the beginning of the Quaternary. However, sedimentary deposits of the Tertiary and the Quaternary can be found in the study area.

In the Paleogene, the region continued to be in a submerged shelf setting throughout the Palaeocene to the Middle Eocene. The Late Eocene to Oligocene was marked by an unconformity that can be related to the Neotethys ocean retreat. The main sediments of Paleogene are clay, sandstone, limestone and marl (Kazmin and Kulakov, 1968).

In the Neogene, the Miocene to Late Pliocene age was marked by another marine transgression. So, the depositional conditions of the Neogene sediments are shallow-water to very-shallow-water conditions, but occasionally passes laterally into pelagic conditions. The main Neogene sediments are coarse conglomerate, sandstone, clay, siltstone and marl (Al-Riyami et al., 2000).

During the Quaternary age, non-marine deposition was dominating. Recent sediments were recorded in all river valleys and along the coast. These sediments are mainly coarse gravel and sandy loams (Dubertret, 1955).

3.3.2 Ophiolite complex deposits

Ophiolite complex deposits represent fragments of oceanic crust and lithospheric mantle exposed on land by tectonic processes (Mesorian, 1973). The ophiolites deposits extend from Italy to the Eastern Mediterranean, and via Oman reaching the Indian subcontinent (Lippard et al., 1986) as shown in the map of the ophiolite suture zones from the Eastern Mediterranean to India (Figure 3.10).

The ophiolite complex outcrop in the study area is dominated by two massifs, Baer in the east and Bassit in the west near to the coast. The Baer massif rocks is relatively structurally intact, while the Bassit massif rocks are over-thrusted by thin imbricate thrust sheets of pillow lavas (Al-Riyami et al., 2000).

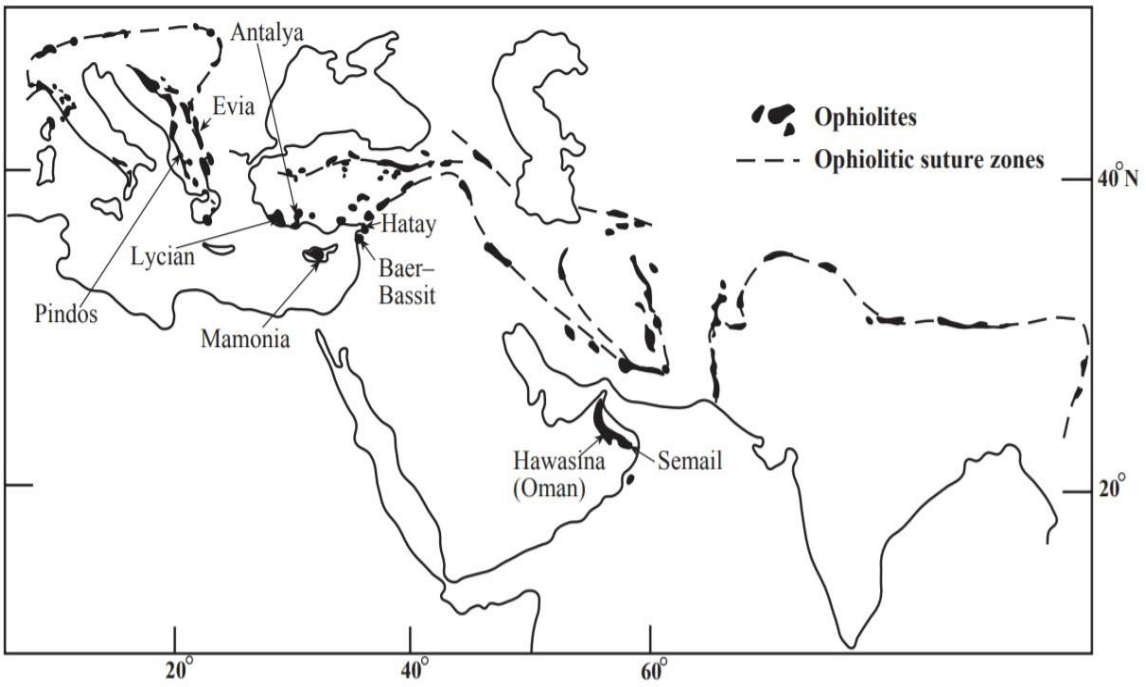

Figure 3.10: Ophiolite suture zones extending from the Eastern Mediterranean to India (after Lippard et al., 1986).

Baer-Bassit ophiolite complex was originally described by Dubertret in 1955 and mapped by Kazmin and Kulakov in 1968 who have determined the following units in the Syrian Baer-Bassit ophiolite complex, from the deepest levels to the shallowest:

- **Metamorphic sole:** A well-developed metamorphic sole forms the base of the ophiolite complex sequence and can be divided into mostly amphibolite facies and less greenschist facies assemblages. The protoliths of both facies are interpreted to be alkaline basalts (Parrot and Whitechurch, 1978).

- **Ultrabasic and basic rocks (ophiolite):** The mainly rocks of this unit are serpentines, diabases and harzburgitic peridotites which contain 70% olivine. The ophiolite rocks are cut by dykes of gabbro and dolerite (Parrot, 1980).

- **Volcanic sedimentary rocks (Melange):** The Melange has a group of volcanic rocks from Upper Triassic to lower Cretaceous age exist as separated blocks and outcrops of pillow lavas associated with different sedimentary rocks containing mainly ribbon radiolarite deposits which are very potential shear horizons. These volcanic sedimentary rocks can be grouped into two main categories:

  - Triassic - Jurassic volcanic sedimentary rocks which are alkaline extrusive rocks produced in deep-water conditions where radiolarian deposits were present. The rocks of this category are mainly pillow lavas and rarely lava breccia, and they are intercalated with mostly ribbon radiolarite and less hemipelagic limestone (Al-Riyami et al., 2000).

- Cretaceous volcanic sedimentary rocks in which the volcanic rocks are compositionally identical to the Triassic - Jurassic volcanic rocks, although lavas are more peralkaline. Moreover, the lavas are intercalated with ribbon radiolarite and bounded by tectonic contacts (Al-Riyami et al., 2000).

The lithology has a big influence on the occurrence of landslides in the study area as mentioned in many geotechnical reports carried out by the General Establishment of Geology and Mineral Resources for several landslide events in the past, such as Al-Samra landslide in 1991 and the geotechnical reports about fourteen different sites where landslides were occurred during the last two decades of the last century and the first decade of this century. The geotechnical reports have indicated that the ribbon radiolarite deposits associated with the pillow lavas of Melange were the main lithology in all the places where these landslides took place, and that all the landslides in these places were rotational landslides (Tahhan et al., 2009).

3.2.3 Structural geology

The Arabian plate collided with the Anatolian plate during the Mesozoic Era profoundly changed both the regional paleogeography and the lithofacies regimes (De Ruiter et al., 1995). Due to the regional tectonic evolution, the study area was affected by a complicated tectonism throughout the Mesozoic and Cenozoic Eras (Brew et al., 2001; Hempton, 1987; Litak et al., 1997). So, different structural elements including simple folds and small fractures are characteristic for the study area and its ophiolite complex deposits which form thrust sheets emplaced over the Arabian platform's Mesozoic carbonates in the Maastrichtian age (Trifonov et al., 1991).

The ophiolite complex deposits have experienced extremely relative anticlockwise rotations, up to 200°, on a local scale. Regional comparisons with the Troodos ophiolite in Cyprus and the Hatay ophiolite in Turkey suggest that a significant part of rotation may be attributed to intra-oceanic deformation of a coherent region of oceanic crust within the southern basin of the Neotethys ocean prior to the ophiolite emplacement process. Then, the partially rotated Baer-Bassit ophiolite complex deposits were emplaced and structurally dismembered by thrust faulting. During the Late Tertiary, the ophiolite complex deposits were further rotated during the initiation and development of the strike-slip East Anatolian fault zone, linking the subduction zone of Cyprus to the Levant Rift system in the east (Morris et al., 2002).

In general, the ophiolite complex deposits are cut by a large number of strike-slip faults with mainly northeast-southwest direction, which reflects the regional trend of faults within the East Anatolian fault system (Kazmin and Kulakov, 1968).

4. Data and methods

In this research, topographic and geological data as well as optical and radar satellite data were used for landslide susceptibility analysis and hazard assessment.

In this context, the topographical map of Kassab 1: 25000, printed in 1990 on the basis of aerial photographs and field work from 1984, was used to represent the topographic characteristics of the study area as they were prior to the occurrence of the landslides under investigation. It is important to know the actual effects of the topographic factors on the landslide occurrence in order to obtain reliable results of landslide susceptibility. The topographic map was used to produce the road network map and to generate the Digital Elevation Model (DEM). Then, this DEM was used to produce all maps of slope, aspect, terrain curvature and stream network. Whereas, the geological map of the Latakia region 1: 50000 was used to prepare the fault map.

Optical multispectral satellite products from Landsat and Sentinel were used to accomplish this research (Table 1). Two Landsat surface reflectance images with 0% cloud cover and 30 m spatial resolution acquired by Landsat-5 Thematic Mapper (TM) and Landsat-8 Operational Land Imager (OLI) on 22 September 1984 and 6 October 2018 respectively, were freely downloaded from https://earthexplorer.usgs.gov/. While, one Sentinel-2 Level-2A Bottom-Of-Atmosphere (BOA) corrected reflectance image of 8 September 2017 with 0% cloud cover and spatial resolution of 10 m for each Visible and Near-InfraRed (VNIR) multispectral band and 20 m for each ShortWave-InfraRed (SWIR) band was freely downloaded from https://scihub.copernicus.eu/.

Table 1: The optical multispectral satellite products used in this research.

Imagery_ID	**Satellite**	**Acquisition date**
LT05_L1TP_174035_19840922_20171213_01_T1	Landsat-5 TM	22 Sep. 1984
LC08_L1TP_174035_20181006_20181010_01_T1	Landsat-8 OLI	6 Oct. 2018
S2A_MSIL2A_20170908T082011_N0205_R121_T36SYE	Sentinel-2A	8 Sep. 2017

The Landsat-5 TM image was used to produce land cover and Normalized Difference Vegetation Index (NDVI) maps to show vegetation cover characteristics prior to the occurrence of the landslides under investigation. The Landsat-5 TM image was also employed in the visual comparison with the Landsat-8 OLI image in order to prepare the landslide inventory map. Whereas, the Sentinel-2A image was employed using Principal Component Analysis (PCA) and band ratios (BR) techniques to produce the lithology map.

Radar satellite products of Sentinel-1A and Sentinel-1B Single Look Complex (SLC) SAR images with 2.3×14.1 m [range×azimuth] pixel size in the Interferometric Wide swath (IW) mode and Vertical-Vertical (VV) polarization were also freely downloaded from the Copernicus website and used to accomplish this research (Table 2).

Table 2: The radar satellite products of Sentinel-1 used in this research.

Imagery_ID	Acquisition date	Track	Orbit cycle
S1A_IW_SLC_1SDV_20141006T153252	06 Oct 2014	9	16
S1A_IW_SLC_1SDV_20141018T153252	18 Oct 2014	9	17
S1B_IW_SLC_1SDV_20181016T033410	16 Oct 2018	21	82
S1B_IW_SLC_1SDV_20181028T033410	28 Oct 2018	21	83
S1B_IW_SLC_1SDV_20181109T033409	09 Nov 2018	21	84
S1B_IW_SLC_1SDV_20181121T033409	21 Nov 2018	21	85
S1B_IW_SLC_1SDV_20181203T033409	03 Dec 2018	21	86
S1B_IW_SLC_1SDV_20181215T033408	15 Dec 2018	21	87
S1B_IW_SLC_1SDV_20181227T033408	27 Dec 2018	21	88
S1B_IW_SLC_1SDV_20190108T033408	08 Jan 2019	21	89
S1B_IW_SLC_1SDV_20190120T033407	20 Jan 2019	21	90
S1B_IW_SLC_1SDV_20190201T033407	01 Feb 2019	21	91
S1B_IW_SLC_1SDV_20190213T033406	13 Feb 2019	21	92
S1B_IW_SLC_1SDV_20190225T033406	25 Feb 2019	21	93
S1B_IW_SLC_1SDV_20190309T033406	09 Mar 2019	21	94
S1B_IW_SLC_1SDV_20190321T033406	21 Mar 2019	21	95

Two SAR images acquired by Sentinel-1A on 6 October 2014 and 18 October 2014 were used to generate a high resolution DEM which was used in InSAR techniques. In addition, fourteen SAR images acquired by Sentinel-1B during the study period from 16 October 2018 to 21 March 2019 were used to produce the mean velocity map of the ground-surface deformations using PSI technique in order to use this map along with the produced landslide susceptibility map to get the final landslide hazard map. Sentinel-1B products were also used to produce the map of total ground-surface deformations during the study period using D-InSAR technique. The map of total ground-surface deformations was used in the validation process of InSAR results through the comparison with the results of the Differential Global Position System (D-GPS) field measurements carried out using Leica system 550 GPS.

Different software packages were used to process the data, acquire and present the final results. ArcGIS version 10.2.2 and all its tools in the ArcMap toolbox were used to prepare all input data maps and standardize their pixel sizes, as well as to help perform and validate the susceptibility analysis process and the hazard assessment.

The Sentinel-1 toolbox in SNAP software package version 6.0.0 was freely downloaded from https://step.esa.int/main/download/snap-download/ and used to process all the SAR satellite data. Moreover, SNAPHU version 2.0.3, which runs on most Unix/Linux platforms and operating systems, was used for phase unwrapping in D-InSAR technique. While, a software package called Stanford Method for Persistent Scatterers (StaMPS) version 4.1b1 Multi-Temporal InSAR (MTI), runs in Matlab under Linux, was used for phase unwrapping in PSI technique. Furthermore, Matlab was used for the artificial neural networks analysis.

Finally, Microsoft Excel was used for the statistical analysis calculations, and an add-in of Real Statistics Resource Pack package was used specifically for the logistic regression analysis.

4.1 Digital elevation model generation

Digital Elevation Model (DEM) is a generic term that includes all different types of digital representation of the topographic ground-surface in an area, such as Digital Surface Model (DSM) and Digital Terrain Model (DTM). The digital elevation model is indispensable for any statistical analysis of landslides. In fact, the digital elevation model can be generated either by field measurement of elevation for a group of coordinate points or by extracting x, y and z values from other data sets such as topographic maps or remote sensing data.

In this research, the DEM was generated using two different approaches for two different purposes. The first DEM, the topography-based DEM, was created on the basis of a topographical map from 1984 and was used to represent the topographical characteristics of the area as before the occurrence of the landslides under investigation and to extract the derivative maps involved in the statistical analysis of landslide susceptibility, i.e. slope gradient, slope aspect, terrain curvature and drainage network. The second DEM, the SAR-based DEM, was created on the basis of Sentinel-1 data and used as a newer and higher-resolution DEM for the PSI technique used in this research.

For the topography-based DEM, the topographical map of Kassab 1: 25000 was digitized from a hardcopy map and stored as a polyline feature class in ArcGIS with 10 m interval spacing between contour lines. The polyline features were used to create a Triangulated Irregular Network (TIN) dataset. Then, the TIN has been interpolated to a raster with WGS_1984_UTM_Zone_36N coordinate system. As a result, a topography-based DEM raster map was generated with a pixel size of 12.5 m, which is the recommended grid resolution of the DEM extraction process from the topographical map of Kassab. The recommended grid resolution was calculated using the following equation (Hengl, 2006):

$$\text{Grid resolution} = Sc * 0.0005 \quad (3)$$

Where, Sc is the scale factor.

For the SAR-based DEM, a workflow was built in SNAP to generate the DEM from the two SAR images (Figure 4.1). The two SAR images acquired by Sentinel-1A on 6 October 2014 and 18 October 2014 with a perpendicular baseline of 40.6 meters and 96% modelled coherence, were co-registered as master and slave, respectively, to generate an interferogram of the area. During the interferogram formation process, the flat-earth phase was subtracted from the complex phase. After the deburst process, the Goldstein-Phase-Filtering tool was applied to subtract the noise phase. Since the displacement and atmospheric components of the phase are relatively negligible due to the short temporary baseline used, the topographic phase was the only remaining phase in the interferogram. The topographic phase was exported to SNAPHU and unwrapped there, before it was

imported back to SNAP and converted to elevation values using the Phase-to-Elevation tool (Braun, 2020).

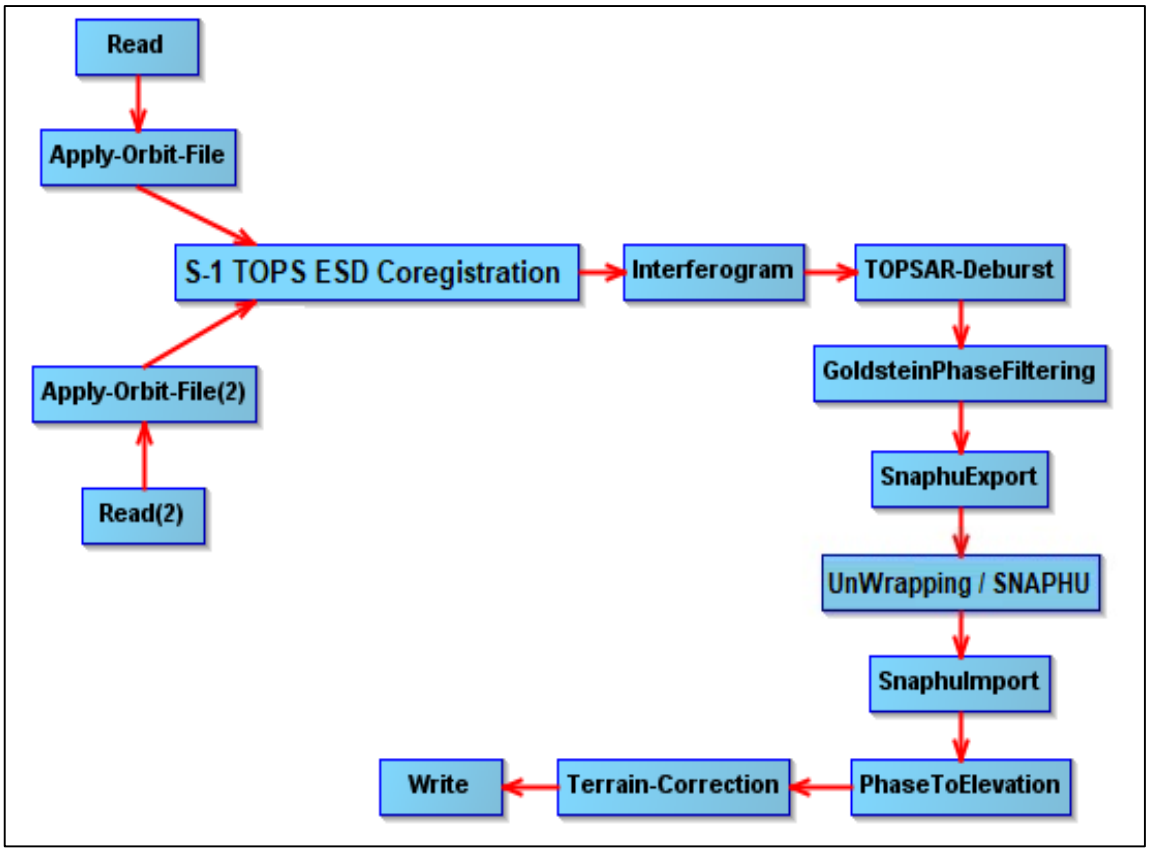

Figure 4.1: Flow chart for generating DEM of the study area using Sentinel-1 data.

After the generation of the SAR-based DEM, it was later used in the PSI technique after the anomalies in all areas with decorrelation or low coherence below 0.3 (Braun, 2020) caused by dense vegetation or atmospheric inhomogeneity were corrected on the basis of a corresponding TanDEM-X® DLR 0.4 arc-second product of the German Aerospace Centre, which has a spatial resolution of 12 m and a relative vertical accuracy of 2 m for areas with inclinations below 20° and 4 m for areas with inclinations above 20° (Wessel, 2016).

4.2 Landslide inventory map preparation

The landslide inventory map, which portrays the location of past landslide events and their characteristics, is the basis for all analyses and assessments of landslide susceptibility and hazard. However, a complete landslide inventory map is not always available, as not all associated data are always available. Landslide inventory maps therefore often only provide the location and spatial extent of landslide events over a period of time.

In fact, past landslides have some common morphological features, such as vegetation breaks and bare soil surfaces that are inconsistent with their surroundings, which can usually be detected by high-resolution optical satellite imagery.

Since there was no landslide inventory map for the study area before, an inventory map for all landslides that occurred in the study area between 1984 and 2018 was prepared for the first time. The landslide inventory map was prepared based on all available geotechnical reports as well as information from the authorities and the local population about past landslides to determine the location of each of these landslides. The spatial extent of these landslides in the landslide inventory map was checked individually and verified by a visual comparison between the Landsat-5 TM image of 22 September 1984 and the Landsat-8 OLI image of 6 October 2018 with help of ancillary information available through the Historical Imagery tool in Google Earth. The Historical Imagery tool in Google Earth was also used to detect changes in texture and characteristics of ground-surface and vegetation cover during this period and to verify whether these changes are indicators of past landslide events or just changes due to human activity or some fire events that occurred during this period, especially after 2011 when the war in Syria began.

As a result, a group of polygons representing locations of past landslides and their spatial extent was identified as the total landslides that occurred in the area over the specified period of time. The landslide polygons were randomly divided into two sets; 70% of all landslide polygons was used as a training set for the statistical analysis methods used in this research to create the landslide susceptibility maps, and the remaining 30% was used as a testing set to validate the resulting susceptibility maps. All landslide polygons were converted to a raster map in ArcGIS with a pixel size of 12.5 m, which is the grid resolution of the topography-based DEM and all causative factor maps. As a result, the final raster map of landslide inventory was created.

The same procedure was done for the non-landslide dataset which was prepared with the same size of the landslide dataset to optimally perform the statistical analysis of the landslide susceptibility. Thus, the non-landslide dataset was prepared with the same number of polygons and the same number of pixels as a whole, based on relevant geotechnical reports and maps as well as personal knowledge from local field work.

4.3 Causative factor maps preparation for susceptibility analysis

For statistical analysis of susceptibility to landslides, nine causative factors influencing the spatial distribution of landslides were taken into account depending on various criteria such as mapping unit and type of landslides in the area, as well as the availability of data and the results of many similar studies (Guzzetti, 2005; Pradhan et al., 2011; Lee et al., 2012). These factors are: slope gradient, slope aspect, terrain curvature, distance to streams, distance to roads, distance to faults, lithology, land cover, and Normalized Differential Vegetation Index (NDVI).

Within the relatively small study area, it is very likely that the amount of rainfall is the same throughout the area according to the available rainfall data. Therefore, it was decided to exclude rainfall data from the statistical analysis of landslide susceptibility. After all, rainfall can be considered as a trigger rather than a causative factor for landslide occurrence in the study area.

The preparation process of the nine causative factor maps was done separately on the basis of the source data of each causative factor. In ArcGIS, the causative factor maps were prepared as a raster grid format, and clipped to the same spatial extent. Then, all resulting raster maps were reprojected using the same coordinate system, WGS_1984_UTM_Zone_36N, and resampled to the same pixel size to make them uniform. The pixel size for all the map layers was set to 12.5 m, which is the recommended grid resolution of the topography-based DEM.

In order to be used in the landslide susceptibility analysis, each of the nine causative factor maps was reclassified into number of classes depending on its own criteria.

4.3.1 Slope gradient map

Slope steepness is one of the main topographic causative factors which play an important role in landslide occurrence. The higher the slope, the greater the risk of landslide due to the higher shears induced by gravity. The slope gradient map was derived from the topography-based DEM to represent the slope gradient values as before the occurrence of the landslides under investigation. The Slope tool in ArcGIS was used to produce the slope gradient map which was reclassified into five classes as:

- Less than 10 degrees;
- Between 10 and 20 degrees;
- Between 20 and 30 degrees;
- Between 30 and 40 degrees; and
- More than 40 degrees.

4.3.2 Slope aspect map

The slope aspect map was also derived from the topography-based DEM using the Aspect tool in ArcGIS. Then, the slope aspect map was reclassified into nine classes according to orientation:

- Flat areas which have no slope aspect orientation;
- North orientation from 0° to 22.5° and from 337.5° to 360°;
- Northeast orientation from 22.5° to 67.5°;
- East orientation from 67.5° to 112.5°;
- Southeast orientation from 112.5° to 157.5°;
- South orientation from 157.5° to 202.5°;
- Southwest orientation from 202.5° to 247.5°;
- West orientation from 247.5° to 292.5°; and
- Northwest orientation from 292.5° to 337.5°.

4.3.3 Terrain curvature map

The terrain curvature map was also derived from the topography-based DEM using the Curvature tool in ArcGIS. Then, the map was reclassified into five classes according to the relevant literature:

- Very concave surfaces for values less than -1;
- Concave surfaces for values between -1 and -0.1;
- Planar surfaces for values between -0.1 and 0.1;
- Convex surfaces for values between 0.1 and 1; and
- Very convex surfaces for values greater than 1.

4.3.4 Map of distance to streams

The map of distance to streams was created on the basis of a drainage network map extracted from the topography-based DEM using the Hydrology tools of ArcGIS.

The extraction process of the drainage network map from the topography-based DEM was done through the following sequence: The Flow-direction and the Flow-Accumulation tools were used first. Then, a threshold for the flow accumulation was set to extract water pixels from the flow accumulation float raster map and store them in a binary raster map, i.e. water or no water pixels. After that, the Stream-Link and the Stream-Order tools were used to build the drainage network. By using the Stream-to-Feature tool, the resulting raster map was converted to a line feature representing the drainage network map (Tarboton and Ames, 2001).

For each pixel, the Euclidean distance to the nearest water stream in the drainage was calculated. Based on the density of stream network in the study area, the maximum distance was set at 300 m. Then, the resulting raster map was reclassified into four distance classes:

- Less than 100 m from the nearest water stream;
- Between 100 m and 200 m from the nearest water stream;
- Between 200 m and 300 m from the nearest water stream; and
- More than 300 m from the nearest water stream.

4.3.5 Map of distance to roads

The road network map was digitized from the topographical map of Kassab 1: 25000 including the highway and local roads, and updated using high resolution satellite images in Google Earth in order to include all the local roads that have been built over the past three and half decades and whose surrounding areas have experienced landslide events during this period of time.

The Euclidean distance to the nearest road was calculated in ArcGIS for each pixel of the road network map. According to the density of road network in the study area, the

maximum distance was set at 500 m. After that, the resulting raster map of distance to roads was reclassified into six distance classes:

- Less than 100 m from the nearest road;
- Between 100 m and 200 m from the nearest road;
- Between 200 m and 300 m from the nearest road;
- Between 300 m and 400 m from the nearest road;
- Between 400 m and 500 m from the nearest road; and
- More than 500 m from the nearest road.

4.3.6 Map of distance to faults

The fault map was prepared from the geological map of the Latakia region 1: 50000 which was compiled by Kazmin and Kulakov in 1962 and published in USSR in 1968. Basically, the fault map area contains only the faults ascertained by Kazmin and Kulakov (1968).

The fault map was used to calculate the Euclidean distance between each pixel and the nearest fault, where the maximum distance was set at 500 m according to the distribution and density of the faults in the study area. After that, the resulting raster map of distance to faults was reclassified into six distance classes:

- Less than 100 m to the nearest fault;
- Between 100 m and 200 m to the nearest fault;
- Between 200 m and 300 m to the nearest fault;
- Between 300 m and 400 m to the nearest fault;
- Between 400 m and 500 m to the nearest fault; and
- More than 500 m to the nearest fault.

Also, a rose diagram of the extracted ascertained faults was prepared to show the main trend of faults within the study area.

4.3.7 Lithology map

To get a map that shows lithological types more than geological ages as shown in the geological map, a lithology map was prepared on the basis of multispectral remote sensing data using the Band Ratios (BR) and Principal Component Analysis (PCA) techniques.

There are a number of studies around the world where they have used multispectral satellite imagery through the band ratios and principal component analysis techniques, for mapping the lithology in general and the spread areas of ophiolite complex as a main lithology in particular (Sultan et al., 1987; Abrams et al., 1988; Sabins, 1999; Pournamdari et al., 2014; Abdelmalik and Abd-Allah, 2018; Ge et al., 2018; El-Atillah et al., 2019).

Since Sentinel-2 data have a better spatial resolution in the VNIR and SWIR spectral ranges than Landsat data, and since the lithology of the study area can be considered relatively constant during the study period, Sentinel-2A image of 8 September 2017 was used to create the lithology map.

Several combinations of band ratios were performed in ArcGIS on the blue, green, red, NIR, SWIR1 and SWIR2 bands of the Sentinel-2A image to determine the optimal combinations of band ratios that could be used to distinguish between different lithological groups in the study area, particularly the ophiolite complex deposits. Based on chromatic differentiation, three combinations of band ratios were used:

- **BR_1:** SWIR1/SWIR2, SWIR1/Blue, and [SWIR1/NIR] ∗ [RED/NIR] (Sultan et al., 1987).
- **BR_2:** SWIR1/SWIR2, Red/Blue, and Red/SWIR1 (Sabins, 1999).
- **BR_3:** SWIR2/NIR, SWIR1/Green, and SWIR1/SWIR2 (Abdelmalik and Abd-Allah, 2018).

in Red, Green, and Blue (RGB) colour composites for each of these combinations, respectively. The three RGB maps of the band ratios were combined into a multiband composite map and the resulting map was transformed into its principal components to create the PCA map that was used to produce the lithology map (Zhang et al., 2007; Corumluoglu et al., 2015; El-Atillah et al., 2019).

Based on the geological map and the detailed knowledge of the study area through personal participation in geotechnical studies carried out by the General Establishment of Geology and Mineral Resources for different landslide sites, 112 training sites were identified representing the six main lithological classes in the study area:

- Amphibolite;
- Carbonate sediments;
- Clay and claystone;
- Conglomerates and sands;
- Lava with radiolarite; and
- Ophiolite.

The 112 training sites were used to create a lithology signature file for the supervised classification of the PCA map into the six defined lithological classes. Supervised classification was performed using the Maximum Likelihood Classifier (MLC) algorithm, which examines the probability function of each pixel for belonging to each of the defined classes and assigns each pixel to the class with the highest probability in that pixel (Lillesand and Kiefer, 1994).

Moreover, 48 additional sites were identified and used for the validation process of the resulting lithology map. Based on an accuracy matrix, the user accuracy of each class was calculated by dividing the number of correctly classified sites in a class by the total number of validation sites in that class, and the overall accuracy is the mean of all user accuracy values (Congalton, 1991).

At the end, the lithology map, which was created and validated, was resampled to a pixel size of 12.5 m for later use in the statistical analysis of landslide susceptibility.

4.3.8 Land cover map

The land cover map was created on the basis of the Landsat-5 TM surface reflectance image of 22 September 1984, by performing the maximum likelihood supervised classification.

Based on the visual discrimination of the Landsat-5 TM image and according to the main thematic land cover types in the Syrian coastal region (Hammad et al., 2018a), 270 training sites were identified representing the four main classes of land cover types in the study area:

- Built-up area;
- Forest and dense vegetation;
- Soil and agriculture land; and
- Water.

The 270 training sites were used to create a land cover signature file for the maximum likelihood supervised classification of the Landsat-5 TM image into the four defined land cover classes.

The validation process of the resulting land cover map was estimated on the basis of the maximum likelihood supervised classification of Landsat multispectral data over the Syrian coastal region (Hammad et al., 2018a).

At the end, the land cover map was resampled also to a pixel size of 12.5 m for later use in the statistical analysis of landslide susceptibility.

4.3.9 Normalized difference vegetation index map

The Normalized Difference Vegetation Index (NDVI) provides a good indication of vegetation density influencing susceptibility to landslides (Tseng et al., 2015). The value of the NDVI ranges from −1 to 1; the higher the value of the NDVI, the denser the vegetation cover.

The NDVI map was created on the basis of the red and near-infrared bands of the Landsat-5 TM surface reflectance image of 22 September 1984 using the traditional formula of the NDVI: $[\mathrm{NIR} - \mathrm{Red}]/[\mathrm{NIR} + \mathrm{Red}]$.

At the end, the resulting NDVI map was resampled to 12.5 m pixel size and reclassified into five classes uniformly according to positive NDVI values as follows:

- Very low NDVI values;
- Low NDVI values;
- Moderate NDVI values;
- High NDVI values; and
- Very high NDVI values.

4.4 Landslide susceptibility mapping using statistical analysis

For landslide susceptibility mapping using statistical analysis, the landslide inventory map and all causative factor maps prepared were used (Figure 4.2). The spatial linking of the landslide data with each causative factor map and other resulting maps was carried out with the help of ArcGIS, which was indispensable for the susceptibility analysis of landslides and the validation process of all statistical analysis methods used.

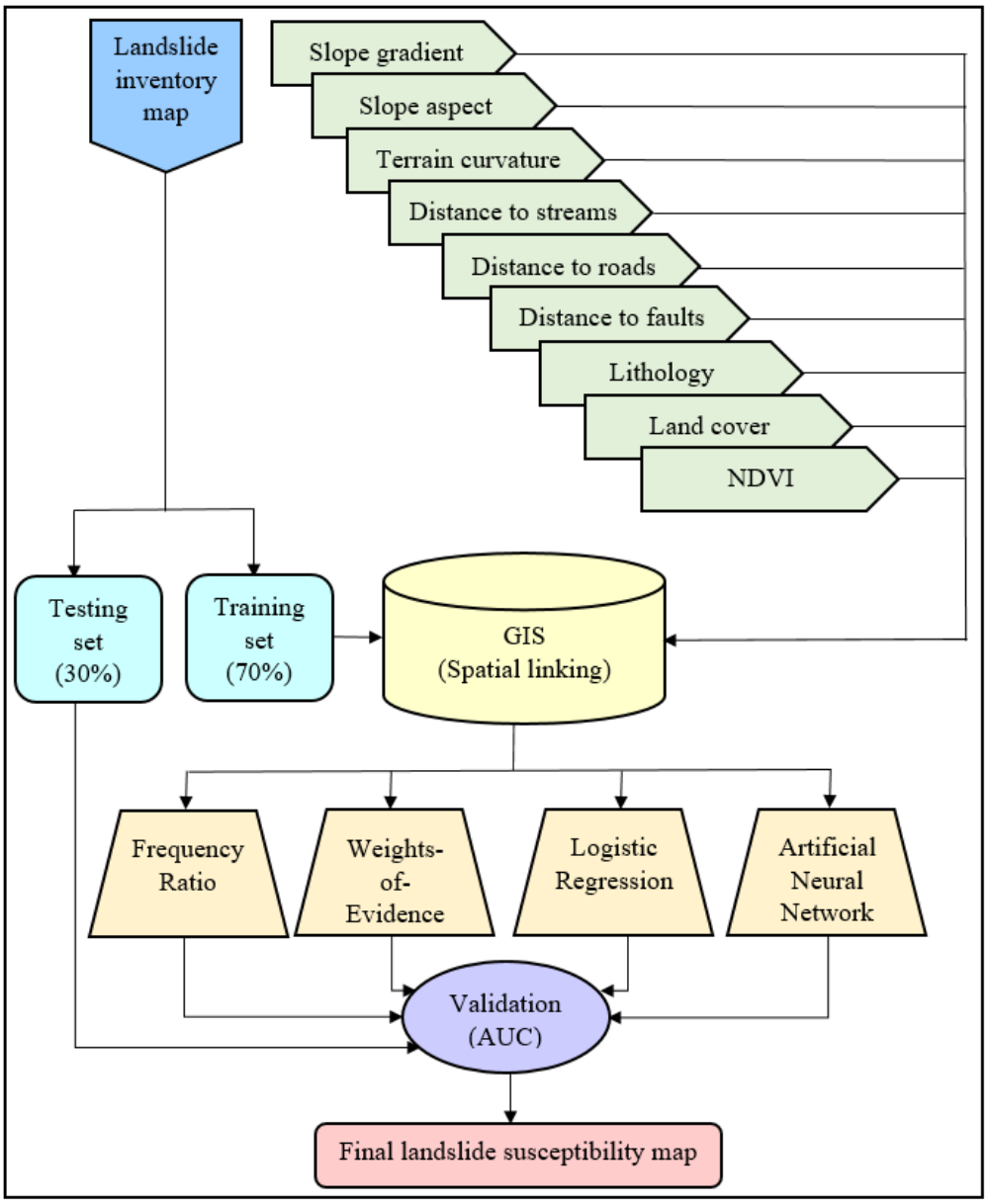

Figure 4.2: Workflow of landslide susceptibility mapping.

In ArcGIS, the training set extracted from the landslide inventory map was converted to a raster set. Then, the training set was spatially linked to each of the causative factor maps to determine within each factor the class corresponding to each pixel of the training set, thus allowing to perform a susceptibility statistical analysis and produce a landslide susceptibility map according to each of the four statistical methods used.

At the end, each landslide susceptibility map resulting from the different statistical analysis methods was validated using the Area Under the Curve (AUC) analysis. The landslide susceptibility map with the best AUC, was selected as the final landslide susceptibility map in order to be later reclassified into low, moderate and high susceptibility zones to be later used for the landslide hazard assessment.

It should be noted that during this research, various classification methods were used, including the Geometrical Interval method for classifying the final susceptibility map, the Equal Interval method for sorting both the positive and negative mean velocity of the LOS ground-surface deformations resulting from the PSI technique and classifying the NDVI map, and the Jenks Natural Breaks method for classifying the total ground-surface deformation values resulting from the D-InSAR technique. The Geometrical Interval classification is considered a good method for visualizing the prediction results (Frye, 2007). The Equal Interval classification emphasizes the amount of an attribute value in relation to the other values (Osaragi, 2002). The Jenks Natural Breaks classification determines the best arrangement of values in different classes in a way that reduces variance within classes and maximizes variance between classes (Chen et al., 2013).

4.4.1 Frequency ratio method

The main principle of the frequency ratio method depends on the relationship between an area where landslides have occurred and all causative factors of landslides in that area (Lee et al., 2004).

The frequency ratio of a causative factor class is the ratio of the probabilities of landslide occurrence for this class. So, if landslide occurrence is denoted by L, and a given causative factor class is denoted by C, then the frequency ratio of this class is the ratio of probabilities L to C. The higher this ratio is than 1, the stronger the relationship between landslide occurrence and the given causative factor class. In contrast, the lower the ratio is than 1, the weaker this relationship is.

To perform the frequency ratio method, a table was constructed for the classes of each causative factor. Then by using Tabulate-Area tool from the Spatial-Analyst tools in ArcGIS, the ratios of landslide area in each class to the total landslide area were calculated, and the ratios of each class area to the total area was also calculated. After that, the frequency ratio of each class in each causative factor was calculated by dividing the landslide area ratio by the class area ratio as the following equation (Bonham-Carter, 1994):

$$FR_{Class} = \frac{N\_L(Class) / N\_L(Total)}{N\_Class / N\_Total} \quad (4)$$

Where, $FR_{Class\ is}$ the frequency ratio of a landslide causative factor class;

$N\_{L(Class)}$ is the area or number of landslide pixels in a causative factor class;

$N\_{L(Total)}$ is the area or number of total landslide pixels in the study area;

N_{Class} is the area or number of pixels in a causative factor class; and

N_{Total} is the area or number of total pixels in the study area.

Then, the Relative Frequency (RF) value of each causative factor class was calculated by dividing the frequency ratio of each class in a causative factor (FR_{Class}) by the total sum of all frequency ratios of all classes in that factor (FR_{Factor}) as follows:

$$RF = \frac{FR_{Class}}{FR_{Factor}} \quad (5)$$

Where, RF is the relative frequency of each causative factor class; and
FR_{Factor} is the total sum of all frequency ratios of all classes in that factor.

After that, the participation rate (PR) for each causative factor was calculated by dividing the difference between the maximum and minimum relative frequency values in one causative factor by the minimum value of these differences in all the causative factors as follows:

$$PR = \frac{[\max(RF) - \min(RF)]}{\min[\max(RF) - \min(RF)]} \quad (6)$$

Where, PR is the participation rate of each causative factor;
[max(RF) - min(RF)] is the difference value between the maximum and minimum relative frequency values within one causative factor; and
min[max(RF) - min(RF)] is the minimum value of all difference values of all causative factors.

Later, the final frequency ratio of each causative factor class (FR_{Final}) was calculated by multiplying the relative frequency (RF) of each class by the participation rate (PR) which was calculated within each causative factor using the following equation:

$$FR_{Final} = PR * RF \quad (7)$$

Where, FR_{Final} is the final frequency ratio of each causative factor class;
PR is the participation rate of each causative factor; and
RF is the relative frequency of each causative factor class.

The greater the final frequency ratio for a causative factor class, the stronger the correlation between this causative factor class and landslides and the stronger the influence of this class on the occurrence of landslides. If the final frequency ratio is 1, it represents an average; if the final frequency ratio is less than 1, it indicates that the correlation between the causative factor class and the occurrence of landslides is weak; if the final frequency ratio is greater than 1, it indicates that the causative factor class has a strong correlation with the occurrence of landslides.

Finally, the FR_{Final} values of all causative factor classes present in each pixel of the area were added to this pixel and written to the output raster map attribute table of each causative factor using the Lookup tool in ArcGIS. So, the output raster map of each causative factor got new values for each pixel according to its FR_{Final} values. Then, the raster maps of all causative factors were summed together using Raster-Calculator tool in ArcGIS to get the

landslide susceptibility index and the landslide susceptibility map based on the FR method using the following equation (Lee and Talib, 2005):

$$LSI_{FR} = \sum FR_{Final} \quad (8)$$

Where, LSI_{FR} is the landslide susceptibility index based on the FR method in each pixel; and

$\sum FR_{Final}$ is the sum of all final frequency ratios of all classes in each corresponding pixel.

4.4.2 Weights-of-Evidence method

The Weights-of-Evidence (WoE) method is a bivariate statistical analysis method that uses a Bayesian probability model (Agterberg et al., 1990; Lee et al., 2002). It was originally developed at the Canadian Geological Survey for GIS-based mineral potential assessment (Bonham-Carter et al., 1990) and later it was adapted by Sabto (1991) and Van Westen (1993) for GIS-based landslide susceptibility mapping depending on bivariate datasets, i.e. landslide and non-landslide.

To perform the bivariate statistical analysis using the WoE method, the training set of non-landslides, which was prepared with same size as the training set of landslides, was merged with the training set of landslides into a total training dataset.

In general, the WoE method gives uncertainty of landslide occurrence based on the relationship of both landslides and non-landslides with all causative factors involved (Chung and Fabbri, 1999). In Bayes' theorem, the conditional probability $P_{L|C}$ can be expressed as (Bonham-Carter, 1994):

$$P_{L|C} = \frac{P_{L \cap C}}{P_C} \quad (9)$$

Where, $P_{L|C}$ is the conditional probability of landslide occurrence L conditioned by the presence of a causative factor class C;

$P_{L \cap C}$ is the proportion of the total area occupied by the L and C intersection; and

P_C is the probability of the presence of class C in the study area.

In statistics and GIS environment, $P_{L \cap C}$ can be expressed as:

$$P_{L \cap C} = \frac{N_{L \cap C}}{N_{Total}} \quad (10)$$

Where, $N_{L \cap C}$ is the number of landslide pixels in the class C; and

N_{Total} is the number of total pixels in the study area.

And P_C can be expressed as:

$$P_C = \frac{N_C}{N_{Total}} \quad (11)$$

Where, N_C is the number of class pixels of the class C.

So, substituting equations 10 and 11 into equation 9 gives:

$$P_{L|C} = \frac{N_{L \cap C}}{N_C} \tag{12}$$

Similarly, the conditional probability $P_{C|L}$ can be expressed as follows:

$$P_{C|L} = \frac{P_{C \cap L}}{P_L} \tag{13}$$

Where, $P_{C|L}$ is the conditional probability of a causative factor class C presence conditioned by landslide occurrence;

$P_{C \cap L}$ is the proportion of the total area occupied by the L and C intersection and can be expressed similarly to equation 10; and

P_L is the prior probability of landslides in the study area, and equal to the number of the total landslide pixels in the study area N_L divided by the number of the total pixels in the study area N_{Total}.

By substituting the value of P_L into the equation 13, and since $P_{L \cap C}$ is the same as $P_{C \cap L}$, so the conditional probability $P_{C|L}$ can be expressed as follows:

$$P_{C|L} = \frac{N_{C \cap L}}{N_L} \tag{14}$$

Where, $N_{C \cap L}$ is the number of landslide pixels in the class C; and

N_L is the number of the total landslide pixels in the study area.

A similar expression can be derived for non-landslide $\overline{L}$ to get the posterior probability $P_{C|\overline{L}}$:

$$P_{C|\overline{L}} = \frac{N_{C \cap \overline{L}}}{N_{\overline{L}}} \tag{15}$$

Where, $P_{C|\overline{L}}$ is the conditional probability of the class C presence conditioned by non-landslides presence;

$N_{C \cap \overline{L}}$ is the number of non-landslides pixels in the class C; and

$N_{\overline{L}}$ is the number of the total non-landslide pixels in the study area.

To perform the Weights-of-Evidence method, the positive weight W^+ and the negative weight W^- were calculated using the following natural logarithm equations (Lee and Choi, 2004):

$$W^+ = \ln\left(\frac{P_{C|L}}{P_{C|\overline{L}}}\right) = \ln\left(\frac{\frac{N_{C \cap L}}{N_L}}{\frac{N_{C \cap \overline{L}}}{N_{\overline{L}}}}\right) = \ln\left(\frac{[N_{C \cap L} * N_{\overline{L}}]}{[N_{C \cap \overline{L}} * N_L]}\right) \tag{16}$$

$$W^- = \ln\left(\frac{P_{\overline{C}|L}}{P_{\overline{C}|\overline{L}}}\right) = \ln\left(\frac{\frac{N_{\overline{C}\cap L}}{N_L}}{\frac{N_{\overline{C}\cap \overline{L}}}{N_{\overline{L}}}}\right) = \ln\left(\frac{[N_{\overline{C}\cap L} * N_{\overline{L}}]}{[N_{\overline{C}\cap \overline{L}} * N_L]}\right) \quad (17)$$

Where, W^+ is the positive weight of a causative factor class.

W^- is the negative weight of a causative factor class.

$P_{\overline{C}|L}$ is the conditional probability of a causative factor class C absence conditioned by landslide occurrence;

$P_{\overline{C}|\overline{L}}$ is the conditional probability of a causative factor class C absence conditioned by non-landslides presence;

$N_{\overline{C}\cap L}$ is the number of landslide pixels in all classes of a causative factor except class C and equal to $[N_L - N_{C\cap L}]$; and

$N_{\overline{C}\cap \overline{L}}$ is the number of non-landslide pixels in all classes of a causative factor except class C and equal to $[N_{\overline{L}} - N_{C\cap \overline{L}}]$.

The Tabulate-Area tool in ArcGIS was used to calculate the number of pixels of landslides and non-landslides in each class of each causative factor based on the total training dataset, to calculate their W^+ and W^- values, and to calculate the final weight of each class of each causative factor as an indicator reflects the influence of each class on the occurrence of landslides. The final weight was calculated as (Van Westen, 2002):

$$W_{Final(class)} = W^+ + [\sum W^-] - W^- \quad (18)$$

Where, $W_{Final(class)}$ is the final weight of a causative factor class.

$\sum W^-$ is the sum of all negative weights in a multiclass causative factor.

Moreover, $W_{Final(class)}$ values in each causative factor were summed to get the final weight of each causative factor $W_{Final(factor)}$ as an indicator reflects the influence of each causative factor on the occurrence of landslides. Finally, $W_{Final(class)}$ values of all classes present in each pixel of the study area were added to this pixel and written to the output raster map attribute table of each causative factor using the Lookup tool in ArcGIS. So, the output raster map of each causative factor got new values for each pixel according to its $W_{Final(class)}$ values. Then, the raster maps of all causative factors were summed together in each pixel using Raster-Calculator tool in ArcGIS to get the landslide susceptibility index and the landslide susceptibility map based on the WoE method using this equation:

$$LSI_{WoE} = \sum W_{Final(class)} \quad (19)$$

Where, LSI_{WoE} is the landslide susceptibility index based on the WoE method in each pixel; and

$\sum W_{Final(class)}$ is the sum of all final weights of all classes in each corresponding pixel.

4.4.3 Logistic regression method

Logistic Regression (LR) is a multivariate statistical analysis method considered suitable for landslide studies because it facilitates the dichotomous classification of dependent variables, i.e. landslides or non-landslides, based on a group of independent variables, i.e. causative factors. The LR method identifies the causative factors that are relatively most responsible for landslide occurrence in a given area (Atkinson and Massari, 1998; Dai and Lee, 2003).

In general, the method of logistic regression aims to estimate and assess the influence of each causative factors on the occurrence of landslides on the basis of the odds and logit of landslides. In statistics, the odds of a binary event are the ratio of the probability that the event will happen to the probability that the event will not happen, and can be expressed for landslides as follows (Kleinbaum and Klein, 1994; Chau and Chan, 2005):

$$\mathrm{Odds(L)} = \frac{P_L}{1-P_L} \tag{20}$$

Where, $\mathrm{Odds(L)}$ is the odds of landslides, expressed as the ratio of landslide probability to non-landslide probability; and

P_L is the landslide probability, which together with the non-landslide probability gives a value of 1.

In logistic regression, the natural logarithm of the odds is the logit (Kleinbaum and Klein, 1994). Therefore, the logit of landslides, which represents a logistic function for the Bernoulli distribution, can be expressed as follows:

$$\mathrm{Logit(L)} = \ln\left(\frac{P_L}{1-P_L}\right) \tag{21}$$

Where, $\mathrm{Logit(L)}$ is the logit of landslides.

Instead of fitting a line to the data as in linear regression, logistic regression fits an S-shaped curve to the landslide probabilities. Depending on a specified cut-off value in the logistic function, the landslide probabilities are classified as a binary outcome of landslides and non-landslides. For each causative factor, probability values higher than the cut-off value are classified as landslides, i.e. 1, and probability values less than the cut-off value are classified as non-landslides, i.e. 0. Furthermore, only probabilities higher than the cut-off value are used to calculate the coefficient of each causative factor, while other probabilities are withheld.

In logistic models, the logit can be simplified by a linear relationship with a combination of independent variables and their contributions as follows (Kleinbaum and Klein, 1994):

$$\mathrm{Logit(L)} = c_0 + \sum(c_i * F_i) \tag{22}$$

Where, c_0 is the intercept of the model;
F_i is the independent variables, i.e. the causative factors; and
c_i is the coefficients reflecting the contribution and influence of each causative factor F_i.

To apply the statistical analysis of the logistic regression method, the total training raster dataset, previously prepared from both landslide and non-landslide training sets, was used. Initially, all 2706 pixels of the total training raster dataset were converted to points using the Raster-To-Point tool in ArcGIS. Using the Extract-Multi-Values-To-Points tool in ArcGIS, numeric values were extracted at each point representing the class number from each of the nine raster maps of the causative factors, resulting in a numeric table with rows for all points and columns for each dependent and independent variable. The table was then used as input for statistical analysis of logistic regression.

The Real Statistics Resource Pack in Microsoft Excel was used to calculate the intercept and coefficients of the causative factors, so that the influence of each causative factor on the landslide occurrence can be estimated and assessed.

The equation for the landslide susceptibility index based on the LR method used in ArcGIS to create the landslide susceptibility map based on this method can be written as follows (Lee and Pradhan, 2007):

$$LSI_{LR} = \frac{1}{1+e^{-Logit(L)}} = \frac{1}{1+e^{-[c_0+\sum(c_i*F_i)]}} \quad (23)$$

Where, LSI_{LR} is the landslide susceptibility index based on the LR method.

4.4.4 Artificial neural networks method

Artificial Neural Network (ANN) is a computational model that can acquire, represent and compute a mapping from one multivariate space of information to another, given a dataset representing that mapping (Garrett, 1994). The purpose of an artificial neural network is to build a model of the data training process allows the neural network to predict a final output from any new input of the same data type (Michie et al., 1994).

For nearly three decades, the artificial neural network method has been used as a special type of machine learning algorithms in a wide range of classification applications in the geosciences. Moreover, a number of studies have also applied artificial neural networks as a statistical analysis for landslide susceptibility mapping (Yesilnacar and Topal, 2005; Ermini et al., 2005; Melchiorre et al., 2008; Falaschi et al., 2009).

The increasing use of artificial neural networks as a statistical analysis method over the past years is mainly due to its ability to process data on any scale and in any nominal, ordinal or other representational format. In addition, artificial neural networks can easily process qualitative variables making it widely used in an integrated analysis of the multiple-source spatial data for classification and prediction (Kawabata and Bandibas, 2009).

Artificial neural networks simulate the way the human brain works in solving problems. The decision-making in artificial neural networks is performed over a network of connected processing elements, known as nodes or neurons. These neural networks provide a prediction based on an analysis of a training set with known input and output parameters or data (Van Leeuwen, 2012).

The Multi-Layer Perceptron (MLP) neural network is one of the most widely used ANNs. The MLP consists of three main layers, i.e. input, hidden and output layers of neurons (Figure 4.3), and can identify relationships that are nonlinear in nature (Rumelhart et al., 1986; Van Leeuwen, 2012).

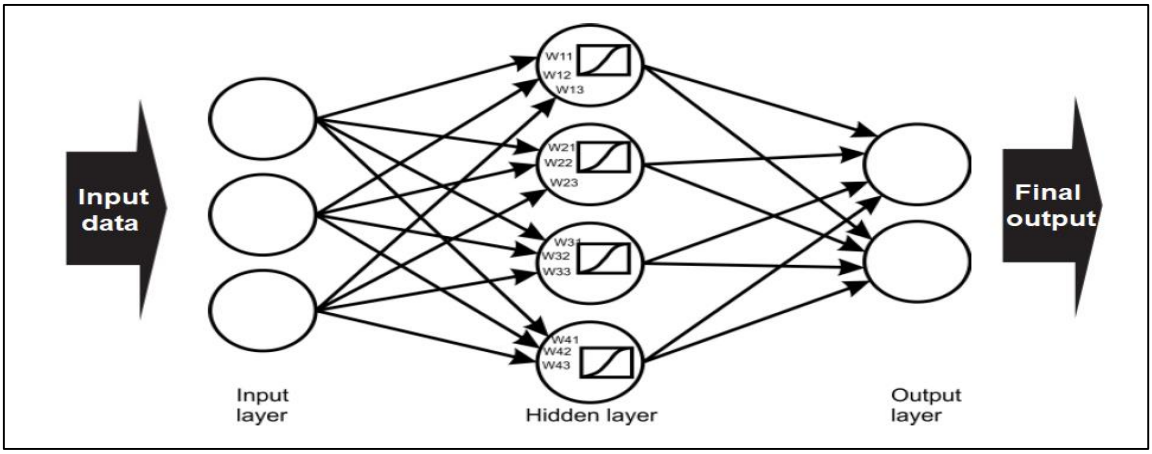

Figure 4.3: Basic artificial neural network with layers and neurons (Van Leeuwen, 2012).

The MLP networks are trained by error-correction learning using a Back-Propagation (BP) learning algorithm (Zurada, 1992). The training phase is performed over all these three main layers while the neural network investigates the links between input and output. These links are investigated through the adjustment of the weights in response to the mean-square errors or another performance function to measure the error between the predicted, i.e. calculated, and the expected results (Lee et al., 2003). The number of hidden layers in the training phase is not easy to determine and depends on the independent variables (Kawabata and Bandibas, 2009). The training phase ends at the moment when the error stabilizes at a low level or when a minimal error is reached after an iteratively repeated process of feeding forward signals and back-propagating errors. Then, the network is applied via a feed-forward structure or a simulation phase to produce predictions for the whole dataset or the final output (Kawabata and Bandibas, 2009; Van Leeuwen, 2012). The complexity and performance of a network depends on the number of hidden layers and the number of neurons per layer (Van Leeuwen, 2012).

Figure 4.4 shows schematically how the ANN-driven algorithm is applied to landslide susceptibility mapping. As it can be seen, the input causative factors data are arranged into a network of input neurons, then the following phases of training and feed-forward structure or simulation will provide the final prediction output. This final output is presented by a distribution of landslide probability values showing the likelihood of each pixel to belong to the stable or unstable group (Kawabata and Bandibas, 2009).

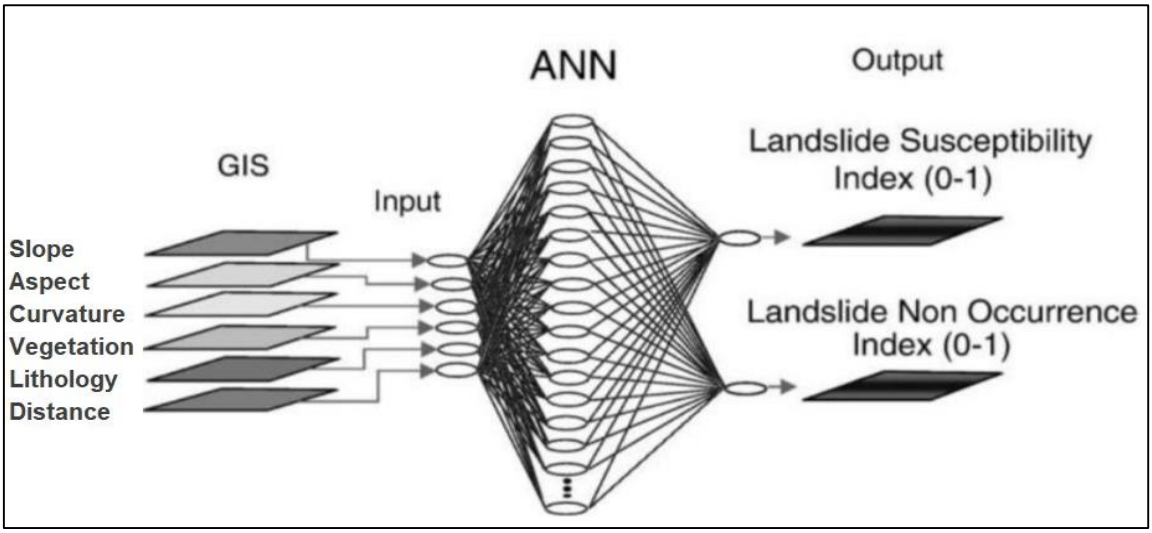

Figure 4.4: Schematic representation of the landslide susceptibility mapping using ANN-driven algorithm (after Kawabata and Bandibas, 2009).

The main limitation of ANN results from the fact that the user often does not know how it works and which input neurons or causative factors are the most influential causative factors for the occurrence of landslides in the study area. Therefore, the ANN method is considered as a case-specific statistical analysis method (Lee et al., 2003).

To apply the statistical analysis of the ANN method, a MLP neural network using a BP learning algorithm was applied to the total training raster dataset of 2706 pixels after it was prepared in a numeric table with 2706 rows for all points and 10 columns for each dependent and independent variable. The numeric table was imported to Matlab as a numeric matrix in order to set the inputs and outputs, i.e. targets, and to start the training phase of the neural network.

The structure of 9 input layers, 5 hidden layers and 2 output layers was selected for the neural network training phase (Figure 4.5), with setting up a random subdivision of the input landslide and non-landslide training dataset into 70% for training, 15% for validation and 15% for testing (Figure 4.6).

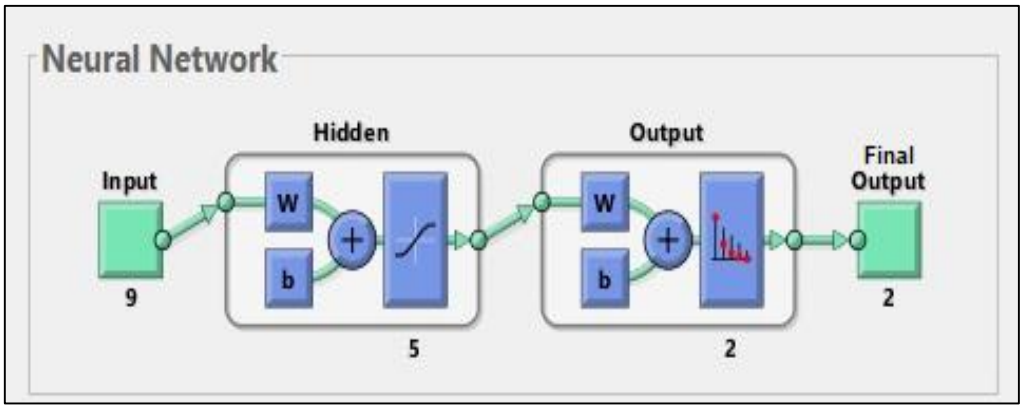

Figure 4.5: The structure of the neural network training used in this research.

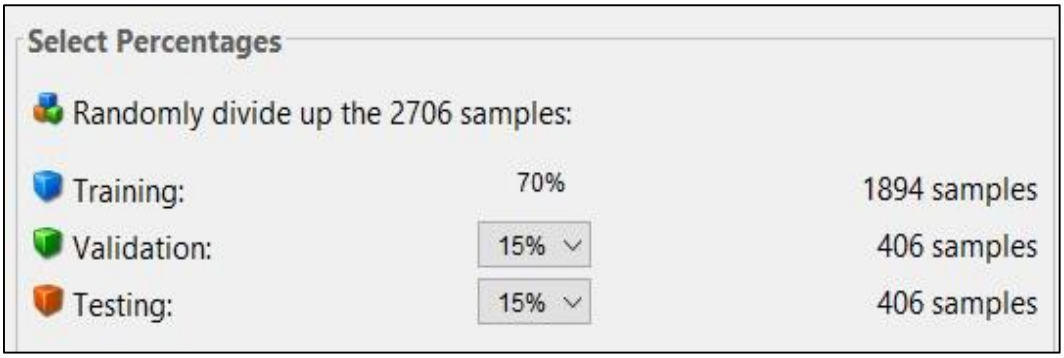

Figure 4.6: Input training data subdivision during the training phase in the ANN analysis.

It should be noted that all input training data used in the training phase were numeric, and these numeric values were not ordinal data, but nominal data indicating the different classes of the causative factors.

After training the network and storing the weights, the simulation phase was applied which required to import the complete causative factors data of all the pixels in the entire study area. So, a single raster dataset was created from multiple bands of the nine causative factor maps by using the Composite-Bands tool in ArcGIS. As a result, a raster map with 1,631 columns and 1,863 rows of all causative factor data was created before being converted in Matlab into a two-dimensional matrix from which the final output was calculated based on the saved trained neural network (Figure 4.7).

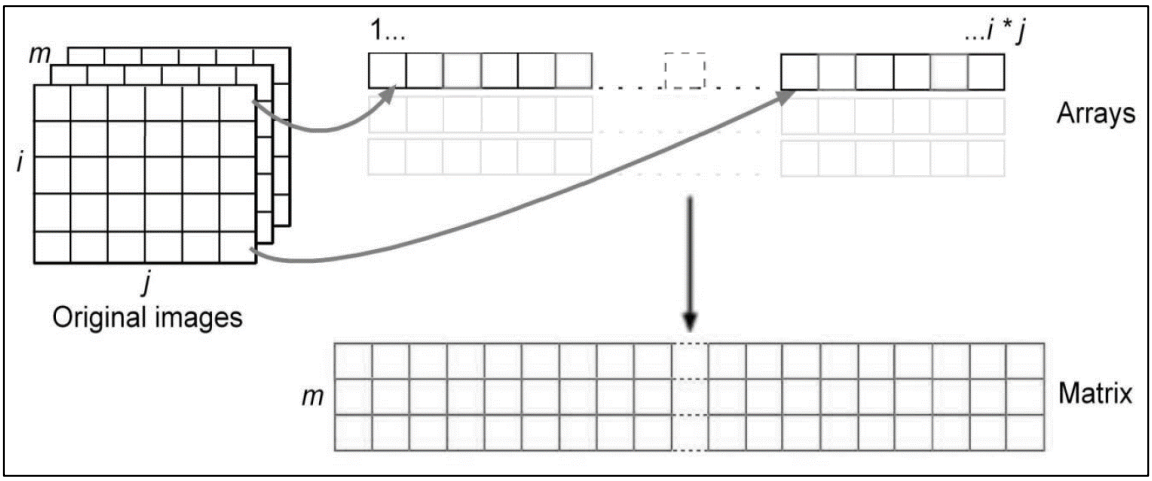

Figure 4.7: Data conversion in the artificial neural network method (Van Leeuwen, 2012).

After the simulation phase, the final output of each pixel in the study area was determined as an array of floating-point numbers in the range [0, 1]. Then, the array was converted back to a matrix before converting it to a raster map again as 8-bit integers in the range [0, 255] which represents the landslide susceptibility index based on the ANN method (LSI_{ANN}) in each pixel. As a result, the landslide susceptibility map based on the ANN method was created.

4.4.5 Validation and comparisons of the statistical analysis methods

The same validation process was performed for the resulting susceptibility map of each of the four statistical analysis methods used in this research.

Area Under the Curve (AUC) analysis was applied to the result of each statistical analysis using the cumulative validation curve of the testing set prediction rate, which allows to describe the statistical analysis ability of correctly predicting the occurrence of landslides and also allows to characterize and represent the efficiency of each statistical analysis method and to compare their efficiencies (Pradhan et al., 2010b).

For each statistical analysis method, the landslide susceptibility map created was reclassified in ArcGIS into one hundred equal interval classes of the landslide susceptibility index and sorted in descending order, i.e. from the highest value to the lowest value.

Afterwards, the resulting reclassified map was used to calculate the landslide areas and pixels in each class based on the landslide testing set using the Tabulate-Area tool in ArcGIS.

As a result, the percentage of landslide pixels in each class was calculated in addition to the cumulative percentage of landslide pixels based on the landslide testing set.

The cumulative validation curve for each statistical analysis method was plotted based on the cumulative percentage of landslide pixels on the y-axis and the one hundred classes of landslide susceptibility index on the x-axis (Pradhan et al., 2017).

The AUC in each class was calculated according to the simple trapezoid rule as follows (Purves, 1992; Begueria, 2006):

$$AUC = \sum_{i=1}^{n} \left(\frac{1}{2} * (X_{\{i+1\}} - X_{\{i\}}) * (Y_{\{i+1\}} + Y_{\{i\}}) \right) \quad (24)$$

Where, $(X_{\{i+1\}} - X_{\{i\}})$ is the difference value between two consecutive susceptibility classes; and

$(Y_{\{i+1\}} + Y_{\{i\}})$ is the sum of the cumulative percentage of landslide pixels in these two consecutive susceptibility classes, starting with the first class, i = 1, which has the highest susceptibility value, to the last class, n, which has the lowest susceptibility value.

At the end, the sum of AUC values was calculated and divided by one hundred to obtain the final value of the AUC for each of the four statistical analysis methods used.

After comparing the AUC of the landslide susceptibility maps created using the four statistical analysis methods used, the landslide susceptibility map with the optimal AUC was selected as the final landslide susceptibility map which was used as input for landslide hazard mapping.

4.5 Ground-surface deformation mapping using advanced remote sensing techniques

Ground-surface deformation mapping using advanced remote sensing techniques was carried out for a period between October 2018 and March 2019 to cover the majority of a rainfall season. Two advanced remote sensing techniques were applied to obtain ground-surface deformation data. The first technique was the Persistent Scatterer Interferometry (PSI) technique which was used to create the mean velocity map of ground-surface deformations in satellite LOS direction during the study period, to be later used to create the intensity map of the ground-surface deformations required for landslide hazard assessment and mapping process. The second technique was the Differential Interferometric Synthetic Aperture Radar (D-InSAR) technique which was used to create the map of total ground-surface deformations in satellite LOS direction during the same period to be used in the validation process of interferometry results by comparison with D-GPS field measurements.

4.5.1 Mean velocity map of ground-surface deformations using PSI technique

The mean velocity map of ground-surface deformations was obtained on the basis of 14 Sentinel-1B SAR images from 16 October 2018 to 21 March 2019 using PSI technique.

All images were co-registered in SNAP software to one unique master image chosen from them using the Stack-Overview-and-Optimal-InSAR-Master-Selection tool in the Sentinel-1 toolbox. The thirteen resulting master-slave pair images with different temporal and perpendicular baselines were also processed in SNAP to generate two final products for all pair images with and without interferogram formation. The two final products in SNAP are required to export the combination of amplitude and wrapped phases of these SAR time-series images to StaMPS in order to unwrap all the wrapped phases using advanced logarithms, as well as to estimate the Persistent Scatterer (PS) probability for each pixel in the interferograms that were formed.

At the beginning in SANP, the split of the sub-swath and bursts related to the study area was done for each image separately. After that, orbit metadata of each resulting product was updated using Apply-Orbit-File tool to provide accurate information about the satellite position and velocity. Then, S-1-Back-Geocoding tool was used for the co-registration process of all slaves to the optimum master, using the orbit parameters of all products used and a DEM generated from Sentinel-1 SAR data for the same area (Hammad et al., 2017). The DEM was used after correcting the anomalies caused by dense vegetation in the area, using a corresponding TanDEM-X® DLR product from the German Aerospace Center. After applying the Enhanced-Spectral-Diversity (ESD) process to perform range and azimuth corrections for each burst and ensure accurate continuity of the phase across all bursts, the resulting product was processed twice, once by applying only the deburst step before the subset step to the same study area extent, and once by applying all of the interferogram formation, deburst, topographic phase removal steps before the subset step. The two resulting products from the two processing paths were used to export the SAR time-series data from SNAP to StaMPS using Stamps-Export tool (Figure 4.8).

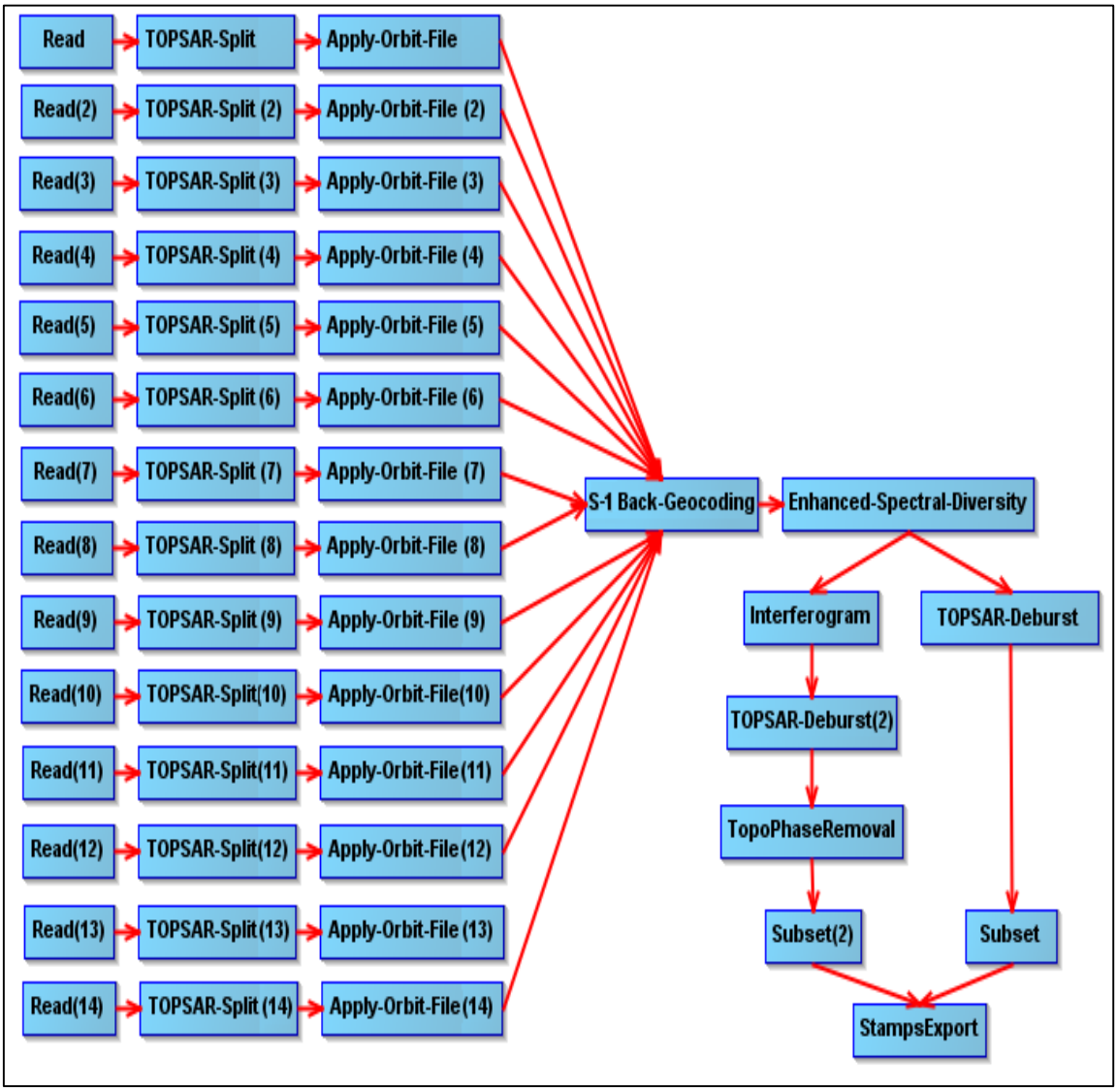

Figure 4.8: Flow chart of preparing SAR time-series images in SNAP to export the SAR data to StaMPS for producing mean velocity data of ground-surface deformations using PSI technique (Hammad et al., 2020).

After exporting the SAR time-series data products from SNAP, the resulting products were processed using StaMPS v4.1b in Matlab under Linux to perform the PS estimation process and calculate the mean velocity of ground-surface deformation in the satellite LOS direction at each persistent scatterer point.

Eight steps were performed in StaMPS on the resulting products exported from SNAP to StaMPS (Hooper et al., 2013).

The first step was loading the data for selecting the initial PS candidates using an amplitude dispersion threshold value which usually set to 0.4. In the second step which is an iterative step, the estimation process of the phase noise value for each PS candidate in every interferogram was performed. Then, in the third step, PS and non-PS points were sorted

based on their noise characteristics. In the fourth step, the PS points selected in the previous step were weeded, dropping those caused by signal contribution of neighbouring ground resolution elements and those deemed too noisy. In the fifth step, the wrapped phase of the selected points is corrected for spatially-uncorrelated look angle error. After that, in the sixth step, filtering and unwrapping phase processes were performed. Then, in the seventh step, spatially-correlated look angle error was calculated, and the master atmosphere and orbit error (AOE) phase was also estimated simultaneously. In the final step, the mean velocity of ground-surface deformations in the satellite LOS direction were calculated in each of the PS points.

As the result, a multipoint data set of all persistent scatterers with the mean velocity values was generated, representing the ground-surface deformations over the study area during the study period.

The resulting dataset was then exported as a GIS shapefile in a point feature format to be processed further in ArcGIS in order to prepare the deformation intensity map required for the assessment process of landslide hazard.

4.5.2 Total ground-surface deformation mapping using D-InSAR technique

To create a total ground-surface deformation map using D-InSAR technique, the two SAR images acquired by Sentinel-1B on 16 October 2018 and 21 March 2019 were co-registered as master and slave and used to generate an interferogram along the highway in the Balloran Dam area so that the D-InSAR results of the total deformation could be compared with the D-GPS field measurements carried out there. The data of the total ground-surface deformations during the period between the two acquisitions were produced on the basis of the workflow shown in figure 4.9.

Where in SNAP, the Sentinel-1 toolbox was used to split the sub-swath and bursts related to the Balloran Dam area first to reduce data size and processing time. Then, orbit metadata of the products were updated using the Apply-Orbit-File tool to provide accurate information about the satellite's position and velocity. After that, Back-Geocoding tool was used for the co-registration process using the orbit parameters of the two products and a related DEM before applying Enhanced-Spectral-Diversity (ESD) tool to perform range and azimuth corrections of all bursts. Next, Interferogram-Formation tool was applied to generate a complex interferogram and to subtract both of the flat-earth phase and the topographic phase from it. Then, deburst process was applied to seamlessly join all the involved bursts into one single image to ensure the continuous coverage of the ground (Grandin, 2015). Since the original SAR images contains a lot of inherent speckle noise, multilooking step was applied to reduce speckle appearance and to improve image interpretability. Also, Goldstein phase filtering was applied to remove noise phase from the complex interferogram, which is directly related to the interferometric coherence and the number of looks (Li et al., 2008).

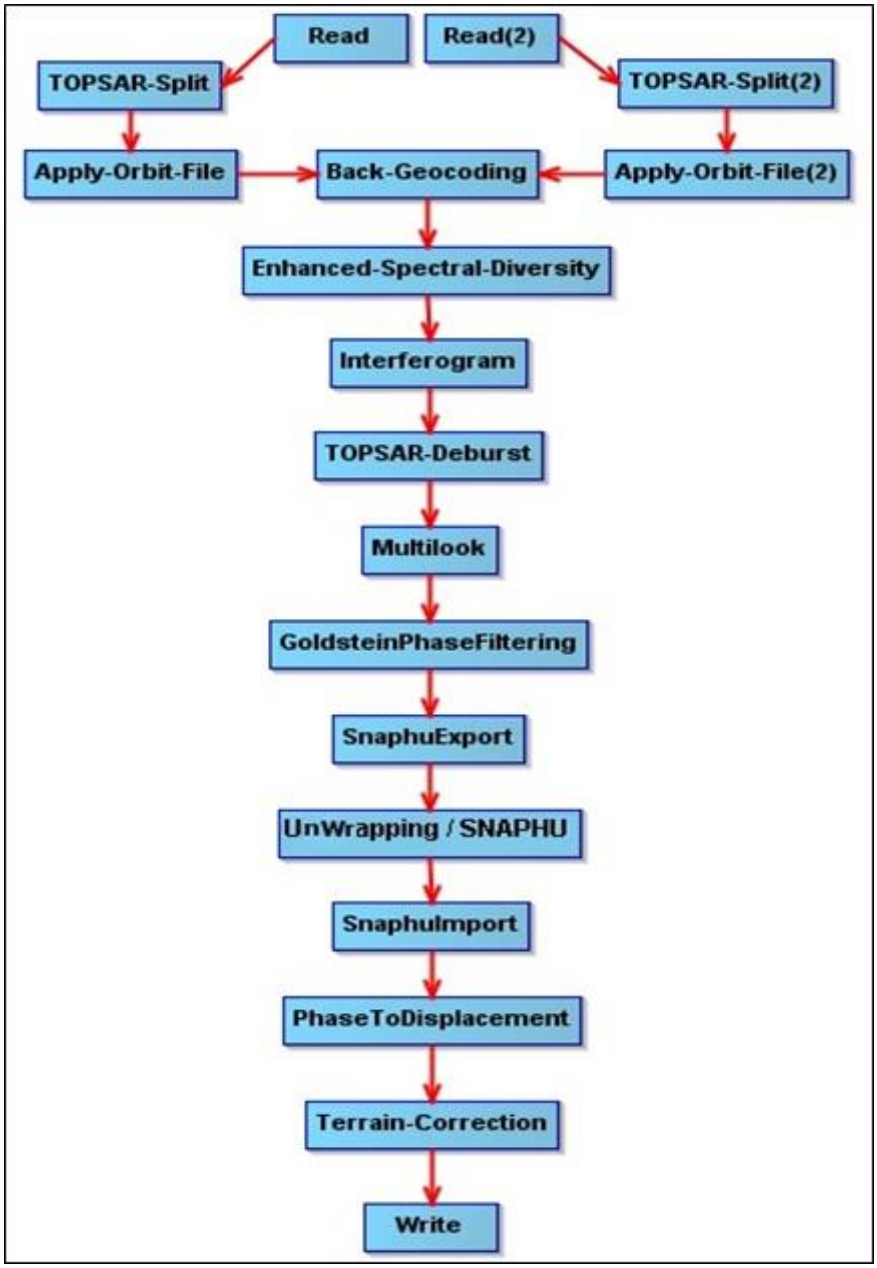

Figure 4.9: Flow chart for producing a total value map of ground-surface deformations using the D-InSAR technique.

Finally, the remaining displacement phase was exported to SNAPHU and unwrapped before being imported back into SNAP and converted to displacement values using the Phase-to-Displacement tool.

AS the results were still in radar geometry, the distances were still distorted. Therefore, a terrain correction process using Range Doppler terrain correction was applied before exporting the final projected result of the total ground-surface deformations as a raster grid format to ArcGIS to be used in the validation process of interferometry results by comparison with D-GPS field measurements.

4.5.3 Comparison of interferometry results with D-GPS field measurements

For D-GPS field measurements, two campaigns with the Leica System 550 GPS were conducted in October 2018 and March 2019 at the beginning and end of the study period to obtain elevation data from 10 validation points along the highway in the Balloran Dam area, to investigate the ground-surface deformation there between 16 October 2018 and 21 March 2019. It should be noted that the D-GPS field measurements were limited to the highway in the area, as mines that were randomly placed outside the roads during the current war in Syria have not yet been removed.

A base station of the General Organization of Remote Sensing in the city of Latakia was used as a starting / closing reference point of the D-GPS field measurements (Figure 4.10a), and the D-GPS field measurements of the 10 validation points were carried out with a base antenna on a tripod (Figure 4.10b). At each validation point, the geographic coordinates and ellipsoidal height data were measured through time-based averaging, with observation time of at least 30 minutes until the accuracy indicated in the receiver became acceptable. Later in ArcGIS, a shapefile was created from the difference values between the two campaigns at each validation point to compare the D-GPS deformation values at these ten validation points with the corresponding D-InSAR deformation values from the total ground-surface deformation map.

Figure 4.10: D-GPS field measurements. a- Reference point. b- Validation point.

4.6 Landslide hazard assessment

Since a spatiotemporal systematic record of landslides in the study area in last decades is not available to make the analysis of landslide recurrence or the analysis of the rainfall intensity-duration thresholds for landslide occurrence, the assessment of landslide hazard was carried out using a landslide hazard matrix (Hürlimann et al., 2008; Lu et al., 2014). The landslide hazard matrix focuses mainly on two parameters: the first is the probability of landslide occurrence, i.e. the landslide susceptibility, and the second is the intensity of ground-surface deformations, i.e. the mean velocity of ground-surface deformations during the study period. The study period was chosen from October 2018 to March 2019 to cover the majority of a rainfall season, which is the main period for landslide events.

In order to assess the landslide hazard on the basis of both susceptibility and intensity criteria, the landslide susceptibility map and intensity map were reclassified as low-moderate-high zones and used in a 3-by-3 matrix, which can be called landslide hazard matrix, to classify the landslide hazard as low, moderate and high (Figure 4.11).

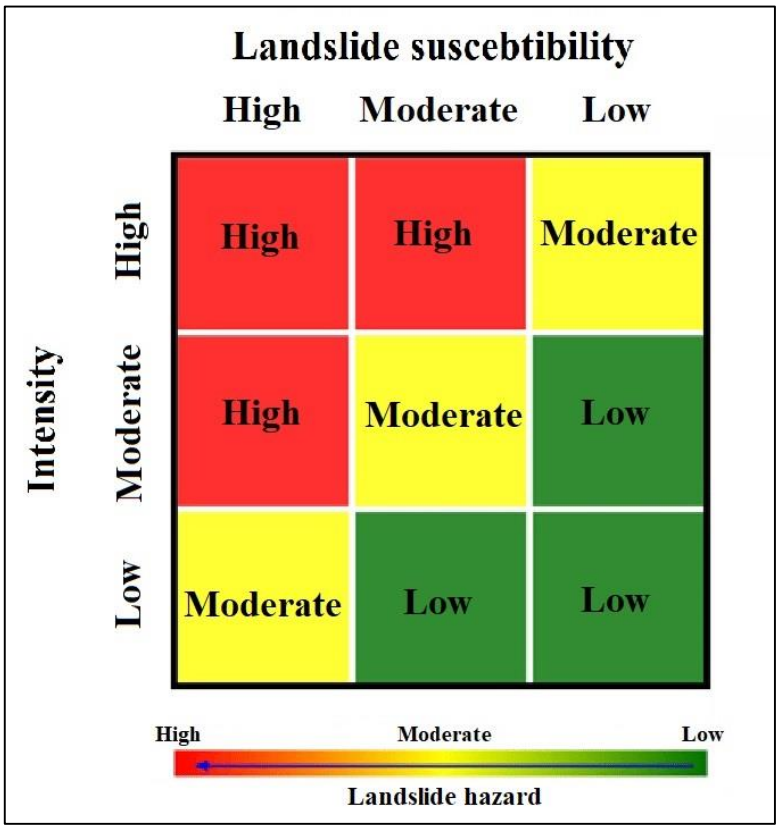

Figure 4.11: The landslide hazard assessment based on the landslide hazard matrix (after Lu et al., 2014).

The intensity map of the ground-surface deformations was created by interpolating the resulting multipoint data set of positive and negative mean velocities of ground-surface deformations in the LOS direction to create a mean velocity raster map. The mean velocity raster map was then reclassified into three positive mean velocity levels and three negative

mean velocity levels using the Equal Interval classification method, so that the same levels were compiled to obtain the intensity map with the low-moderate-high intensity zones. At the end, the intensity map and the landslide susceptibility map were used in the landslide hazard matrix to obtain the landslide hazard map as the final result (Figure 4.12).

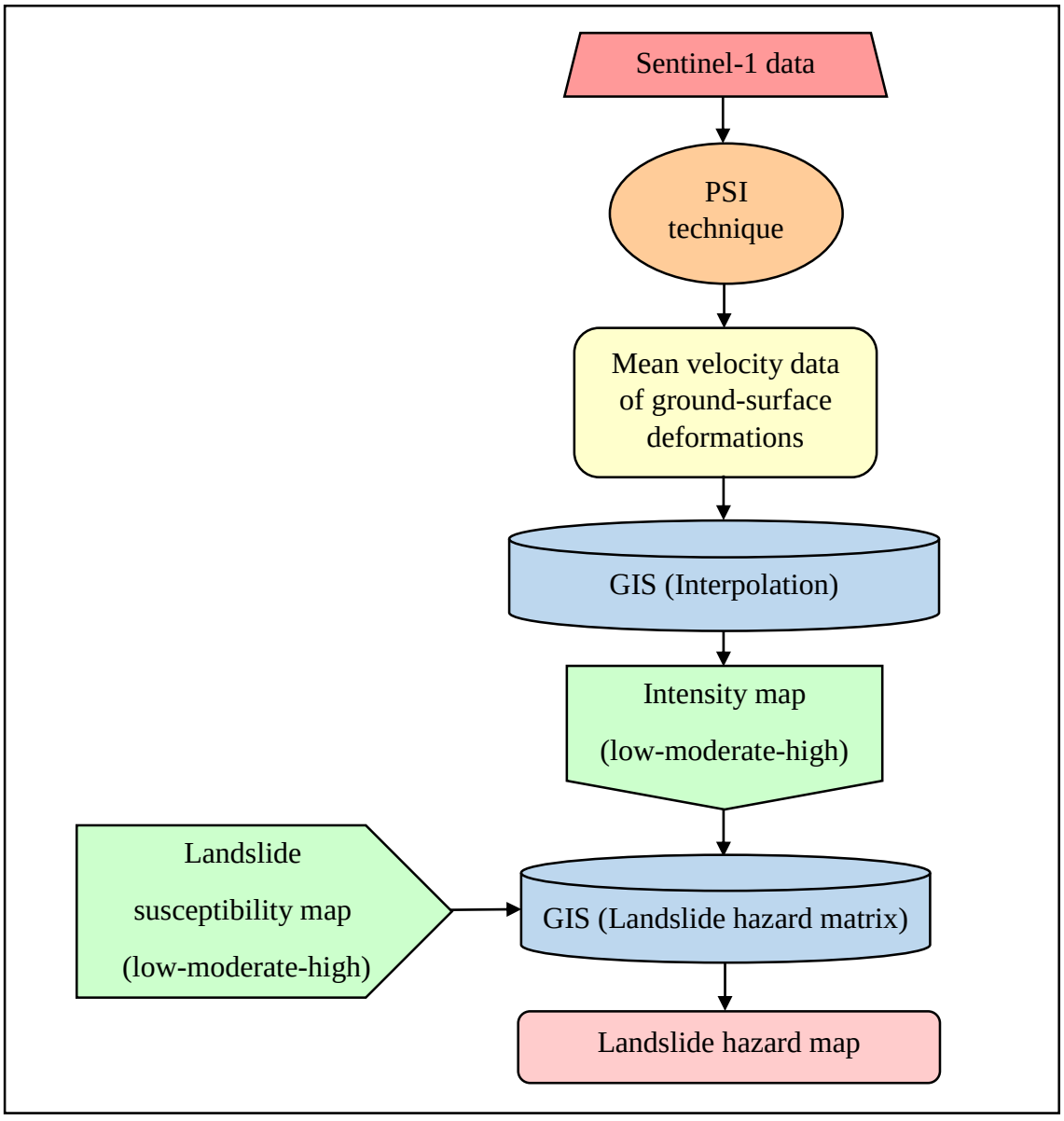

Figure 4.12: Workflow of landslide hazard assessment.

The interpolation process of the mean velocity values was performed using the method of the Inverse Distance Weighted (IDW) interpolation in ArcGIS to obtain a continuous spatial extent from the generated mean velocity data of the ground-surface deformations (García-Davalillo et al., 2013; Notti et al., 2014). In fact, the multipoint data set of the mean velocity is an interconnected dataset in the spatiotemporal domain (Liu et al., 2019).

5. Results and Discussion

This chapter presents and discusses the results of this doctoral research in the context of related literature and methods for investigating the spatial characterization of landslides in the study area in general and for landslide susceptibility analysis and hazard assessment in particular.

5.1 Digital elevation model generation

As mentioned in chapter four, the digital elevation model was generated twice using two different approaches.

The topography-based DEM, which was generated with a spatial resolution of 12.5 m, contains 1693340 pixels with a maximum elevation value of 1130 m above mean sea level (Figure 5.1).

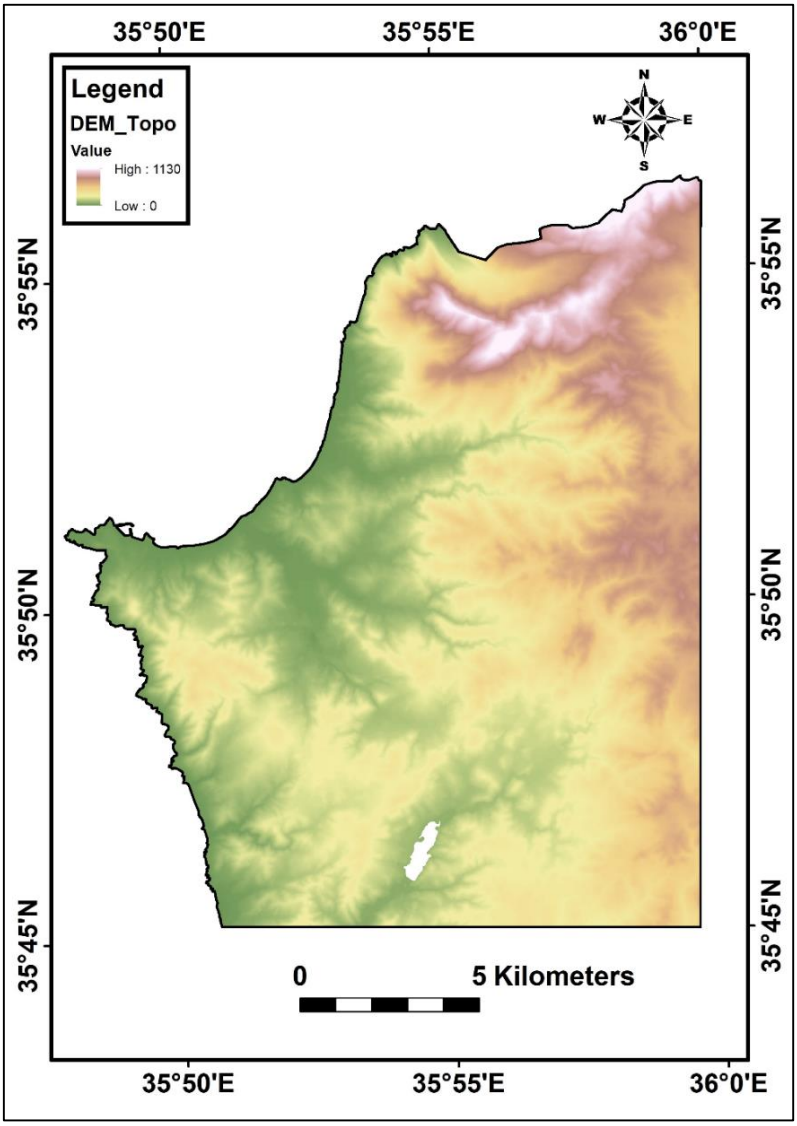

Figure 5.1: The topography-based DEM generated from the topographical map of Kassab.

The SAR-based DEM, which was generated for the whole Syrian coastal region and part of Lebanon, was produced with a [range × azimuth] pixel size of [2.3×14.1] m. The highest elevation was in Lebanon with 2734.6 m, while the highest elevation in the Syrian coastal region was 1582 m at the Turkish border.

The Statistic-Analysis tool in SNAP was applied to the SAR-based DEM, the coefficient of variation was 2.26 while the maximum error was 2.74 m (Hammad et al., 2017). However, comparison of the resulting SAR-based DEM with some corresponding points from D-GPS measurements showed that the difference was more than 20 m in low coherence areas.

In order to use the SAR-based DEM later in the PSI technique, it was clipped to the same spatial extent of the study area and all areas with decorrelation or low coherence due to dense vegetation or atmospheric inhomogeneity were masked and corrected on the basis of the TanDEM-X® product of the area to get the SAR-based DEM of the area (Figure 5.2).

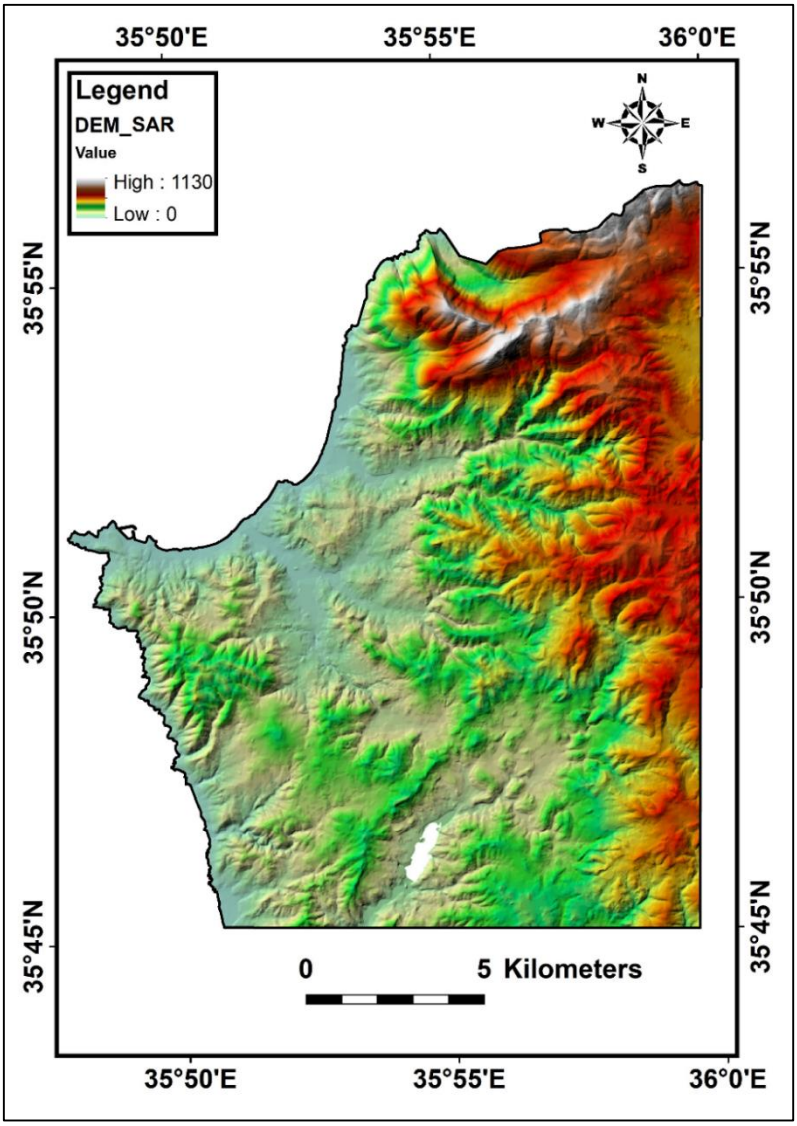

Figure 5.2: The SAR-based DEM of [2.3×14] m pixel size generated from Sentinel-1A data and corrected on the basis of the TanDEM-X® DLR product of the area.

5.2 Landslide inventory map preparation

The prepared landslide inventory map contained 57 polygons representing all landslides that occurred in the area between 1984 and 2018.

The 57 polygons were randomly divided into two sets; 40 landslide polygons were used as a training set for statistical analysis of landslide susceptibility, and 17 landslide polygons were used as a testing set to validate the resulting landslide susceptibility maps. The final raster map of the landslide inventory contained 1353 pixels of the landslide training set and 362 pixels of the landslide testing set (Figure 5.3a).

Similarly, the same number of polygons and total pixels was prepared for non-landslides (Figure 5.3b).

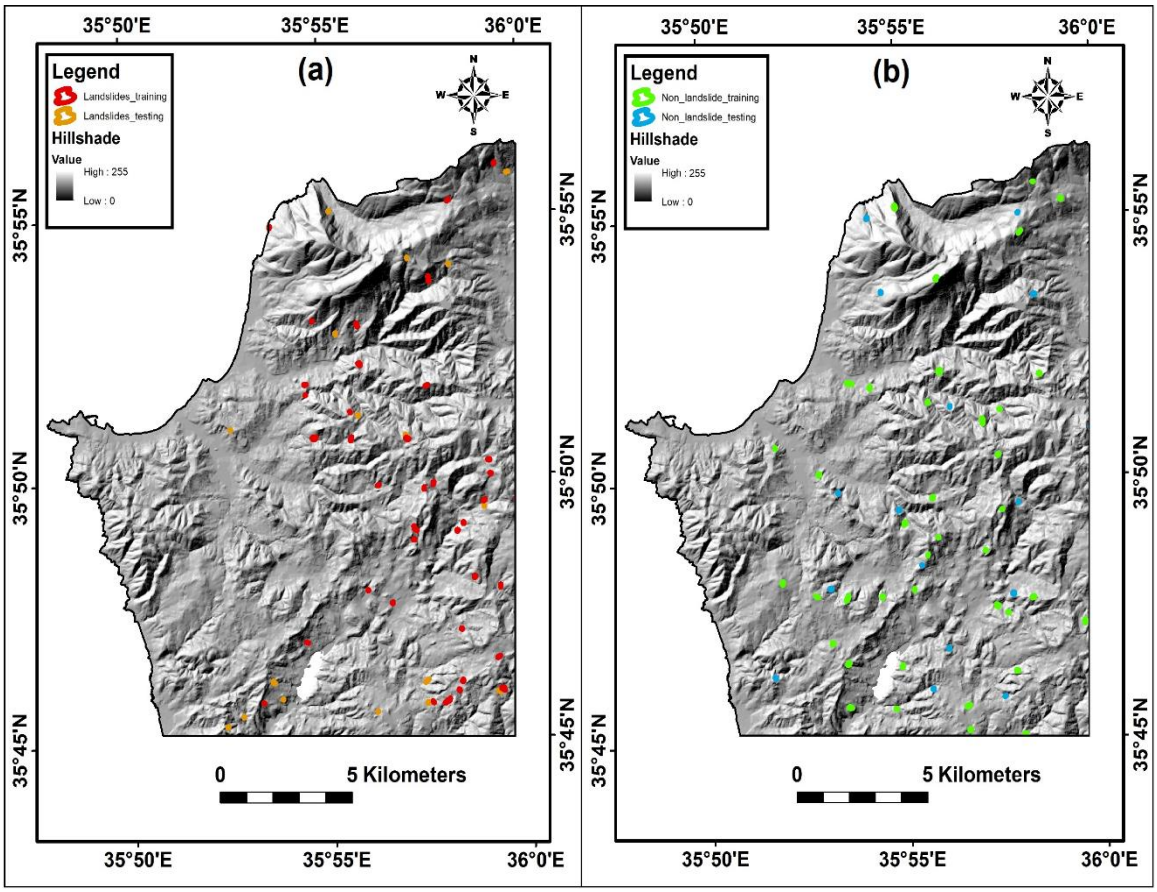

Figure 5.3: The landslide and non-landslide training and testing sets on a hillshade map. a- The landslide dataset and inventory map. b- The non-landslide dataset.

According to the landslide inventory map statistics, 46 out of 57 landslides, corresponding to 80% of the total landslides, cover an area between 1000 m^2 and 4000 m^2 (Figure 5.4). The smallest landslide covers an area of 1000.09 m^2, while the largest landslide covers an area of 12610.9 m^2. The total area of landslides is 176514.34 m^2, corresponding to 0.06% of the total study area.

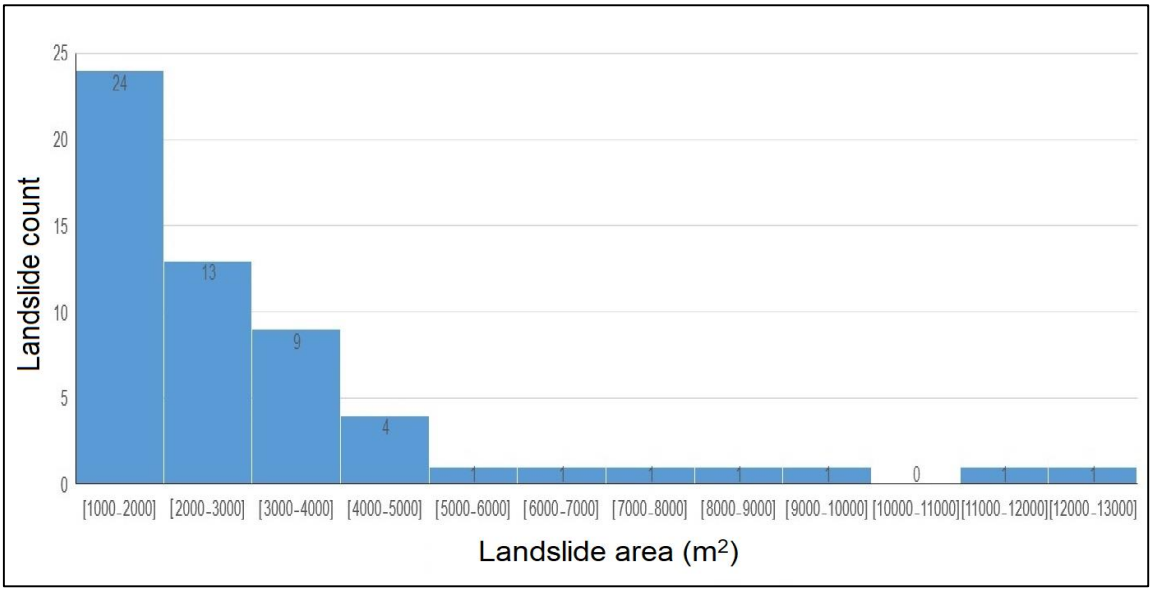

Figure 5.4: Frequency distribution from landslide inventory statistics.

5.3 Causative factor maps preparation for susceptibility analysis

The nine causative factor maps were created in ArcGIS with the same spatial extent, coordinate system and pixel size. Consequently, all nine causative factor maps contained 1693340 pixels distributed over 1863 rows and 1631 columns.

5.3.1 Slope gradient map

The slope gradient map derived from the topography-based DEM showed values from 0 to 83.03 degrees (Figure 5.5).

According to the slope gradient map statistics (Figure 5.6), the first class, which includes slope gradients of less than 10 degrees, covers 28.3% of the total study area and contains 13.29% of the total landslides.

The second class, which includes slope gradients between 10 and 20 degrees, covers the largest area with 35.8% of the total area and contains 26.06% of the total landslides.

The third class, which includes slope gradients between 20 and 30 degrees, covers 25% of the total area and contains 38.83% of the total landslides.

The fourth class, which includes slope gradients of between 30 and 40 degrees, covers 9.2% of the total area and contains 16.50% of the total landslides.

The fifth class, which includes slope gradients of more than 40 degrees, covers the smallest area with only 1.4% of the total area and contains 5.30% of the total landslides.

Based on the area of each class and the percentage of total landslides in each class, slope gradients of more than 20 degrees have a greater association with landslides than slope gradients of less than 20 degrees.

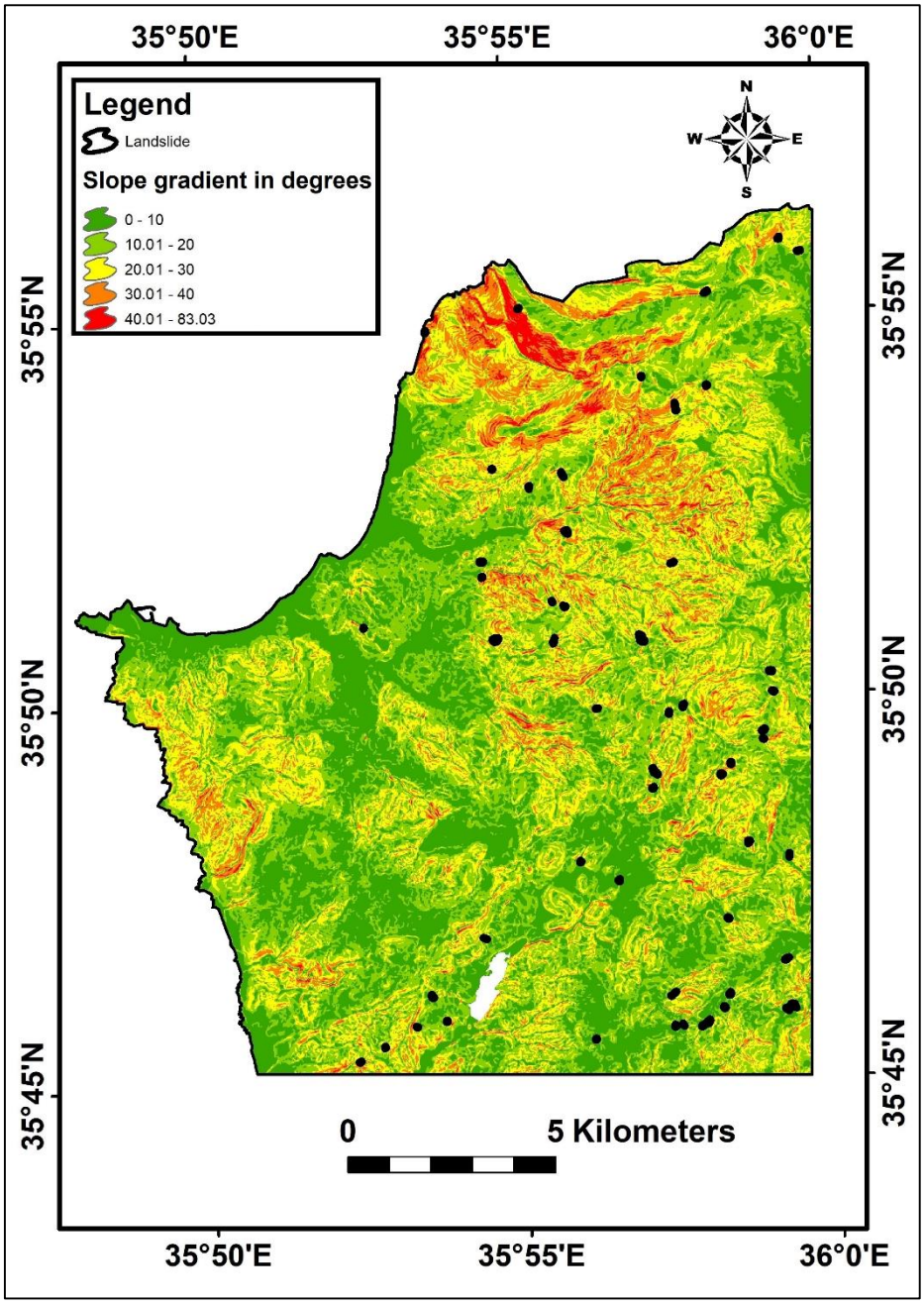

Figure 5.5: The slope gradient map with all landslide locations.

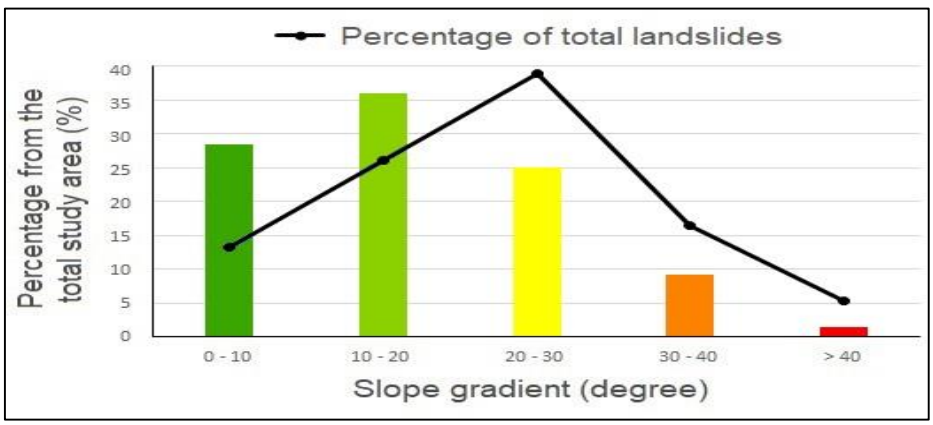

Figure 5.6: Statistics of the slope gradient map.

5.3.2 Slope aspect map

The slope aspect map, which was derived from the topography-based DEM and reclassified into nine classes according to orientation, is shown in figure 5.7.

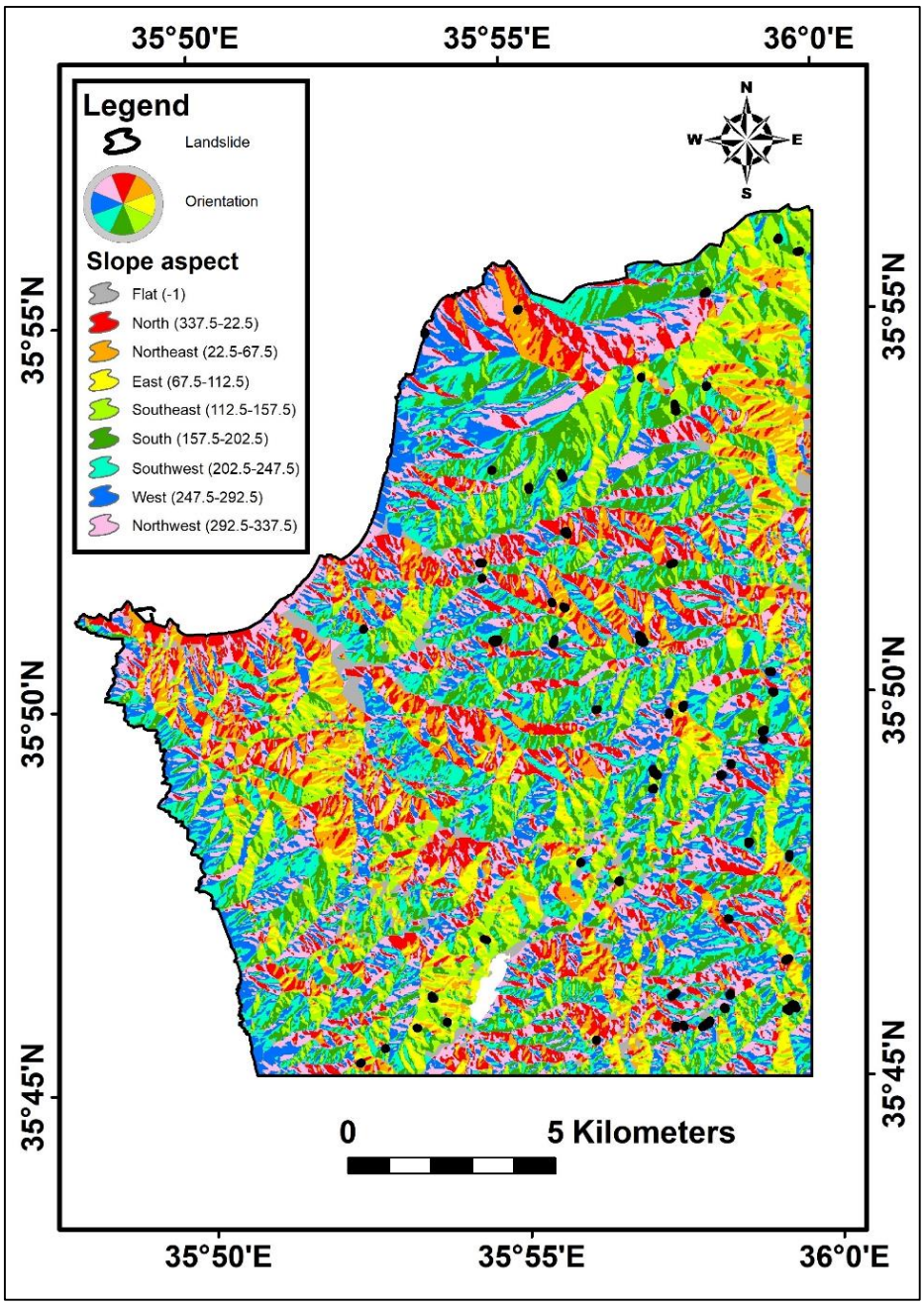

Figure 5.7: The reclassified slope aspect map with all landslide locations.

According to the slope aspect map statistics (Figure 5.8), the distribution of the slope aspect classes is similar, ranging from 8.1% for the east-facing slope aspect class to 14.4% for the northwest-facing slope aspect class, while the flat area covers only 3.5% of the total area.

Based on the area of each class and the percentage of total landslides in each class, the south-facing slope aspect has a greater association with landslides than other slope aspects. The south-facing slope aspect class covers 13.6% of the total area and contains the largest percentage of landslides with 29.44% of the total landslides.

The slope aspect map statistics are compatible with the relevant literature, which indicates a strong correlation between the south-facing slope aspect and the occurrence of landslides in the Mediterranean region.

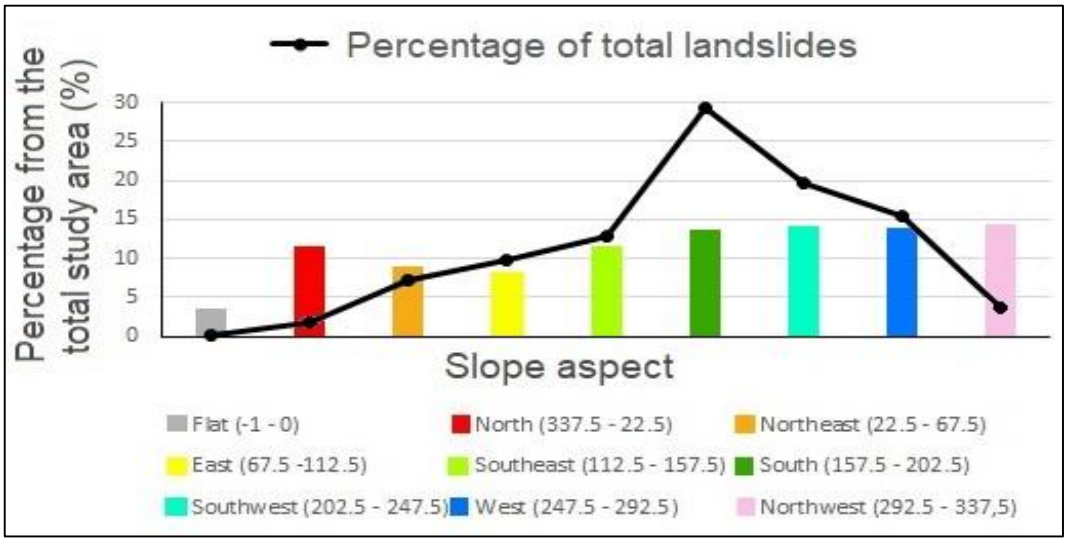

Figure 5.8: Statistics of the slope aspect map.

5.3.3 Terrain curvature map

The terrain curvature map, which was derived from the topography-based DEM, showed values from -209.78 to 131.19 before it was reclassified into the five classes: very concave; concave; planar; convex; very convex (Figure 5.9).

According to the terrain curvature map statistics (Figure 5.10), the very concave class covers the smallest area with 15.4% of the total area and contains 20.05% of the total landslides. The concave class covers 22.94% of the total area and contains 24.66% of the total landslides. The planar class covers 18.26% of the total area and contains the lowest percentage of landslides with only 9.38% of the total landslides. The convex class covers the largest area with 27.62% of the total area and contains 23.55% of the total landslides. The very convex class covers 15.77% of the total area and contains 22.33% of the total landslides.

Based on the area of each class and the percentage of total landslides in each class, planar surfaces have a lower association with landslides than other surfaces, which is also consistent with the relevant literature stating that planar surfaces are relatively more stable than concave and convex surfaces.

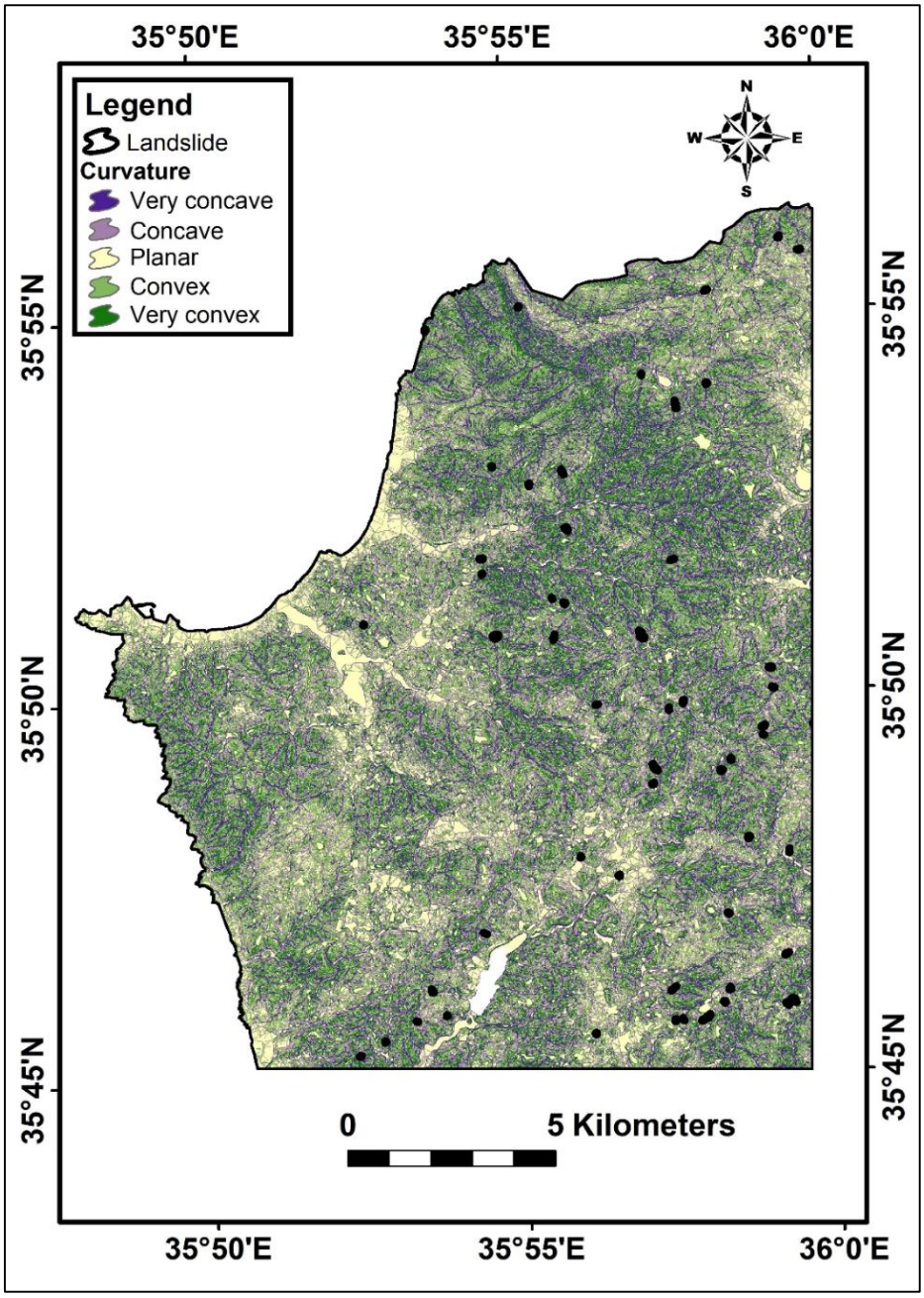

Figure 5.9: The terrain curvature map with all landslide locations.

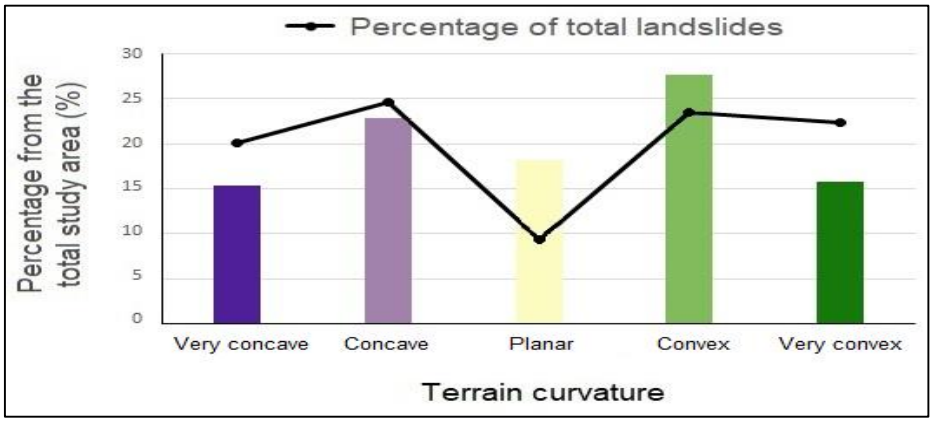

Figure 5.10: Statistics of the terrain curvature map.

5.3.4 Map of distance to streams

Based on a threshold of 500 pixels for the flow accumulation step in ArcGIS mentioned in chapter four, the drainage network map (Figure 5.11a) was extracted from the topography-based DEM and used to create the distance-to-streams map (Figure 5.11b).

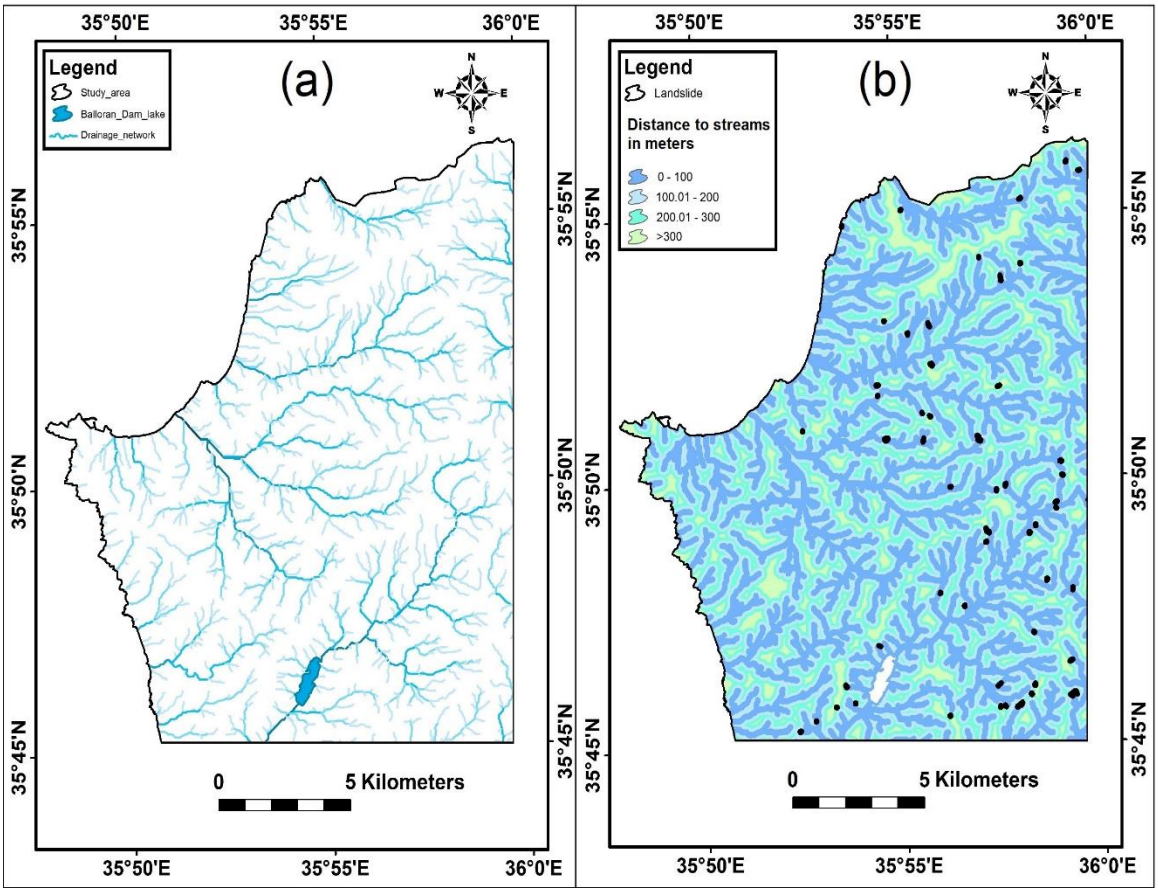

Figure 5.11: a- The drainage network map. b- The distance-to-streams map with all landslide locations.

According to the distance-to-streams map statistics (Figure 5.12), the first class, which includes distance-to-streams of less than 100 meters, covers the largest area with 41.02% of the total study area and contains the largest percentage of landslides with 54.05% of the total landslides.

The second class, which includes distance-to-streams between 100 and 200 meters, covers 31.18% of the total area and contains 31.77% of the total landslides.

The third class, which includes distance-to-streams between 200 and 300 meters, covers 19.75% of the total area and contains 12.24% of the total landslides.

The fourth class, which includes distance-to-streams more than 300 meters, covers 8.03% of the total area and contains 1.92% of the total landslides.

It is clear that the shorter the distance to streams, the greater the percentage of landslides.

Based on the area of each class and the percentage of total landslides in them, the distance-to-streams class of less than 100 m has a greater relation to landslides than the other classes.

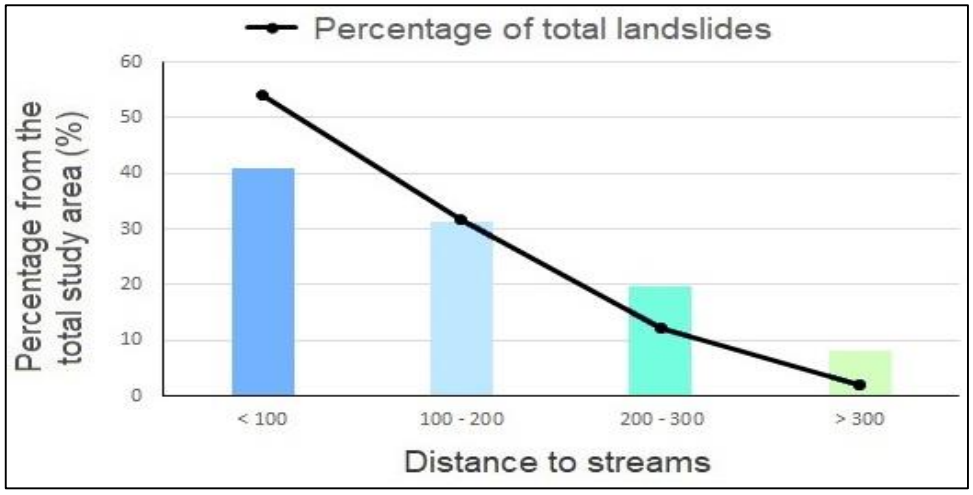

Figure 5.12: Statistics of the distance-to-streams map.

5.3.5 Map of distance to roads

The road network map (Figure 5.13a) prepared on the basis of the topographical map and high resolution satellite images, was used to create the distance-to-road map (Figure 5.13b).

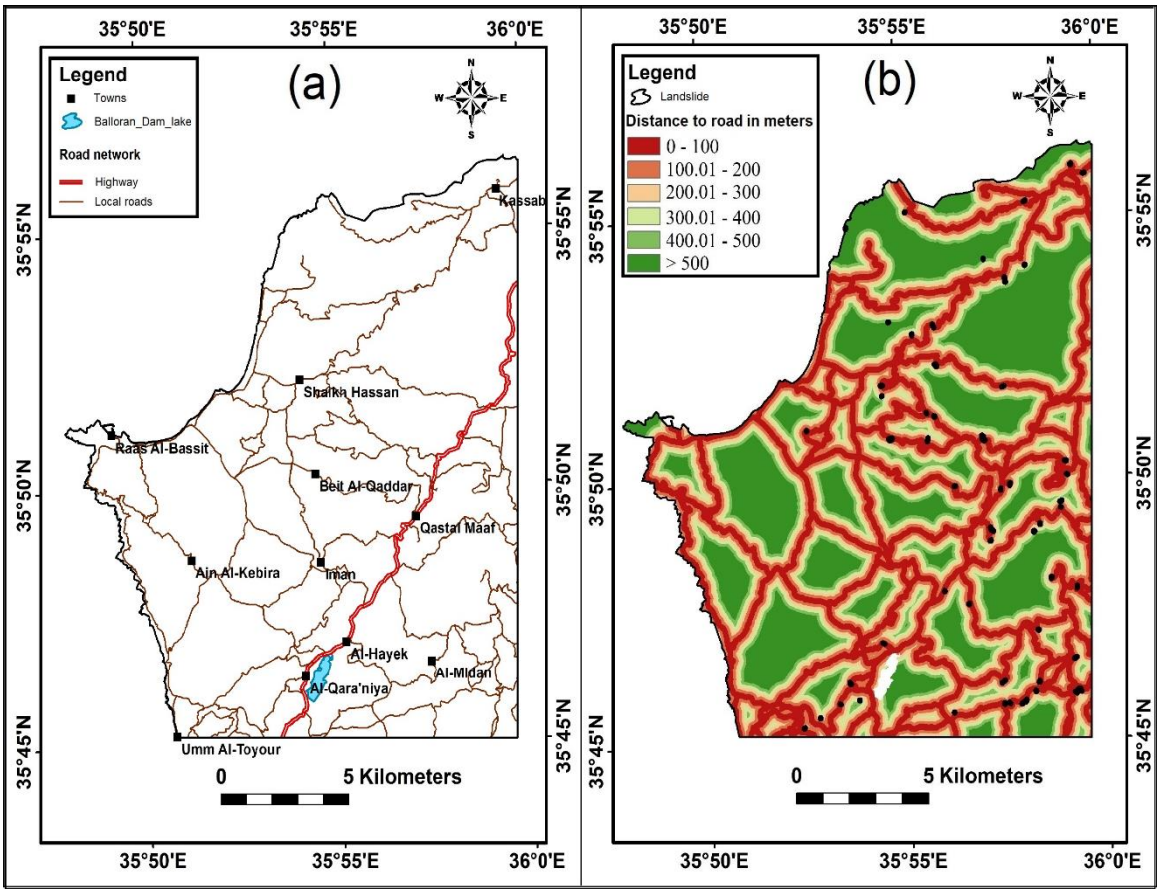

Figure 5.13: a- The road network map. b- The distance-to-road map with all landslide locations.

According to the road network map, the length of the highway is 23.75 km, and the total length of all roads in the study area is 317.8 km.

According to the distance-to-road map statistics (Figure 5.14), the first class, which includes distance-to-road of less than 100 meters, covers 22.70% of the total study area and contains the largest percentage of landslides with 58.19% of the total landslides.

The second class, which includes distance-to-road between 100 and 200 meters, covers 17.33% of the total area and contains 27.05% of the total landslides.

The third class, which includes distance-to-road between 200 and 300 meters, covers 13.80% of the total area and contains 7.63% of the total landslides.

The fourth class, which includes distance-to-road between 300 and 400 meters, covers 11.15% of the total area and contains 2.50% of the total landslides.

The fifth class, which includes distance-to-road between 400 and 500 meters, covers 8.68% of the total area and contains 1.16% of the total landslides.

The sixth class, which includes distance-to-road more than 500 meters, covers 26.32% of the total area and contains 3.44% of the total landslides.

Based on the area of each class and the percentage of total landslides in each class, the two distance-to-road classes of less than 100 m and 100-200 m have a greater association with landslides than other distance-to-road classes in the study area.

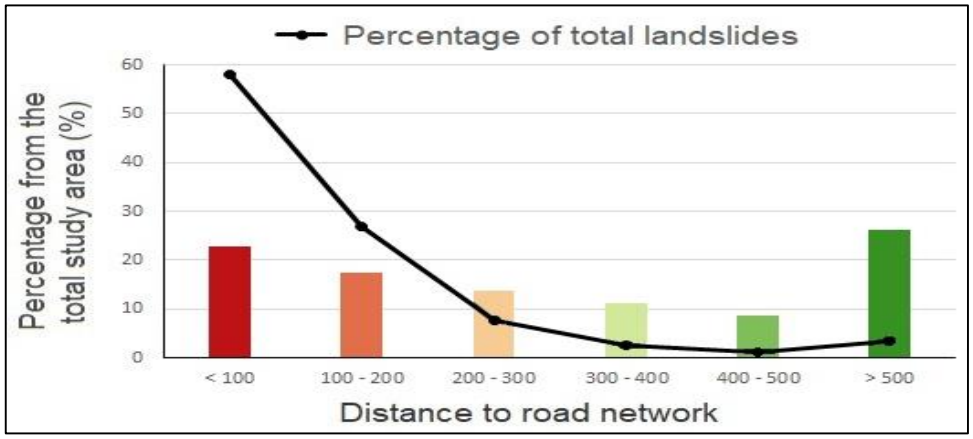

Figure 5.14: Statistics of the distance-to-road map.

5.3.6 Map of distance to faults

The fault map (Figure 5.15a) prepared from the geological map, was used to create the distance-to-fault map (Figure 5.15b).

According to the fault map, the study area contains 139 ascertained faults where the smallest fault in the study area has a length of 222 m and the largest fault is 2608 m. A rose diagram of the extracted faults was prepared showing that the northeast-southwest direction is the main trend of faults within the study area, which corresponds to the regional trend of faults within the East Anatolian fault system (Figure 5.16).

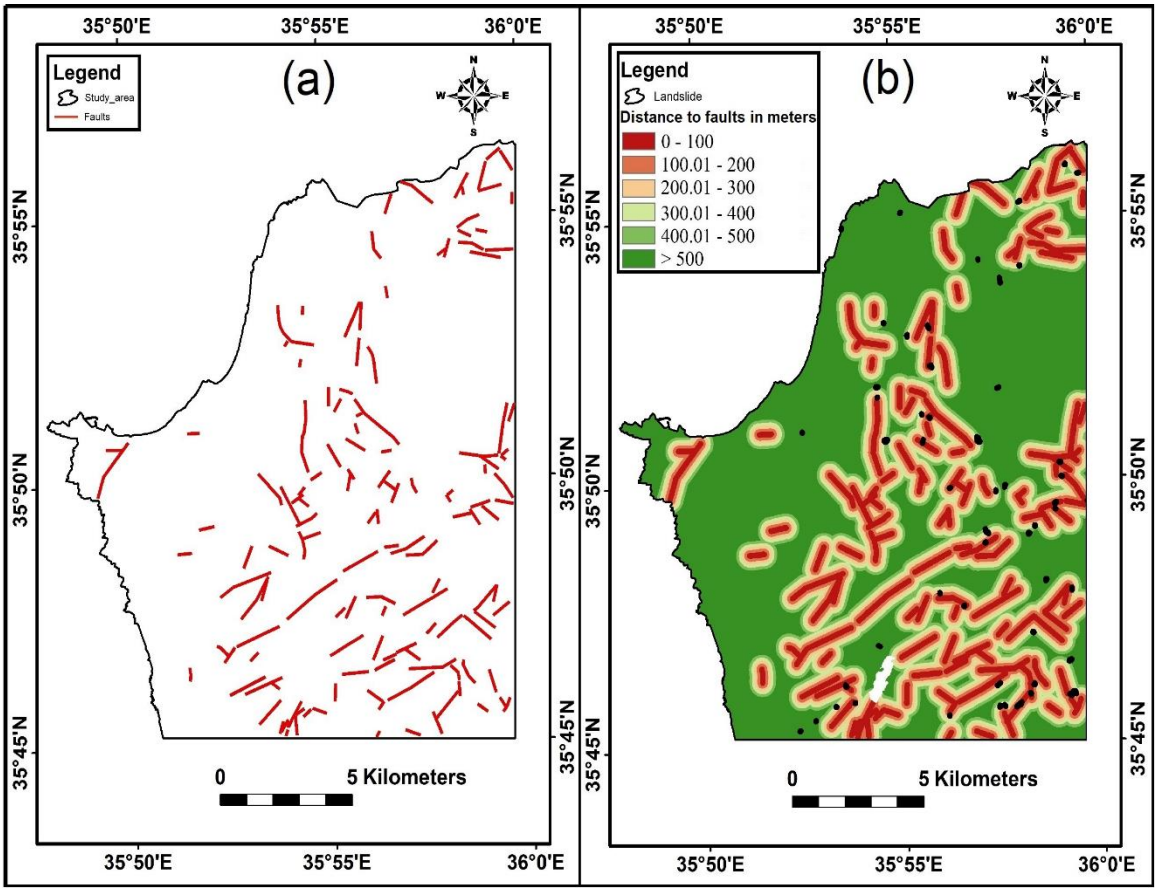

Figure 5.15: a- The fault map. b- The distance-to-fault map with all landslide locations.

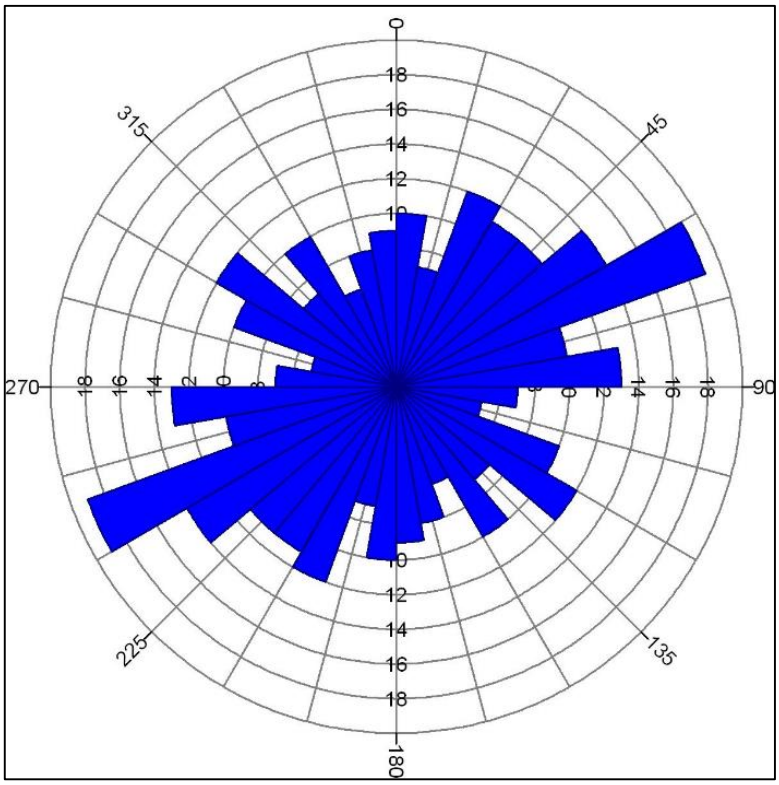

Figure 5.16: The rose diagram of the ascertained faults.

According to the distance-to-fault map statistics (Figure 5.17), the first class, which includes distance-to-fault of less than 100 meters, covers the smallest area with only 4.09% of the total study area and contains the largest percentage of landslides with 44.66% of the total landslides. The second class, which includes distance-to-fault between 100 and 200 meters, covers 5.21% of the total area and contains 26.18% of the total landslides. The third class, which includes distance-to-fault between 200 and 300 meters, covers 6.15% of the total area and contains 6.53% of the total landslides. The fourth class, which includes distance-to-fault between 300 and 400 meters, covers 6.86% of the total area and contains 2.33% of the total landslides. The fifth class, which includes distance-to-fault between 400 and 500 meters, covers 6.79% of the total area and contains 2.62% of the total landslides. The sixth class, which includes distance-to-fault more than 500 meters, covers 70.87% of the total area and contains 17.66% of the total landslides.

Based on the area of each class and the percentage of total landslides in each class, the two distance-to-fault classes of less than 100 m and between 100 and 200 m have a greater association with landslides than other distance-to-fault classes in the study area.

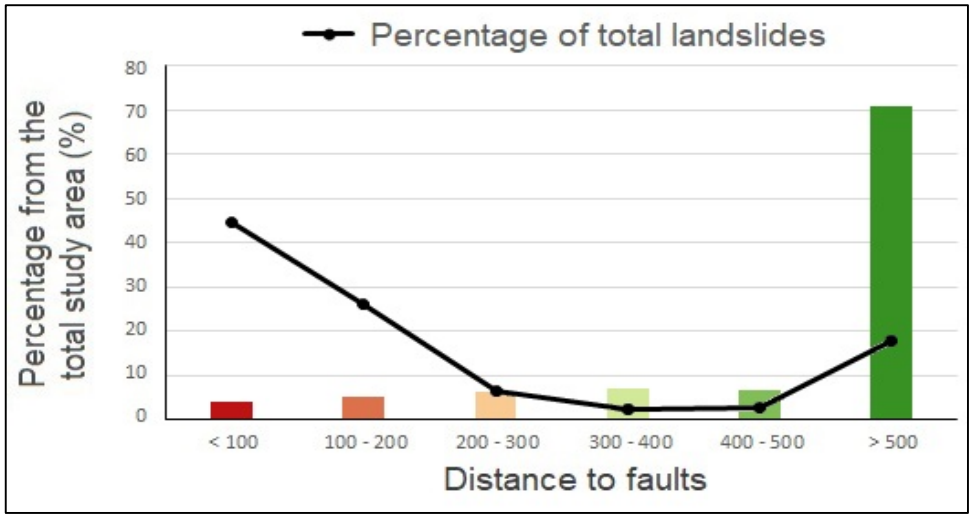

Figure 5.17: Statistics of the distance-to-fault map.

5.3.7 Lithology map

Based on Sentinel-2A image of 8 September 2017, three RGB maps of band ratios were prepared. The first composite map of band ratios (Sultan et al., 1987) shown in figure 5.18a, the second composite map of band ratios (Sabins, 1999) shown in figure 5.18b and the third composite map of band ratios (Abdelmalik and Abd-Allah, 2018) shown in figure 5.18c were all used to create the PCA map (Figure 5.18d) as described in chapter four.

The PCA map showed a relatively better chromatic differentiation suitable for performing the lithological classification. Based on a signature file of 112 training polygons of lithology representing the six main lithological classes, the supervised classification using the MLC algorithm was used to create the lithology map (Figure 5.19). Based on the 48 testing sites, the overall accuracy of the supervised classification result was 81.25%.

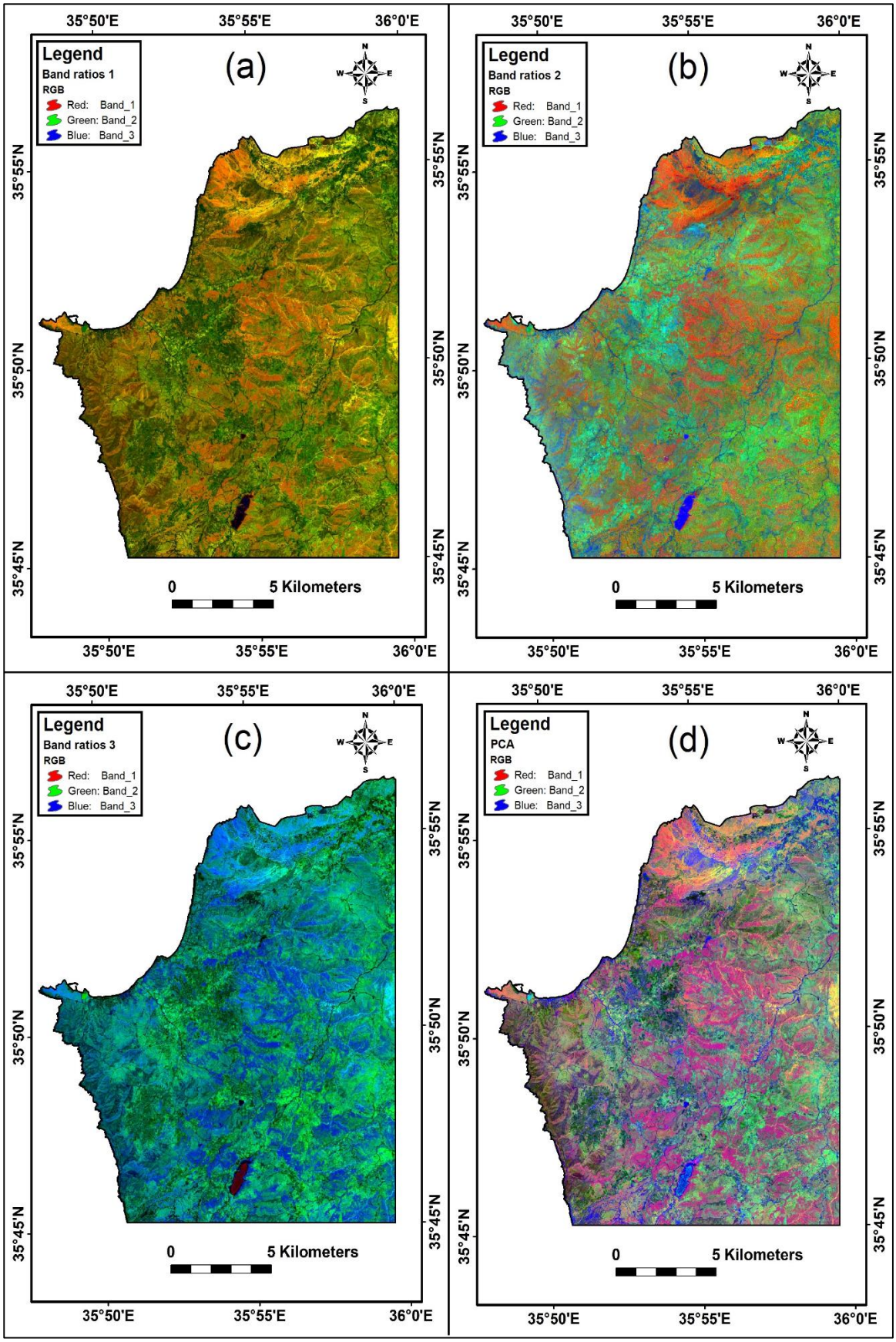

Figure 5.18: a- The first composite map of band ratios. b- The second composite map of band ratios. c- The third composite map of band ratios. d- The PCA map.

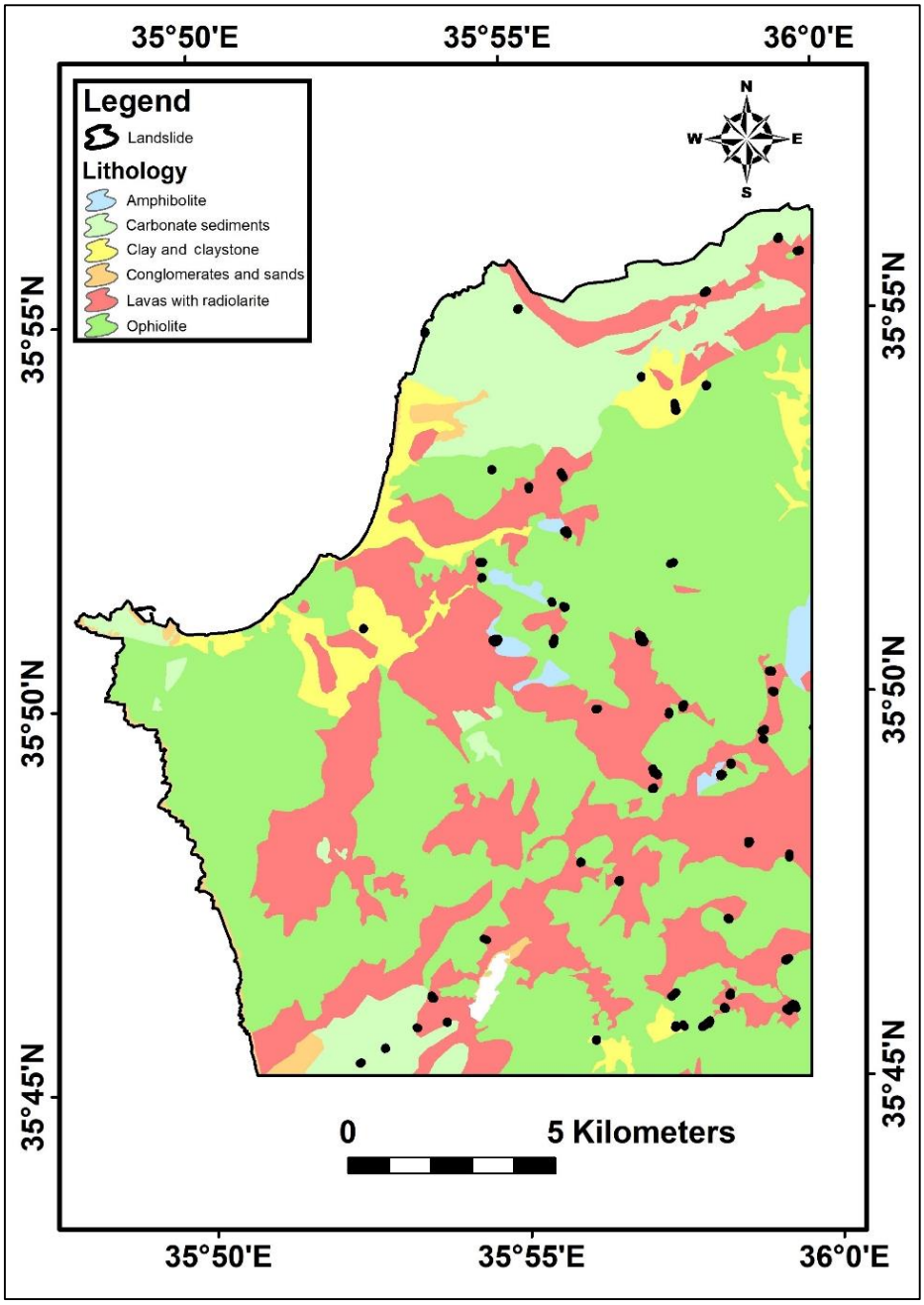

Figure 5.19: The lithology map with all landslide locations.

According to the lithology map statistics (Figure 5.20), the amphibolite class covers the smallest area with only 1.27% of the total area and does not contain landslides. The carbonate sediment class covers 12.2% of the total area and contains 4.89% of the total landslides. The clay and claystone class covers 5.08% of the total area and contains 6.70% of the total landslides. The conglomerate and sand class covers 1.45% of the total area and does not contain landslides. The lava with radiolarite class covers 28.06% of the total area and contains the majority of landslides with 80.52% of the total landslides. The ophiolite class covers the largest area with 51.91% of the total area and contains 7.87% of the total landslides.

Based on the area of each class and the percentage of total landslides in each class, the lava with radiolarite class has a greater association with landslides than all other classes of lithology in the study area.

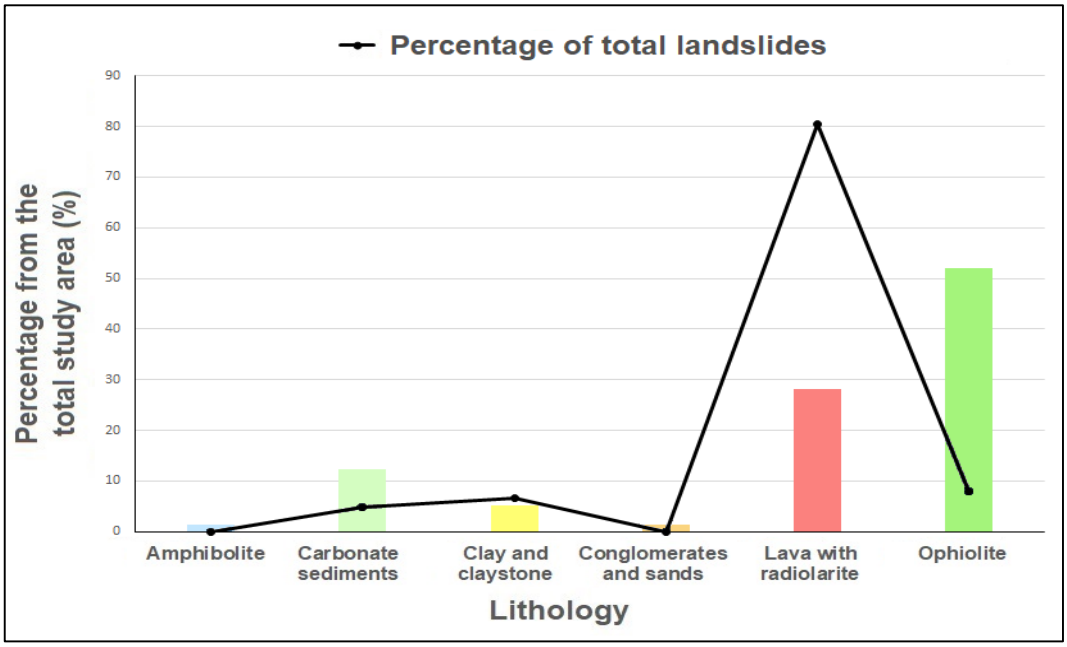

Figure 5.20: Statistics of the lithology map.

5.3.8 Land cover map

Based on the maximum likelihood supervised classification of the Landsat-5 TM image of 22 September 1984 (Figure 5.21a), the land cover map (Figure 5.21b) was created showing the four classes of the four main land cover types in the study area, i.e. the forest and dense vegetation class, the soil and agriculture land class, the built-up area class and the water class. The overall accuracy of the land cover classification based on Landsat data was 83.75% in the Syrian coastal region (Hammad et al., 2018a).

According to the land cover map statistics (Figure 5.22), the forest and dense vegetation class covers the largest area with 75.32% of the total area and contains 21.22% of the total landslides. The soil and agriculture land class covers 24.18% of the total area and contains the majority of landslides with 63.09% of the total landslides. The built-up area class covers only 0.46% of the total area and contains 15.68% of the total landslides. Whereas, the water class covers the smallest area with only 0.02% of the total area.

Based on the area of each class and the percentage of total landslides in each class, the soil and agriculture land as well as the built-up area classes have a greater association with landslides than other land cover classes in the area. Furthermore, the influence of forests and vegetation on reducing the likelihood of landslides can be derived. However, the landslides in the forest and dense vegetation class could be due to the land cover changes after 1984, as the reduction in forest and natural vegetation area in the Syrian coastal region reached 25.66% between 1987 and 2017 (Hammad et al., 2018a).

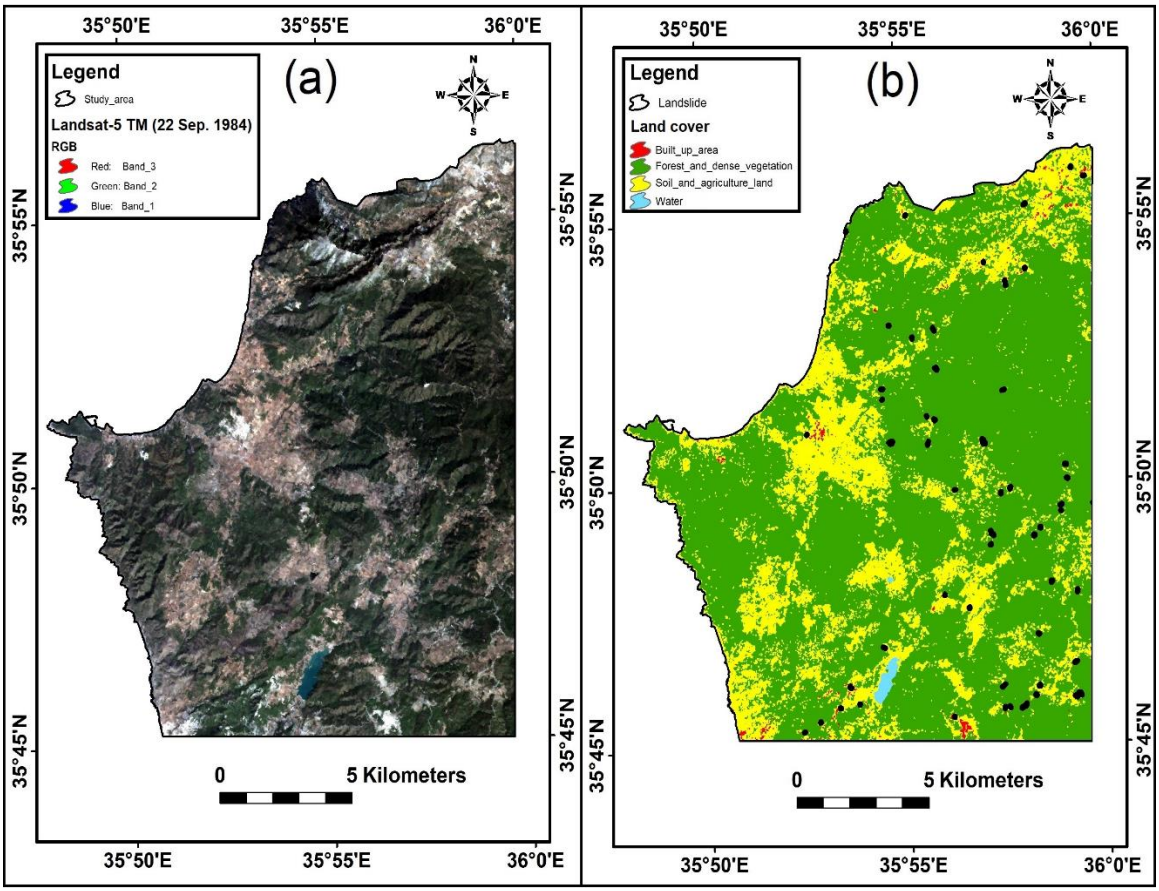

Figure 5.21: a- The true colour composite of Landsat-5 TM image of 22 September 1984. b- The land cover map with all landslide locations.

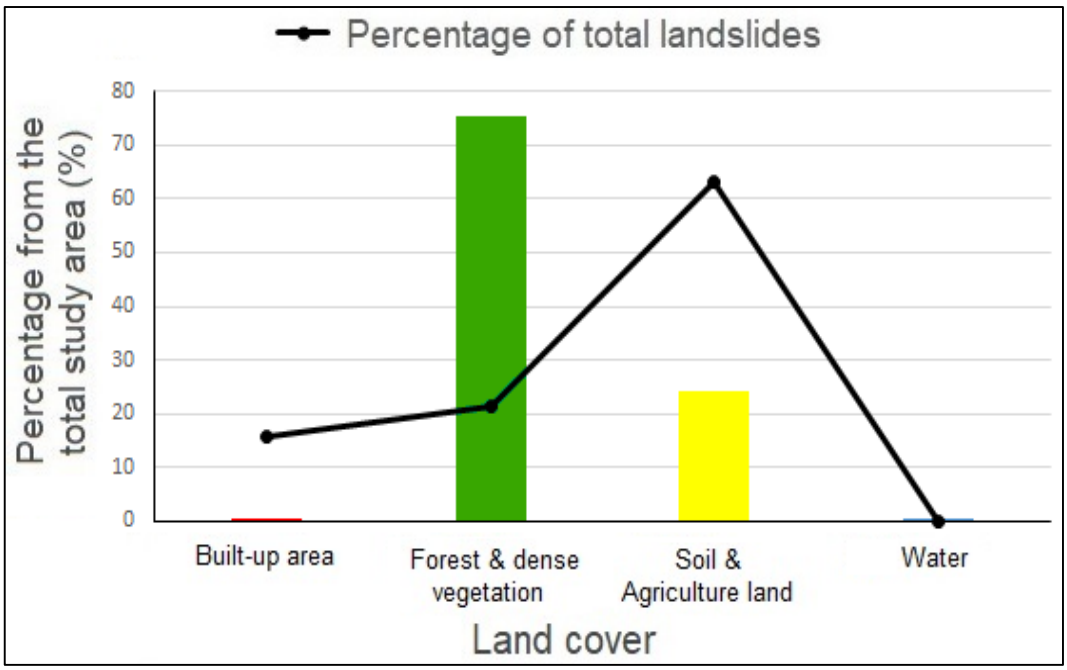

Figure 5.22: Statistics of the land cover map.

5.3.9 Normalized difference vegetation index map

The resulting Normalized Difference Vegetation Index (NDVI) map, based on the Landsat-5 TM image of 22 September 1984, showed values from -0.24 to 0.75, thus the NDVI map was reclassified into five classes uniformly according to positive NDVI values as follows (Figure 5.23):

- Very low NDVI for values less than 0.15;
- Low NDVI for values between 0.15 and 0.3;
- Moderate NDVI for values between 0.3 and 0.45;
- High NDVI for values between 0.45 and 0.6; and
- Very high NDVI for values more than 0.6.

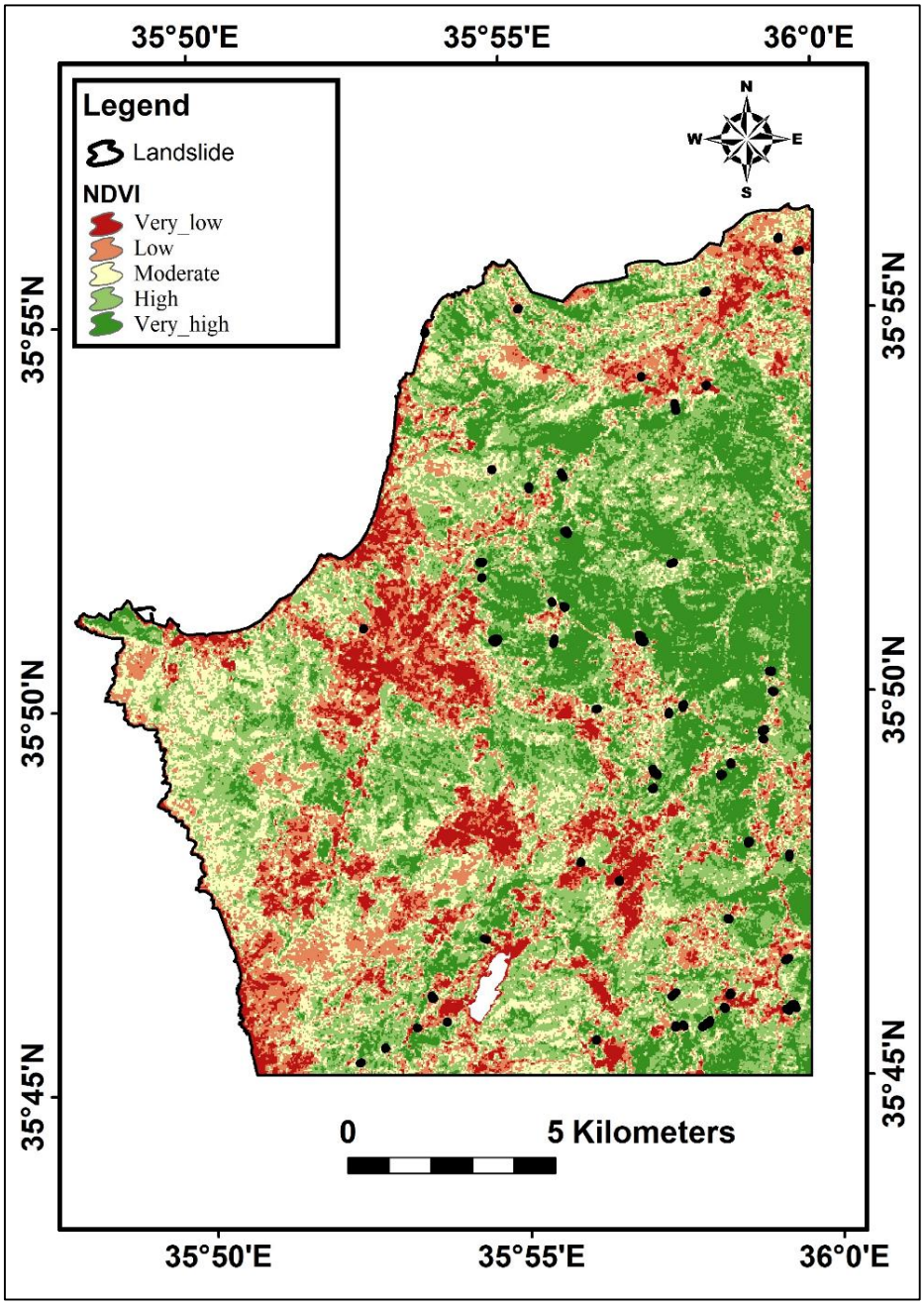

Figure 5.23: The NDVI map with all landslide locations.

According to the NDVI map statistics (Figure 5.24), the very low NDVI class covers the smallest area with 9.52% of the total area and contains the largest percentage of landslides with 43.14% of the total landslides. The low NDVI class covers 17.08% of the total area and contains 33.17% of the total landslides. The moderate NDVI class covers 21.05% of the total area and contains 13.11% of the total landslides. The high NDVI class covers 29.51% of the total area and contains 7.87% of the total landslides. The very high NDVI class covers 22.81% of the total area and contains only 2.68% of the total landslides. It can be seen that the lower the NDVI value, the higher the percentage of total landslides. This also reflects the impact of forests and vegetation, which reduces the likelihood of landslides.

Based on the area of each class and the percentage of total landslides in each class, it is clear that the very low and low NDVI classes have a greater association with landslides than other NDVI classes.

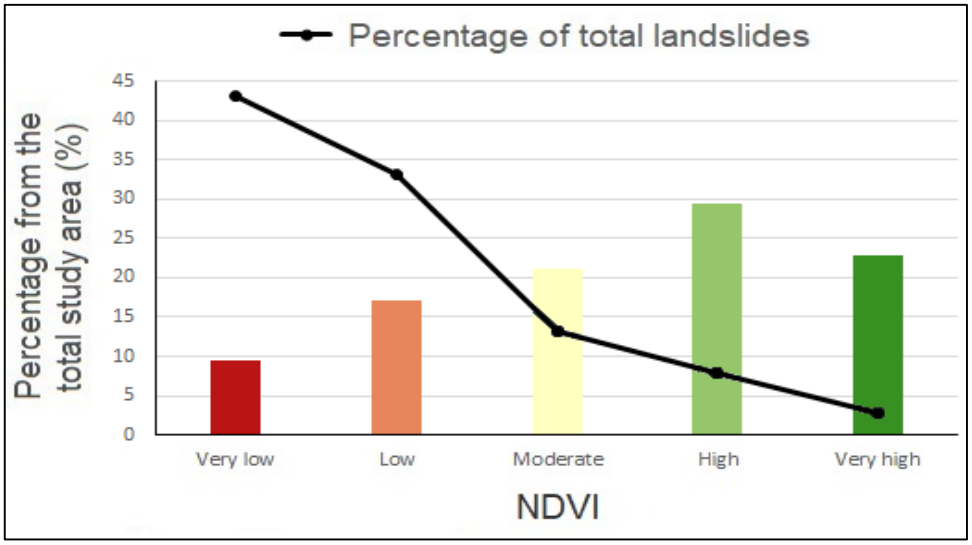

Figure 5.24: Statistics of the NDVI map.

5.4 Statistical analysis methods for landslide susceptibility mapping

After preparing all the data related to the landslide inventory map, the training and testing sets of landslides and non-landslides, and all the nine causative factor maps, the second step was to define the relative relationship between the landslides and all causative factors during the study period between 1984 and 2018 using the four statistical analysis methods explained in detail in chapter four. In addition, the landslide testing set was used to validate each resulting landslide susceptibility map of each statistical analysis method to select the optimal landslide susceptibility map to be used later in landslide hazard assessment.

According to statistics of 1353 pixels of landslide training set and 1353 pixels of non-landslide training set in all classes of causative factor maps extracted from the DEM, the highest proportion of landslide pixels in the slope gradient map is in the 20-30 degree class with 519 pixels, which corresponds to 38.35% of the landslide training set, while the highest proportion of non-landslide pixels in the slope gradient map is in the less than 10

degree class with 632 pixels, which corresponds to 46.71% of the non-landslide training set (Figure 5.25a). Besides, the highest proportion of landslide pixels in the slope aspect map is in the south-facing slope aspect class with 466 pixels, which corresponds to 34.44% of the landslide training set, while the highest proportion of non-landslide pixels in the slope aspect map is in the north-facing slope aspect class with 459 pixels, which corresponds to 33.92% of the non-landslide training set (Figure 5.25b). Moreover, all concave and convex classes in the terrain curvature map show higher proportions of landslide pixels compared to the proportion of landslide pixels in the planar class, and the highest proportion of landslide pixels is in the concave class with 346 pixels, which corresponds to 25.57% of the landslide training set, while the highest proportion of non-landslide pixels in the terrain curvature map is in the planar class with 461 pixels, which corresponds to 34.07% of the non-landslide training set (Figure 5.25c). Furthermore, the majority of landslide pixels in the distance-to-streams map are in the distance-to-streams class of less than 100 m with 800 pixels, which corresponds to 59.12% of the landslide training set, and the quantity of landslide pixels gradually decreased with the increase in the distance to streams, while non-landslide pixels in the distance-to-streams map are distributed almost equally within the classes of the map, and the highest proportion of non-landslide pixels in the distance-to-streams map is in the distance-to-streams class of 200-300 m with 372 pixels, which corresponds to 27.49% of the non-landslide training set (Figure 5.25d).

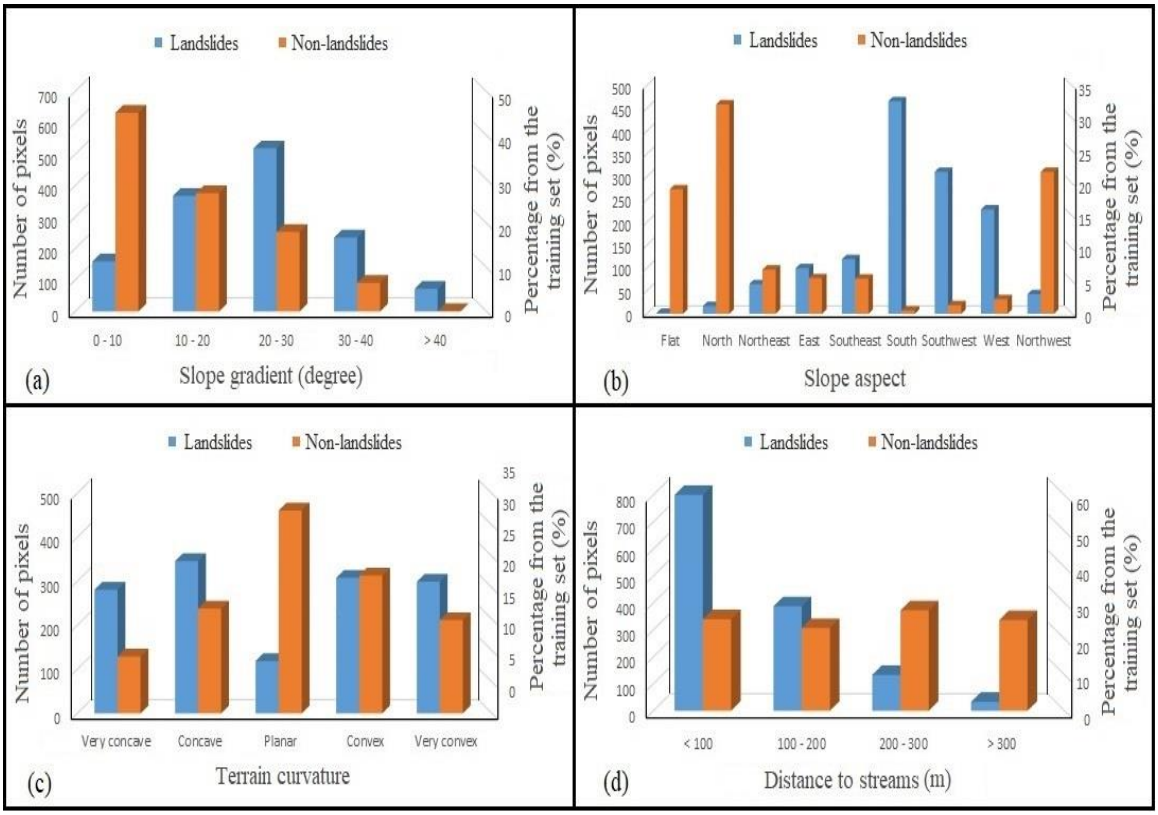

Figure 5.25: Statistics of the training sets of landslides and non-landslides within all classes of causative factor maps extracted from the DEM. a- Slope gradient. b- Slope aspect. c- Terrain curvature. d- Distance to streams.

Additionally, statistics of landslide and non-landslide training sets in all classes of causative factor maps extracted from topographical, optical remote sensing and geological data show that the majority of landslide pixels in the distance-to-road map are in the distance-to-road class of less than 100 m with 778 pixels, which corresponds to 57.50% of the landslide training set, while the highest proportion of non-landslide pixels in the distance-to-road map is in the distance-to-road class of 200-300 m with 399 pixels, which corresponds to 29.49% of the non-landslide training set (Figure 5.26a). Besides, the highest proportion of landslide pixels in the distance-to-fault map is in the distance-to-fault class of less than 100 m with 618 pixels, which corresponds to 45.67% of the landslide training set, while the majority of non-landslide pixels in the distance-to-fault map are in the distance-to-fault class of more than 500 m with 1087 pixels, which corresponds to 80.33% of the non-landslide training set (Figure 5.26b). Moreover, the majority of landslide pixels in the lithology map are in the lava with radiolarite class with 1147 pixels, which corresponds to 84.77% of the landslide training set, while the majority of non-landslide pixels in the lithology map are in the ophiolite class with 1084 pixels, which corresponds to 80.11% of the non-landslide training set (Figure 5.26c). Furthermore, the majority of landslide pixels in the land cover map are in the soil and agriculture land class with 978 pixels, which corresponds to 72.28% of the landslide training set, while the majority of non-landslide pixels in the land cover map are in the forest and dense vegetation class with 1338 pixels, which corresponds to 98.89% of the non-landslide training set (Figure 5.26d). Also, the highest proportion of landslide pixels in the NDVI map is in the very low NDVI class with 527 pixels, which corresponds to 38.95% of the landslide training set, while the highest proportion of non-landslide pixels in the NDVI map is in the very high NDVI class with 691 pixels, which corresponds to 51.07% of the non-landslide training set (Figure 5.26e).

These proportions of the training sets of landslide pixels and non-landslide pixels within each class of the causative factor maps are important for the statistical analysis process of landslide susceptibility. Besides, these proportions provide an overview of the classes most associated with landslide occurrence, especially when the majority of landslide pixels within a class are associated with the minority of non-landslide pixels within the same class.

For example, the distance-to-road class of less than 100 m in the distance-to-road map has the majority of landslide pixels and at the same time the minority of non-landslide pixels. In addition, the lava with radiolarite class in the lithology map has the majority of landslide pixels and at the same time the minority of non-landslide pixels. Moreover, the soil and agriculture land class in the land cover map has the majority of landslide pixels and at the same time the minority of non-landslide pixels. Furthermore, the very low NDVI class in the NDVI map has the majority of landslide pixels and at the same time the minority of non-landslide pixels. Therefore, the distance-to-road class of less than 100 m in the distance-to-road map, the lava with radiolarite class in the lithology map, the soil and agriculture land class in the land cover map and the very low NDVI class in the NDVI map can mainly be considered as the classes most associated with landslides in the study area, which will be verified later in this chapter by the statistical analysis of the landslide susceptibility.

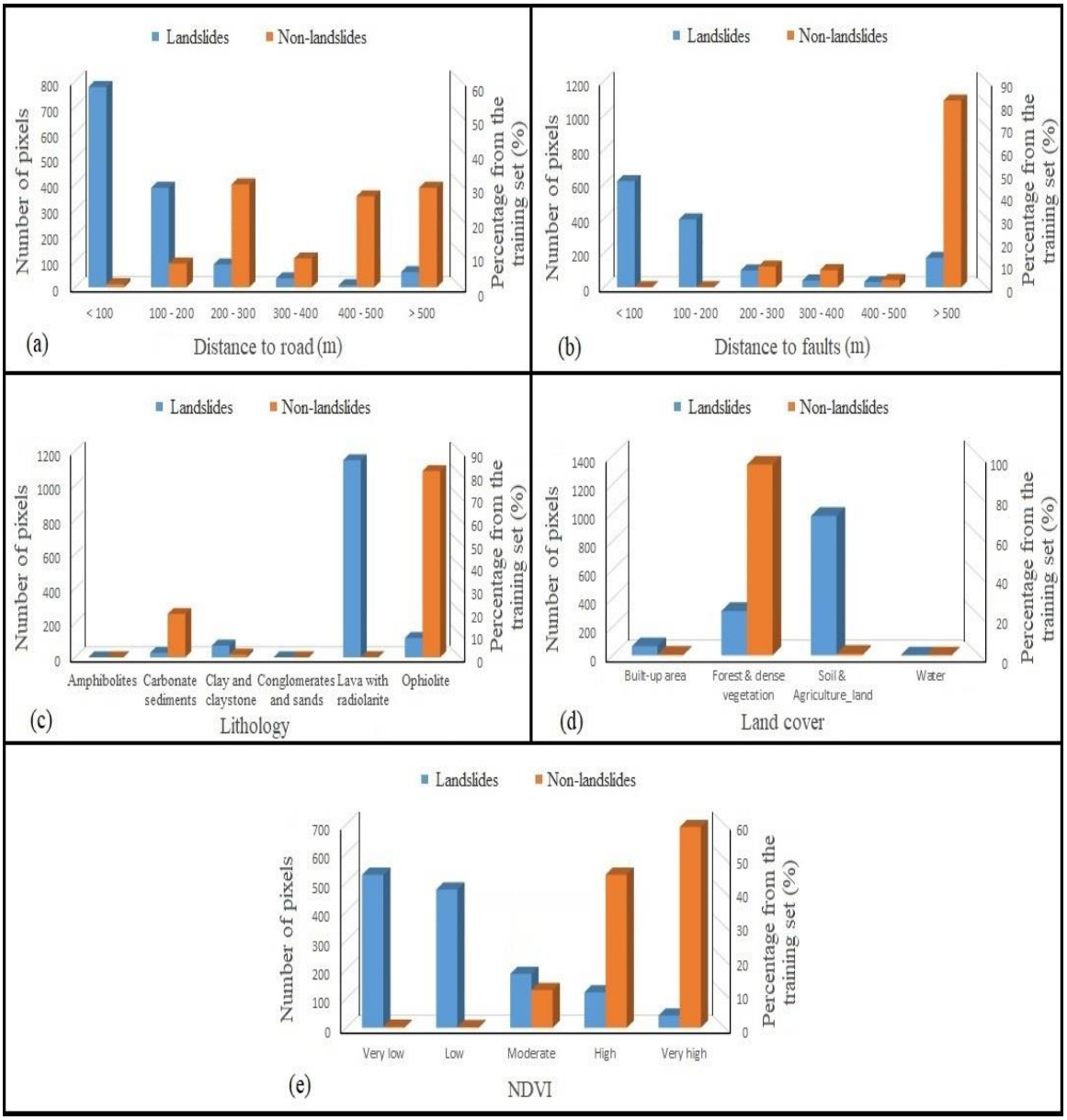

Figure 5.26: Statistics of the training sets of landslides and non-landslides in all classes of causative factor maps extracted from topographical, optical remote sensing and geological data. a- Distance to road. b- Distance to fault. c- Lithology. d- Land cover. e- NDVI.

5.4.1 Frequency ratio method

Statistical analysis of landslides using the frequency ratio method was performed using the landslide training set only. First, the relative frequency (RF) value of landslides was calculated for each class in each causative factor (Table 3), then the resulting RF values were used to calculate the participation rate for each causative factor and the final frequency ratio for each class.

Table 3: The relative frequency (RF) value for each class in each causative factor.

No.	Factor name	Slope gradient (degree)	N_{Class}	N_{class} / N_{Total}	$N_{L(Class)}$	$N_{L(Class)} / N_{L(Total)}$	FR_{Class}	$RF = FR_{Class}/FR_{Factor}$
1	Slope gradient	0 - 10	480665	0.283856166	159	0.11751663	0.414000624	0.050137148
		10 - 20	607702	0.358877721	368	0.271988174	0.75788537	0.091782981
		20 - 30	424424	0.250643108	519	0.383592018	1.530431143	0.185341396
		30 - 40	155993	0.092121488	235	0.173688101	1.885424398	0.228332513
		> 40	24556	0.014501518	72	0.053215078	3.669621254	0.444405962
			N_{Total} = 1693340		**$N_{L(Total)}$ = 1353**		**FR_{Factor} = 8.25**	
No.	**Factor name**	**Slope aspect**	**N_{Class}**	**N_{class} / N_{Total}**	**$N_{L(Class)}$**	**$N_{L(Class)} / N_{L(Total)}$**	**FR_{Class}**	**$RF = FR_{Class}/FR_{Factor}$**
2	Slope aspect	Flat	60452	0.035699859	2	0.001478197	0.04140623	0.005212053
		North	197187	0.116448557	17	0.012564671	0.107898899	0.013581889
		Northeast	152176	0.089867363	65	0.04804139	0.534581054	0.067290959
		East	138394	0.081728418	100	0.07390983	0.90433452	0.11383407
		Southeast	194310	0.114749548	120	0.088691796	0.772916298	0.097291661
		South	231770	0.136871508	466	0.344419808	2.51637329	0.316751164
		Southwest	240191	0.14184452	311	0.229859571	1.62050371	0.203982628
		West	233604	0.137954575	229	0.169253511	1.226878563	0.154434644
		Northwest	245256	0.14483565	43	0.031781227	0.219429587	0.027620933
			N_{Total} = 1693340		**$N_{L(Total)}$ = 1353**		**FR_{Factor} = 7.94**	
No.	**Factor name**	**Terrain curvature**	**N_{Class}**	**N_{class} / N_{Total}**	**$N_{L(Class)}$**	**$N_{L(Class)} / N_{L(Total)}$**	**FR_{Class}**	**$RF = FR_{Class}/FR_{Factor}$**
3	Terrain curvature	Very concave	260784	0.154005693	281	0.207686622	1.348564579	0.260843358
		Concave	388513	0.229435908	346	0.255728012	1.114594548	0.215588181
		Planar	309223	0.182611289	119	0.087952698	0.481638886	0.093160021
		Convex	467732	0.276218598	308	0.227642276	0.824138123	0.159407238
		Very convex	267088	0.157728513	299	0.220990392	1.401080805	0.271001202
			N_{Total} = 1693340		**$N_{L(Total)}$ = 1353**		**FR_{Factor} = 5.17**	
No.	**Factor name**	**Distance to streams (m)**	**N_{Class}**	**N_{class} / N_{Total}**	**$N_{L(Class)}$**	**$N_{L(Class)} / N_{L(Total)}$**	**FR_{Class}**	**$RF = FR_{Class}/FR_{Factor}$**
4	Distance to streams (m)	0 - 100	694686	0.410246023	800	0.59127864	1.441278178	0.456161445
		100 - 200	528046	0.311836961	387	0.286031042	0.917245476	0.290306222
		200 - 300	334484	0.197529144	133	0.098300074	0.497648459	0.157504667
		> 300	136124	0.080387872	33	0.024390244	0.303407008	0.096027666
			N_{Total} = 1693340		**$N_{L(Total)}$ = 1353**		**FR_{Factor} = 3.15**	
No.	**Factor name**	**Distance to roads (m)**	**N_{Class}**	**N_{class} / N_{Total}**	**$N_{L(Class)}$**	**$N_{L(Class)} / N_{L(Total)}$**	**FR_{Class}**	**$RF = FR_{Class}/FR_{Factor}$**
5	Distance to road (m)	0 - 100	384417	0.22701702	778	0.575018477	2.532931136	0.495777094
		100 - 200	293524	0.173340262	386	0.285291944	1.645849267	0.322146289
		200 - 300	233696	0.138008905	88	0.06504065	0.471278648	0.092244576
		300 - 400	188971	0.111596608	34	0.025129342	0.225180162	0.044075089
		400 - 500	147012	0.086817768	8	0.005912786	0.068105717	0.013330506
		> 500	445720	0.263219436	59	0.0436068	0.165667096	0.032426445
			N_{Total} = 1693340		**$N_{L(Total)}$ = 1353**		**FR_{Factor} = 5.10**	
No.	**Factor name**	**Distance to faults (m)**	**N_{Class}**	**N_{class} / N_{Total}**	**$N_{L(Class)}$**	**$N_{L(Class)} / N_{L(Total)}$**	**FR_{Class}**	**$RF = FR_{Class}/FR_{Factor}$**
6	Distance to fault (m)	0 - 100	69359	0.040959878	618	0.456762749	11.1514675	0.590777504
		100 - 200	88247	0.052114165	395	0.291943829	5.60200531	0.296780555
		200 - 300	104282	0.061583616	98	0.072431633	1.176151034	0.062309608
		300 - 400	116239	0.068644808	40	0.029563932	0.430679794	0.022816363
		400 - 500	115026	0.067928473	31	0.022912047	0.337296665	0.017869153
		> 500	1200187	0.70876906	171	0.126385809	0.178317334	0.009446817
			N_{Total} = 1693340		**$N_{L(Total)}$ = 1353**		**FR_{Factor} = 18.87**	
No.	**Factor name**	**Lithology**	**N_{Class}**	**N_{class} / N_{Total}**	**$N_{L(Class)}$**	**$N_{L(Class)} / N_{L(Total)}$**	**FR_{Class}**	**$RF = FR_{Class}/FR_{Factor}$**
7	Lithology	Amphibolites	21575	0.012905522	0	0	0	0
		Carbonate sediments	206661	0.123618451	26	0.019216556	0.155450547	0.036398965
		Clay and claystone	86135	0.05152339	68	0.050258684	0.975453759	0.228403877
		Conglomerates and sands	24687	0.014767028	0	0	0	0
		Lava with radiolarite	475196	0.284248085	1147	0.84774575	2.982414991	0.698336687
		Ophiolite	879086	0.525843046	112	0.08277901	0.157421516	0.036860471
			N_{Total} = 1693340		**$N_{L(Total)}$ = 1353**		**FR_{Factor} = 4.27**	
No.	**Factor name**	**Land cover**	**N_{Class}**	**N_{class} / N_{Total}**	**$N_{L(Class)}$**	**$N_{L(Class)} / N_{L(Total)}$**	**FR_{Class}**	**$RF = FR_{Class}/FR_{Factor}$**
8	Land cover	Built-up area	7879	0.004652934	64	0.047302291	10.16612029	0.755256642
		Forest & dense vegetation	1275500	0.753245066	311	0.229859571	0.30515908	0.022670735
		Soil & agriculture lands	409477	0.241816174	978	0.722838137	2.989205088	0.222072623
		Water	484	0.000285826	0	0	0	0
			N_{Total} = 1693340		**$N_{L(Total)}$ = 1353**		**FR_{Factor} = 13.46**	
No.	**Factor name**	**NDVI**	**N_{Class}**	**N_{class} / N_{Total}**	**$N_{L(Class)}$**	**$N_{L(Class)} / N_{L(Total)}$**	**FR_{Class}**	**$RF = FR_{Class}/FR_{Factor}$**
9	NDVI	Very low	161280	0.09524372	527	0.389504804	4.089558935	0.564607574
		Low	289292	0.17084106	476	0.351810791	2.059287103	0.284306722
		Moderate	356606	0.210593265	186	0.137472284	0.652785755	0.090124091
		High	499775	0.295141555	122	0.090169993	0.305514392	0.042179546
		Very high	386387	0.228180401	42	0.031042129	0.136042046	0.018782067
			N_{Total} = 1693340		**$N_{L(Total)}$ = 1353**		**FR_{Factor} = 7.24**	

The RF values shown in table (3) indicate the classes that are more susceptible to landslides in each causative factor, as these RF values reflect the probability of landslides in the range of 0 to 1 for all classes in each causative factor separately.

For the slope gradient factor, the slope gradient class above 40 degrees has the highest RF value of 0.44, which indicates that this class is the most slope gradient class susceptible to landslides.

For the slope aspect factor, the south-facing slope aspect class has the highest RF value of 0.31, which indicates that this class is the most slope aspect class susceptible to landslides.

For the terrain curvature factor, the very concave and very convex classes have the highest RF values of 0.26 and 0.27, respectively, which indicates that these two classes are the most terrain curvature classes susceptible to landslides.

For the distance-to-streams factor, the distance-to-streams class of less than 100 meters has the highest RF value of 0.45, which indicates that this class is the most distance-to-streams class susceptible to landslides.

For the distance-to-road factor, the distance-to-road class of less than 100 meters has the highest RF value of 0.49, which indicates that this class is the most distance-to-road class susceptible to landslides.

For distance-to-fault factor, the distance-to-fault class of less than 100 meters has the highest RF value of 0.59, which indicates that this class is the most distance-to-fault class susceptible to landslides.

For the lithology factor, the lava with radiolarite class has the highest RF value of 0.69, which indicates that this class is the most lithological class susceptible to landslides.

For the land cover factor, the built-up area class has the highest RF value of 0.75, which indicates that this class is the most land cover class susceptible to landslides.

For the NDVI factor, the very low NDVI class has the highest RF value of 0.56, which indicates that this class is the most NDVI class susceptible to landslides.

As already mentioned, the resulting RF values were used to calculate the participation rate (PR) for each causative factor to calculate the final frequency ratio (FR_{Final}) for each class in each causative factor, to define the influence of causative factors and classes on the occurrence of landslides, because the higher the participation rate for a causative factor and the final frequency ratio for a causative factor class, the stronger the correlation between this causative factor and landslides and the stronger the influence of this causative factor class on the occurrence of landslides.

According to the results of the participation rate and the final frequency ratio in table (4), the most influential causative factor in the occurrence of landslides in the study area is the land cover factor with the highest PR value of 4.24, and the most influential land cover class is the built-up area class with a final frequency ratio of 3.20.

Table 4: The final frequency ratio (FR_{Final}) for each class in each causative factor.

No.	Factor name	Slope gradient (degree)	min(RF)	max(RF)	max(RF)-min(RF)	min[max(RF)-min(RF)]	PR_slope	$FR_{Final\_(slope)}$
1	Slope gradient	0 - 10						0.111152624
		10 - 20						0.203480244
		20 - 30						0.410896575
		30 - 40						0.506206653
		> 40						0.985235311
			0.050137	0.444406	0.394268814	0.177841181	2.216971407	
No.	**Factor name**	**Slope aspect**	**min(RF)**	**max(RF)**	**max(RF)-min(RF)**	**min[max(RF)-min(RF)]**	**PR_aspect**	**$FR_{Final\_(aspect)}$**
2	Slope aspect	Flat						0.009130385
		North						0.023792518
		Northeast						0.11787914
		East						0.199412558
		Southeast						0.170433852
		South						0.554879221
		Southwest						0.357333246
		West						0.270535943
		Northwest						0.048385873
			0.005212	0.316751	0.311539111	0.177841181	1.751782736	
No.	**Factor name**	**Terrain curvature**	**min(RF)**	**max(RF)**	**max(RF)-min(RF)**	**min[max(RF)-min(RF)]**	**PR_curvature**	**$FR_{Final\_(curvature)}$**
3	Terrain curvature	Very concave						0.260843358
		Concave						0.215588181
		Planar						0.093160021
		Convex						0.159407238
		Very convex						0.271001202
			0.09316	0.271001	0.177841181	0.177841181	1	
No.	**Factor name**	**Distance to streams (m)**	**min(RF)**	**max(RF)**	**max(RF)-min(RF)**	**min[max(RF)-min(RF)]**	**PR_streams**	**$FR_{Final\_(streams)}$**
4	Distance to streams (m)	0 - 100						0.923740745
		100 - 200						0.587878893
		200 - 300						0.318951723
		> 300						0.194458932
			0.096028	0.456161	0.360133779	0.177841181	2.025030293	
No.	**Factor name**	**Distance to roads (m)**	**min(RF)**	**max(RF)**	**max(RF)-min(RF)**	**min[max(RF)-min(RF)]**	**PR_roads**	**$FR_{Final\_(roads)}$**
5	Distance to road (m)	0 - 100						1.344941401
		100 - 200						0.8739167
		200 - 300						0.250240583
		300 - 400						0.119566662
		400 - 500						0.036162925
		> 500						0.087966283
			0.013331	0.495777	0.482446588	0.177841181	2.712794555	
No.	**Factor name**	**Distance to faults (m)**	**min(RF)**	**max(RF)**	**max(RF)-min(RF)**	**min[max(RF)-min(RF)]**	**PR_faults**	**$FR_{Final\_(faults)}$**
6	Distance to fault (m)	0 - 100						1.931144911
		100 - 200						0.970122008
		200 - 300						0.203678851
		300 - 400						0.074582569
		400 - 500						0.058411033
		> 500						0.030879937
			0.009447	0.590778	0.581330687	0.177841181	3.268819309	
No.	**Factor name**	**Lithology**	**min(RF)**	**max(RF)**	**max(RF)-min(RF)**	**min[max(RF)-min(RF)]**	**PR_lithology**	**$FR_{Final\_(lithology)}$**
7	Lithology	Amphibolites						0
		Carbonate sediments						0.142929397
		Clay and claystone						0.89688342
		Conglomerates and sands						0
		Lava with radiolarite						2.742188989
		Ophiolite						0.14474161
			0	0.698337	0.698336687	0.177841181	3.926743417	
No.	**Factor name**	**Land cover**	**min(RF)**	**max(RF)**	**max(RF)-min(RF)**	**min[max(RF)-min(RF)]**	**PR_LC**	**$FR_{Final\_(LC)}$**
8	Land cover	Built-up area						3.207426939
		Forest & dense vegetation						0.09627817
		Soil & agriculture lands						0.943098906
		Water						0
			0	0.755257	0.755256642	0.177841181	4.246804015	
No.	**Factor name**	**NDVI**	**min(RF)**	**max(RF)**	**max(RF)-min(RF)**	**min[max(RF)-min(RF)]**	**PR_NDVI**	**$FR_{Final\_(NDVI)}$**
9	NDVI	Very low						1.732878816
		Low						0.872586764
		Moderate						0.276606506
		High						0.129456361
		Very high						0.057645429
			0.018782	0.564608	0.545825507	0.177841181	3.069173875	

The second most influential causative factor in the occurrence of landslides in the study area is the lithology factor with a PR value of 3.92, and the most influential lithological class is the lava with radiolarite class with a final frequency ratio of 2.74.

Third, the distance-to-fault factor with a PR value of 3.26, and the most influential distance-to-fault class is the distance-to-faults class below 100 m with a final frequency ratio of 1.93.

Fourth, the NDVI factor with a PR value of 3.06, and the most influential NDVI class is the very low NDVI class with a final frequency ratio of 1.73.

Fifth, the distance-to-road factor with a PR value of 2.71, and the most influential distance-to-road class is the distance-to-road class below 100 m with a final frequency ratio of 1.34.

Sixth, the slope gradient factor with a PR value of 2.21, and the most influential slope gradient class is the slope gradient class above 40 degrees with a final frequency ratio of 0.98.

Seventh, the distance-to-streams factor with a PR value of 2.02, and the most influential distance-to-streams class is the distance-to-streams class below 100 m with a final frequency ratio of 0.92.

Eighth, the slope aspect factor with a PR value of 1.75, and the most influential slope aspect class is the south-facing slope aspect class with a final frequency ratio of 0.55.

Whereas, the causative factor least affecting the occurrence of landslides in the study area is the terrain curvature factor with a PR value of 1 since it has the minimum value of all difference values between minimum relative frequency and maximum relative frequency within each causative factor involved in the statistical analysis, and the most influential terrain curvature classes are the very convex and the very concave classes with a final frequency ratio of 0.27 and 0.26, respectively.

The resulting values of the final frequency ratio of all classes of all causative factors were used to calculate the landslide susceptibility index of the frequency ratio method (LSI_{FR}), which was used to create the landslide susceptibility map of the frequency ratio method according to the following equation:

$$LSI_{FR} = [(\text{Slope\_gradient.tif} * FR_{Final\_(slope)}) + (\text{Slope\_aspect.tif} * FR_{Final\_(aspect)}) + (\text{Terrain\_curvature.tif} * FR_{Final\_(curvature)}) + (\text{Dist\_to\_streams.tif} * FR_{Final\_(stream)}) + (\text{Dist\_to\_road.tif} * FR_{Final\_(road)}) + (\text{Dist\_to\_fault.tif} * FR_{Final\_(fault)}) + (\text{Lithology.tif} * FR_{Final\_(lithology)}) + (\text{Land\_cover.tif} * FR_{Final\_(LC)}) + (\text{NDVI.tif} * FR_{Final\_(NDVI)})] \quad (25)$$

The resulting landslide susceptibility map of the frequency ratio method shows values ranging from 0.62, which is the lowest susceptibility to landslides, to 13.29, which is the highest susceptibility to landslides (Figure 5.27).

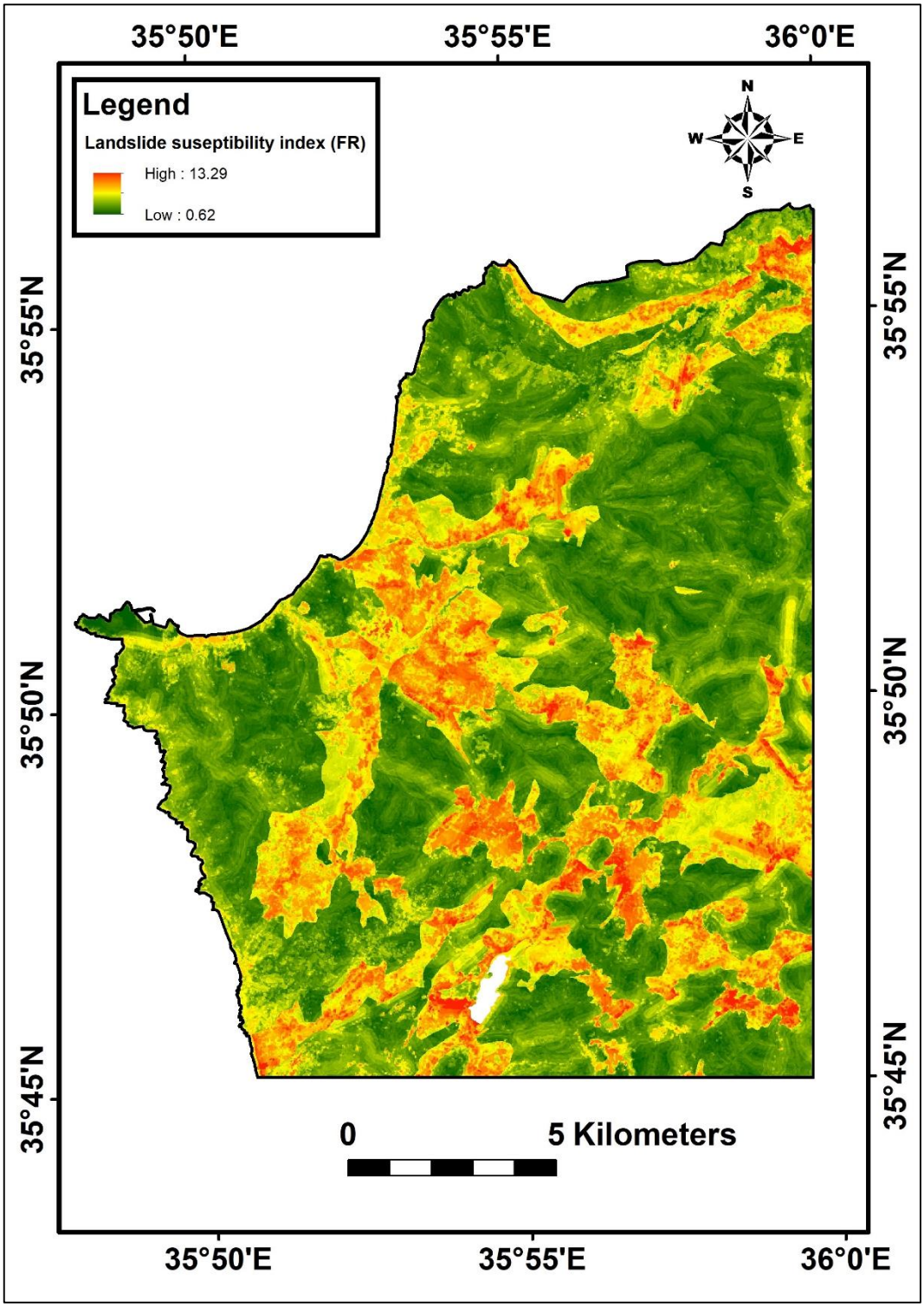

Figure 5.27: The landslide susceptibility map based on the frequency ratio method.

In order to evaluate the landslide susceptibility map of the frequency ratio method and also to compare the results of the frequency ratio method with the results of other statistical analysis methods used, a validation process was carried out using the Area Under the Curve (AUC) analysis based on the testing set of landslides as explained in detail in chapter four. The AUC of the frequency ratio statistical analysis method was 70.03% (Figure 5.28).

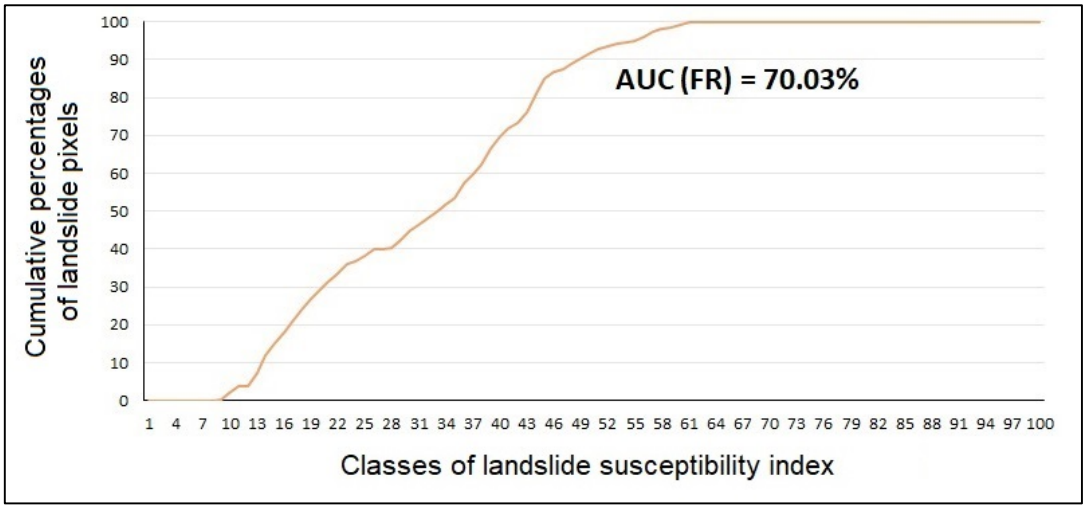

Figure 5.28: The area under the curve of the frequency ratio statistical analysis method.

5.4.2 Weights-of-evidence method

The weight-of-evidence statistical analysis method used the training sets of the landslide and the non-landslide pixels to calculate the positive weight (W^+) and the negative weight (W^-) values for each class in each causative factor to calculate the final weight value of each class and the final weight value of each causative factor (Table 5).

According to the results of the weight-of-evidence method in table (5), the most influential causative factor in the occurrence of landslides in the study area is the distance-to-fault factor with the highest $W_{Final(fault)}$ value of 12.16, and the most influential distance-to-fault class is the distance-to-fault class of less than 100 m with a $W_{Final(class\_fault)}$ value of 7.64.

Second, the land cover factor with a $W_{Final(LC)}$ value of 11.64, and the most influential land cover class is the soil and agriculture land class with a $W_{Final(class\_LC)}$ value of 8.68.

Third, the NDVI factor with a $W_{Final(NDVI)}$ value of 7.18, and the most influential NDVI class is the low NDVI class with a $W_{Final(class\_NDVI)}$ value of 6.01.

Forth, the slope gradient factor with a $W_{Final(slope)}$ value of 4.78, and the most influential slope gradient class is the slope gradient class above 40 degrees with a $W_{Final(class\_slope)}$ value of 4.39.

Fifth, the lithology factor with a $W_{Final(lithology)}$ value of 3.33, and in the most influential lithological class is the lava with radiolarite class with a $W_{Final(class\_lithology)}$ value of 8.72.

Sixth, the terrain curvature factor with a $W_{Final(curvature)}$ value of 0.18, and the most influential terrain curvature class is the very concave class with a $W_{Final(class\_curvature)}$ value of 0.92.

Whereas, the least influential causative factors are all of the slope aspect, the distance-to-streams and the distance-to-road factors with a $W_{Final(factor)}$ value of -0.91, -2.87 and -3.66, respectively.

Table 5: The result of the susceptibility statistical analysis using the WoE method.

Slope gradient (degree)	**N(C∩L)**	**P(C|L)**	**N(C∩Ĺ)**	**P(C|Ĺ)**	**W⁺**	**P(Ć|L)**	**P(Ć|Ĺ)**	**W⁻**	**W** Final(class_slope)
0 - 10	159	0.1175	632	0.4671	-1.38	0.8825	0.5329	0.5044	-1.823760349
10 - 20	368	0.272	376	0.2779	-0.022	0.728	0.7221	0.0082	0.030988806
20 - 30	519	0.3836	253	0.187	0.7185	0.6164	0.813	-0.277	1.055996451
30 - 40	235	0.1737	91	0.0673	0.9487	0.8263	0.9327	-0.121	1.130532397
> 40	72	0.0532	1	0.0007	4.2767	0.9468	0.9993	-0.054	4.391260074
	N(L) = 1353		**N(Ĺ) = 1353**					**∑=0.06**	**W** Final(slope)=4.785
Slope aspect	**N(C∩L)**	**P(C|L)**	**N(C∩Ĺ)**	**P(C|Ĺ)**	**W⁺**	**P(Ć|L)**	**P(Ć|Ĺ)**	**W⁻**	**W** Final(class_aspect)
Flat	2	0.0015	273	0.2018	-4.916	0.9985	0.7982	0.2239	-5.137819552
North	17	0.0126	459	0.3392	-3.296	0.9874	0.6608	0.4017	-3.695177364
Northeast	65	0.048	97	0.0717	-0.4	0.952	0.9283	0.0252	-0.423093188
East	100	0.0739	78	0.0576	0.2485	0.9261	0.9424	-0.017	0.268255943
Southeast	120	0.0887	77	0.0569	0.4437	0.9113	0.9431	-0.034	0.480355362
South	466	0.3444	7	0.0052	4.1983	0.6556	0.9948	-0.417	4.617712094
Southwest	311	0.2299	19	0.014	2.7954	0.7701	0.986	-0.247	3.044783018
West	229	0.1693	32	0.0237	1.968	0.8307	0.9763	-0.161	2.131870456
Northwest	43	0.0318	311	0.2299	-1.979	0.9682	0.7701	0.2289	-2.20508891
	N(L) = 1353		**N(Ĺ) = 1353**					**∑=0.002**	**W** Final(aspect)=-0.918
Terrain curvature	**N(C∩L)**	**P(C|L)**	**N(C∩Ĺ)**	**P(C|Ĺ)**	**W⁺**	**P(Ć|L)**	**P(Ć|Ĺ)**	**W⁻**	**W** Final(class_curvature)
Very concave	281	0.2077	129	0.0953	0.7785	0.7923	0.9047	-0.133	0.926697097
Concave	346	0.2557	238	0.1759	0.3742	0.7443	0.8241	-0.102	0.491603603
Planar	119	0.088	461	0.3407	-1.354	0.912	0.6593	0.3246	-1.663267911
Convex	308	0.2276	313	0.2313	-0.016	0.7724	0.7687	0.0048	-0.005342869
Very convex	299	0.221	212	0.1567	0.3439	0.779	0.8433	-0.079	0.43872663
	N(L) = 1353		**N(Ĺ) = 1353**					**∑=0.015**	**W** Final(curvature)=0.188
Distance to streams (m)	**N(C∩L)**	**P(C|L)**	**N(C∩Ĺ)**	**P(C|Ĺ)**	**W⁺**	**P(Ć|L)**	**P(Ć|Ĺ)**	**W⁻**	**W** Final(class_streams)
0 - 100	800	0.5913	339	0.2506	0.8586	0.4087	0.7494	-0.606	1.256899541
100 - 200	387	0.286	306	0.2262	0.2348	0.714	0.7738	-0.081	0.107347706
200 - 300	133	0.0983	372	0.2749	-1.029	0.9017	0.7251	0.218	-1.454590666
> 300	33	0.0244	336	0.2483	-2.321	0.9756	0.7517	0.2608	-2.78939048
	N(L) = 1353		**N(Ĺ) = 1353**					**∑=-0.20**	**W** Final(streams)=-2.879
Distance to road (m)	**N(C∩L)**	**P(C|L)**	**N(C∩Ĺ)**	**P(C|Ĺ)**	**W⁺**	**P(Ć|L)**	**P(Ć|Ĺ)**	**W⁻**	**W** Final(class_road)
0 - 100	778	0.575	12	0.0089	4.1718	0.425	0.9911	-0.847	4.836361646
100 - 200	386	0.2853	92	0.068	1.434	0.7147	0.932	-0.265	1.517251563
200 - 300	88	0.065	399	0.2949	-1.512	0.935	0.7051	0.2822	-1.976047403
300 - 400	34	0.0251	111	0.082	-1.183	0.9749	0.918	0.0602	-1.425579637
400 - 500	8	0.0059	353	0.2609	-3.787	0.9941	0.7391	0.2964	-4.265679599
> 500	59	0.0436	386	0.2853	-1.878	0.9564	0.7147	0.2913	-2.351853976
	N(L) = 1353		**N(Ĺ) = 1353**					**∑=-0.18**	**W** Final(road)=-3.665
Distance to fault (m)	**N(C∩L)**	**P(C|L)**	**N(C∩Ĺ)**	**P(C|Ĺ)**	**W⁺**	**P(Ć|L)**	**P(Ć|Ĺ)**	**W⁻**	**W** Final(class_fault)
0 - 100	618	0.4568	1	0.0007	6.4265	0.5432	0.9993	-0.609	7.647851215
100 - 200	395	0.2919	1	0.0007	5.9789	0.7081	0.9993	-0.344	6.935271244
200 - 300	98	0.0724	121	0.0894	-0.211	0.9276	0.9106	0.0185	0.382573226
300 - 400	40	0.0296	100	0.0739	-0.916	0.9704	0.9261	0.0468	-0.351171651
400 - 500	31	0.0229	43	0.0318	-0.327	0.9771	0.9682	0.0091	0.275561485
> 500	171	0.1264	1087	0.8034	-1.85	0.8736	0.1966	1.4915	-2.72908722
	N(L) = 1353		**N(Ĺ) = 1353**					**∑=0.611**	**W** Final(fault)=12.16
Lithology	**N(C∩L)**	**P(C|L)**	**N(C∩Ĺ)**	**P(C|Ĺ)**	**W⁺**	**P(Ć|L)**	**P(Ć|Ĺ)**	**W⁻**	**W** Final(class_lithology)
Amphibolites	0	#DIV/0!	0	#DIV/0!	0	#DIV/0!	#DIV/0!	0	0
Carbonate sediments	26	0.0192	252	0.1863	-2.271	0.9808	0.8137	0.1867	-2.663504811
Clay and claystone	68	0.0503	16	0.0118	1.4469	0.9497	0.9882	-0.04	1.281118198
Conglomerates and sands	0	#DIV/0!	0	#DIV/0!	0	#DIV/0!	#DIV/0!	0	0
Lava with radiolarite	1147	0.8477	1	0.0007	7.0449	0.1523	0.9993	-1.881	8.720898841
Ophiolite	112	0.0828	1084	0.8012	-2.27	0.9172	0.1988	1.529	-4.004346081
	N(L) = 1353		**N(Ĺ) = 1353**					**∑= -0.20**	**W** Final(lithology)=3.334
Land cover (LC)	**N(C∩L)**	**P(C|L)**	**N(C∩Ĺ)**	**P(C|Ĺ)**	**W⁺**	**P(Ć|L)**	**P(Ć|Ĺ)**	**W⁻**	**W** Final(class_LC)
Built-up area	64	0.0473	4	0.003	2.7726	0.9527	0.997	-0.045	5.738445452
Forest & dense vegetation	311	0.2299	1338	0.9889	-1.459	0.7701	0.0111	4.2408	-2.779625473
Soil & agriculture lands	978	0.7228	11	0.0081	4.4876	0.2772	0.9919	-1.275	8.682964565
Water	0	#DIV/0!	0	#DIV/0!	0	#DIV/0!	#DIV/0!	0	0
	N(L) = 1353		**N(Ĺ) = 1353**					**∑=2.92**	**W** Final(LC)=11.641
NDVI	**N(C∩L)**	**P(C|L)**	**N(C∩Ĺ)**	**P(C|Ĺ)**	**W⁺**	**P(Ć|L)**	**P(Ć|Ĺ)**	**W⁻**	**W** Final(class_NDVI)
Very low	527	0.3895	3	0.0022	5.1686	0.6105	0.9978	-0.491	5.771891691
Low	476	0.3518	2	0.0015	5.4723	0.6482	0.9985	-0.432	6.016402353
Moderate	186	0.1375	130	0.0961	0.3582	0.8625	0.9039	-0.047	0.51712106
High	122	0.0902	527	0.3895	-1.463	0.9098	0.6105	0.399	-1.750128523
Very high	42	0.031	691	0.5107	-2.8	0.969	0.4893	0.6833	-3.3717118
	N(L) = 1353		**N(Ĺ) = 1353**					**∑=0.112**	**W** Final(NDVI)=7.183

The resulting values of the final weight value of each class within all causative factors were used to calculate the landslide susceptibility index of the weight-of-evidence method (LSI_{WoE}), which was used to create the landslide susceptibility map of the WoE method (Figure 5.29) according to the following equation:

$$LSI_{WoE} = [(\text{Slope\_gradient.tif} * W_{Final(class\_slope)}) + (\text{Slope\_aspect.tif} * W_{Final(class\_aspect)}) + (\text{Terrain\_curvature.tif} * W_{Final(class\_curvature)}) + (\text{Dist\_to\_streams.tif} * W_{Final(class\_streams)}) + (\text{Dist\_to\_road.tif} * W_{Final(class\_roads)}) + (\text{Dist\_to\_fault.tif} * W_{Final(class\_faults)}) + (\text{Lithology.tif} * W_{Final(class\_lithology)}) + (\text{Land\_cover.tif} * W_{Final(class\_LC)}) + (\text{NDVI.tif} * W_{Final(class\_NDVI)})] \quad (26)$$

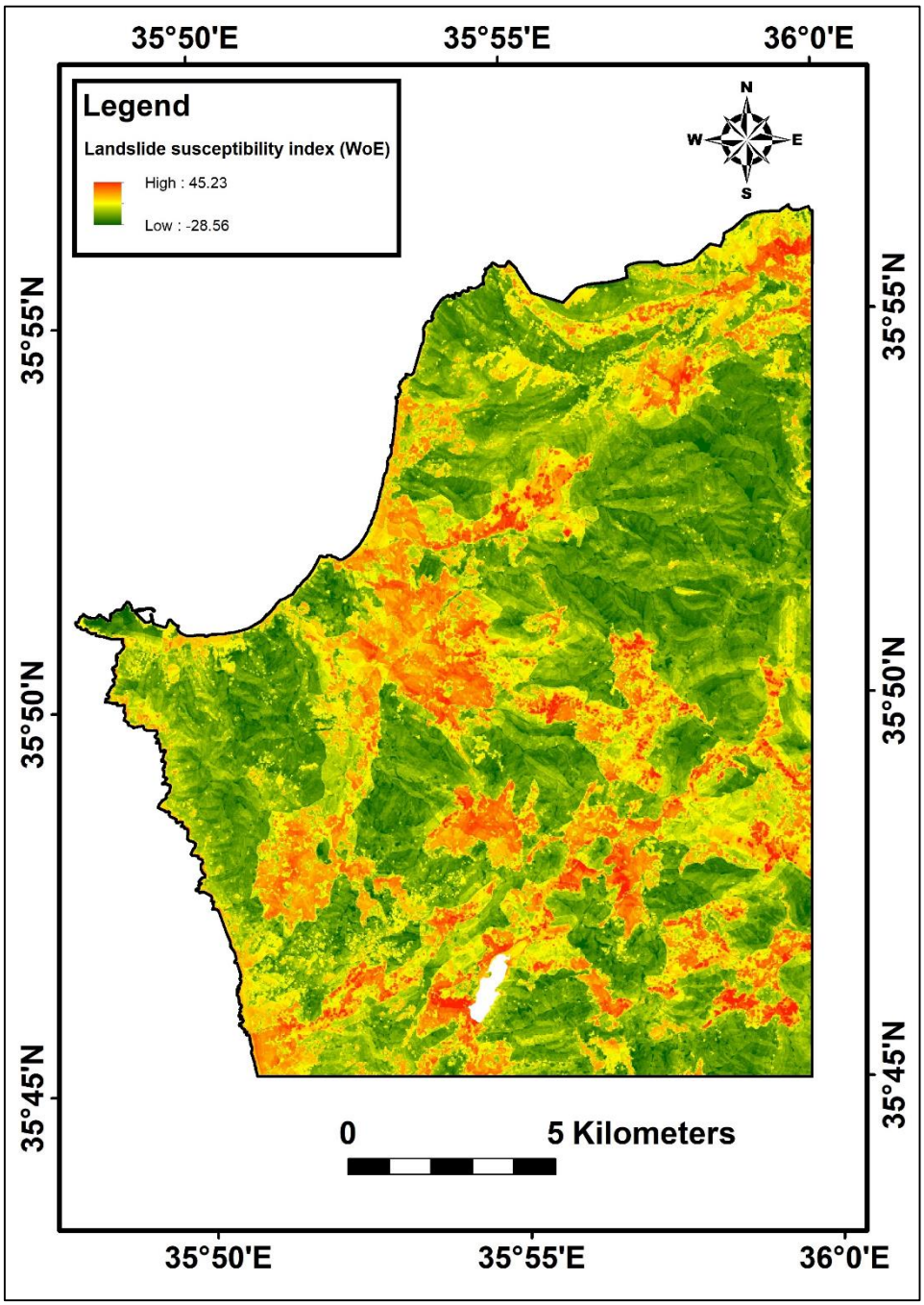

Figure 5.29: The landslide susceptibility map based on the weight-of-evidence method.

The resulting landslide susceptibility map of the WoE method (Figure 5.29) shows values ranging from -28.56, which is the lowest susceptibility to landslides, to 45.23, which is the highest susceptibility to landslides.

A validation process of the landslide susceptibility map of the WoE method was carried out using the area under the curve analysis based on the testing set of landslides. The AUC of the weight-of-evidence statistical analysis method was 84.79% (Figure 5.30).

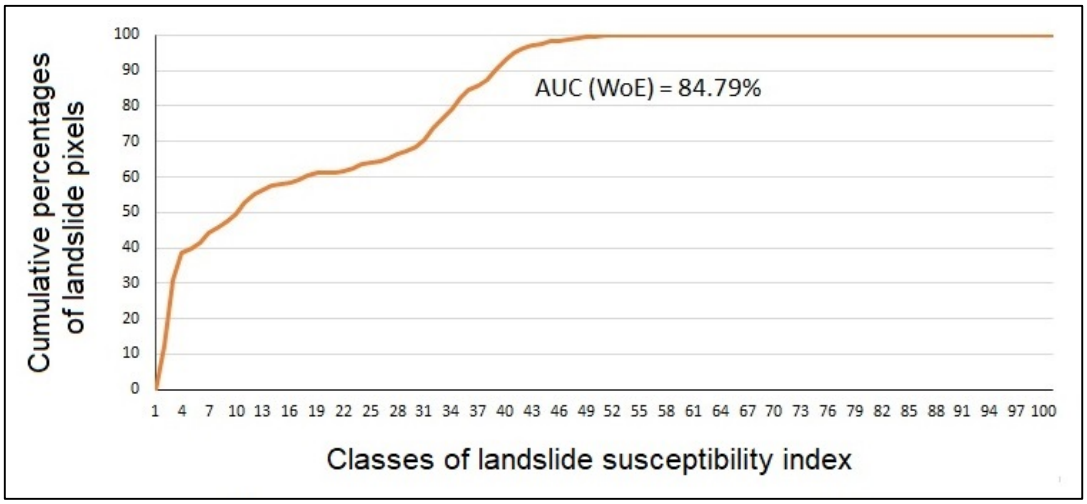

Figure 5.30: The area under the curve of the WoE statistical analysis method.

5.4.3 Logistic regression method

The logistic regression method used both the training sets of the landslide and non-landslide pixels to create a numeric table of 2706 rows representing all training pixels and 10 columns, with one column representing the binary landslide or non-landslide and the other nine columns representing the numeric values of the class number of each causative factor raster map at each training pixel (Table 6).

The Real Statistics Resource Pack in Microsoft Excel was used to perform the logistic regression statistical analysis. The intercept value (C_0) and the coefficient value of each causative factor (C_i) were calculated (Table 7) to assess the influence of each causative factor on the occurrence of landslides and to calculate the logit value in each pixel in the area.

According to the results of the logistic regression statistical analysis shown in table (7), each causative factor of slope gradient, slope aspect, lithology and land cover has a positive coefficient reflecting the relatively high influence of these factors on the landslide occurrence in the study area. Of these causative factors, the slope gradient is the most influential causative factor in the occurrence of landslides in the study area with the highest coefficient of 2.46. Then the land cover with a coefficient of 0.73. Then the lithology with a coefficient of 0.55. Then the slope aspect with a coefficient of only 0.48.

Table 6: Structure of the table prepared for the logistic regression statistical analysis.

FID	Landslide	Slope	Aspect	Curvature	Streams_D	Road_D	Fault_D	Lithology	Land_cover	NDVI
1	1	4	5	1	1	1	1	3	1	1
2	1	4	6	2	1	1	1	3	1	2
3	1	4	6	2	1	1	1	3	1	2
4	1	5	6	2	1	2	2	3	3	1
5	1	5	6	5	2	2	2	5	3	1
6	1	5	6	5	2	2	2	5	1	1
7	1	4	6	2	1	1	2	5	1	2
8	1	4	5	4	1	1	1	5	3	2
9	1	4	5	4	1	3	1	5	3	1
10	1	4	5	1	1	3	1	5	1	1
.	.	.	.	.	.	.	.	.	.	.
.	.	.	.	.	.	.	.	.	.	.
.	.	.	.	.	.	.	.	.	.	.
.	.	.	.	.	.	.	.	.	.	.
1351	1	4	5	2	2	2	1	3	3	2
1352	1	4	6	1	2	2	2	3	3	2
1353	1	3	6	2	1	2	2	3	3	2
1354	0	2	2	3	4	5	3	2	2	4
1355	0	2	2	3	4	5	3	6	2	5
1356	0	2	2	3	4	5	3	6	2	5
.	.	.	.	.	.	.	.	.	.	.
.	.	.	.	.	.	.	.	.	.	.
.	.	.	.	.	.	.	.	.	.	.
.	.	.	.	.	.	.	.	.	.	.
2701	0	2	1	3	4	4	5	2	2	4
2702	0	2	1	3	4	4	5	2	2	4
2703	0	1	2	3	4	5	4	6	2	5
2704	0	1	2	3	4	5	4	6	2	5
2705	0	2	2	3	3	4	6	6	2	5
2706	0	2	1	3	3	4	6	6	2	5

Table 7: Results of the logistic regression analysis using Real Statistics Resource Pack.

Intercept (C_0)	Coefficients of the causative factors (C_i)								
	Slope	Aspect	Curvature	Streams_D	Road_D	Fault_D	Lithology	Land_cover	NDVI
13.5885	2.462	0.4896	-0.1174	-1.1478	-1.4817	-0.9832	0.5534	0.7387	-3.8969

The coefficient values and the intercept of the model resulting from the logistic regression analysis were used to calculate the logit value in each pixel according to the following equation:

$$\begin{aligned}\text{Logit} = [13.5885 + (2.462*\text{Slope\_gradient.tif}) + (0.489*\text{Slope\_aspect.tif}) - \\ (0.117*\text{Terrain\_curvature.tif}) - (1.147*\text{Dist\_to\_streams.tif}) - \\ (1.481*\text{Dist\_to\_road.tif}) - (0.983*\text{Dist\_to\_fault.tif}) + (0.553*\text{Lithology.tif}) + \\ (0.738*\text{Land\_cover.tif}) - (3.896*\text{NDVI.tif})]\end{aligned} \quad (27)$$

Then, the logit was used to calculate the landslide susceptibility index of the logistic regression method (LSI_{LR}) according to the equation (23), which was used to create the landslide susceptibility map of the logistic regression method (Figure 5.31).

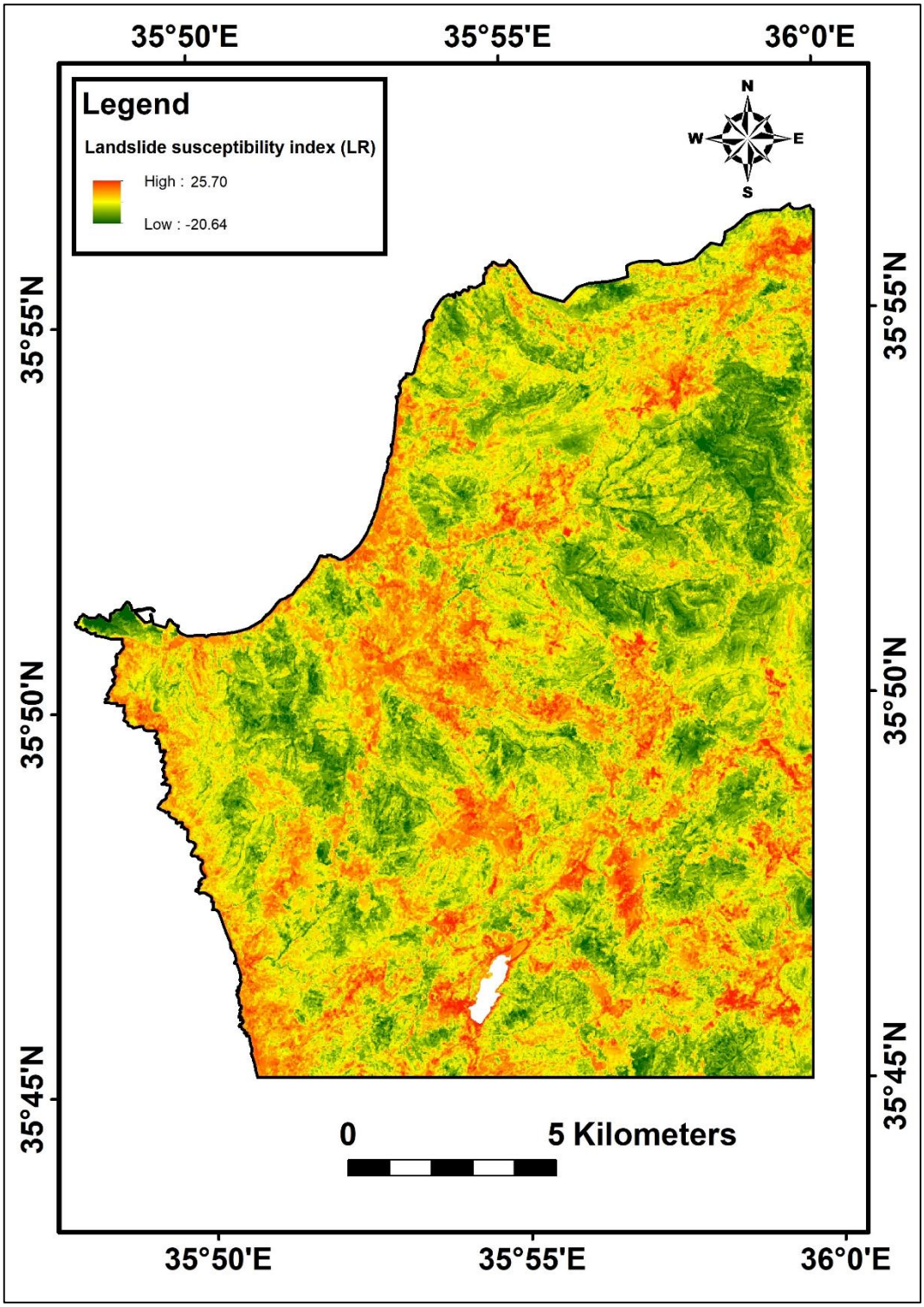

Figure 5.31: The landslide susceptibility map based on the logistic regression method.

The resulting landslide susceptibility map of the logistic regression method (Figure 5.31) shows values ranging from -20.64, which is the lowest susceptibility to landslides, to 25.70, which is the highest susceptibility to landslides.

A validation process of the landslide susceptibility map of the logistic regression method was carried out using the area under the curve analysis based on the testing set of landslides. The AUC of the logistic regression analysis method was 87.99% (Figure 5.32).

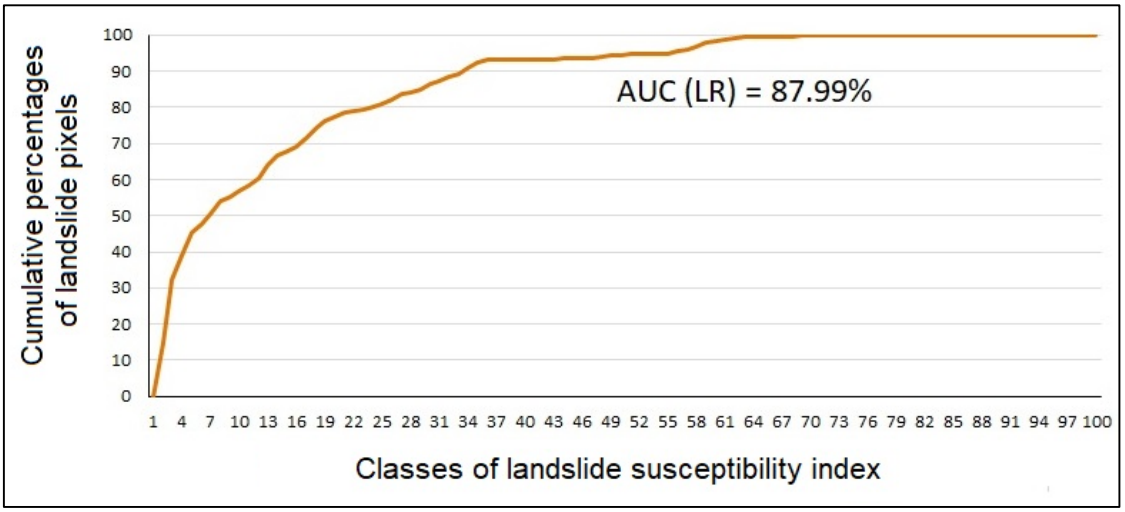

Figure 5.32: The area under the curve of the logistic regression statistical analysis method

5.4.4 Artificial neural networks method

The Artificial Neural Network method was performed using the same table (Table 6) as prepared for the logistic regression method from the landslide and non-landslide training pixels. The numeric table was imported to Matlab as a numeric matrix to perform the statistical analysis of the artificial neural networks method in Matlab. The best performance of the neural network used for the statistical analysis of landslides was after 23 iterations (Figure 5.33).

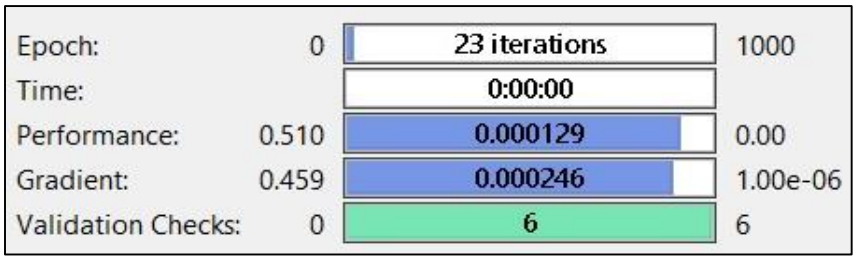

Figure 5.33: The performance of the neural network used for the susceptibility analysis.

As a result, the landslide susceptibility index based on the ANN method (LSI_{ANN}) for each pixel in the study area was calculated as an 8-bit integer in the range [0, 255], resulting in the landslide susceptibility map.

The resulting landslide susceptibility map of the artificial neural network (ANN) method shows values ranging from 128, which is the lowest susceptibility to landslides, to 255, which is the highest susceptibility to landslides (Figure 5.34).

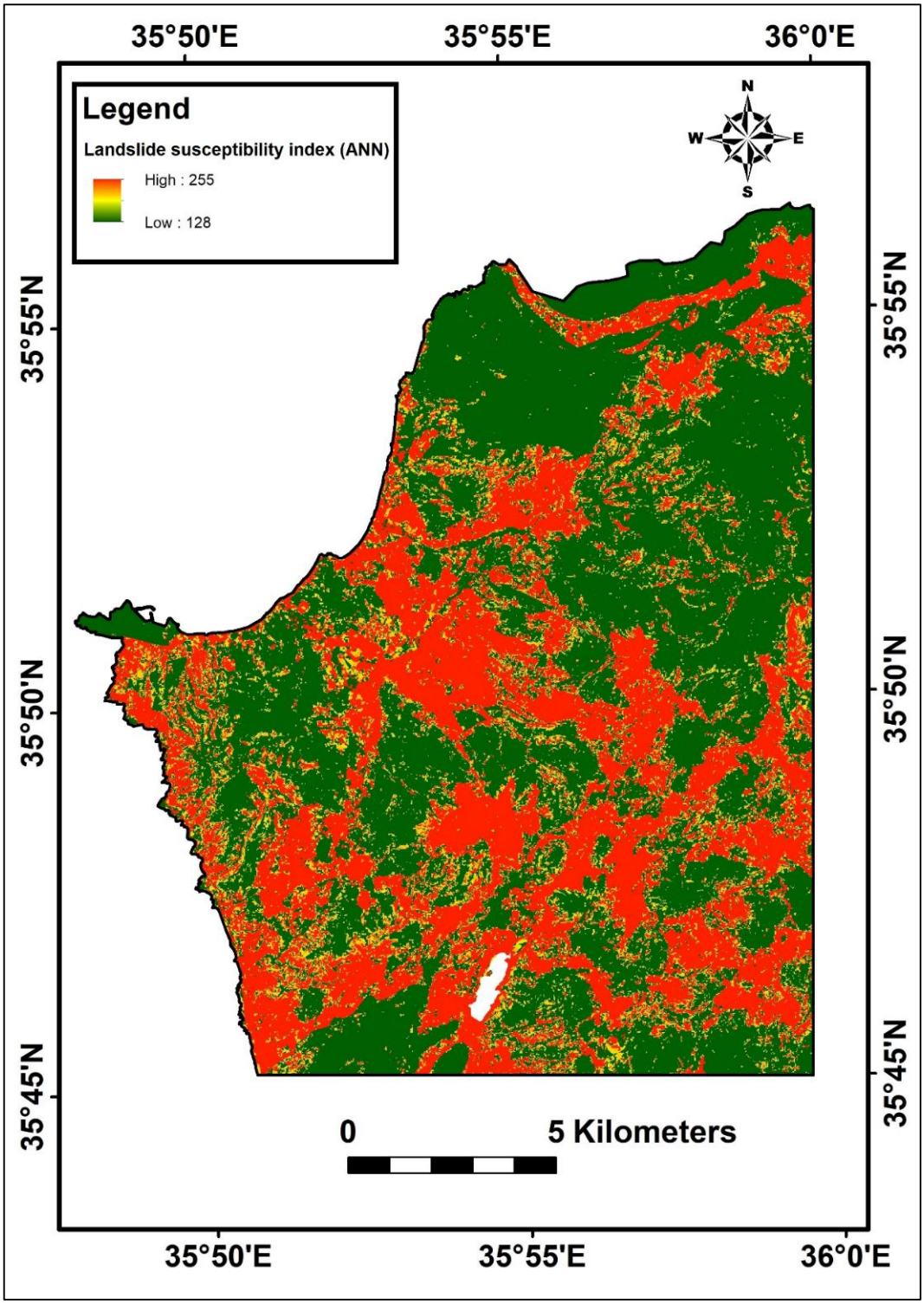

Figure 5.34: The landslide susceptibility map based on the ANN method.

A validation process of the landslide susceptibility map of the artificial neural network method was carried out using the area under the curve analysis based on the testing set of landslides as explained in detail in chapter four. The AUC of the artificial neural network statistical analysis method was 90.28% (Figure 5.35).

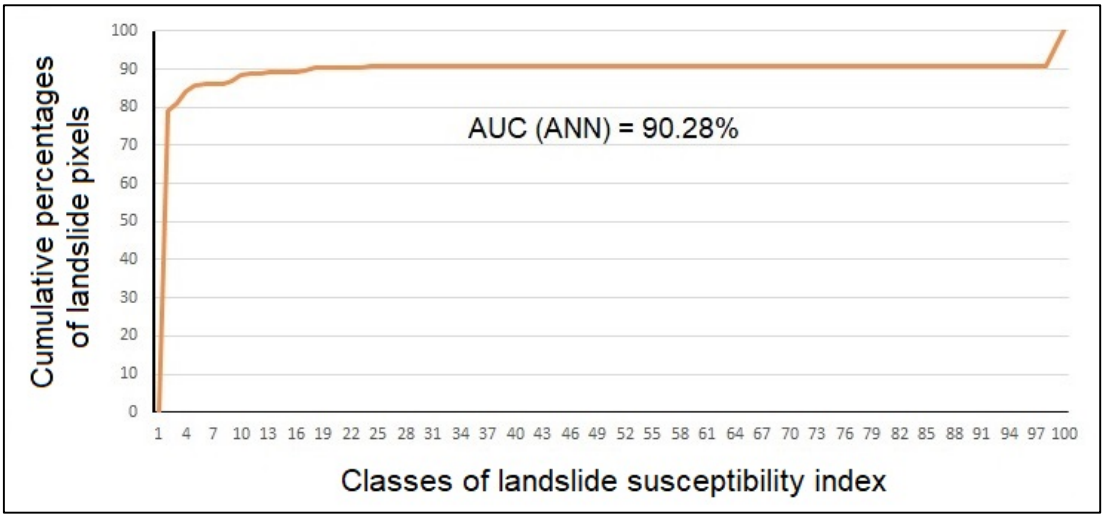

Figure 5.35: The area under the curve of the artificial neural network method.

A comparison of the results of all statistical analysis methods reveals that land cover, lithology and slope gradient were the common factors that significantly influenced and controlled the spatial distribution of landslides in the study area within all statistical analysis methods, with the exception of the ANN method, which, as previously mentioned, does not provide information on the influential factors causing landslides. The most influential causative factor was land cover, which was the first in the FR method and the second in the WoE method and the LR method, where the soil and agriculture land class and the built-up area class had the largest influence on the spatial distribution of landslides.

Furthermore, the comparison of the validation results of the four statistical analysis methods clearly reveals that the ANN method has a better AUC than the other three statistical analysis methods, proving that the use of the ANN method in northwest Syria gives better results in terms of susceptibility to landslides than the use of the other three methods used, which is consistent with the results of other studies in other parts of the world where these methods have been verified. Consequently, the landslide susceptibility map based on the ANN method can be selected as the final map of the landslide susceptibility of the study area, which can later be used for landslide hazard assessment.

5.5 Ground-surface deformation mapping using advanced remote sensing techniques

During the study period between 16 October 2018 and 21 March 2019, both the PSI and D-InSAR techniques were used to investigate ground-surface deformations.

5.5.1 Mean velocity map of ground-surface deformations using PSI technique

Among the fourteen Sentinel-1B SAR images from 16 October 2018 to 21 March 2019, the image of 27 December 2018 was selected as a master image, resulting in thirteen master-slave pairs with different temporal and perpendicular baselines (Figure 5.36) and modelled coherence (Table 8).

After splitting the IW3 sub-swath for each SAR image separately and selecting the bursts related to the area, all the steps mentioned in the method section of the PSI technique were performed to produce the two products required for exporting the SAR data from SNAP to StaMPS to unwrap all the resulting wrapped phases (Figure 5.37) and to perform the persistent scatterer estimation process to calculate the mean velocity of ground-surface deformation in the satellite LOS direction in each of the persistent scatterers.

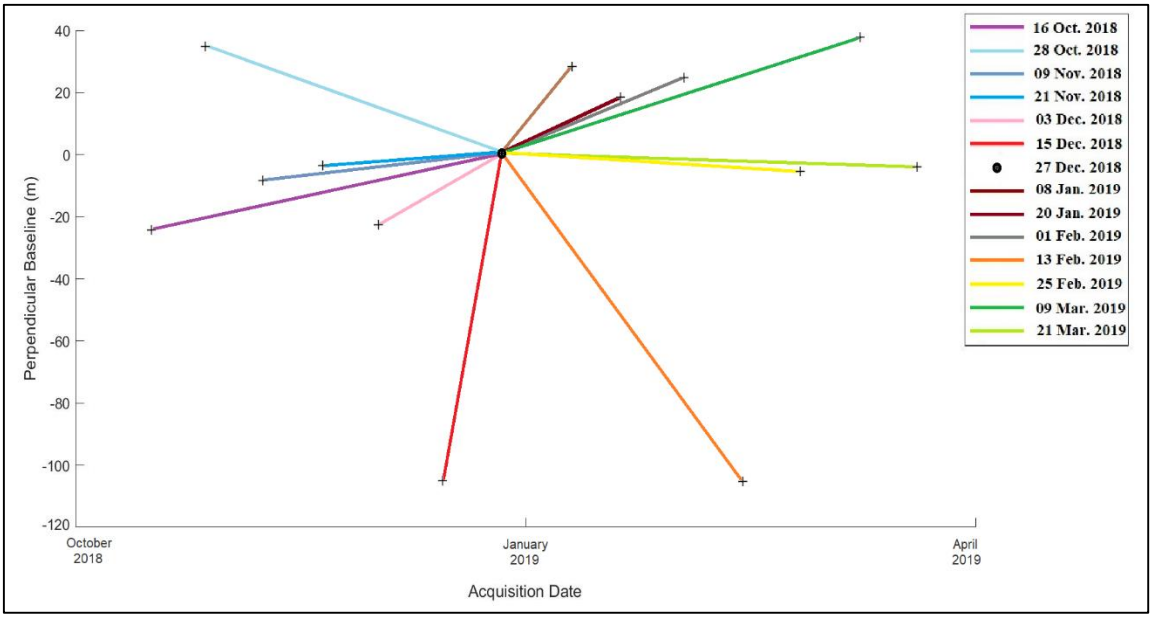

Figure 5.36: Perpendicular baselines of all master-slave pairs used in the PSI technique.

Table 8: Perpendicular and temporal baselines and modelled coherence of all master-slave pairs used in the PSI technique.

Imagery_ID	Master /slave	Acquisition date	B.perp [m]	B.temp [days]	Modelled coherence
S1B_IW_SLC_1SDV_20181227	Master	27 Dec 2018	0.00	0	1.00
S1B_IW_SLC_1SDV_20181016	Slave	16 Oct 2018	-43.21	72	0.90
S1B_IW_SLC_1SDV_20181028	Slave	28 Oct 2018	23.26	60	0.93
S1B_IW_SLC_1SDV_20181109	Slave	09 Nov 2018	-24.82	48	0.94
S1B_IW_SLC_1SDV_20181121	Slave	21 Nov 2018	-16.37	36	0.95
S1B_IW_SLC_1SDV_20181203	Slave	03 Dec 2018	-25.48	24	0.96
S1B_IW_SLC_1SDV_20181215	Slave	15 Dec 2018	-99.23	12	0.91
S1B_IW_SLC_1SDV_20190108	Slave	08 Jan 2019	28.17	-12	0.96
S1B_IW_SLC_1SDV_20190120	Slave	20 Jan 2019	14.66	-24	0.97
S1B_IW_SLC_1SDV_20190201	Slave	01 Feb 2019	17.19	-36	0.95
S1B_IW_SLC_1SDV_20190213	Slave	13 Feb 2019	-125.79	-48	0.86
S1B_IW_SLC_1SDV_20190225	Slave	25 Feb 2019	-40.37	-60	0.91
S1B_IW_SLC_1SDV_20190309	Slave	09 Mar 2019	-20.88	-72	0.92
S1B_IW_SLC_1SDV_20190321	Slave	21 Mar 2019	-70.77	-84	0.87

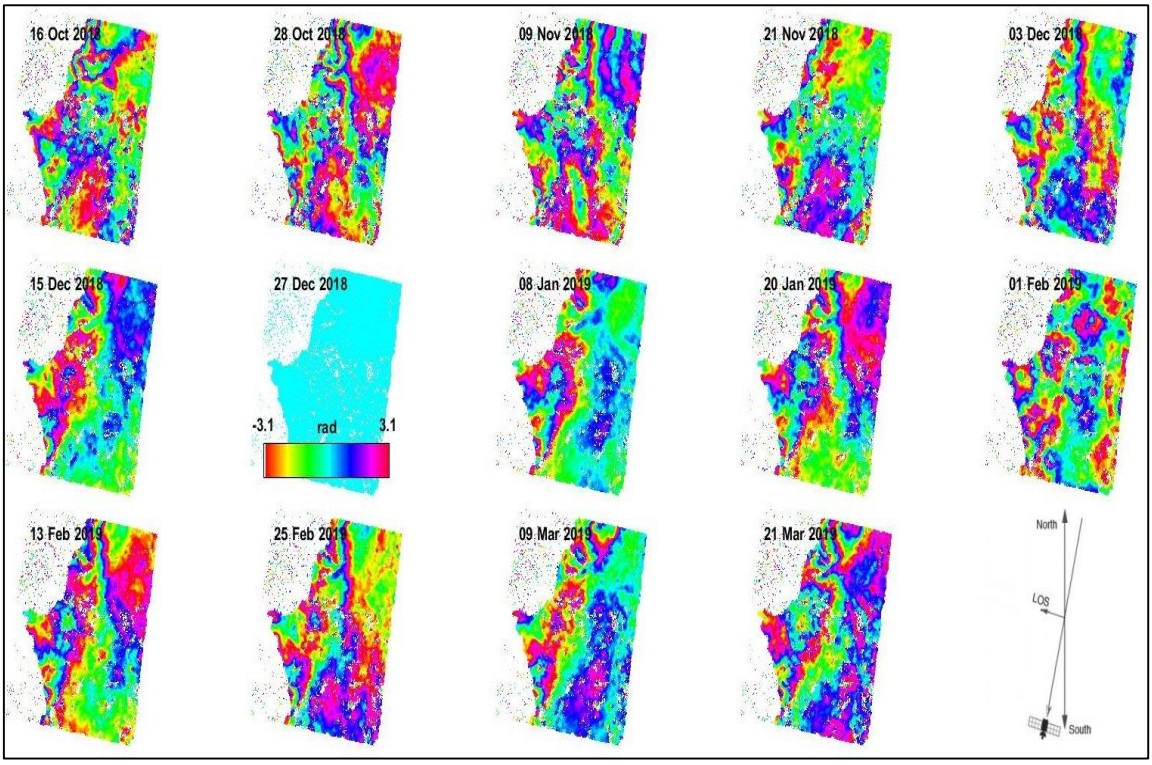

Figure 5.37: The wrapped phases of 13 interferograms exported from SNAP to StaMPS.

As shown in figure 5.37, the wrapped phases of the 13 interferograms exported from SNAP to StaMPS contain patterns of narrow InSAR fringes in several places, which essentially indicates the presence of remarkable ground-surface deformations at these locations, as each InSAR fringe represents 2.77 cm of displacement in the LOS, which is half the wavelength of Sentinel-1. The patterns of narrow InSAR fringes are more present in the wrapped phases between the master image and the slave images of October, December, February, and March, probably due to heavy rainfall during these months. In particular, the narrow InSAR fringes are more pronounced in the northern mountains, the western lowland, and around the Balloran Dam.

After exporting the SAR time-series data products from SNAP to StaMPS and completing the previously mentioned eight steps using StaMPS in Matlab, a multipoint data set for the locations and mean velocity values of 23,528 persistent scatterers was generated, which allows to create the persistent scatterer distribution map with mean velocity of ground-surface deformations in the satellite line-of-sight direction (Figure 5.38). As a result, the Sentinel-1 SAR data was capable of detecting ground-surface deformations in northwest Syria using PSI technique. The mean velocity ranged from -47.70 mm per year to 101.64 mm per year, which confirms the presence of ground-surface deformations or landslides in the study area during the 156 days of the study period, especially in places where the extreme values of the mean velocity are present.

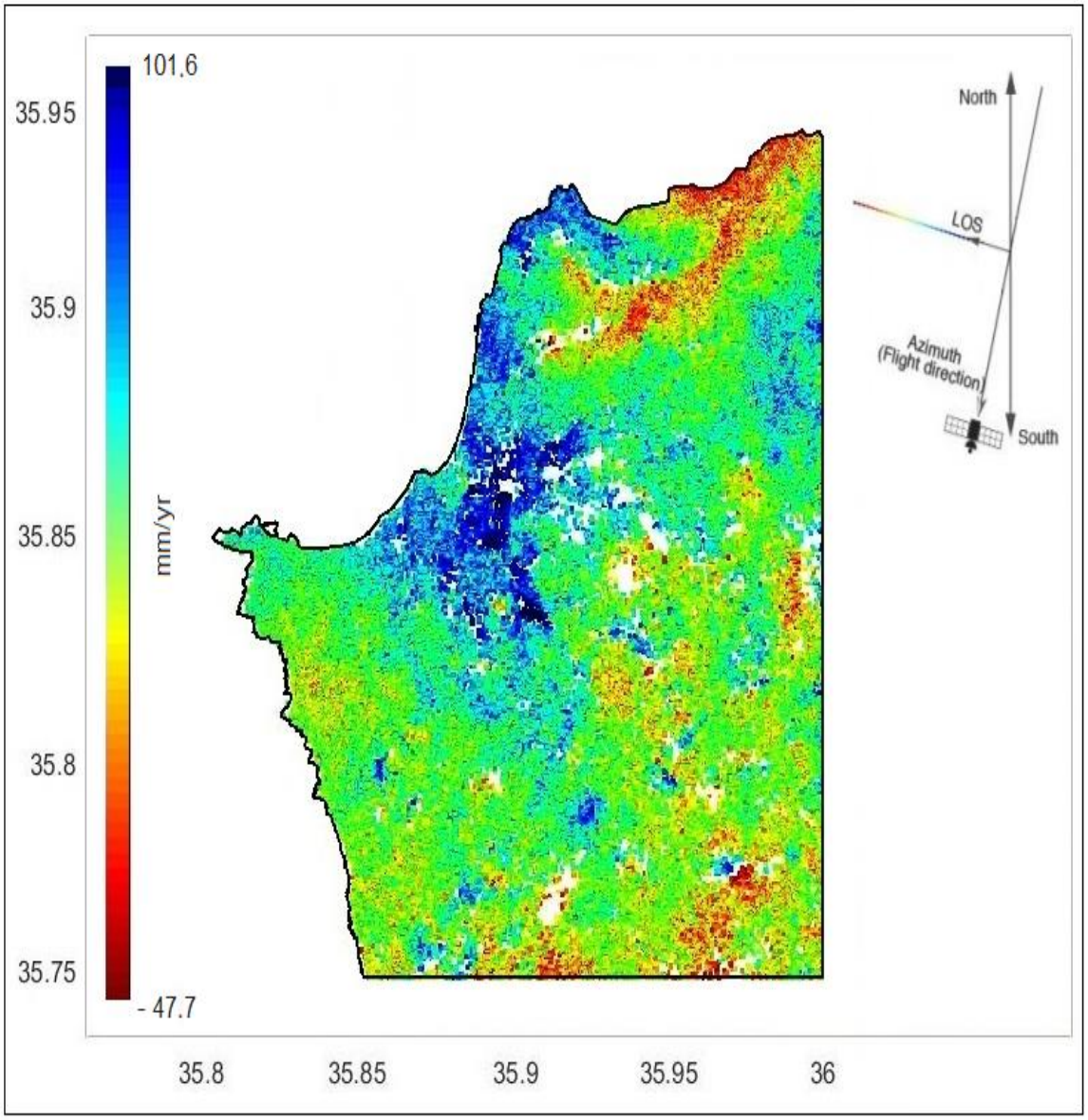

Figure 5.38: The persistent scatterer distribution map with mean velocity of ground-surface deformations in the satellite LOS direction (after Hammad et al., 2020).

The extreme values of negative mean velocities, which correspond to movements towards the satellite and appear red on the mean velocity map, are located in the northern mountains near the Turkish border and in the south near the Balloran Dam. In addition, the extreme values of positive mean velocities, which correspond to movements away from the satellite and appear blue on the mean velocity map, are located in the western lowland. All locations of extreme mean velocities can be considered places of high deformation intensity of the ground-surface.

The resulting multipoint data set generated in Matlab was exported as a point shapefile to be interpolated in ArcGIS to create a mean velocity raster map for later use in the landslide hazard assessment.

5.5.2 Total ground-surface deformation mapping using D-InSAR technique

The two SAR images acquired by Sentinel-1B on 16 October 2018 and 21 March 2019 were co-registered as master and slave, respectively, using the Sentinel-1 toolbox in SNAP (Table 9).

Table 9: Perpendicular and temporal baselines and modelled coherence of the master-slave pair used in D-InSAR technique.

Imagery_ID	Master /slave	Acquisition date	B.perp [m]	B.temp [days]	Modelled coherence
S1B_IW_SLC_1SD_20181016	Master	16 Oct 2018	0.00	0.00	1.00
S1B_IW_SLC_1SD_20190321	Slave	21 Mar 2019	-28.81	-156.00	0.84

After splitting the IW3 sub-swath for each SAR image and selecting the bursts related to the Balloran Dam area, all steps mentioned in the methodology section of the D-InSAR technique were performed to obtain total deformation values, which were reclassified in ArcGIS into five classes using the Jenks Natural Breaks classification. Two classes with the highest deformation were overlaid on a Google Earth image to illustrate the results along the highway (Figure 5.39).

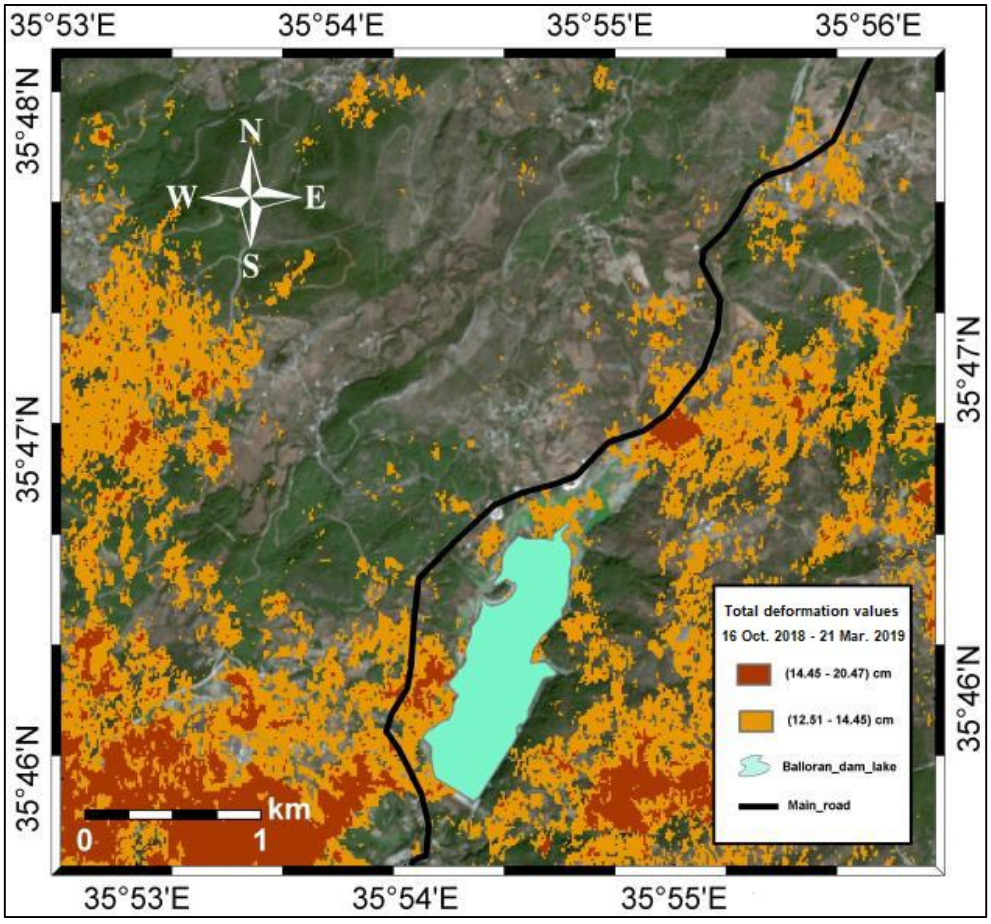

Figure 5.39: The total ground-surface deformation map based on the two Sentinel_1B images of 16 October 2018 and 21 March 2019 along the highway in the Balloran Dam area, masked from low values and overlaid on a Google Earth image as a base map.

According to the resulting map of total ground-surface deformations, the use of D-InSAR enabled the detection of ground-surface deformations in areas with good coherence along the highway with a maximum ground-surface deformation value of 20.47 cm during the study period. The total ground-surface deformation values exceeded 20 cm in two places, the first one near the village of Al-Qara'niya next to the dam in the southern part of the area and the second one near the village of Al-Hayek northeast of the lake.

5.5.3 Comparison of interferometry results with D-GPS field measurements

The results of the D-GPS field measurements of the two campaigns at the beginning and end of the study period show the ground-surface deformations in 10 validation points (P) during the study period (Figure 5.40). The maximum value of the ground-surface deformation was at the validation point P3 with a deformation value of 75 cm in the southeast direction. However, the ground-surface deformation values of the other validation points were between 2 and 5 cm (Hammad et al., 2019).

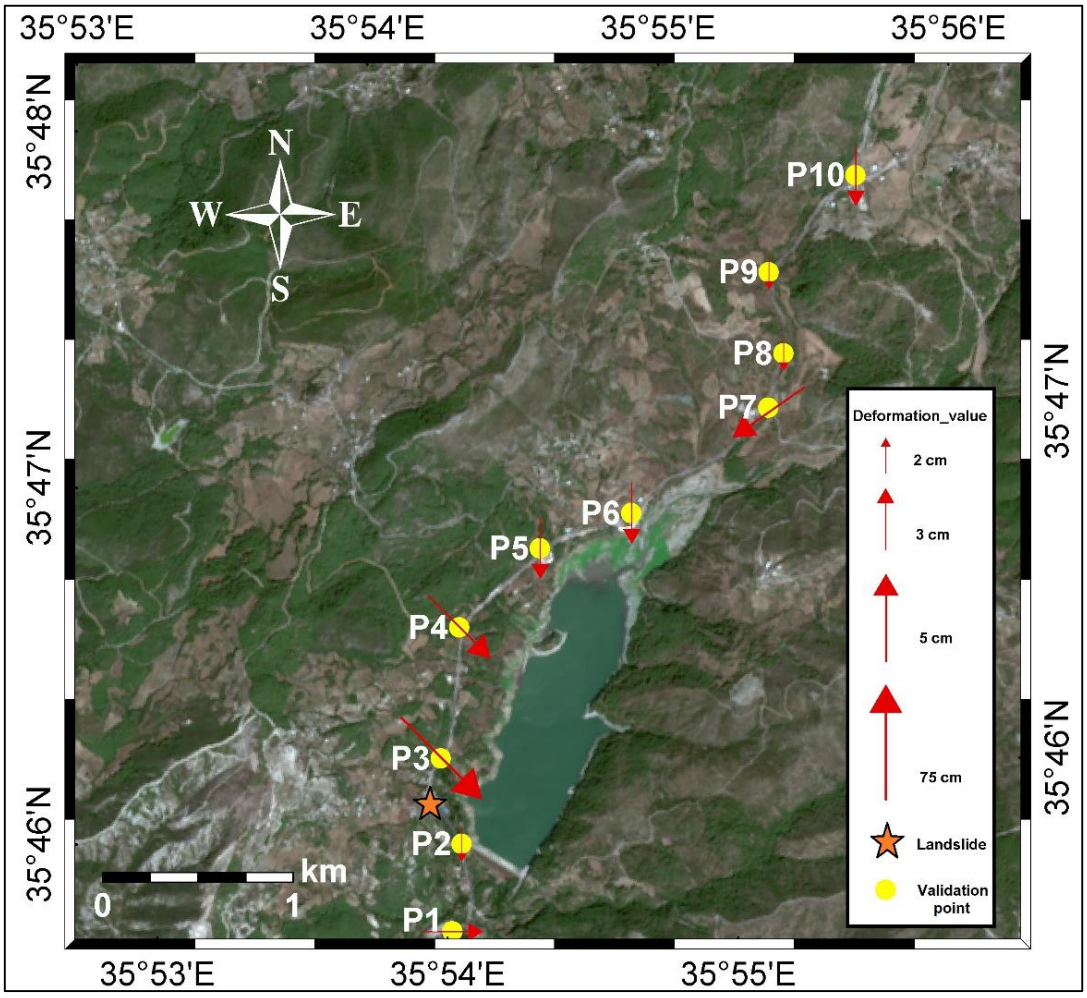

Figure 5.40: Ground-surface deformation direction and magnitude values using D-GPS field measurements from 10 validation points in the Balloran Dam area during the study period. The star indicates the location of the landslide that occurred in March 2019 (Hammad et al., 2019).

During the study period, a landslide was occurred near Balloran Dam in early March 2019, as shown in figure 5.40. The maximum displacement value of this landslide was about one meter in the south-southeast direction (Figure 5.41) (Hammad et al., 2019).

Figure 5.41: The landslide near the Balloran Dam in March 2019 (Hammad et al., 2019).

Comparing the D-InSAR deformation results with the D-GPS deformation results at the 10 validation points showed a difference at all validation points. The minimum difference was 6.4 cm at validation point P8. The maximum difference was 58.87 cm at the validation point P3, mainly because of the impact of the landslide near this point. Due to the movement of this landslide in an almost north-south direction, causing a deformation parallel to the azimuth of Sentinel-1B and perpendicular to the LOS direction, it was difficult to derive a better result about this deformation from Sentinel-1 SAR data. The Root Mean Square (RMS) of the difference values between the D-InSAR and D-GPS results was calculated and reached 20.14 cm (Table 10) (Hammad et al., 2019).

Table 10: Differences between the results of D-InSAR and D-GPS at the validation points along the highway in Balloran area and the root mean square of these differences.

Validation point name	D-InSAR results (cm)	D-GPS results (cm)	Difference values (cm)	Validation point name	D-InSAR results (cm)	D-GPS results (cm)	Difference values (cm)
P1	10.64	3.10	7.54	P6	10.56	3.02	7.54
P2	12.97	2.04	10.93	P7	12.10	5.08	7.02
P3	16.20	75.07	58.87	P8	8.810	2.41	6.4
P4	12.83	5.06	7.77	P9	10.11	2.03	8.08
P5	10.77	3.12	7.65	P10	12.35	3.05	9.3
RMS = $\sqrt{405.97}$ = 20.14 cm							

The differences between the results of D-InSAR and D-GPS in the Balloran Dam area are almost in the same range of the results of other comparison studies in other places around the world (Ng et al., 2012; Putri et al., 2013). Even with the difference between D-GPS and D-InSAR results since the first is a measurement in the vertical direction and the second is a measurement in the LOS direction, D-InSAR results can still show us places where severe ground-surface deformations have occurred.

5.6 Landslide hazard assessment

The intensity map of the ground-surface deformations and the optimal landslide susceptibility map were prepared as low-moderate-high zones for use in the landslide hazard matrix.

First, the values of the mean velocity raster map, which was created by interpolating the multipoint mean velocity data resulting from the PSI technique, were classified using the Equal Interval classification into three positive mean velocity levels and three negative mean velocity levels (Figure 5.42).

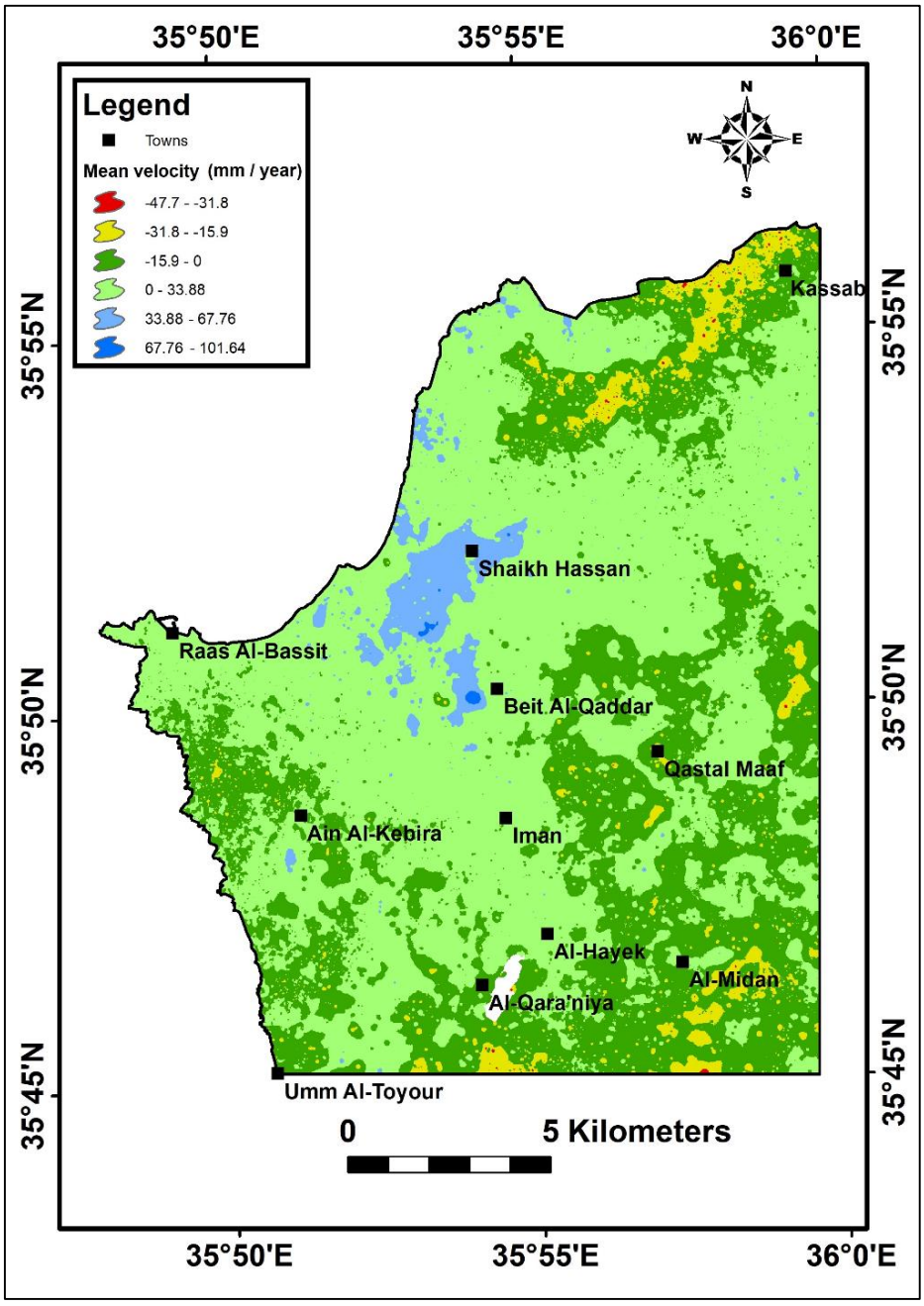

Figure 5.42: The mean velocity raster map shows three equal interval levels of positive and negative deformations based on SAR data from 16 October 2018 to 21 March 2019.

The mean velocity raster map of the ground-surface deformations reveals that the extreme negative values were mainly on the high slopes of mountains near Kassab in the north and on the high slopes of hills at Qastal Maaf and near Al-Midan in the south, while the extreme positive values were mainly in the lowlands near Beit Al-Qaddar and Shaikh Hassan in the west.

By comparing the positional data of the extreme positive and negative mean velocities with the elevation data, it can be explained that the location of extreme positive mean velocities between Beit Al-Qaddar and Shaikh Hassan reflects an uplift caused by the accumulation of soil erosion or landslide debris transported to the lowlands from the places of extreme negative mean velocities in the upper mountains and hills due to the heavy rainfall, which reached 734.64 mm during the study period, in addition to the high daily rainfall, which reached 39.08 mm on 19 December 2018.

After classifying the values of the mean velocity raster map into three positive levels and three negative levels based on the Equal Interval classification, each of the low, moderate and high levels of the negative and positive mean velocity were compiled to obtain the intensity map with the low-moderate-high intensity zones (Figure 5.43a). Furthermore, the landslide susceptibility map resulting from the ANN statistical analysis method was also reclassified using the Geometrical Interval classification into low-moderate-high zones of the landslide susceptibility (Figure 5.43b).

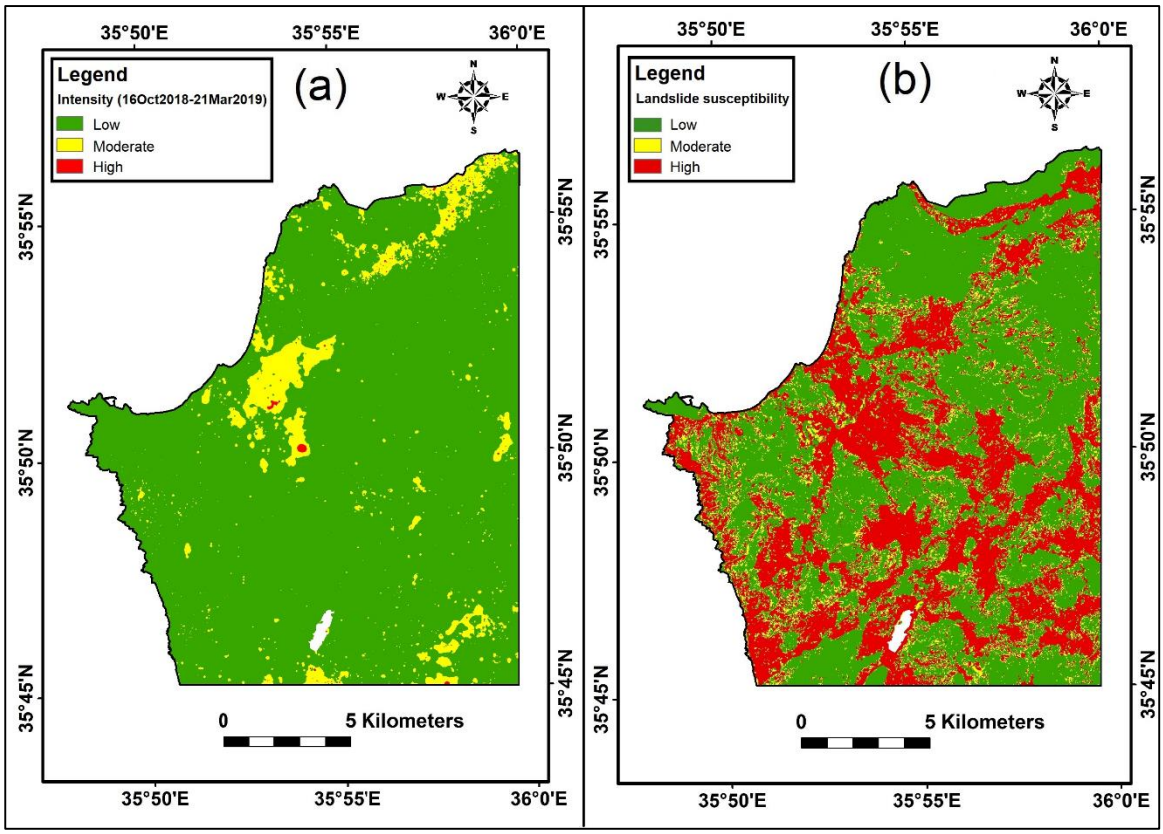

Figure 5.43: a- The intensity map of the ground-surface deformations in the LOS direction from October 2018 to March 2019. b- The landslide susceptibility map in low-moderate-high zones.

Based on the landslide hazard matrix already mentioned in the sixth section of the fourth chapter, the two resulting low-moderate-high zone maps were used to obtain the landslide hazard map during the main rainfall season of 2018-2019 (Figure 5.44).

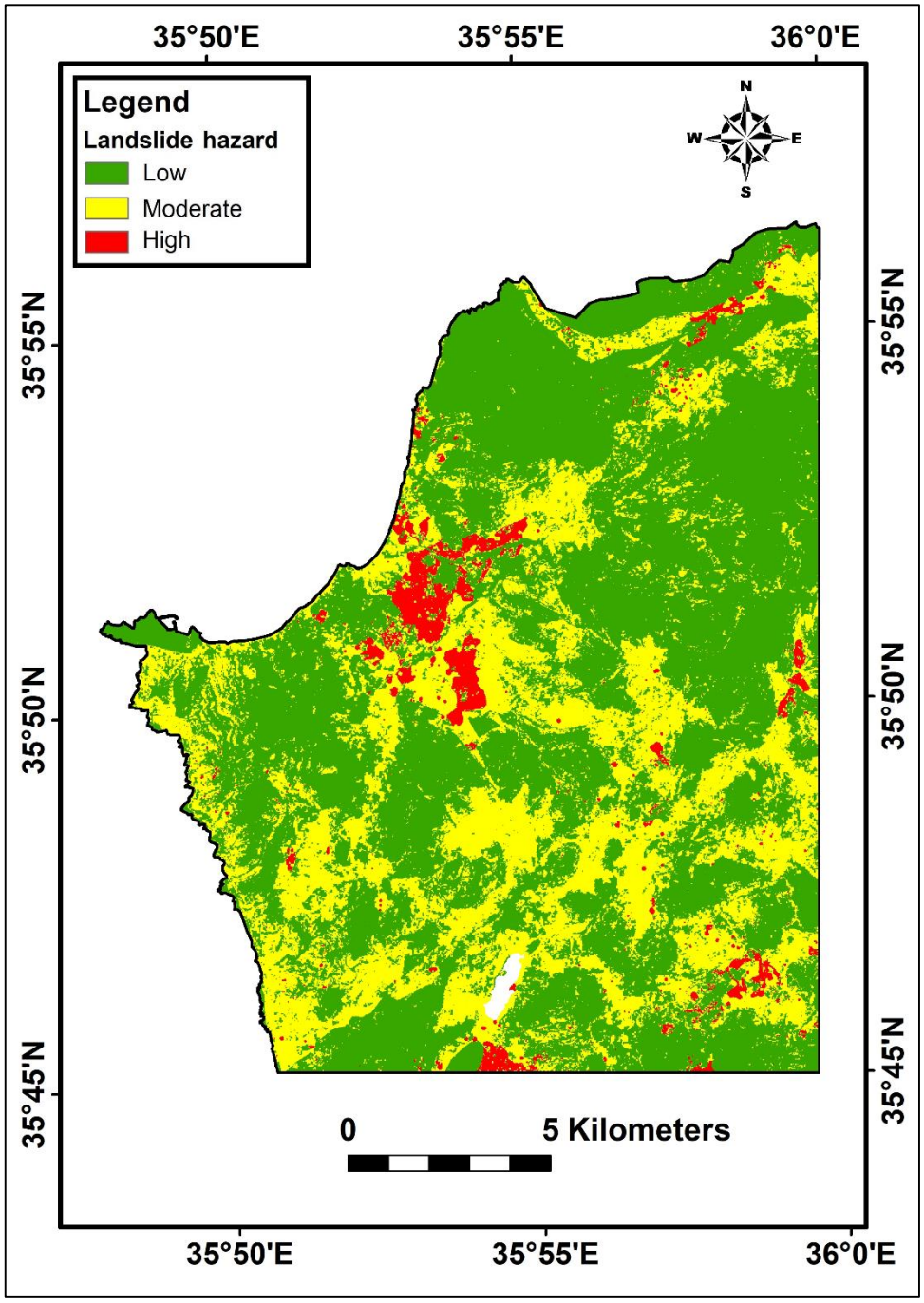

Figure 5.44: The landslide hazard map during the main rainfall season of 2018/2019.

According to landslide hazard map statistics, the low hazard zone covers an area of 170.68 km^2, which corresponds to 64.5% of the total study area. The moderate hazard zone covers an area of 84.75 km^2, which corresponds to 32.03% of the total area. The high hazard zone covers an area of 9.14 km^2, which corresponds to 3.45% of the total area.

A perusal of the high hazard zone for landslides reveals that this zone is mainly concentrated in the western part between Beit Al-Qaddar and Shaikh Hassan, and to a lesser extent in the southern part near Al-Qara'niya and near Al-Midan, with scattered distributions in the northern part near Kassab and in the eastern part near Qastal Maaf, where it is clear that the high hazard zone for landslides is located directly along the highway, similarly to the part of the highway south of the Balloran Dam (Figure 5.45).

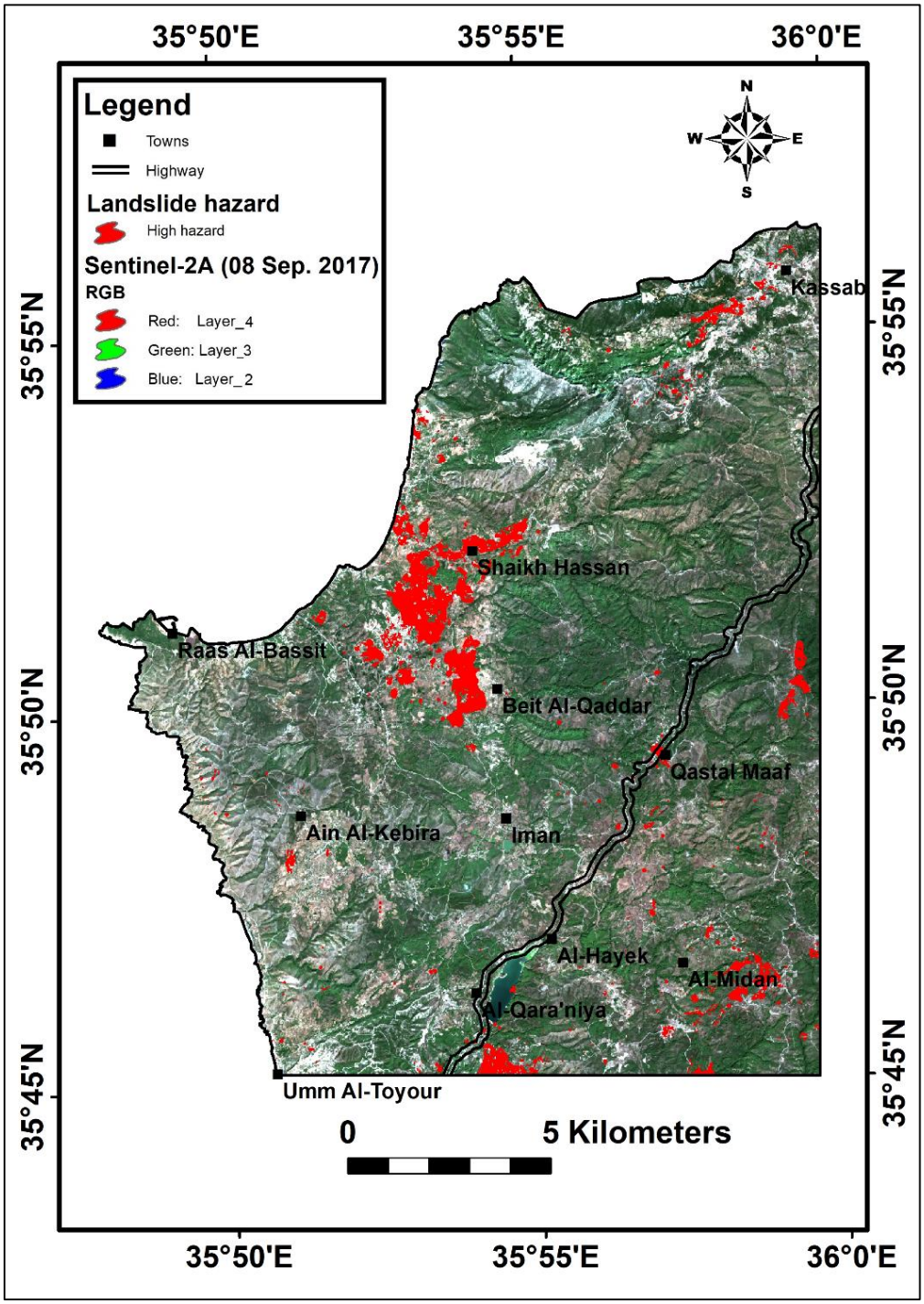

Figure 5.45: The distribution of the high hazard zone for landslides near residential areas and along the highway, overlaid on a true colour composite image of Sentinel-2A data.

Taking into account the distance-to-road class most susceptible to landslides according to the results of the statistical analysis, a 100-meter wide buffer zone was created for the entire road network on the landslide hazard map to determine the spatial distribution of the three hazard zones for landslides over the road network (Figure 5.46) and the percentage of these zones along the road network, which were 43.9%, 49.6% and 6.3% respectively for low, moderate and high hazard zones (Figure 5.47).

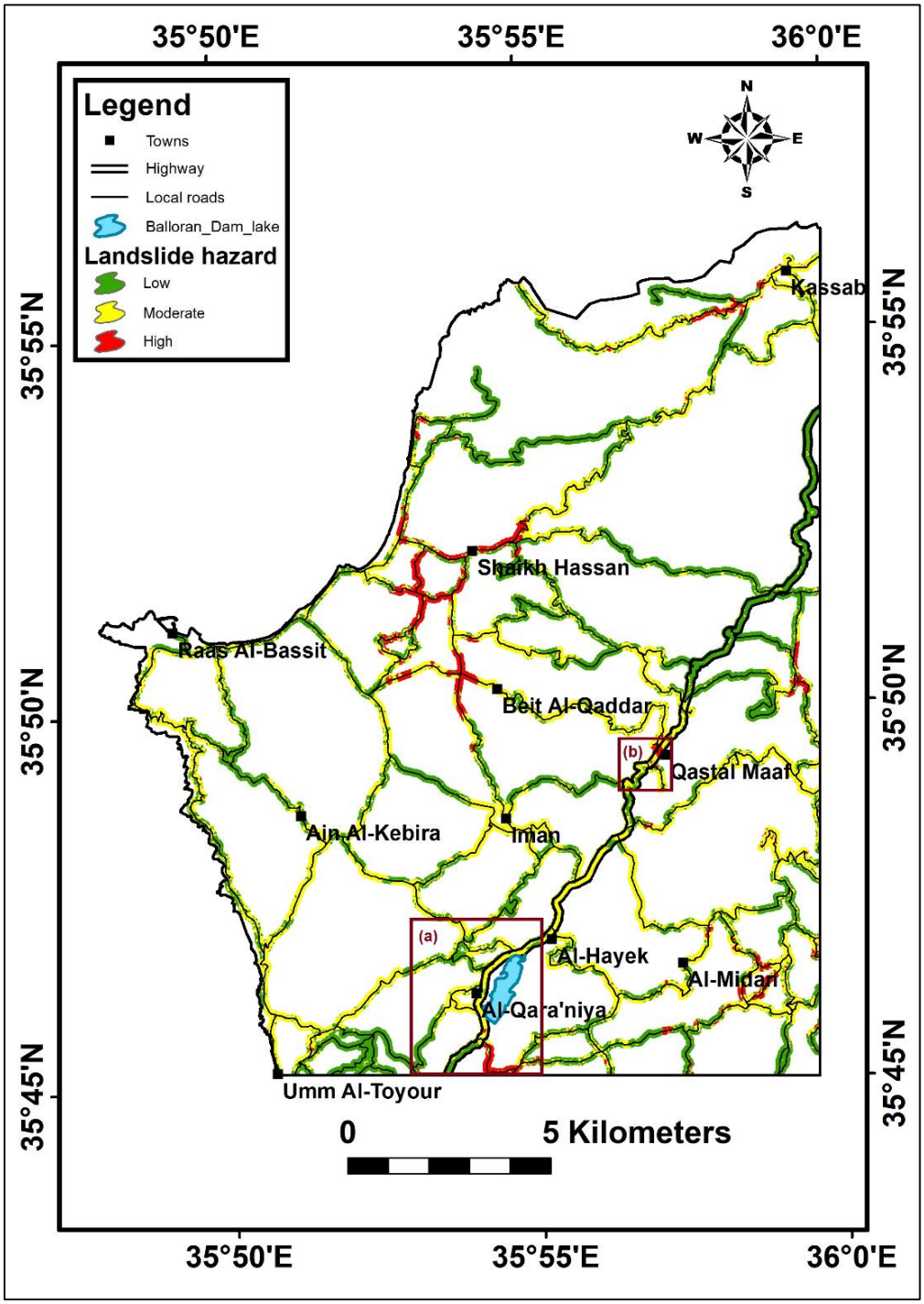

Figure 5.46: The spatial distribution of the three landslide hazard zones along the road network and the location of the two sites with a high hazard for landslides along the highway during the main rainfall season of 2018/2019.

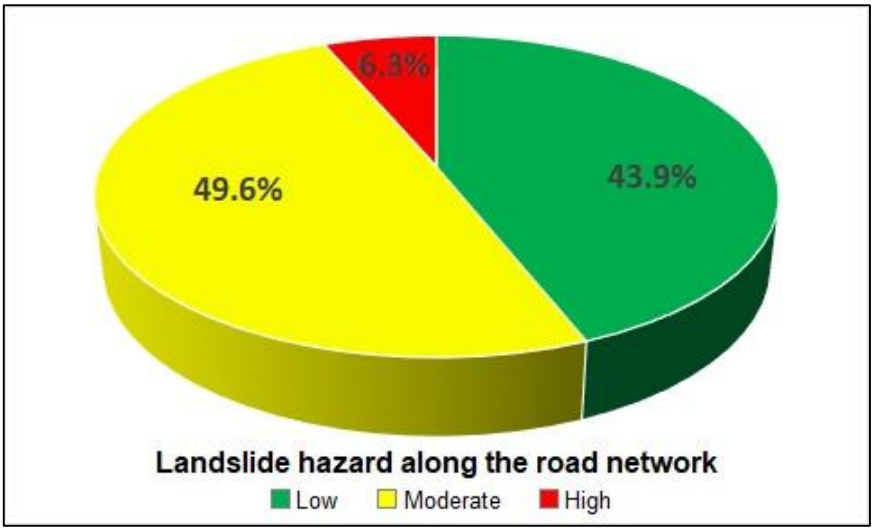

Figure 5.47: The percentage of the three hazard zones for landslides within the road network during the main rainfall season of 2018/2019.

It is important to give priority to emergency preparedness and to take the necessary precautions at all sites with a high hazard for landslides along the road network shown in figure 5.46, in particular at the two sites along the highway at the Al-Qara'niya site (Figure 5.48a) and at the Qastal Maaf site (Figure 5.48b), in order to avoid losses due to landslides that may occur there as a result of future heavy rainfall. In addition, further monitoring and investigations should be carried out regularly for all other places with a moderate landslide hazard to check whether the landslide hazard situation has changed.

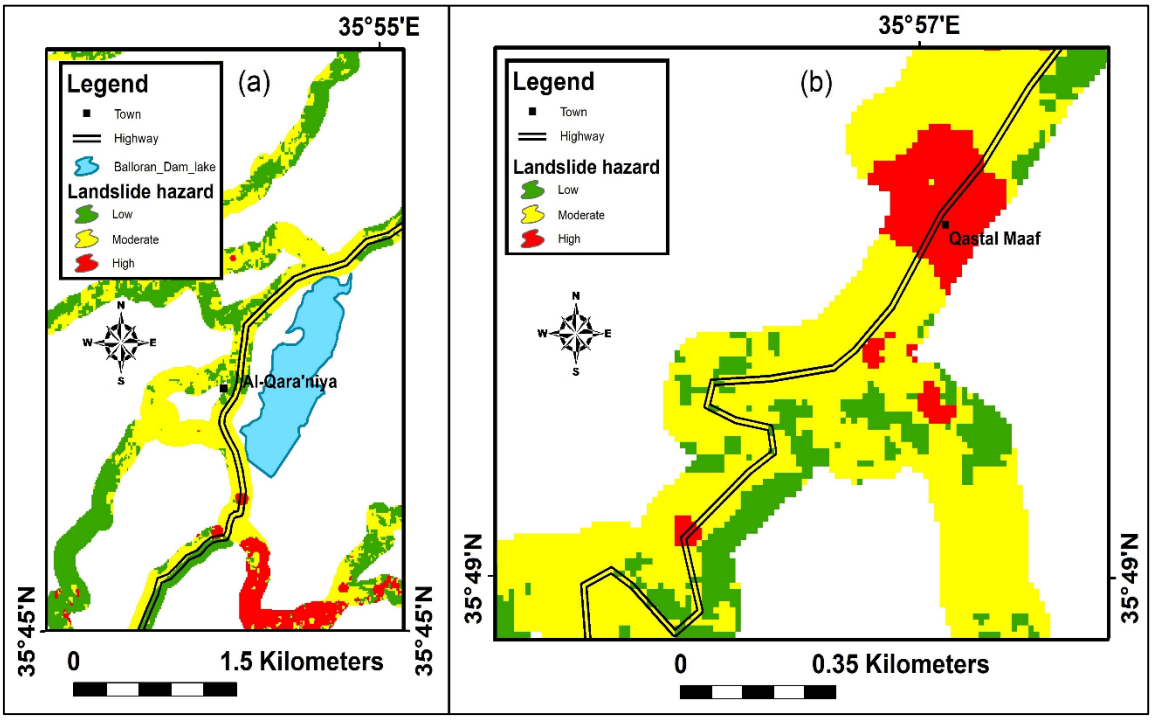

Figure 5.48: The two sites with a high hazard for landslides along the highway during the main rainfall season of 2018/2019. a- The Al-Qara'niya site. b- The Qastal Maaf site.

6. Conclusion

This doctoral research aimed to develop a workflow to create the landslide hazard map using freely available Sentinel-1 data, advanced remote sensing techniques and GIS. The landslide hazard was assessed according to a landslide hazard matrix based on both the landslide susceptibility of the statistical analysis and the mean velocities of ground-surface deformations during the main rainfall season of 2018-2019 using PSI technique.

The landslide susceptibility analysis was performed using four statistical analysis methods based on landslide and non-landslide training sets and nine causative factors influencing the spatial distribution of landslides, including slope gradient, slope aspect, terrain curvature, distance to streams, distance to roads, distance to faults, lithology, land cover and Normalized Differential Vegetation Index (NDVI). All causative factor maps were prepared from data sources that represent characteristics of the study area as they were prior to the occurrence of the landslides under investigation. As a result, the four different statistical analysis methods used for predicting landslide susceptibility produced different results. Therefore, the statistical analysis methods to create the landslide susceptibility map were evaluated and compared using Area Under the Curve (AUC) analysis based on a landslide testing set that was not included in the landslide training set.

According to Frequency Ratio (FR), Weight-of-Evidence (WoE) and Logistic Regression (LR) statistical analysis methods, the most influential causative factor was land cover, in which the soil and agriculture land class and the built-up area class have the largest influence on the occurrence of landslides, while the forests reduce the likelihood of landslides. This finding reflects the need to preserve the remaining forests and vegetation areas in northwest Syria, as the reduction in forest and vegetation area in the Syrian coastal region reached 25.66% between 1987 and 2017. In addition to land cover, lithology and slope gradient were also factors that significantly influenced and controlled the spatial distribution of landslides in the study area.

The results of the landslide susceptibility analysis showed that the use of the Artificial Neural Network (ANN) method in northwest Syria achieved excellent results in terms of susceptibility to landslides compared to the good and very good results obtained by using FR, WoE and LR methods. So, the first landslide susceptibility map for northwest Syria was created with 90.28% prediction accuracy based on the ANN method. Although the result of the ANN method reflects excellent statistical analysis, the impossibility of identifying the most influential causative factors in the occurrence of landslides reflects the inherent limitation of this method in this respect.

The capability of Sentinel-1 data and Interferometric Synthetic Aperture Radar (InSAR) techniques to generate high resolution Digital Elevation Models (DEMs) and also to detect and measure millimetre mean velocities of ground-surface deformations and landslides in northwest Syria was confirmed. However, the use of Sentinel-1 data to measure and monitor ground-surface deformations and landslides using PSI technique has proven to be more reliable and recommended than the use of this data to generate DEMs, especially when there is atmospheric inhomogeneity or in areas of dense vegetation where a large

amount of decorrelation and low coherence can be generated between the two images used in the DEM generation process, resulting in significant errors in the final result.

The two interferometric techniques used - Persistent Scatterer Interferometry (PSI) and the Differential InSAR (D-InSAR) - were conducted considering images represent the period of a rainfall season, as rainfall is the main trigger of the studied landslides.

The comparison process between the interferometric results and the D-GPS results showed a difference at 10 validation points along the highway in the Balloran area, where the root mean square of the differences was 20.14 cm, as the D-GPS measurements are made in the vertical direction and the interferometric measurements are made in the LOS direction. The difference was considerable where the ground-surface deformation or landslide occurred parallel to the satellite azimuth direction and perpendicular to the LOS direction. However, the interferometric results can show us places where severe ground-surface deformations have occurred, which is adequate for the purpose of landslide hazard assessment.

The mean velocities of ground-surface deformation during the study period were measured using PSI technique based on Sentinel-1 data for northwest Syria. The results ranged from -47.70 to 101.64 mm per year in the satellite LOS direction and were classified into low-medium-high zones with the Equal Interval classification for each of the positive and negative groups, since there are no reference studies that have determined a mean velocity sliding threshold that can be used to assess the landslide hazards in northwest Syria. Therefore, further studies should be carried out to establish the mean velocity sliding threshold that can provide an optimal input for landslide hazard assessment in the future.

Moreover, further studies on future landslides should be carried out whenever a high spatial and temporal resolution rainfall dataset is available to investigate the relationship between rainfall and landslide occurrence and to determine the rainfall intensity-duration thresholds for the occurrence of these future landslides in the study area, which can be very useful when integrated with the outcome of landslide hazard assessment.

Integrating the landslide susceptibility results of the ANN statistical analysis and the mean velocity results of the PSI technique using the landslide hazard matrix with the help of the GIS has proven to be a promising method of assessing landslide hazard using free SAR data and provides important results along the road network.

The first landslide hazard map for northwest Syria was created as well as the spatial distribution and percentage of the three landslide hazard zones along the road network. Moreover, two sites with a high hazard for landslides have been identified along the highway in the study area at Al-Qara'niya and Qastal Maaf. It is important to give priority to emergency preparedness and traffic warnings at these two sites in the event of heavy rainfall. The results of the landslide hazard assessment need to be regularly updated to identify possible future landslide sites where the necessary precautions need to be taken to avoid losses and minimize the risk at these sites.

Ultimately, the workflow of this research can be followed to monitor the landslide hazard along the road network in other places around the world, especially in areas with high rainfall and frequent landslides.

Acknowledgements

This PhD work would not have been possible without the support and guidance I have received from many people over the past four years. Therefore, I would like to thank all those who have helped me to complete this work.

First of all, I would like to thank my supervisor, **Assoc. Prof. László Mucsi**, for his support and directions, which were indispensable. His guidance has helped me all the time in carrying out this research and writing this dissertation. I am very grateful to him.

I would also like to thank my co-supervisor, **Asst. Prof. Boudewijn van Leeuwen**, for his immense support of this work and the related research and for his continued motivation for me. I could not have imagined having a better co-supervisor for my PhD.

I would also like to express my profound gratitude to the former head of the doctoral school, **Prof. Gábor Mezősi**, and the current head of the doctoral school, **Prof. Tivadar Tóth**, for their full support during my doctoral studies.

I am also grateful to all lecturers, staff and colleague PhD researchers of the Department of Physical Geography and Geoinformatics of the University of Szeged for their moral and scientific support.

Sincere thanks to the Tempus Public Foundation for granting me the Stipendium Hungaricum scholarship to undertake my doctoral studies in Hungary.

Many thanks to the General Establishment of Geology and Mineral Resources (GEGMR) in Syria for providing the data sources for this work.

Deep thanks to the General Organization of Remote Sensing (GORS) in Syria for its technical assistance in carrying out the D-GPS field measurements.

I would also like to thank my parents, my whole family and my friends for their moral support during my doctoral studies. Their strong belief in my abilities and their constant encouragement to me have always been an additional motive that led me to this point.

My special thanks go to my wife **Hala**, who has always believed in my success and supported my decisions. I know how hard it was to be away, but you have been with me in all the moments during these years. Last but not least, I would like to dedicate this work to my two children **Zeina** and **Adam** and wish them all the best for their lives.

Muhannad Hammad

Szeged, December 2020

References

Abdelmalik, K.W. and Abd-Allah, A.M.A. (2018). Integration of remote sensing technique and field data in geologic mapping of an ophiolitic suture zone in western Arabian Shield. Journal of African Earth Sciences, 146, 180-190.

Abe, K. and Ziemer, R.R. (1990). Effect of tree roots on shallow-seated landslides. Paper presented at the Technical Session on Geomorphic Hazards in Managed forests, XIX World Congress, IUFRO, August 5-11, 1990, Montreal, Canada.

Abrams, M. J., Rothery, D. A. and Pontual, A. (1988). Mapping in the Oman ophiolite using enhanced Landsat Thematic Mapper images. Tectonophysics, 151(1-4), 387-401.

Agterberg, F.P., Bonham-Carter, G.F. and Wright, D.F. (1990). Statistical pattern integration for mineral exploration. In: Gaal, G. and Merriam D.F. (eds.), Proceedings of Computer Applications in Resource Exploration symposium in 1988, Helsinki, Finland.

Akgun, A. (2011). A Comparison of Landslide Susceptibility Maps Produced by Logistic Regression, Multi-Criteria Decision, and Likelihood Ratio Methods: A Case Study at İzmir, Turkey. Landslides, 9(1), 93-106.

Aleotti, P. and Chowdhury, R. (1999). Landslide Hazard Assessment: Summary Review and New Perspectives. Bulletin of Engineering Geology and the Envir., 58(1), 21-44.

Alexander, E.D. (1989). Urban landslides. Progress in Physical Geography, 13, 157-191.

Al-Riyami, K., Robertson, A., Xenophontos, C., Danelian, T. and Dixon, J.E. (2000). Mesozoic tectonic and sedimentary evolution of the Arabian continental margin in Baer-Bassit (NW Syria). In: Malpas, J., Xenophontos, C. and Panayides, A. (eds.), Proceedings of the 3rd International Conference on the Geology of the Eastern Mediterranean, Nicosia, Cyprus, 61-81.

Al-Riyami, K. and Robertson, A. (2002). Mesozoic sedimentary and magmatic evolution of the Arabian continental margin, northern Syria: Evidence from the Baer-Bassit Melange. Geological Magazine, 139(4), 395-420.

Amatruda, G., Bonnard, C., Castelli, M., Forlati, F., Giacomelli, M., Morelli, M., Paro, L., Piana, F., Pirulli, M., Polino, R., Prat, P., Ramasco, M., Scavia, C., Bellardone, G., Campus, S., Durville, J.L., Poisel, R., Preh, A., Roth, W. and Tentschert, E.H. (2004). A key approach: the IMIRILAND project method. In: Bonnard, C., Forlati, F. and Scavia, C. (eds.), Identification and mitigation of large landslide risks in Europe - advances in risk assessment. European Commission Fifth Framework Program, Rotterdam, 13-44.

Atkinson, P.M. and Massari, R. (1998). Generalized linear modeling of susceptibility to landsliding in the central Apennines, Italy. Computers and Geosciences, 24, 373-385.

Ayalew, L. and Yamagishi, H. (2005). The Application of GIS-Based Logistic Regression for Landslide Susceptibility Mapping in the Kakuda-Yahiko Mountains, Central Japan. Geomorphology, 65(1-2), 15-31.

Ayenew, T. and Barbieri, G. (2005). Inventory of landslides and susceptibility mapping in the Dessie area, northern Ethiopia. Engineering Geology, 77(1-2), 1-15.

Begueria, S. (2006). Validation and evaluation of predictive models in hazard assessment and risk management. Natural Hazards, 37(3), 315-329.

Bianchini, S., Solari, L. and Casagli, N. (2017). A GIS-based procedure for landslide intensity evaluation and specific risk analysis supported by persistent scatterers interferometry (PSI). Remote Sensing, 9(11), 1093.

Biswajeet, P. and Saro, L. (2007). Utilization of Optical Remote Sensing Data and GIS Tools for Regional Landslide Hazard Analysis Using an Artificial Neural Network Model. Earth Science Frontiers, 14(6), 143-151.

Bonham-Carter, G.F. (1994). Geographic information systems for geoscientists, modelling with GIS. Pergamon Press, Oxford, 398 p.

Bonham-Carter, G.F., Agterberg, F.P. and Wright, D.F. (1990) Weights of evidence modeling: a new approach to mapping mineral potential. In: Agterberg, F.P. and Bonham-Carter, G.F. (Eds.), Statistical Applications in the Earth Science: Geological Survey of Canada, 89(9), 171-183.

Brabb, E. (1984). Innovative Approaches for Landslide Hazard Evaluation. IV International Symposium on Landslides, Toronto, 307-323.

Braun, A. and Veci, L. (2020). Sentinel-1 Toolbox: TOPS interferometry tutorial. ESA online publications, 25 p.

Braun, A. (2020). Sentinel-1 Toolbox: DEM generation with Sentinel-1 Workflow and challenges. ESA online publications, 27 p.

Brew, G., Lupa, J., Barazangi, M., Sawaf, T., Al-Imam, A. and Zaza, T. (2001). Structure and tectonic development of the Ghab basin and the Dead Sea fault system, Syria. Journal of the Geological Society, 158, 665-674.

Brunsden, D. (1999). Some geomorphological considerations for the future development of landslide models. Geomorphology, 30, 13-24.

Bunch, B.H. and Hellemans, A. (2004). The History of Science and Technology: a browser's guide to the great discoveries, inventions, and the people who made them, from the dawn of time to today. Houghton Mifflin Harcourt, Boston, 695 p.

Canuti, P., Casagli, N., Ermini, L., Fanti, R. and Farina, P. (2004). Landslide activity as a geoindicator in Italy: significance and new perspectives from remote sensing. Environmental Geology, 45, 907-919.

Canuti, P., Casagli, N., Catani, F., Falorni, G. and Farina, P. (2007). Integration of remote sensing techniques in different stages of landslide response. In: Sassa, K., Fukuoka, H., Wang, F. and Wang, G. (eds.), Progress in Landslide Science, 251-260.

Capes, R. and Teeuw, R. (2017). On Safe Ground? Analysis of European Urban Geohazards Using SAR Interferometry. Int. Journal of Applied Earth Observation and Geoinformatics, 58, 74-85.

Capitani, M., Ribolini, A. and Bini, B. (2013). The slope aspect: A predisposing factor for landsliding?, Comptes Rendus Geoscience. 345(11-12), 427-438.

Cardinali, M., Reichenbach, P., Guzzetti, F., Ardizzone, F., Antonini, G., Galli, M., Cacciano, M., Castellani, M. and Salvati, P. (2002). A geomorphological approach to the estimation of landslide hazards and risks in Umbria, Central Italy. Natural Hazards and Earth System Sciences, 2, 57-72.

Carrara, A., Cardinali, M., Detti, R., Guzzetti, F., Pasqui, V. and Reichenbach, P. (1991). GIS Techniques and statistical models in evaluating landslide hazard. Earth Surface Processes and Landform. 16(5), 427-445.

Casagli, N., Tofani, V., Morelli, S., Frodella, W., Ciampalini, A., Raspini, F. and Intreri, E. (2017). Remote sensing techniquesin landslide mapping and monitoring, keynote lecture. Advancing Culture of Living with Landslides, 1-19.

Catani, F., Farina, P., Moretti, S., Nico, G. and Strozzi, T. (2005). On the application of SAR interferometry to geomorphological studies: Estimation of landform attributes and mass movements. Geomorphology, 68, 119-131.

Chau, K.T., and Chan, J.E. (2005). Regional bias of landslide data in generating susceptibility maps; Case of Hong Kong Island. Landslides, 2, 280-290.

Chauhan, S., Sharma, M. Arora, M.K. and Gupta, N.K. (2010). Landslide Susceptibility Zonation through Ratings Derived from Artificial Neural Network. International Journal of Applied Earth Observation and Geoinformation, 12(5), 340-350.

Chen, J., Yang, S., Li, H., Zhang, B. and Lv, J. (2013). Research on Geographical Environment Unit Division Based on the Method of Natural Breaks (Jenks). International Archives of the Photogrammetry, Remote Sensing and Spatial Information Sciences - ISPRS Archives, XL-4/W3, 47-50.

Choi, J., Oh, H.J., Won, J.S. and Lee, S. (2009). Validation of an Artificial Neural Network Model for Landslide Susceptibility Mapping. Environmental Earth Sci., 60(3), 473-483.

CHRR - Center for Hazards and Risk Research at Columbia University, Center for International Earth Science Information Network at Columbia University, and Norwegian Geotechnical Institute (2005). Global Landslide Hazard Distribution. NASA Socioeconomic Data and Applications Center (SEDAC), Palisades, NY.

Chung, C-J.F. and Fabbri, A.G. (1999). Probabilistic prediction models for landslide hazard mapping. Photogrammetric Engineering & Remote Sensing, 65(12), 1389-1399.

Cigna, F., Bianchini, S. and Casagli, N. (2013). How to assess landslide activity and intensity with Persistent Scatterer Interferometry: the PSI-based matrix approach. Landslides, 10, 267-283.

Clarke, K.C. (1986). Advances in geographic information systems, computers, environment and urban systems, 10, 175-184.

Committee on the Review of the National Landslide Hazards Mitigation Strategy (2004). Partnerships for Reducing Landslide Risk. Assessment of the National Landslide Hazards Mitigation Strategy. Board on Earth Sciences and Resources, Division on Earth and Life Studies, The National Academic Press, Washington, D.C., 143 p.

Conforti, M., Pascale, S., Robustelli, G. and Sdao, F. (2014). Evaluation of Prediction Capability of the Artificial Neural Networks for Mapping Landslide Susceptibility in the Turbolo River Catchment (northern Calabria, Italy). CATENA, 113, 236-250.

Congalton, R.G. 1991. A review of assessing the accuracy of classifications of remotely sensed data. Remote Sensing of Environment 37(1), 35-46.

Corsini, A., Farina, P., Antonello, G., Barbieri, M., Casagli, N., Coren, F., Guerri, L., Ronchetti, F., Sterzai, P. and Tarchi, D. (2006). Space-borne and ground-based SAR interferometry as tools for landslide hazard management in civil protection. International Journal of Remote Sensing, 27(12), 2351-2369.

Corumluoglu, O., Vural, A. and Asri, I. (2015). Determination of Kula basalts in Turkey using remote sensing techniques. Arabian Journal of Geosciences, 8, 10105-10117.

CRED (Centre for Research on the Epidemiology of Disasters) (2019). Natural Disasters 2018. Brussels, Belgium. https://emdat.be/ sites/default/files/adsr_2018.pdf

Crozier, M.J. (1986). Landslides: causes, consequences and environment. Croom Helm Publications, London, 252 p.

Cruden D.M. (1991). A simple definition of a landslide. Bulletin of Engineering Geology and the Environment, 43(1), 27-29.

Cruden, D.M. and Varnes, D.J. (1996). Landslide types and processes. In: Turner, A.K. and Schuster, R.L. (eds.), Landslides, Investigation and Mitigation. Transportation Research Board, special report 247, National Research Council, National Acad. Press, Washington D.C., 36-75.

Dai, F.C. and Lee, C.F. (2003). A spatiotemporal probabilistic modelling of storm induced shallow landsliding using aerial photographs and logistic regression. Earth Surface Processes and Landforms, 28, 527-545.

Delaune-Mayere, M. and Saint-Marc, P. (1979/80). Données stratigraphiques nouvelles sur les sediments oceaniques Mésozoiques associées aux nappes ophiolitiques du Baer-Bassit. Cahiers de l'ORSTOM, Géologie, 11, 151-64. (in French, translated into Arabic).

De Ploey, J., Imeson, A. and Oldeman, L.R. (1991). Soil erosion, soil degradation and climatic change. In: Brouwer, F.M., Thomas, A.J. and Chadwick, M.J. (eds.), Land use changes in Europe. Kluwer Academic Publishers, Dordrecht, 275-292.

De Ruiter, R.S.C., Lovelock, P.E.R. and Nabulsi, N. (1995). The Euphrates graben of Eastern Syria: A new petroleum province in the Northern Middle East. In: Al-Husseini, M.I. (ed.), Middle East petroleum Geosciences, GEO 94, Manama, Bahrain, 1, 357-368.

Dietrich, E.W., Reiss, R., Hsu, M.L. and Montgomery, D.R. (1995). A process-based model for colluvial soil depth and shallow landsliding using digital elevation model. Hydrological processes, 9, 383-400.

Dikau, R., Brunsden, D., Schrott, L. and Ibsen, M.L. (1996). Landslide recognition. Identification, movements and causes. John Wiley & Sons Ltd, Chichester, U.K., 251 p.

Dilley, M., Chen, R.S., Deichmann, U., Lerner-Lam, A.L., Arnold, M., Arnold, M., Buys, P., Kjekstad, O., Lyon, B. and Yetman, G. (2005). Natural Disaster Hotspots: A Global Risk Analysis. World Bank, Washington, D.C.

Dubertret, L. (1955). Géologie des roches vertes du nord-ouest de la Syrie et du Hatay. Notes et mémoires sur le Moyen-Orient, 6, 1-179. (in French, translated into Arabic).

El-Atillah, A., El-Morjani, Z. and Souhassou, M. (2019). Use of the Sentinel-2A Multispectral Image for Litho-Structural and Alteration Mapping in Al Glo'a Map Sheet (1/50,000) (Central Anti-Atlas, Morocco). Artificial Satellites, 54 (3), 73-96.

Ermini, L., Catani, F. and Casagli, N. (2005). Artificial Neural Networks applied to landslide susceptibility assessment. Geomorphology, 66, 327-343.

Esfahany, S., Hanssen, R., Van Thienen-Visser, K. and Muntendam-Bos, A. (2009). On the effect of horizontal deformation on InSAR subsidence estimates. Proceedings of Fringe 2009 workshop, ESA.

Falaschi, F., Giacomelli, F., Federici, P.R., Pucinelli, A., Avanzi, G., Pochini, A. and Ribolini, A. (2009). Logistic regression versus artificial neural networks: landslides susceptibility evaluation in a sample area of the Serchio River valley, Italy. Natural Hazards, 50, 551-569.

Fell, R. (1994). Landslide risk assessment and acceptable risk. Canadian Geotechnical Journal, 32(2), 261-272.

Fell, R., Corominas, J., Bonnard, C., Cascini, L., Leroi, E. and Savage, W. (2008). Guidelines for landslide susceptibility, hazard and risk zoning for land use planning. Engr. Geo., 102, 83- 84.

Fernández, T., Jiménez, J., Delgado, J., Cardenal, J., Pérez, J.L., El-Hamdouni, R., Irigaray, C. and Chacón, J. (2013). Methodology for Landslide Susceptibility and Hazard Mapping Using GIS and SDI. In: Zlatanova S., Peters R., Dilo A. and Scholten H. (eds.) Intelligent Systems for Crisis Management. Lecture Notes in Geoinformation and Cartography, Springer, Berlin, 185-198.

Ferretti, A., Prati, C. and Rocca, F. (2001) Permanent Scatterers in SAR Interferometry. IEEE Trans. Geoscience and Remote Sensing, 39(1), 8-20.

Ferretti, A., Monti-Guarnieri, A., Prati, C., Rocca, F. and Massonnet, D. (2007). InSAR Principles: Guidelines for SAR Interferometry Processing and Interpretation (TM-19), ESA Publications.

Fick, S.E. and Hijmans, R.J. (2017). WorldClim 2: new 1km spatial resolution climate surfaces for global land areas. International Journal of Climatology, 37(12), 4302-4315.

Fielding, E.J., Blom, R.G. and Goldstein, R.M. (1998). Rapid Subsidence Over Oil Fields Measured by SAR Interferometry. Geophysical Research Letters, 25(17), 3215-3218.

Fruneau, B., Achache, J. and Delacourt, C. (1996). Observation and modelling of the Saint-Etienne-de-Tinee landslide using SAR interferometry. Tectonophysics, 265, 181-190.

Frye, C. (2007). About the Geometrical Interval classification method. ESRI online publication.

Fukuzono, T. (1990). Recent studies on time prediction of slope failure. Landslide News, 4, 9-12.

Gabriel, A.K., Goldstein, R.M. and Zebker, H.A. (1989). Mapping Small Elevation Changes Over Large Areas: Differential Radar Interferometry. Journal of Geophysical Research: Solid Earth, 94(B7), 9183–9191.

García-Davalillo, J.C., Herrera, G., Notti, D., Hernández-Ruiz, M., Fernández-Merodo, J.-A., Álvarez-Fernández, I., González-Nicieza, C., Strozzi, T. and Mora, O. (2013). InSAR Data for Mapping and Monitoring Landslides in Tena Valley. In: Margottini, C., Canuti, P. and Sassa, K. (eds.) Landslide Science and Practice. Springer, Berlin, 2, 243-250.

Garthwaite, M.C., Nancarrow, S., Hislop, A., Thankappan, M., Dawson, J.H. and Lawrie, S. (2015). The Design of Radar Corner Reflectors for the Australian Geophysical Observing System: A single design suitable for InSAR deformation monitoring and SAR calibration at multiple microwave frequency bands. Geoscience Australia record, 2015/003, 77 p.

Garrett, J.H. (1994). Where and why artificial neural networks are applicable in civil engineering. Journal of Computing in Civil Engineering, 8(2), 129-130.

Ge, W., Cheng, Q., Jing, L., Armenakis, C. and Ding, H. (2018). Lithological discrimination using ASTER and Sentinel-2A in the Shibanjing ophiolite complex of Beishan orogenic in Inner Mongolia, China. Advances in Space Research, 62, 1702-1716.

Gens, R. and Van Genderen, J.L. (1996). Review article: SAR interferometry issues, techniques, applications. International Journal of Remote Sensing, 17(10), 1803-1835.

Gomez, H., Bradshow, R. and Mather, P. (2000). Monitoring the distribution of shallow landslide prone areas using Remote Sensing, DTM and GIS - a case study from the tropical Andes of Venezuela. In: Casanova, E. (ed.), Remote Sensing in 21st century: Economic and Environmental applications. Rotterndam, Balkema, 395-401.

Gomez, H. and Kavzoglu, T. (2005). Assessment of shallow landslide susceptibility using artificial neural networks in Jabonosa River Basin, Venezuela. Engr. Geology,78, 11-27.

Grandin, R. (2015). Interferometric processing of SLC Sentinel-1 TOPS data. Proceedings of the 2015 ESA Fringe workshop. ESA Special Publication, SP-731, Frascati, Italy.

Griffiths, J.S. (1999). Proving the occurrence and cause of a landslide in a legal context. Bulletin of Engineering Geology and the Environment, 58, 75-85.

Guzzetti, F., Carrara, A., Cardinali, M. and Reichenbach, P. (1999). Landslide hazard evaluation: an aid to a sustainable development. Geomorphology, 31, 181-216.

Guzzetti, F. (2005). Landslide hazard and risk assessment. PhD dissertation, University of Bonn, Germany, 389 p.

Guzzetti, F., Reichenbach, P., Cardinali, M., Galli, M. and Ardizzone, F. (2005). Probabilistic landslide hazard assessment at the basin scale. Geomorphology, 72(1-4), 272-299.

Guzzetti, F., Peruccacci, S., Rossi, M. and Stark, C.P. (2007). Rainfall thresholds for the initiation of landslides in central and southern Europe. Meteorology and atmospheric physics, 98(3-4), 239-267.

Hammad, M., Van Leeuwen, B. and Mucsi, L. (2017). Generation of DEMs of the Syrian coastal mountains from Sentinel-1 data. In: Balázs, B. (ed.), The 8th conference of theory meets practice in GIS. Debrecen, Hungary, 133-137.

Hammad, M., Van Leeuwen, B. and Mucsi, L. (2018a). Land Cover Change Investigation in the Southern Syrian Coastal Basins During the Past 30-Years Using Landsat Remote Sensing Data. Journal of environmental geography, 11(1), 45-51.

Hammad, M., Van Leeuwen, B. and Mucsi, L. (2018b). Ground- surface deformation investigation in Paks NPP area in Hungary using D-InSAR and PSI techniques. In:

Molnár, V. (ed.), The 9th conference of theory meets practice in GIS. Debrecen, Hungary, 129-136.

Hammad, M., Mucsi, L. and Van Leeuwen, B. (2019). Landslide investigation using differential synthetic aperture radar interferometry: A case study of Balloran dam area in Syria. International Archives of the Photogrammetry, Remote Sensing and Spatial Information Sciences - ISPRS Archives, 42(3/W8), 133-138.

Hammad, M., Van Leeuwen, B., and Mucsi, L. (2020). Integration of GIS and advanced remote sensing techniques for landslide hazard assessment: a case study of northwest Syria. ISPRS Annals of the Photogrammetry, Remote Sensing and Spatial Information Sciences, 6(3/W1-2020), 27-34.

Hansen, M.J. (1984). Strategies for classification of landslides. Brunsden, D. and Prior, D.B. (eds.), Slope Instability. John Wiley and Sons, 1-25.

Hansen, A., Franks, C.A.M., Kirk, P.A., Brimicombe, A.J. and Tung, F. (1995). Application of GIS to hazard assessment, with particular reference to landslides in Hong Kong. In: Carrara, A. and Guzzetti, F. (eds.), Geographical Information Systems in Assessing Natural Hazards, Kluwer Academic Publisher, The Netherlands, 135-175.

Hempton, M.R. (1987). Constraints on Arabian plate motion and extensional history of the Red Sea. Tectonics, 6(6), 687-705.

Hengl, T. (2006). Finding the right pixel size, Computers and Geosci., 32(9), 1283-1298.

Hervás, J. and Bobrowsky, P. (2009). Mapping: Inventories, Susceptibility, Hazard and Risk. In: Sassa, K. and Canuti, P. (eds.), Landslides - Disaster Risk Reduction. Springer, Berlin, 321-349.

Highland, L.M. and Bobrowsky, P. (2008). The landslide handbook - A guide to understanding landslides. U.S. Geological Survey, Reston, Virginia, USA, 129 p.

Hollingsworth, R. and Kovacs, G.S. (1981). Soil slumps and debris flows: prediction and protection. Bulletin American Association of Engineering Geologists, 18(1), 17-28.

Hooper, A. (2006). Persistent scatterer radar interferometry for crustal deformation studies and modeling of volcanic deformation, Ph.D. thesis, Stanford University.

Hooper, A., Bekaert, D., Spans, K. and Arikan, M. (2012). Recent advances in SAR interferometry time series analysis for measuring crustal deformation, Tectonophysics, 514-517, 1-13.

Hooper, A., Bekaert, D. and Spaans, K. (2013). Stamps/MTI Manual Version 3.3b1. Leeds University Publication, U.K., 36 p.

Hungr, O., Corominas, J. and Eberhardt, E. (2005). State of the Art Paper #4, Estimating landslide motion mechanism, travel distance and velocity. In: Hungr, O., Fell, R., Couture, R. and Eberhardt, E. (eds.), Landslide Risk Management, Taylor and Francis Group, 99-128.

Hürlimann, M., Rickenmann, D., Medina, V. and Bateman, A. (2008). Evaluation of approaches to calculate debris-flow parameters for hazard assessment. Engineering Geology, 102(3), 152-163.

Hutchinson, J.N. (1988). General report: Morphological and geotechnical parameters of landslides in relation to geology and hydrology. In: Bonnard, C. (ed.), Proceedings of 5th International Symposium on Landslides, 1, 3-35.

Hutchinson, J.N. (1995) Landslide Hazard Assessment. Keynote Paper. In: Bell, D.H. (ed.), Proceeding of 6th International Symposium on Landslides, 1, 1805-1841.

Jibson, R.W., Harp, E.L. and Michael, J.A. (1998). A method for producing digital probabilistic seismic landslide hazard maps: an example from the Los Angeles, California, area. U.S. Geological Survey Open-File Report, 98-113.

Joftic, L., Milliman, J. and Sestini, G. (1992). Climate change and the Mediterranean. UNEP-E. Arnold Pub. NY, 20p.

Józsa, E., Lóczy, D., Soldati, M., Drăguţ, L.D., and Szabó, J. (2019). Distribution of landslides reconstructed from inventory data and estimation of landslide susceptibility in Hungary. Hungarian Geographical Bulletin, 68(3), 255-267.

Kalia, A. (2018). Classification of Landslide Activity on a Regional Scale Using Persistent Scatterer Interferometry at the Moselle Valley. Remote Sensing, 10(12), 1880.

Kawabata, D. Bandibas, J. (2009). Landslide susceptibility mapping using geological data, a DEM from ASTER images and an ANN. Geomorphology, 113(1-2), 97-109.

Kazmin, V.G. and Kulakov, V.V. (1968). The Geological Map of Syria, Sheet-1: I-36-XXIV-4d Scale (1: 50.000), and Explanatory Notes. Contracts No. (944) between the Syrian Ministry of Petroleum and the USSR Technoexport company, Moscow, 124 p.

Keefer, D.K. (1993). The susceptibility of rock slopes to earthquake-induced failure. Association of Engineering Geologists Bulletin, 30(3), 353-361.

Khawlie, M. (2003). The impacts of climate change on water resources of Lebanon – Eastern Mediterranean. In: Giupponi, C. and Schecter, M. (eds.), Climate change in the Mediterranean socio-economic perspectives of impacts, vulnerability and adaptation. Edward Edgar pub., United Kingdom, 94-107.

Khawlie, M. and Hassanain, H. (1984). Failure phenomena and environmental control of the relatively unstable Hammana area, Lebanon. Engineering Geology, 20, 253-264.

Kienholz, H., Hafner, H., Schneider, G. and Tamrakar, R. (1983). Mountain hazards mapping in Nepal's Middle Mountains. Maps of land use and geomorphic damages (Kathmandu-Kakani area). Mountain Research and Development, 3(3), 195-220.

Kleinbaum, D.G. and Klein, M. (1994). Logistic Regression: A Self-Learning Text. Springer Publishers, New York, Inc.

Kovács, I.P., Bugya, T., Czigány, S. Defilippi, M., Lóczy, D., Riccardi, P., Ronczyk, L. and Pasquali, P. (2019). How to avoid false interpretations of Sentinel-1A TOPSAR interferometric data in landslide mapping? A case study: recent landslides in Transdanubia, Hungary. Natural Hazards, 96, 693-712.

Lateltin, O., Haemmig, C., Raetzo, H. and Bonnard, C. (2005). Landslide risk management in Switzerland. Landslides, 2(4), 313-320.

Lazzari, M. and Piccarreta, M. (2018). Landslide Disasters Triggered by Extreme Rainfall Events: The Case of Montescaglioso (Southern Italy). Geosciences, 8(10), 377, 17 p.

Lee, E.M. and Jones, D.K.C. (2004). Landslide risk assessment. Thomas Telford Publishing, 464 p.

Lee, S. (2004). Application of Likelihood Ratio and Logistic Regression Models to Landslide Susceptibility Mapping Using GIS. Environmental Management, 34(2), 223-232.

Lee, S. (2007). Landslide Susceptibility Mapping Using an Artificial Neural Network in the Gangneung Area, Korea. International Journal of Remote Sensing, 37-41.

Lee, S., Choi, J. and Min, K. (2002). Landslide susceptibility analysis and verification using the Bayesian probability model. Environmental Geology, 43(1-2), 120-131.

Lee, S., Ryu, J.H., Min, K. and Won J.N. (2003). Use of an artificial neural network for analysis of the susceptibility to landslides at Bou, Korea. Environmental Geology, 44(7), 820- 833.

Lee, S. and Choi, J. (2004). Landslide susceptibility mapping using GIS and the weights-of-evidence model. International Journal of Geographical Information Sci., 18, 789-814.

Lee, S., Choi, J. and Min, K. (2004). Probabilistic Landslide Hazard Mapping Using GIS and Remote Sensing Data at Boun, Korea. International Journal of Remote Sensing, 25(11), 37-41.

Lee, S. and Talib, J.A. (2005). Probabilistic landslide susceptibility and factor effect analysis. Environmental Geology, 47**,** 982-990.

Lee, S. and Pradhan, B. (2007). Landslide Hazard Mapping at Selangor, Malaysia Using Frequency Ratio and Logistic Regression Models. Landslides, 4, 33-41.

Lee, S., Song, K.Y., Oh, H.J. and Choi, J. (2012). Detection of Landslides Using Web-Based Aerial Photographs and Landslide Susceptibility Mapping Using Geospatial Analysis. International Journal of Remote Sensing, 33(16), 4937-4966.

Lepore, C., Kamal, S.A., Shanahan, P. and Bras, R.L. (2011). Rainfall Induced Landslide Susceptibility Zonation of Puerto Rico. Environmental Earth Sciences, 66(6), 1667-1681.

Li, Z.W., Ding, X.L., Huang, C., Zhu, J.J. and Chen, Y.L. (2008). Improved filtering parameter determination for the Goldstein radar interferogram filter. ISPRS Journal of Photogrammetry and Remote Sensing, 63(6), 621-634.

Li, Z., Nadim, F., Huang, H., Uzielli, M., and Lacasse, S. (2010). Quantitative vulnerability estimation for scenario-based landslide hazards. Landslides, 7(2), 125-134.

Lillesand, T.M. and Kiefer, R.W. (1994). Remote Sensing and Image Interpretation. (3rd edition). John Wiley & Sons, Inc., Hoboken, 750 p.

Lin, M.L. and Tung, C.C. (2004). A GIS-based potential analysis of the landslides induced by the Chi-Chi earthquake. Engineering Geology, 71(1-2), 63-77.

Lippard, S.J., Shelton, A.W. and Gass, I.G. (1986). The ophiolite of Northern Oman. The Geological Society Memoir, Blackwell Scientific Publications, Oxford, 178 p.

Litak, R.K., Barazangi, M., Beauchamp, W., Seber, D., Brew, G., Sawaf, T. and Al-Youssef, W. (1997). Mesozoic-Cenozoic evolution of the Intraplate Euphrates fault system, Syria: Implications for regional tectonics. Journal of the Geological Society, London, 154, 653-666.

Liu, Y., Chen, Z., Hu, B., Jin, J., and Wu, Z. (2019). A non-uniform spatiotemporal kriging interpolation algorithm for landslide displacement data. Bulletin of Engineering Geology and the Environment. Springer, Germany, 78, 4153-4166.

Lu, P., Catani, F., Tofani, V. and Casagli, N. (2014). Quantitative hazard and risk assessment for slow-moving landslides from Persistent Scatterer Interferometry. Landslides, 11, 685-696.

Luzi, L. and Pergalani, F. (2000). A correlation between slope failures and accelerometric parameters: the 26 September 1997 earthquake (Umbria-Marche, Italy). Soil Dynamics and Earthquake Engineering, 20, 301-313.

Mancini, F., Ceppi, C. and Ritrovato, G. (2010). GIS and Statistical Analysis for Landslide Susceptibility Mapping in Daunia, Italy. Natural Hazards and Earth System Sciences, 10(9), 1851-1864.

Mandal, S. and Mondal, S. (2018). Statistical Approaches for Landslide Susceptibility Assessment and Prediction. Springer, 193 p.

Manotvani, F., Soeters, R. and Westen, C.J. (1996). Remote sensing techniques for landslides studies and hazard zonation in Europe. Geomorphology, 15, 213-225.

Massonnet, D. and Feigl, K.L. (1998). Radar interferometry and its application to changes in the earth's surface. Reviews of Geophysics, 36(4), 441-500.

Melchiorre, C., Matteucci, M., Azzoni, A. and Zanchi, A. (2008). Artificial neural networks and cluster analysis in landslide susceptibility zonation. Geomorphology, 94, 379-400.

Mesorian, H., Juteau, T., Lapierre, H., Nicolas, A., Parrot, J.F., Ricou, L.E., Rocci, G. and Rollet, M. (1973). Idées actuelles sur la constitution, l'origine et l'évolution des assemblages ophiolitiques mésogéens, Bulletin of the Geology Society of France, 15(5-6), 478-493. (in French).

Metternicht, G., Hurni, L. and Gogu, R. (2005). Remote sensing of landslides: An analysis of the potential contribution to geo-spatial systems for hazard assessment in mountainous environments. Remote Sensing of Environment 98, 284-303.

Mezösi, G., Meyer, B.C., Loibl, W., Aubrecht, C., Csorba, P. and Bata, T. (2013). Assessment of regional climate change impacts on Hungarian landscapes. Regional Environmental Change, 13, 797-811.

Michie, D., Spiegelhalter, D.J. and Taylor, C.C. (1994). Machine Learning, Neural and Statistical Classification. 290 p.

Miles, S.B. and Ho, C.L. (1999). Rigorous landslide hazard zonation using Newmark's method and stochastic ground motion simulation. Soil Dynamics and Earthquake Engineering, 18(4), 305-323.

Móga, J., Kiss, K., Szabó, M., Kériné B.A., Kéri, A., Mari, L., Knáb, M., and Iván, V. (2013). Hazards and landscape changes (degradations) on Hungarian karst mountains due to natural and human effects. Journal of Mountain Science, 10, 16-28.

Mohammady, M., Pourghasemi, H.R. and Pradhan, B. (2012). Landslide Susceptibility Mapping at Golestan Province, Iran: A Comparison between Frequency Ratio,

Dempster–Shafer, and Weights-of-Evidence Models. Journal of Asian Earth Sciences, 61, 221-236.

Montgomery, D.R., Wright, R.H. and Booth, T. (1991). Debris flow hazard mitigation for colluvium–filled swales. Bulletin Association of Engineering Geologists, 28(3), 303-323.

Montgomery, D.R. and Dietrich, W.E. (1994). A physically based model for the topographic control of shallow landsliding. Water Resources Research, 30(4), 1153-1171.

Mora, O., Mallorqui, J.J. and Broquetas, A. (2003). Linear and nonlinear terrain deformation maps from a reduced set of interferometric SAR images. IEEE Transactions on Geoscience and Remote Sensing, 41(10), 2243-2253.

Moreiras, S.M. (2005). Landslide susceptibility zonation in the Rio Mendoza valley, Argentina. Geomorphology, 66(1-4), 345-357.

Morgan, G.C., Rawlings, G.E. and Sobkowicz, J.C. (1992). Evaluating total risk to communities from large debris flows. Proceedings of the 1992 symposium on Geohazard, Toronto, 225-236.

Morris, A., Anderson, M.W., Robertson, A.H.F. and Al-Riyami, K. (2002). Extreme tectonic rotations within eastern Mediterranean ophiolite (Baër–Bassit, Syria). Earth and Planetary Science Letters, 202(2), 247-261.

Naithani, A. (2007). Macro landslide hazard zonation mapping using univariate statistical analysis in parts of Garhwal Himalaya. Journal Geological Society of India, 70, 353-368.

Nandi, A. and Shakoor, A. (2010). A GIS-Based Landslide Susceptibility Evaluation Using Bivariate and Multivariate Statistical Analyses. Engineering Geology, 110(1-2), 11-20.

NASA-POWER (2019). NASA-POWER Data from R. The NASA Langley Research Center (LaRC) POWER Project funded through the NASA Earth Science/Applied Science Program. URL: https://CRAN.R-project.org/package=nasapower.

Ng, A.H.M., Ge, L., Li, X., Abidin, H.Z., Andreas, H. and Zhang, K. (2012). Mapping land subsidence in Jakarta, Indonesia using persistent scatterer interferometry technique with ALOS PALSAR. International Journal of Applied Earth Observation and Geoinformation, 18, 232-242.

Nilsen, T.H. and Brabb, E.E. (1977). Slope stability studies in the San Francisco Bay region, California. Geological Society of America, Reviews in Engineering Geology, 3, 235-243.

Notti, D., Herrera, G., Bianchini, S., Meisina, C., García-Davalillo, J.C. and Zucca, F. (2014). A methodology for improving landslide PSI data analysis. International Journal of Remote Sensing, 35(6), 2186-2214.

Oh, H.J., Lee, S. and Soedradjat, G.M. (2009). Quantitative Landslide Susceptibility Mapping at Pemalang Area, Indonesia. Environmental Earth Sciences, 60(6), 1317-1328.

Ojeda-Moncayo, J., Locat, J., Couture, R. and Leroueil, S. (2004). The magnitude of landslides: anoverview. In: Lacerda et al. (eds.), Landslides: Evaluation and Stabilization. Proceedings of the 9th International Symposium on Landslides, Rio de Janeiro, 379-384.

Osaragi, T. (2002). Classification methods for spatial data representation. Centre for Advanced Spatial Analysis, University College London, Paper 40, 19 p.

Ozdemir, A. and Altural, T. (2013). A Comparative Study of Frequency Ratio, Weights of Evidence and Logistic Regression Methods for Landslide Susceptibility Mapping: Sultan Mountains, SW Turkey. Journal of Asian Earth Sciences, 64, 180-197.

Pachauri, A.K. and Pant, M. (1992). Landslide hazard mapping based on geological attributes. Engineering Geology, 32, 81-100.

Parrot, J.F. (1980). The Baer-Bassit (Northwest Syria) ophiolitic area. Ofioliti, 2, 279-295.

Parrot, J.F. and Whitechurch, H. (1978). Subductions antérieures au charriage nord-sud de la croûte téthysienne: facteur de métamorphisme de séries sédimentaires et volcaniques liées aux assemblages ophiolithiques syro-turcs, en schistes verts et amphibolites. Revue de Géographie Physique et de Géologie Dynamique, 20(2), 153-170. (in French).

Pellegrini, G.B. and Surian, N. (1996). Geomorphological study of the Fadalto landslide, Venetian Prealps, Italy. Geomorphology, 15, 337-350.

Pellicani, R., Argentiero, I. and Spilotro, G. (2017). GIS-based predictive models for regional-scale landslide susceptibility assessment and risk mapping along road corridors. Geomatics, Natural Hazards and Risk, 8(2), 1012-1033.

Pepe, A. (2017). Generation of Earth's Surface Three-Dimensional Displacement Time-Series by Multiple-Platform SAR Data. Time Series Analysis and Applications, 55-75.

Poudyal, C.P., Chang, C., Oh, H.J. and Lee, S. (2010). Landslide Susceptibility Maps Comparing Frequency Ratio and Artificial Neural Networks: A Case Study from the Nepal Himalaya. Environmental Earth Sciences, 61(5), 1049-1064.

Pournamdari, M., Hashim, M. and Pour, A.B. (2014). Spectral transformation of ASTER and Landsat TM bands for lithological mapping of Soghan ophiolite complex, south Iran. Advances in Space Research, 54(4), 694-709.

Pradhan, B. and Lee, S. (2009). Delineation of Landslide Hazard Areas on Penang Island, Malaysia, by Using Frequency Ratio, Logistic Regression, and Artificial Neural Network Models. Environmental Earth Sciences, 60(5), 1037-1054.

Pradhan, B., Lee, S. and Buchroithner, M.F. (2010a). A GIS-Based Back Propagation Neural Network Model and Its Cross-Application and Validation for Landslide Susceptibility Analyses. Computers, Environment and Urban Systems, 34(3), 216-235.

Pradhan, B., Lee, S. and Buchroithner, M.F. (2010b). Remote sensing and GIS-based landslide susceptibility analysis and its cross-validation in three test areas using a frequency ratio model. Photogrammetrie, Fernerkundung and Geoinformation, 1, 17-32.

Pradhan, B., Mansor, S., Pirasteh, S. and Buchroithner, M.F. (2011). Landslide Hazard and Risk Analyses at a Landslide Prone Catchment Area Using Statistical Based Geospatial Model. International Journal of Remote Sensing, 32(14), 4075-4087.

Pradhan B., Seeni M.I. and Kalantar B. (2017). Performance Evaluation and Sensitivity Analysis of Expert-Based, Statistical, Machine Learning, and Hybrid Models for Producing Landslide Susceptibility Maps. In: Pradhan B. (ed.) Laser Scanning Applications in Landslide Assessment. Springer, Cham, Switzerland, 193-232.

Purves, R.D. (1992). Optimum numerical integration methods for estimation of area-under-the-curve (AUC) and area-under-the-moment-curve (AUMC). Journal of Pharmacokinetics and Biopharmaceutics, 20(3), 211-226.

Putri, R.F., Wibirama, S., Alimuddin, I., Kuze, H. and Sumantyo, J.T.S. (2013). Monitoring and analysis of landslide hazard using DInSAR technique applied to ALOS PAlSAR imagery: A case study in Kayangan catchment area, Yogyakarta, Indonesia. Journal of Urban and Environmental Engineering, 7(2), 308-323.

Reddy, A. (2001). Remote Sensing and Geographical Information Systems. B.S. Publications, Hyderabad, 453 p.

Reichenbach, P., Galli, M., Cardinali, M., Guzzetti, F. and Ardizzone, F. (2005). Geomorphologic mapping to assess landslide risk: concepts, methods and applications in the Umbria Region of central Italy. In: Glade, T., Anderson, M.G. and Crozier, M.J. (eds.) Landslide risk assessment. John Wiley, 429-468.

Remondo, J., González, A., De Terán, J.R.D., Cendrero, A., Fabbri, A. and Chung, C.F. (2003). Validation of Landslide Susceptibility Maps; Examples and Applications from a Case Study in Northern Spain. Natural Hazards, 30, 437-449.

Rib, H.T. and Liang, T. (1978). Recognition and identification. In: Schuster, R.L. and Krizek, R.J. (eds.), Landslide Analysis and Control, National Academy of Sciences, Transportation Research Board Special Report 176, Washington, 34-80.

Righini, G., Pancioli, V., & Casagli, N. (2012). Updating landslide inventory maps using Persistent Scatterer Interferometry (PSI). International Journal of Remote Sensing, 33(7), 2068-2096.

Rosen, P.A., Hensley, S., Joughin, I.R., Li, K., Madsen, S.N., Rodriguez, E. and Goldstein, R.M. (2000). Synthetic aperture radar interferometry. Proceedings of the IEEE, 88(3), 333-382.

Rothery, D.A. (1984). Reflectances of ophiolite rocks in the Landsat MSS bands: relevance to lithological mapping by remote sensing. Journal of the Geological Society, 141(5), 933-939.

Rott, H., Scheuchl, B., Siegel, A. and Grasemann, B. (1999). Monitoring very slow slope movements by means of sar interferometry: A case study from a mass waste above a reservoir in the otztal Alps, Austria. Geophysical Research Letters, 26(11), 1629-1632.

Rott, H. and Nagle, T. (2006). The contribution of radar interferometry to the assessment of landslide hazards. Advances in Space Research, 37(4),710-719.

Ruccia, A., Ferrettib, A., Monti Guarnieria, A. and Roccaa, F. (2012). Sentinel-1 SAR interferometry applications: The outlook for sub millimetre measurements. Remote Sensing of Environment. 120, 156-163.

Rumelhart, D.E. Hinton, G.E. and Williams, R.J. (1986). Learning representations by back-propagating errors, Nature, 323, 533–536.

Sabins, F.F. (1999). Remote Sensing for Mineral Exploration. Ore Geology Reviews, 14, 157-183.

Sabto M. (1991). Probabilistic modelling applied to landslide in central Colombia using GIS procedures. MSc thesis, ITC, Enschede, Netherlands, 26 p.

Schleier, M., Bi, R., Rohn, J., Ehret, D. and Xiang, W. (2013). Robust Landslide Susceptibility Analysis by Combination of Frequency Ratio, Heuristic GIS-Methods and Ground Truth Evaluation for a Mountainous Study Area with Poor Data Availability in the Three Gorges Reservoir Area, PR China. Environmental Earth Sci., 71(7), 3007-3023.

Shahabi, H., Khezri, S., Bin Ahmad, B. and Hashim, M. (2014). Landslide Susceptibility Mapping at Central Zab Basin, Iran: A Comparison between Analytical Hierarchy Process, Frequency Ratio and Logistic Regression Models. CATENA, 115, 55-70.

Sharma, R.H. (2013). Evaluating the effect of slope curvature on slope stability by a numerical analysis. Australian Journal of Earth Sciences, 60(2), 283-290.

Silalahi, F.E.S., Pamela, Arifianti, Y. and Hidayat, F. (2019). Landslide susceptibility assessment using frequency ratio model in Bogor, West Java, Indonesia. Geoscience Letters, 6, 10.

Singh, A. and Harrison, A. (1985). Standardized principal components. International Journal of Remote Sensing, 6(6), 883-896.

Singhroy, V., Mattar, K.E. and Gray, A.L. (1998). Landslide characterisation in Canada using interferometric SAR and combined SAR and TM images. Advances in Space Research, 21(3), 465-476.

Soeters, R. and Van Westen, C.J. (1996). Slope stability: recognition, analysis and zonation. In: Turner, A. and Shuster, R. (eds.), Landslides: investigation and mitigation, National Academy Press, Washington, D. C., 129-177.

Solaimani, K., Mousavi, S.Z. and Kavian, A. (2012). Landslide Susceptibility Mapping Based on Frequency Ratio and Logistic Regression Models. Arabian Journal of Geosciences, 6(7), 2557-2569.

Solari, L., Bianchini, S., Franceschini, R., Barra, A., Monserrat, O., Thuegaz, P., Bertolo, D., Crosetto, M. and Catani, F. (2020). Satellite interferometric data for landslide intensity evaluation in mountainous regions. International Journal of Applied Earth Observation and Geoinformation, 87(102028)

Spieker, E.C. and Gori, P.L. (2000). National landslide hazards mitigation strategy: a framework for loss reduction. Open-file report 00-450, Department of Interior, U.S.G.S., USA, 49 p.

Squarzoni, C., Delacourt, C. and Allemand, P. (2003). Nine years of spatial and temporal evolution of the La Valette landslide observed by SAR interferometry. Engineering Geology, 68, 53-66.

Strozzi, T., Farina, P., Corsini, A., Ambrosi, C., Thuring, M., Zilger, J., Wiesmann, A., Wegmuller, U. and Werner, C. (2005). Survey and monitoring of landslide displacements by means of L-band satellite SAR interferometry. Landslides, 2(3), 193-201.

Stumpf, A. (2013). Landslide recognition and monitoring with remotely sensed data from passive optical sensors. PhD dissertation, University of Strasbourg, France, 263 p.

Sultan, M., Arvidson, R.E, Sturchio, N.C. and Guiness, E.A. (1987). Lithologic mapping in Arid Regions with Landsat thematic mapper data: Meatig Dome, Egypt. Geological Society of America Bulletin, 99, 748-762.

Tahhan, I., Jallad, Z., Yazbek, M.K., Alshair, E., Shaban, M. and Hammad, M. (2009). Geotechnical reports of fourteen landslide sites in Latakia province. Contracts No. (114/2004 and 131/2007) between the General Establishment of Road Transport and the General Establishment of Geology and Mineral Resources. (in Arabic).

Tarboton, D.G. and Ames, D.P. (2001). Advances in the mapping of flow networks from digital elevation data. In Bridging the Gap: World Water and Environmental Resources Congress, Orlando, Florida, USA, 1-10.

Tarikhi, P. (2010). Synthetic Aperture Radar Persistent Scatterer Interferometry (PSInSAR). (Lecture III - 13 May 2010); Power Point Presentation to the ISNET/CRTEAN Training Course on Synthetic Aperture Radar (SAR) Imagery: Processing, Interpretation and Applications, Tunis, Tunisia.

Tayara, Z. (1998). Étude hydro-pluviométrique comparative des bassins versants de la région côtière intermédiaire du Liban. Publications de l'Université Libanaise, Section des études géographiques, 1, 225p. (in French, translated into Arabic).

Terzaghi, K. (1950). Mechanism of landslides. In: Paige, A. (ed.), Application of Geology to Engineering Practice (Berkey Volume), Geological Society of America, 83-123.

Trifonov, V.G., Trubikhin, V.M., Adzhamyan, Z., Dzhallad, S., El-Khair, Y. and Ayed, K. (1991). Levant fault zone in northeast Syria. Geotectonics, 25(2), 145-154.

Tseng, C.M., Lin, C.W. and Hsieh, W.D. (2015). Landslide susceptibility analysis by means of event-based multi-temporal landslide inventories. Natural Hazards and Earth System Sciences, 3, 1137-1173.

Van Leeuwen, B. (2012). Artificial neural networks and geographic information systems for inland excess water classification. PhD dissertation, University of Szeged, 111 p.

Van Westen, C.J. (1993). Application of Geographical Information System to landslide hazard zonation. ITC Publication, ITC, Enschede, the Netherlands, 15, 245 p.

Van Westen, C.J. (2002). Use of weights of evidence modeling for landslide susceptibility mapping. International Institute for Geo-Information Science and Earth Observation, Enschede, the Netherlands, 21 p.

Van Westen, C.J., Castellanos, E. and Kuriakose, S.L. (2008). Spatial Data for Landslide Susceptibility, Hazard, and Vulnerability Assessment: An Overview. Engineering Geology, 102(3-4), 112-131.

Vandine, D.F., Moore, G., Wise, M., Vanbuskirk, C. and Gerath, R. (2004). Chapter 3 - Technical Terms and Methods. In: Wise et al. (eds.), Landslide Risk Case Studies in Forest Development Planning and Operations. B.C., Ministry of Forests, Forest Science Program, Abstract of Land Management Handbook 56, 13-26.

Varnes, D.J. (1978). Slope Movement Types and Processes. In Landslides: Analysis and Control, edited by Schuster R.L. and Krizek R.J., National Research Council, Transportation Research Board, National Academy Press, Washington D.C., 11-33.

Varnes, D.J. (1984). Landslide Hazard Zonation: A Review of Principles and Practice. UNESCO.

Varnes, D.J. and IAEG Commission on Landslides and other Mass-Movements (1984). Landslide hazard zonation: a review of principles and practice. The UNESCO Press, Paris, 63 p.

Vasco, D.W., Rucci, A., Ferretti, A., Novali, F., Bissell, R.C., Ringrose, P.S. and Wright, I.W. (2010). Satellite-Based Measurements of Surface Deformation Reveal Fluid Flow Associated with the Geological Storage of Carbon Dioxide. Geophysical Research Letters, 37(3), 1–5.

Veci, L. (2016). Sentinel-1 Toolbox: TOPS interferometry tutorial. ESA online publications. URL: https://www.scribd.com/document/353837718/S1TBX-TOPSAR-Interferometry-With-Sentinel-1-Tutorial. Downloaded: March 2018.

Watson, D.F. and Philip, G.M. (1985). A Refinement of Inverse Distance Weighted Interpolation. Geoprocessing, 2, 315-327.

Weier, J. and Herring, D. (2000). Measuring Vegetation (NDVI & EVI). NASA Earth Observatory, Washington DC.

Wessel, B. (2016). TanDEM-X Ground Segment – DEM Products Specification Document. EOC, DLR, Oberpfaffenhofen, Germany, Online Public Document TD-GS-PS-0021, Issue 3.1.

Xu, C., Xu, X. Lee, Y.H., Tan, X., Yu, G. and Dai, F. (2012). The 2010 Yushu Earthquake Triggered Landslide Hazard Mapping Using GIS and Weight of Evidence Modeling. Environmental Earth Sciences, 66(6), 1603-1616.

Yagüe-Martínez, N., P. Prats-Iraola, F. R. Gonzalez, R. Brcic, R. Shau, D. Geudtner, Eineder, M. and Bamler R. (2016). Interferometric Processing of Sentinel-1 TOPS Data. In: IEEE Transactions on Geoscience and Remote Sensing, 54(4), 2220-2234.

Ye, X., Kaufmann, H. and Guo, X.F. (2004). Landslide monitoring in the three gorges area using D-InSAR and corner reflectors. Photogrammetric Engineering and Remote Sensing, 70(10), 1167-1172.

Yesilnacar, E. and Topal, T. (2005). Landslide susceptibility mapping: A comparison of logistic regression and neural networks methods in a medium scale study, Hendek region (Turkey). Engineering Geology, 79(3-4), 251-266.

Yilmaz, I. (2009). Landslide susceptibility mapping using frequency ratio, logistic regression, artificial neural networks and their comparison: a case study from Kat landslides (Tokat-Turkey). Computers and Geosciences, 35(6), 1125-1138.

Zhang, X., Pazner, M. and Duke, N. (2007). Lithologic and mineral information extraction for gold exploration using ASTER data in the south Chocolate Mountains (California). ISPRS Journal of Photogrammetry and Remote Sensing, 62(4), 271-282.

Zorn M. (2018). Natural Disasters and Less Developed Countries. In: Pelc S. and Koderman M. (eds.) Nature, Tourism and Ethnicity as Drivers of (De)Marginalization. Perspectives on Geographical Marginality, 3, 59-78.

Zurada, J.M. (1992). Introduction to Artificial Neural Systems. West Pub. Co., NY, 683 p.

Summary

Geohazards are natural phenomena containing all the different geological processes and geographical features that are capable of triggering catastrophic events or natural disasters that threaten human beings and damage property, critical infrastructure and the natural environment. Since landslides are an important type of geohazards, it is necessary to assess and map the susceptibility of a region to landslides and the hazard of landslides with the highest available spatial and temporal resolution. Landslide hazard maps identify potential locations and sites that could be affected by landslides in an area, to reduce the risk to people living there.

The road network in northwest Syria is susceptible to unforeseen landslides. Several roads are damaged by landslides annually after intense rainfall events. These unpredicted landslides and the resulting damage to the road network threaten the lives and properties of the people who live there and cause both direct and indirect losses. Therefore, the area in northwest Syria needs a comprehensive landslide susceptibility and hazard assessment study, leading to produce a landslide hazard map and identify potential landslide areas to be taken into account by the authorities in order to guide the regional planning processes and minimize the risk in these potential landslide areas.

The main aim of this research was to develop a methodology for the creation of a landslide hazard map for the entire study area that can be updated regularly to identify all sites with a high hazard for landslides throughout the area and along the road network, in particular along the highway. This will help local authorities to take the necessary precautions at all these sites to avoid losses due to potential landslides along the highway.

In this research, a Digital Elevation Model (DEM) was generated using two different approaches for two different purposes. The first DEM, the topography-based DEM, was created on the basis of a topographical map from 1984 and was used to represent the topographical characteristics of the area before the occurrence of the landslides under investigation and to extract the derivative maps involved in the statistical analysis of landslide susceptibility, i.e. slope gradient, slope aspect, terrain curvature and drainage network. The second DEM, the SAR-based DEM, was created based on Sentinel-1 data and used as a newer and higher-resolution DEM for the PSI technique applied in this research.

Since there was no landslide inventory map for the study area before, an inventory map for all landslides that occurred in the area between 1984 and 2018 was prepared. The landslide inventory map contained 57 polygons of landslides, which were randomly divided into two sets; 70% of all landslide polygons was used as training set for the statistical analysis, and the remaining 30% was used as testing set to validate the resulting susceptibility maps. The same procedure was applied to create the non-landslide dataset which was prepared with the same size of the landslide dataset to optimally perform the statistical analysis of the landslide susceptibility. Thus, the non-landslide dataset was prepared with the same number of polygons and the same number of pixels.

The landslide susceptibility analysis was carried out using four statistical analysis methods based on the landslide and non-landslide training sets and nine causative factors influencing the spatial distribution of landslides including slope gradient, slope aspect, terrain curvature, distance to streams, distance to roads, distance to faults, lithology, land cover, and Normalized Differential Vegetation Index (NDVI). The spatial linking of the landslide data with each causative factor map and other resulting maps was carried out with the help of ArcGIS, which was indispensable for the susceptibility analysis of landslides and the validation process of all applied statistical analysis methods. Different statistical analysis methods to create the landslide susceptibility map were validated using the Area Under the Curve (AUC) analysis based on the landslide testing set and the results of the validation process were compared to select the optimal result of the landslide susceptibility.

The four statistical analysis methods used in this PhD research used for predicting landslide susceptibility were the Frequency Ratio (FR), weight-of-evidence (WoE), logistic regression (LR) and Artificial Neural Network (ANN) methods produced different results. However, the most influential causative factor according to the FR, WoE and LR statistical analysis methods was land cover, in which the soil and agriculture land class and the built-up area class have the largest influence on the occurrence of landslides, while the forests reduce the likelihood of landslides. In addition to land cover, lithology and slope gradient were also the common factors that significantly influenced and controlled the spatial distribution of landslides in the study area.

The results of the landslide susceptibility analysis showed that the use of the artificial neural network method in northwest Syria achieved excellent results in terms of susceptibility to landslides compared to the very good results obtained by applying the weight-of-evidence and logistic regression methods and the good results obtained by applying the frequency ratio method according to the literature. So, the first landslide susceptibility map for northwest Syria was created with excellent prediction accuracy based on the ANN method. Although the result of the artificial neural network method indicates excellent statistical analysis, the impossibility of identifying the most influential causative factors in the occurrence of landslides reflects the inherent limitation of this method. The AUC of the artificial neural network method was 90.28%, while for the FR, WoE and LR methods it was 70.03%, 84.79% and 87.99% respectively. Therefore, the landslide susceptibility map resulting from using the artificial neural network statistical analysis was selected as the final landslide susceptibility map and reclassified into low, moderate and high susceptibility zones to be used for the landslide hazard assessment.

Sentinel-1 SAR data and interferometric SAR techniques were used in this research to generate a high resolution digital elevation model and also to detect and measure millimetre mean velocities of ground-surface deformations and landslides in northwest Syria. However, the use of SAR data has proved to be more reliable and recommended for measuring and monitoring ground-surface deformations and landslides than for generating DEMs in northwest Syria. This is due to the decorrelation and low coherence caused mostly by dense vegetation or due to atmospheric inhomogeneity, resulting in significant errors in the final result of the DEM generation process.

The two interferometric SAR techniques used - Persistent Scatterer Interferometry (PSI) and the Differential Interferometric Synthetic Aperture Radar (D-InSAR) – in the research were conducted considering images represent the period of a main rainfall season, as rainfall is the main trigger of the landslides studied.

The comparison process between the interferometric results and the D-GPS results showed a difference at 10 validation points along the highway in the Balloran area, where the root mean square of the differences was 20.14 cm, as the D-GPS measurements are made in the vertical direction and the interferometric measurements are made in the LOS direction. The difference was considerable where the ground-surface deformation or landslide occurred parallel to the satellite azimuth direction and perpendicular to the LOS direction. However, the interferometric results can show us places where severe ground-surface deformations have occurred, which is adequate for the purpose of landslide hazard assessment.

The mean velocities of ground-surface deformation during the study period were measured using PSI technique based on Sentinel-1 data for northwest Syria. The results ranged from -47.70 to 101.64 mm per year in the satellite LOS direction and were classified into low-medium-high zones with the Equal Interval classification for each of the positive and negative groups to produce the low-medium-high zones of the ground-surface deformations in order to be used in the landslide hazard assessment.

The landslide hazard was assessed according to a landslide hazard matrix based on the integration of the landslide susceptibility results of the ANN statistical analysis and the mean velocity results of the PSI technique with the help of the GIS. This has proven to be a promising method of assessing landslide hazard using free SAR data and provides important results along the road network.

The first landslide hazard map for northwest Syria was created as well as the spatial distribution of the three landslide hazard zones along the road network and percentage of these zones along the road network, which were 43.9%, 49.6% and 6.3% respectively for low, moderate and high hazard zones. Moreover, two sites with a high hazard for landslides have been identified along the highway in the study area at Al-Qara'niya and Qastal Maaf. Therefore, it is important to give priority to emergency preparedness and traffic warnings at these two sites in the event of heavy rainfall. The results of the landslide hazard assessment need to be regularly updated to identify possible future landslide sites where the necessary precautions need to be taken to avoid losses and minimize the risk at these sites.

The workflow presented in this doctoral research showed for the first time how to create a landslide hazard map along the road network in northwest Syria using freely available Sentinel-1 data, advanced remote sensing techniques and GIS. The workflow can be used to monitor landslide hazard along the road network in other places around the world as well, particularly in areas with high rainfall and frequent landslides.